2020

Lattice Boltzmann Method For 2D and 3D Flows in Channels and Ducts with Slip and no-Slip Walls

Bu sinnah, Zainab Ali

Lattice Boltzmann Method For 2D and 3D Flows in Channels and Ducts with Slip and no-Slip Walls

by

Zainab Ali Bu Sinnah

A thesis submitted to the University of Plymouth

in partial fulfilment for the degree of

DOCTOR OF PHILOSOPHY

School of Engineering, Computing and Mathematics

July 2020

Dedication

This thesis is dedicated to the memory of my father, whose name I proudly bear. Since childhood I have missed him, and he is always in my mind and heart. I also dedicate it to the great woman in my life, my mother, who has endured me being away from her in order to support and encourage my scientific career from afar.

Acknowledgements

I would like to express my sincere thanks to the following people, who have assisted and supported me during the process of completing this thesis. Firstly, to my first supervisor and director of studies Dr David Graham, who has helped and supported me for this time. Then, to Dr Tim Reis, my second supervisor for his help with this topic and general support. I also wish to thank my wonderful family. To my mother Amnah and my dear departed father Ali, I thank you for everything you have done for me. Also my siblings: my sisters Amal, Maryam and Hawraa and my brothers Fareed, Adel and Hussain, for their encouragement and love. Thanks also to the rest of my family, and in particular Uncle Yousef, for their support and encouragement from afar. Thanks to all my supportive friends, particularly Doaa Althalathini, Randa Ali Bafadhel, Maali Al Kadhem and Toni Page, as well as countless others here in the UK and at home in Saudi Arabia. Thanks also to my colleagues in the Mathematics department at Plymouth University. Finally, thanks to Katy Richardson my English teacher for helping with the grammar.

Zainab Ali Bu Sinnah

Authors Declaration

At no time during the registration for the degree of Doctor of Philosophy has the author been registered for any other University award. Work submitted for this research degree at Plymouth University has not formed part of any other degree either at Plymouth University or at another establishment.

Workshop

- What is LaTex? (27 November 2015).
- The Postgraduate Society Conference (2 December 2015).
- Latex getting start (8 December 2015).
- Math3610 fluid dynamics (Semester 2 2016).
- SALT (Supporting Assessment, Learning and Teaching) workshop on Wednesday (10th January 2017- 4th July 2018).
- (UKCOMES Workshop 2016) UK Consortiun on Mesoscale Engineering Sciences. Work shop about Lattice Boltzmann Methods and Applications (12-13 December 2016).
- Online course (Fundamentals of Lattice Boltzmann Method) 15 January -6 February 2018.

Self Learning

- I learned to write algorithms or codes using Fortran language (Online).
- I learned to parallel computing by using message passing interface (MPI) (Online).
- I learned to plot the data by using LaTex, Gnuplot and CorelDRAW (Online).

Posters and conference presentations:

Applied mathematics seminar Plymouth Univerity, UK. Presentation: 2017-2018-2019.

Postgraduate Research Showcase Plymouth Univerity, UK. Poster: 2017.

Particle-based Methods conference 2017 Hannover, Germany, UK. Attend: 26-28 September 2017.

BAMC conference 2018 university of St Andrews, Scotland,UK. Poster: 26-29 March 2018.

ECCM 6-ECFD 7 confrence 2018 6th European Conference on Computational Mechanics (ECCM 6) 7th European Conference on Computational Fluid Dynamics (ECFD 7), Glasgow, UK. Oral Presentation : 11-15 June 2018.

Publications:

Bu Sinnah, Z and Graham, D. I and Reis, T. *LATTICE BOLTZMANN MODELLING OF PULSATILE FLOW USING MOMENT BOUNDARY CONDITIONS.* 6th European Conference on Comput. Mech. (ECCM 6) 7th European Conference on Comput. Fluid Dynamics (ECFD 7), Glasgow, UK. 2018

Word count for the main body of this thesis: **78525**

Signed: Zainab Ali Bu sinnah

Date:

Lattice Boltzmann Method For 2D and 3D Flows in Channels and Ducts with Slip and no-Slip Walls.

Zainab Ali Bu Sinnah

Abstract

THE aim of this thesis is to study the Lattice Boltzmann method for fluid dynamics by using moment based boundary condition to implement no-slip and partial slip boundary conditions in two and three dimensions. The main topics are the theory of the Lattice Boltzmann method, an examination of boundary conditions and the application of the Lattice Boltzmann method to a variety of fluid flows. We developed and successfully implemented combinations of no-slip, Navier-slip, pressure boundaries and inlet conditions in two and three dimensions using moment-based boundary conditions including careful treatments of conditions along edges and at corners. A useful advantage of the use of moment-based boundary conditions is that it allows for Navier-slip conditions to be implemented exactly *i.e.* without the use of arbitrary coefficients required in some other methods.

The first application of the method is pulsatile fluid flow with no-slip and Navier-slip boundary conditions in two and three dimensions. The results are in good agreement with exact solutions and some interesting results related to non-conver gence of acoustic scaling for the two dimensions are found. The next application is three-dimensional laminar flow in a square duct driven by a body force. The results agree well with the analytical solution. Next, a study is presented of the rarefaction and compressibility effect on laminar flow between two parallel plates and in a three-dimensional micro-duct which are driven by differential pressures at the inlet and outlet. The results are again compatible with those found in the literature. Finally, we investigate the developing three-dimensional laminar flow in the entrance region of a rectangular channel. Results demonstrate some interesting Reynolds number dependence and are found to be in line with the literature for high Reynolds number.

Contents

List of Figures

List of Tables

Chapter 1

Introduction

1.1 Overview and History

1.1.1 General Overview

In order to find the numerical solution to the governing equations of motion in fluid dynamics, the use of the Computational Fluid Dynamics (CFD) has become an increasingly common method [12]. In using CFD, the continuum domain is deconstructed into a set of sub-domains as part of a computational mesh. Furthermore, CFD techniques are used to numerically solve mathematical models of these equations of motion. For example, as the Navier-Stokes equations are not generally solvable analytically due to their non-linear terms, they are instead solved using numerical methods [63]. Consequently, the macroscopic quantities such as density, velocity and pressure which need to be identified in order to solve Navier-Stokes equations must be found using numerical methods [64]. In recent years, while conventional methods such as the Finite Difference method (FDM) and the Finite Volume method (FVM) have still been used extensively, the Lattice Boltzmann method (LBM) has become increasingly common. This method has successfully achieved the simulation of a wide variety of fluid flows. Within the LBM, macroscopic quantities are acquired by computing the hydrodynamic moments of the distribution function [26]. Within this method, the simplest model or approach is the Bhatnagar-Gross-Krook model (BGK) created by Bhatnagar, Gross and Krook [7], which consists of the Lattice Boltzmann eqaution (LBE) with a linearised collision operator. In LBM, it is commonly known that the equations for continuity and momentum in the case of low Mach numbers are obtained when using the Chapman-Enskog approach [27].

1.1.2 Overview of LBM

Originally, the LBM was derived from the Lattice Gas Automata (LGA) method. The original model behind this LGA method is the HPP model, which was invented by Hardy-Pomeaude and Pazzi in 1973 [24], [74]. Under the Lattice Gas Automata method, the lattice is regular, and is used to model the attributes of the gas. The gas is expressed by the Boolean particles in which velocity is 0 or 1. The two processes of collision and propagation (or streaming) for the dynamics of gas particles are also represented. Moreover, the space, time and particle velocity are discretised in the Lattice Gas Automata method. However, the LGA method has many shortcomings such as the presence of noise which is caused by the nature of the Boolean method and non-Galilean invariance. The FHP model, on the other hand, invented by Frish, Hasslacher, and Pomeau in 1986, comprises a hexagonal lattice and is able to recover the correct Euler and Navier-Stokes equations [24], [74]. In addition to this improvement, Zanetti and McNamara [44] in 1988 were able to mitigate the effect of statistical noise by replacing the Boolean number of the LGA with ensemble average of the Boolean number, known as distribution functions, and it is this replacement that led to the creation of the LBM. Further, Higuera and Jimenez [31] simplified the LBE with a linearised collision operator based on the supposition that the distribution functions are near to local equilibrium state. The BGK model is a simple linearised collision operator, containing a local equilibrium function [7]. This model is also able to recover the Navier-Stokes equations by using the equilibrium function, even in the lattice BGK (LBGK) model.

1.1.3 Properties of the LBM

The LBM overcame the shortfalls of the LGA by using the simple model of a linearised collision operator, which is based on the LBGK collision model [7]. While the approach of using the Lattice Boltzmann method does not model the behaviour of individual molecules, it does describe how a fluid behaves at a macroscopic level. Due to this approach, the behaviour of many microscopic molecules remains unidentified by this macroscopic dynamic. However, the approach of

using LBM is able to efficiently present a numerical calculation of how a fluid behaves at this macroscopic level.

Over the course of the last decades, this appeal of using the LBM to numerically solve the Navier-Stokes equations has become a popular topic among researchers in the area of fluid dynamics [74]. However, while some have used the LBM as an alternative method to the numerical approach of the Navier-Stokes equations, many differences exist between the Lattice Boltzmann method and the Navier-Stokes approach. For example:

- The discrete velocity model of the LBM consists of a set of partial differential equations (PDEs) of the first order of kinetic equations [8] [75], while the Navier-Stokes equations consist PDEs of the second order.
- The LBM involves the use of linear advection terms, while the Navier-Stokes equations contain non-linear convection terms that require discretisation [75]. Moreover, the Navier-Stokes equations enable the identification of integral or differential formulations [75].
- The pressure represented in the LBM is produced according to an ideal equation of state, whereas the presence of pressure under other methods that derive solutions using the Navier-Stokes equation is often calculated from a Poisson solver [75] [62].

In addition to these above points, the LBM is derived either from LGCA (Lattice Gas Cellular Automata) [24], [74] or a direct discretisation for the Boltzmann equation (BE) [8], [7], and has many advantages, such as:

- The Lattice Boltzmann method can be an explicit formula, a finite approximation of the Navier-Stokes equations or Lagrangian forms. In the latter, the equilibrium distribution function consists of macroscopic Lagrangian variables at time steps t and $t + \delta_t$. This method was proposed by Yan in 1998 [19]. The Lagrangian lattice Boltzmann method is suggested for solving Euler equations.

- The LBM lattice is usually fixed and regular, its programming is simple and the influence of microscopic interaction can easily be accounted for.

- As with other methods there are many different boundary conditions that can be treated within LBM. Some of these boundary conditions have exact form to determine the slip velocity [48] such as moment-based boundary conditions [58], [23]. Whilst, many treatments of these boundaries using combination of boundaries such as the combination of bounce back and specular boundary conditions which used some parameters to determine the slip velocity [68], [65], [40]. These boundary conditions are explained in details in chapter 4.

- The LBM with moment-based boundary conditions is a good choice to implement Navier-slip boundary conditions in slip regime. The reason for this is the special advantages of moment-based boundary conditions such as locality, exact and a direct equivalence between the lattice Boltzmann implementation and hydrodynamics conditions. These advantages allow for Navier-Slip conditions to be executed precisely or exactly at grid points without the need for phenomenological coefficients or additional numerical approximations [58]. The locality of moment-based boundary conditions means the the distribution functions used come from the boundary nodes and the exact advantage means the hydrodynamics conditions are allocated on the boundaries.

- The Lattice Boltzmann method is effective for dealing with complex boundaries, which is important when modelling fluids that are flowing through a porous medium [64], and this is due to the kinetic-style of the Lattice Boltzmann [11].

- The LBM is also ideal for application to flows with multiple phases and components [54].

- The LBM is easy to parallelise on modern computer architectures compared with traditional finite volume or finite element analysis CFD techniques. This

is due to the locality of the LBM algorithm which is discretised in space and time [52], [69].

An alternative approach to derive the Lattice Boltzmann equation is by the truncation of the velocity space of the Boltzmann equation with a simplified collision operator (BGK model) [60], [26],[27] and [28]. This approach will be explained further in chapter 3.

1.2 The Boltzmann Equation, BGK Equation and Hydrodynamic Equations

A fluid is composed of a huge set of molecules (approximation to the order of the Avogrado number, $A_v \sim 10^{23}$) which collide with each other and move in a random way; an interaction that is much weaker than that in a solid. The mathematical models for fluid dynamics will depend on the length and time scales at which the fluid is observed. In general, though, there are three mathematical models that can describe the motion of a fluid, namely: the microscopic model, which traces the motions of individual particles; the mesoscopic model; and the continuum macroscopic model. Each is addressed in more detail below.

1.2.1 Microscopic Description: Molecular Dynamics

The molecular dynamics of fluid are usually described by Newton's second law, which is expressed as $m\ddot{\mathbf{r}} = \mathbf{f}_i$, where m represents the molecule mass, $\ddot{\mathbf{r}}$ is the acceleration, and the dots represent the time derivatives [20]. The $\mathbf{f}_i$ is the total force - which is defined as $\mathbf{f}_i = \sum_{j=1, j\neq i}^{N} f_{ij} + \mathbf{g}_i$ - where f_{ij} represents the force which is exerted by molecule j, N represents the number of molecules in the system and $\mathbf{g}_i$ is an external force such as gravity. By solving Newton's second law we obtain the molecule position and velocity at every time interval, then we can calculate the macroscopic qualities of the fluid such as density, velocity and temperature by taking the average of microscopic quantities.

1.2.2 Mesoscopic Description: Kinetic Theory-Continuous Boltzmann-BGK Equation

The Boltzmann kinetic theory describes the evolution of a mass probability distribution $f(\mathbf{x},\mathbf{c},t)$ where $\mathbf{x}$ is the position and $\mathbf{c}$ is the velocity of particle at time t. This mass probability distribution $f(\mathbf{x},\mathbf{c},t)$ was derived by Ludwig Boltzmann in 1872 [8]. The integral of $f(\mathbf{x},\mathbf{c},t)$ over $\mathbf{x}$ and $\mathbf{c}$ that gives the mass $f(\mathbf{x},\mathbf{c},t)\,d^3\mathbf{x}d^3\mathbf{c}$. We can define the density, ρ, the momentum, $\rho\mathbf{u}$, and the internal energy, $\rho\varepsilon$, from this distribution function, respectively, as:

$$\begin{aligned}\rho(\mathbf{x},t) &= \int f(\mathbf{x},\mathbf{c},t)\,d\mathbf{c},\\ \rho(\mathbf{x},t)\,\mathbf{u}(\mathbf{x},t) &= \int \mathbf{c} f(\mathbf{x},\mathbf{c},t)\,d\mathbf{c},\\ \rho(\mathbf{x},t)\,\varepsilon(\mathbf{x},t) &= \frac{1}{2}\int \mathbf{c}\cdot\mathbf{c} f(\mathbf{x},\mathbf{c},t)\,d\mathbf{c}.\end{aligned} \tag{1.2.1}$$

The integration is performed in molecular or particle velocity $\mathbf{c}$. We can define the internal energy for monatomic ideal-gas as:

$$\rho\varepsilon = \frac{D}{2}\rho\theta, \tag{1.2.2}$$

where D is the dimension of space, $\theta = \frac{k_B}{m}T$ or $\theta = RT = \frac{k_B}{m}T$, where $R = \frac{k_B}{m}$ and R is the universal gas constant, k_B is the Boltzmann constant, m is the mass of a gas molecule and T is the temperature. The Boltzmann equation [10], which is defined as

$$\partial_t f(\mathbf{x},\mathbf{c},t) + \mathbf{c}\cdot\bigtriangledown_{\mathbf{x}} f(\mathbf{x},\mathbf{c},t) = \Omega, \tag{1.2.3}$$

is a kind of non-linear differential equation where Ω is a collision operator and this collision operator represents what happens when particles collide with each other. The collision operator is approximated in a number of simplified models such as the BGK model [7]. This model has been shown to be accurate for modelling the effect of collision between particles [7]. It represents the collision process as

relaxation to a local equilibrium state. This model is written as

$$\partial_t f(x,\mathbf{c},t) + \mathbf{c}\cdot\bigtriangledown_x f(x,\mathbf{c},t) = -\frac{1}{\tau}\left(f - f^0\right), \tag{1.2.4}$$

where τ is the the relaxation time. This model explains the effect of the intermolecular collision and it satisfies the conservation of mass, momentum and energy.

The equilibrium state f^0 is given by using the Maxwell-Boltzmann distribution function [10], which is defined as

$$f^0 = \frac{\rho}{(2\pi\theta)^{\frac{D}{2}}} exp\left(-\frac{(\mathbf{c}-\mathbf{u}(\mathbf{x},t))^2}{2\theta}\right). \tag{1.2.5}$$

1.2.3 Macroscopic Description: Hydrodynamic Equations

The distribution of fluid works as a continuum through the domain regardless of the molecular properties and interactions which are represented by the viscosity and thermal conductivity [20]. The fluid has its own properties such as density, velocity and temperature. To determine the validity of the continuum model we can check the Knudsen number of the fluid system which is defined as $k_n = \frac{L_{mfp}}{L}$, where L_{mfp} is the mean free path that is the average distance travelled between collisions and L is a representative length scale for flow domain or object inside the flow.

The partial differential equations (PDEs) describing the motion of fluid and conservation law are the Navier-Stokes equations, expressed as

$$\frac{\partial\rho}{\partial t} + \bigtriangledown\cdot(\rho\mathbf{u}) = 0, \tag{1.2.6}$$

$$\rho\frac{\partial\mathbf{u}}{\partial t} + \rho(\mathbf{u}\cdot\bigtriangledown)\mathbf{u} = -\bigtriangledown p + \bigtriangledown\cdot\boldsymbol{\tau}. \tag{1.2.7}$$

These are known as the continuity equation and the momentum equation, respectively. Here, p represents the pressure and $\boldsymbol{\tau}$ represents the deviatoric stress tensor, the latter of which is defined as $\boldsymbol{\tau} = 2\mu\mathbf{S} + \mu'(\bigtriangledown\cdot\mathbf{u})\boldsymbol{I}$, where μ and μ' are the first and second dynamic viscosities, respectively, and $\mathbf{S} = \frac{1}{2}\left(\bigtriangledown\mathbf{u} + (\bigtriangledown\mathbf{u})^T\right)$

is the strain-rate tensor. Neglecting the viscosities leads to the Euler equations. The fluid is incompressible if the density does not change with the motion, i.e. $\bigtriangledown \cdot \mathbf{u} = 0$. So, the stress tensor becomes $\tau = 2\mu\mathbf{S}$ and the continuity equation (1.2.6) becomes

$$\frac{\partial \rho}{\partial t} + \mathbf{u} \cdot \bigtriangledown \rho = 0.$$

The compressibility of a flow is measured by the Mach number, which is defined as $Ma = \frac{U}{c_s} \ll 1$, where U is taken as a characteristic velocity and c_s is the sound speed. The fluid is considered incompressible when the Mach number is $Ma \ll 1$. When we combine the BGK equation with the small Knudsen number we obtain the Navier-Stokes equations [9]. There are many other approaches to combine them such as Chapman-Enskog expansions [10] to link the Boltzmann equation with macroscopic hydrodynamics. The aim of this approach is to find solutions Eq (2.1.28) which very slowly over the timescales much longer than the collisions time.

The Chapman-Enskog expansion is based on expanding the distribution function and separating timescales as

$$\begin{aligned} f &= f^0 + \tau f^1 + \tau^2 f^2 + ..., \\ \partial_t &= \partial_{t_0} + \tau \partial_{t_1} ..., \end{aligned} \tag{1.2.8}$$

where f^0 is the equilibrium distribution function, τ is the small parameter, t_1 refers to the linear (sound wave) regime, and t_2 refers to the changes in long term viscous dynamic [56].

1.2.4 The objective of the study

The objective of this thesis is to use the second order approximation of the Lattice Boltzmann equation with moment based boundary conditions to simulate two-dimensional fluid dynamic flows and extend moment-based boundary conditions to simulate three-dimensional fluid dynamic flows. Furthermore, it aims to examine the efficiency and accuracy of moment-based boundary conditions when using different types of geometry, as well as in the implementation of boundary

conditions such as periodic, pressure, inflow, no-slip and Navier-slip. Another aim of this thesis is to use moment-based boundary conditions' advantage of being able to determine the exact value of slip velocity when implementing Navier-slip boundary conditions. This is in contrast with some other boundary conditions, such as the combination of bounce back and specular or diffusive boundary conditions, which estimate the value of slip velocity using parameters.

The fluid flows are simulated using a single relaxation time (LBGK) model. The first simulation is pulsatile flow between two parallel plates in two and three dimensions, under periodic boundary conditions at the inlet and outlet and no-slip boundary conditions and Navier-slip boundary conditions at the wall. The results match very closely with the results in the literature [25], [14], [5], [36] and [4]. The second application is a three-dimensional square duct flow under periodic boundary conditions at the inlet and outlet, and no-slip boundary conditions and Navier-slip boundary conditions at the wall. The results compare positively with the analytical solutions [1]. The third simulation is of two and three dimensional flows in a micro-channel under pressure boundary conditions at the inlet and outlet, and no-slip and Navier-slip boundary conditions at the wall. These results also concur with those in the literature [3], [40], [38] and [33]. The final simulation was created to study the hydrodynamic entrance region of channels. The results for the square and rectangular ducts are comparable with the results presented by Niya *et. al* [41] and the results for the narrow duct concur with analytical solutions [15], [16].

1.2.5 Outline of the thesis

In chapter 2, the derivation of the Lattice Boltzmann equation from kinetic theory is given, using a projection to discretise the velocity distribution function on Hermite polynomials, and time and space using the Trapezoidal Rule. In chapter 3, lattices in two and three dimensions are defined and the Chapman-Enskog approach is clarified to obtain Navier-Stokes equations from the Boltzmann equation.

Various boundary conditions, such as standard bounce back, modified bounce

back, halfway bounce back and periodic, are defined in chapter 4 and used to simulate Poiseuille flow. The moment-based boundary technique is also illustrated, and then applied to Poiseuille flow in two and three dimensions. Chapters 5 and 6 show pulsatile flow simulated using moment-based boundary conditions which implement no-slip and Navier-slip boundary conditions. The results are compared with the analytical solutions.

A new model for moment-based boundary conditions with Navier-slip boundary conditions in three dimensions is presented in Chapter 7. This applies a three dimensional laminar flow in a square duct which is driven by body force. The results are compared with the analytical solution. Chapter 8 then includes two further applications for the moment-based boundary condition with Navier-slip boundary conditions in two and three dimensions using pressure boundary condition at the inlet and outlet. The first focuses on the effects of rarefaction and compressibility on laminar flow between two parallel plates, and the second on a three-dimensional micro-duct. The final chapter 9 contains another model for moment-based boundary conditions with Navier-slip boundary conditions in three dimensions. This is proposed in order to study a fully developed laminar flow in the entrance region of channels.

Chapter 2

Lattice Boltzmann Equation

2.1 Discretisation of the BGK Equation

2.1.1 Discrete Velocity BGK Equation - Projection BGK Equation on Hermite Basis

Grad, in 1949 [18], proposed an approach to approximate the BE. This approach expanded a single particle distribution function on the basis of Hermite orthogonal polynomials. Grad chose the Hermite polynomials because their expansion coefficients are the velocity moments of the distribution function [18]. The velocity moments of the distribution function are not directly changed by truncating the higher order terms in the Hermite expansion [18]. Grad's 13-moment system includes five thermodynamic variables: mass density, fluid velocity, internal energy and their fluxes. The higher order moments, which are obtained by Chapman-Enskog expansions [60], are difficult to solve. In this section, we will focus on the idea of the projection of the distribution function on Hermite polynomials to discretise the BGK equation and force terms [60], [53], [45].

The definition of the projection for the velocity distribution function on Hermite polynomials is

$$f(\mathbf{x},\mathbf{c},t) = \omega(\mathbf{c}) \sum_{n=0}^{\infty} \frac{1}{n!} H^n_{\boldsymbol{\alpha}}(\mathbf{c})\, a^n_{\boldsymbol{\alpha}}(\mathbf{x},t), \tag{2.1.1}$$

where $\omega(\mathbf{c})$ is a weight function which is defined as $\omega(\mathbf{c}) = \frac{1}{(2\pi)^{\frac{D}{2}}} exp\left(\frac{-c^2}{2}\right)$ with $c^2 = \mathbf{c}\cdot\mathbf{c}$. The $H^n_{\boldsymbol{\alpha}}$ is the Hermite polynomials of degree n, defined as $H^n_{\boldsymbol{\alpha}} = \frac{(-1)^n}{\omega(\mathbf{c})} d^n_{c_{\boldsymbol{\alpha}}} \omega(\mathbf{c})$, the $\boldsymbol{\alpha}$ is defined as $\boldsymbol{\alpha} = (\alpha_1, \alpha_2, ..., \alpha_n)$ and $\alpha_i = 1,2,...,D$, $i = 1,2,...,n$, where D is the dimension. The n^{th}-rank symmetric tensor of the n^{th} degree poly-

nomial can be written as

$$H^n_{\boldsymbol{\alpha}} = \frac{(-1)^n}{\omega(\mathbf{c})} \bigtriangledown^n_{c_{\boldsymbol{\alpha}}} \omega(\mathbf{c}). \tag{2.1.2}$$

The Hermite polynomials form an orthogonal set. They have an orthogonal basis on the Hilbert space associated with the inner product $\langle f,g\rangle = \int \omega f g d\mathbf{c}$. The orthogonality relation is

$$\int \omega(\mathbf{c}) H^m_{\boldsymbol{\alpha}} H^n_{\boldsymbol{\beta}} = \delta_{nm} \boldsymbol{\delta}^n_{\boldsymbol{\alpha\beta}}, \tag{2.1.3}$$

where $\boldsymbol{\delta}^n_{\boldsymbol{\alpha\beta}}$ is one if $\boldsymbol{\alpha} = (\alpha_1, \alpha_2, ..., \alpha_n)$ is a permutation of $\boldsymbol{\beta} = (\beta_1, \beta_2, ..., \beta_n)$ and vanishes otherwise. The first five Hermite polynomials are

$$\begin{aligned}
H^0(\mathbf{c}) &= 1, \\
H^1_\alpha(\mathbf{c}) &= c_\alpha, \\
H^2_{\alpha\beta}(\mathbf{c}) &= c_\alpha c_\beta - \delta_{\alpha\beta}, \\
H^3_{\alpha\beta\gamma}(\mathbf{c}) &= c_\alpha c_\beta c_\gamma - \left(\delta_{\alpha\beta} c_\gamma + \delta_{\alpha\gamma} c_\beta + \delta_{\beta\gamma} c_\alpha\right), \\
H^4_{\alpha\beta\gamma\delta}(\mathbf{c}) &= c_\alpha c_\beta c_\gamma c_\delta - \left(\delta_{\alpha\beta} c_\gamma c_\delta + \delta_{\alpha\gamma} c_\beta c_\delta + \delta_{\beta\gamma} c_\alpha c_\delta + \delta_{\alpha\delta} c_\beta c_\gamma + \delta_{\beta\delta} c_\alpha c_\gamma + \delta_{\delta\gamma} c_\beta c_\alpha\right) \\
&\quad + \left(\delta_{\alpha\beta}\delta_{\gamma\delta} + \delta_{\alpha\gamma}\delta_{\beta\delta} + \delta_{\alpha\delta}\delta_{\beta\gamma}\right),
\end{aligned} \tag{2.1.4}$$

where the $a^n_{\boldsymbol{\alpha}}$ are expansion coefficients

$$a^n_{\boldsymbol{\alpha}} = \int f(\mathbf{x}, \mathbf{c}, t) H^n_{\boldsymbol{\alpha}}(\mathbf{c}) d\mathbf{c}. \tag{2.1.5}$$

We notice from formula (2.1.5) that the expansion coefficients represent linear combinations of velocity moments of the distribution function.

After substituting the first five Hermite polynomials in (2.1.5), the first five coeffi-

cients are

$$
\begin{aligned}
a^0_\alpha &= \rho, \\
a^1_\alpha &= \rho u_\alpha, \\
a^2_{\alpha\beta} &= P_{\alpha\beta} + \rho\left(u_\alpha u_\beta - \delta_{\alpha\beta}\right), \\
a^3_{\alpha\beta\gamma} &= Q_{\alpha\beta\gamma} + u_\alpha a^2_{\beta\gamma} + u_\beta a^2_{\alpha\gamma} + u_\gamma a^2_{\alpha\beta} + (1-D)\,\rho u_\alpha u_\beta u_\gamma, \\
a^4_{\alpha\beta\gamma\delta} &= R_{\alpha\beta\gamma\delta} + \left(P_{\alpha\beta}\delta_{\gamma\delta} + P_{\alpha\gamma}\delta_{\beta\delta} + P_{\alpha\delta}\delta_{\beta\gamma} + P_{\beta\gamma}\delta_{\alpha\delta} + P_{\beta\delta}\delta_{\gamma\alpha} + P_{\gamma\delta}\delta_{\alpha\beta}\right) + \\
&\quad \left(\delta_{\alpha\beta}\delta_{\gamma\delta} + \delta_{\alpha\gamma}\delta_{\beta\delta} + \delta_{\alpha\delta}\delta_{\beta\gamma}\right),
\end{aligned} \tag{2.1.6}
$$

where $Q_{\alpha\beta\gamma} = \int c_\alpha c_\beta c_\gamma f(\mathbf{x},\mathbf{c},t)\,d\mathbf{c}$, $R_{\alpha\beta\gamma\delta} = \int c_\alpha c_\beta c_\gamma c_\delta f(\mathbf{x},\mathbf{c},t)\,d\mathbf{c}$ and $P_{\alpha\delta} = \rho c_s^2$.

The truncation of the projection of the velocity distribution function on the Hermite polynomials up to the N^{th} order is

$$
f(\mathbf{x},\mathbf{c},t) \simeq f^N = \omega(\mathbf{c}) \sum_{n=0}^{N} \frac{1}{n!} H^n_{\boldsymbol{\alpha}}(\mathbf{c})\, a^n_{\boldsymbol{\alpha}}(\mathbf{x},t). \tag{2.1.7}
$$

The velocity moments of f^N are the same as the velocity moments which are derived from $f(\mathbf{x},\mathbf{c},t)$.

This leads to the creation of a dynamic system of a finite set of macroscopic equations which match the macroscopic equations in Grad's 13-moment system. Also, the truncation of Eq (2.1.7) is complete, unique and determined by its values at a set of discrete abscissae. This is valid because the integration of the right hand of the Hermite coefficient, Eq (2.1.5), can be written as

$$
a^n_{\boldsymbol{\alpha}} = \int f(\mathbf{x},\mathbf{c},t)\, H^n_{\boldsymbol{\alpha}}(\mathbf{c})\,d\mathbf{c} = \int f^N(\mathbf{x},\mathbf{c},t)\, H^n_{\boldsymbol{\alpha}}(\mathbf{c})\,d\mathbf{c} = \int \omega(\mathbf{c})\, r(\mathbf{x},\mathbf{c},t), \tag{2.1.8}
$$

where $r(\mathbf{x},\mathbf{c},t)$ is a polynomial of degree $\leq 2N$.

The Gauss-Hermite quadrature is defined as "for a given a function $f(\mathbf{c})$ seek to obtain the best estimate of the integral $\int_a^b \omega(c)\, f(c)\,dc$ by choosing the optimal

set of abscissae $c_i, i = 1,...,n$ such that

$$\int_a^b \omega(c) f(c) dc \simeq \sum_{i=1}^{n} \omega_i f(c_i), \tag{2.1.9}$$

where $\omega_i, i = 1,2,...,n$ is a set of constant weights " [60] (p.434).
So, by using Gauss-Hermite quadrature on Hermite coefficient in Eq (2.1.8), we obtain

$$a^n_{\boldsymbol{\alpha}} = \int \omega(\mathbf{c}) r(\mathbf{x},\mathbf{c}_i,t) = \sum_{i=0}^{d-1} \omega_i r(\mathbf{x},\mathbf{c}_i,t) = \sum_{i=0}^{d-1} \frac{\omega_i}{\omega(\mathbf{c}_i)} f^N(\mathbf{x},\mathbf{c}_i,t) H^n_{\boldsymbol{\alpha}}(\mathbf{c}_i), \tag{2.1.10}$$

where $r(\mathbf{x},\mathbf{c}_i,t) = \dfrac{1}{\omega(\mathbf{c}_i)} f^N(\mathbf{x},\mathbf{c}_i,t) H^n_{\boldsymbol{\alpha}}(\mathbf{c}_i)$.

The set of discrete functions $\left\{ f^N(\mathbf{x},\mathbf{c}_i,t) : i = 1,..,d \right\}$ fully determines $f^N(\mathbf{x},\mathbf{c},t)$ and its first moments. We rescale the spatial variable and temporal variable by δ_x and δ_t, respectively. Also, we rescale all velocities by the factor $c = \frac{\delta_x}{\delta_t}$ which is called the lattice velocity and which depends on the sound speed c_s. This has a slight effect on Hermite polynomial and Hermite coefficient

$$\begin{aligned}
H^0_i(\mathbf{c}) &= 1, \\
H^1_{i\alpha}(\mathbf{c}) &= c_{i\alpha}, \\
H^2_{i\alpha\beta}(\mathbf{c}) &= c_{i\alpha}c_{i\beta} - c_s^2\delta_{\alpha\beta}, \\
H^3_{i\alpha\beta\gamma}(\mathbf{c}) &= c_{i\alpha}c_{i\beta}c_{i\gamma} - c_s^2\left(\delta_{\alpha\beta}c_\gamma + \delta_{\alpha\gamma}c_{i\beta} + \delta_{\beta\gamma}c_{i\alpha}\right), \\
H^4_{i\alpha\beta\gamma\delta}(\mathbf{c}) &= c_{i\alpha}c_{i\beta}c_{i\gamma}c_{i\delta} - c_s^2\left(\delta_{\alpha\beta}c_{i\gamma}c_{i\delta} + \delta_{\alpha\gamma}c_{i\beta}c_{i\delta} + \delta_{\beta\gamma}c_{i\alpha}c_{i\delta}\right. \\
&\quad \left. + \delta_{\alpha\delta}c_{i\beta}c_{i\gamma} + \delta_{\beta\delta}c_{i\alpha}c_{i\gamma} + \delta_{\delta\gamma}c_{i\beta}c_{i\alpha}\right) + c_s^4\left(\delta_{\alpha\beta}\delta_{\gamma\delta} + \delta_{\alpha\gamma}\delta_{\beta\delta} + \delta_{\alpha\delta}\delta_{\beta\gamma}\right),
\end{aligned} \tag{2.1.11}$$

and the orthogonality basis of Hermite polynomial will be

$$\sum_i \omega_i H^m_{\alpha_1,\alpha_2,...,\alpha_m} H^n_{\beta_1,\beta_2,...\beta_n} = \delta_{mn} c_s^{2m}\left(\delta_{\alpha_1\beta_1}...\delta_{\alpha_m\beta_n} + perm\right), \tag{2.1.12}$$

where $perm$ means all the α_i permutations in the first index and β_i permutations

in the second index of $\delta_{\alpha_i\beta_i}$ [42]. For non-vanishing products we obtain

$$\begin{aligned}
\sum_i \omega_i H^0_{i\alpha} H^0_{i\beta} &= 1, \\
\sum_i \omega_i H^1_{i\alpha} H^1_{i\beta} &= c_s^2 \delta_{\alpha\beta}, \\
\sum_i \omega_i H^2_{i\alpha\beta} H^2_{i\gamma\delta} &= c_s^4 \left(\delta_{\alpha\gamma}\delta_{\beta\delta} + \delta_{\alpha\delta}\delta_{\beta\gamma}\right), \\
\sum_i \omega_i H^3_{i\alpha\beta\gamma} H^3_{i\delta\varepsilon\zeta} &= c_s^6 \left(\delta_{\alpha\delta}\left(\delta_{\beta\varepsilon}\delta_{\gamma\zeta} + \delta_{\beta\zeta}\delta_{\gamma\varepsilon}\right) + \delta_{\alpha\varepsilon}\left(\delta_{\beta\delta}\delta_{\gamma\zeta} + \delta_{\beta\zeta}\delta_{\gamma\delta}\right)\right. \\
&\quad \left. + \delta_{\alpha\zeta}\left(\delta_{\beta\delta}\delta_{\gamma\varepsilon} + \delta_{\beta\varepsilon}\delta_{\gamma\delta}\right)\right).
\end{aligned} \tag{2.1.13}$$

We can find the $f^N(\mathbf{c}_i)$ by projecting the BGK on the Hermite basis and evaluating them at $\mathbf{c}_i$. [13]. The left hand side of projection is

$$\begin{aligned}
&\int \partial_t f(\mathbf{x},\mathbf{c},t) + \mathbf{c}\cdot\nabla_{\mathbf{x}} f(\mathbf{x},\mathbf{c},t) + g\cdot\nabla_{\mathbf{c}} f(\mathbf{x},\mathbf{c},t) H^n_{\boldsymbol{\alpha}}(\mathbf{c})\, d\mathbf{c} \\
&= \partial_t\left(\int f H^n_{\boldsymbol{\alpha}}(\mathbf{c})\, d\mathbf{c}\right) + \int \nabla_{\mathbf{x}}\cdot\left(\mathbf{c} H^n_{\boldsymbol{\alpha}}\right) f d\mathbf{c} + \int \left(\nabla_{\mathbf{c}}\cdot\left(\mathbf{g}(\mathbf{x},t) f\right)\right) H^n_{\boldsymbol{\alpha}} d\mathbf{c}.
\end{aligned} \tag{2.1.14}$$

Using either the expression $\mathbf{c}_{\alpha 0} H^n_{\boldsymbol{\alpha 1},\boldsymbol{\alpha 2},\ldots\boldsymbol{\alpha n}} = H^{n+1}_{\boldsymbol{\alpha 1},\boldsymbol{\alpha 2},\ldots\boldsymbol{\alpha n}} + d_{c\alpha 0}\left(H^n_{\boldsymbol{\alpha 1},\boldsymbol{\alpha 2},\ldots\boldsymbol{\alpha n}}\right)$ or $\mathbf{c}H^n = H^{n+1} + \nabla_{\mathbf{c}}(H^n)$ with Eq (2.1.5), we can then use the expression $\nabla_{\mathbf{c}}(H^n) = \tilde{n} H^{n-1} I$ with Eq (2.1.5) so that the projection on the left side will be

$$\begin{aligned}
&\int \partial_t f(\mathbf{x},\mathbf{c},t) + \mathbf{c}\cdot\nabla_{\mathbf{x}} f(\mathbf{x},\mathbf{c},t) + g\cdot\nabla_{\mathbf{c}} f(\mathbf{x},\mathbf{c},t) H^n_{\boldsymbol{\alpha}}(\mathbf{c})\, d\mathbf{c} \\
&\quad = \partial_t\left(a^n_{\boldsymbol{\alpha}}\right) + \nabla_{\mathbf{x}}\cdot\left(a^{n+1}_{\boldsymbol{\alpha}}\right) + \tilde{n}\nabla_{\mathbf{x}}\cdot\left(a^{n-1}_{\boldsymbol{\alpha}} I\right) - \tilde{n}\mathbf{g}\cdot\left(a^{n-1}_{\boldsymbol{\alpha}} I\right),
\end{aligned} \tag{2.1.15}$$

and on the right hand side of BGK on the Hermite basis is

$$\int -\frac{1}{\tau}\left(f - f^0\right) H^n_{\boldsymbol{\alpha}} d\mathbf{c} = -\frac{1}{\tau}\left(a^n_{\boldsymbol{\alpha}} - a^0_{\boldsymbol{\alpha}}\right), \tag{2.1.16}$$

where

$$a^0_{\boldsymbol{\alpha}} = \int f^0 H^n_{\boldsymbol{\alpha}} d\mathbf{c}. \tag{2.1.17}$$

So, the projection of BGK on the Hermite basis is

$$\partial_t \left(a^n_{\boldsymbol{\alpha}}\right) + \bigtriangledown_{\mathbf{x}} \cdot \left(a^{n+1}_{\boldsymbol{\alpha}}\right) + \tilde{n} \bigtriangledown_{\mathbf{x}} \cdot \left(a^{n-1}_{\boldsymbol{\alpha}} I\right) - \tilde{n}\mathbf{g} \cdot \left(a^{n-1}_{\boldsymbol{\alpha}} I\right) = -\frac{1}{\tau}\left(a^n_{\boldsymbol{\alpha}} - a^0_{\boldsymbol{\alpha}}\right), \tag{2.1.18}$$

and the projection of f^0 on the Hermite basis which is truncated to N^{th} order is

$$f^0 = \omega\left(\mathbf{c}\right) \sum_{n=0}^{N} \frac{1}{n!} H^n_{\boldsymbol{\alpha}}\left(\mathbf{c}\right) a^n_{\mathbf{0}\boldsymbol{\alpha}}\left(\mathbf{x},t\right). \tag{2.1.19}$$

It is clear we obtain the Eq (2.1.19) when we use Eq (2.1.17) and follow the same steps from Eq (2.1.8) to Eq (2.1.10). Now we can apply the Gauss-Hermite quadrature to (1.2.1), so the conservation law will be

$$\begin{aligned} \rho &= \sum_{i=0}^{d-1} \frac{\omega_i}{\omega\left(\mathbf{c}_i\right)} f\left(\mathbf{x},\mathbf{c}_i,t\right), \\ \rho\mathbf{u} &= \sum_{i=0}^{d-1} \frac{\omega_i}{\omega\left(\mathbf{c}_i\right)} f\left(\mathbf{x},\mathbf{c}_i,t\right)\mathbf{c}_i, \\ \mathbf{P} + \rho\mathbf{u}\mathbf{u} &= \sum_{i=0}^{d-1} \frac{\omega_i}{\omega\left(\mathbf{c}_i\right)} f\left(\mathbf{x},\mathbf{c}_i,t\right)\mathbf{c}_i\mathbf{c}_i. \end{aligned} \tag{2.1.20}$$

To simplify our derivation we define the function

$$f_i = \frac{\omega_i}{\omega\left(\mathbf{c}_i\right)} f\left(\mathbf{x},\mathbf{c}_i,t\right), i = 0,1,...,d-1, \tag{2.1.21}$$

so the conservation law will be

$$\begin{aligned} \rho &= \sum_{i=0}^{d-1} f_i, \\ \rho\mathbf{u} &= \sum_{i=0}^{d-1} f_i\mathbf{c}_i, \\ \mathbf{P} + \rho\mathbf{u}\mathbf{u} &= \sum_{i=0}^{d-1} f_i\mathbf{c}_i\mathbf{c}_i. \end{aligned} \tag{2.1.22}$$

From the definition of the projection for f_i Eq (2.1.7) the last equation (2.1.21) will

be

$$f_i = \omega_i \sum_{n=0}^{N} \frac{1}{c_s^2 n!} H^n_{i\boldsymbol{\alpha}}(\mathbf{c})\, a^n_{\boldsymbol{\alpha}}(\mathbf{x},t) \tag{2.1.23}$$

where $a^n_{\boldsymbol{\alpha}} = \sum_i H^n_{i\boldsymbol{\alpha}} f_i$. Also, the truncation of f^0 of N^{th} order is

$$f^0_i = \omega_i(\mathbf{c}) \sum_{n=0}^{N} \frac{1}{c_s^2 n!} H^n_{i\boldsymbol{\alpha}}(\mathbf{c})\, a^n_{\mathbf{0}\boldsymbol{\alpha}}(\mathbf{x},t), \tag{2.1.24}$$

where $a^n_{\mathbf{0}\boldsymbol{\alpha}} = \sum_i H^n_{i\boldsymbol{\alpha}} f^0_i$ and the expansion of the Hermite coefficient $a^n_{\mathbf{0}\boldsymbol{\alpha}}$ will be

$$\begin{aligned}
a^0_0 &= \rho,\\
a^1_{0\alpha} &= \rho u_{i\alpha},\\
a^2_{0\alpha\beta} &= \rho u_\alpha u_\beta + c_s^2 \rho(\theta-1)\delta_{\alpha\beta}\\
a^3_{0\alpha\beta\gamma} &= \rho u_\alpha u_\beta u_\gamma + c_s^2 \rho(\theta-1)\left(u_\gamma\delta_{\beta\alpha} + u_\beta\delta_{\alpha\gamma} + u_\alpha\delta_{\beta\gamma}\right),\\
a^4_{i\alpha\beta\gamma\delta} &= \rho u_\alpha u_\beta u_\gamma u_\delta + c_s^4\rho(\theta-1)^2\left(\delta_{\delta\gamma}\delta_{\beta\alpha} + \delta_{\beta\beta}\delta_{\alpha\gamma} + \delta_{\delta\alpha}\delta_{\beta\gamma}\right) +\\
&\quad c_s^2\rho(\theta-1)\left(\delta_{\alpha\delta}u_\gamma u_\delta + \delta_{\gamma\alpha}u_\beta u_\delta + \delta_{\alpha\delta}u_\beta u_\gamma + \delta_{\beta\gamma}u_\alpha u_\delta + \delta_{\beta\delta}u_\alpha u_\gamma + \delta_{\gamma\delta}u_\alpha u_\beta\right),
\end{aligned} \tag{2.1.25}$$

so

$$\begin{aligned}
f^0_i &= \omega_i(\mathbf{c}) \sum_{n=0}^{4} \frac{1}{c_s^2 n!} H^n_{i\boldsymbol{\alpha}}(\mathbf{c})\, a^n_{\mathbf{0}\boldsymbol{\alpha}}(\mathbf{x},t)\\
&= \omega_i\rho\left(1 + \frac{\mathbf{c}_i\cdot\mathbf{u}}{c_s^2} + \frac{1}{2c_s^4}\left[(\mathbf{c}_i\cdot\mathbf{u})^2 - c_s^2\mathbf{u}^2 + c_s^2(\theta-1)\left(\mathbf{c}_i{}^2 - c_s^2 D\right)\right]\right.\\
&\quad + \frac{\mathbf{c}_i\cdot\mathbf{u}}{6c_s^6}\left[(\mathbf{c}_i\cdot\mathbf{u})^2 - 3c_s^2\mathbf{u}^2 + 3c_s^2(\theta-1)\left(\mathbf{c}_i{}^2 - c_s^2(D+2)\right)\right] + \frac{1}{24c_s^8}\left[(\mathbf{c}_i\cdot\mathbf{u})^4 - 6c_s^2\mathbf{u}^2(\mathbf{c}_i\cdot\mathbf{u})^2\right]\\
&\quad + 3c_s^4\mathbf{u}^4 + 6c_s^2(\theta-1)\left(\left(\mathbf{c}_i\cdot\mathbf{u}^2\right)\left(\mathbf{c}_i{}^2 - c_s^2(D+4)\right) + c_s^2\mathbf{u}^2\left(c_s^2(D+2) - \mathbf{c}_i{}^2\right)\right)\\
&\quad \left. + 3c_s^4(\theta-1)^2\left(\mathbf{c}_i{}^4 - 2c_s^2(D+2)\,\mathbf{c}_i{}^2 + c_s^4 D(D+2)\right)\right].
\end{aligned} \tag{2.1.26}$$

With isothermal restrictions $\theta = 1$, so all following terms will disappear. By using this property and neglecting the terms of third and fourth order, f^0 will be

$$f^0_i = \omega_i\rho\left(1 + \frac{\mathbf{c}_i\cdot\mathbf{u}}{c_s^2} + \frac{(\mathbf{c}_i\cdot\mathbf{u})^2}{2c_s^4} - \frac{u^2}{2c_s^2}\right), \tag{2.1.27}$$

where the $u^2 = \mathbf{u}\cdot\mathbf{u}$. This equation is used only when the Mach number is small, *i.e.* $\frac{|\mathbf{u}|}{c_s^2} \ll 1$.

By multiplying Eq (1.2.4) by $\frac{\omega_i}{\omega(\mathbf{c}_i)}$ and evaluating it at $\mathbf{c}_i$, the BGK equation will be

$$\partial_t f_i + \mathbf{c}_i \cdot \nabla f_i = -\frac{1}{\tau}\left(f_i - f_i^0\right), \tag{2.1.28}$$

where $\{\mathbf{c}_i\}$ is a finite set of discrete particle velocities or lattice velocities corresponding to the finite set of distribution functions $\{f_i\}$. This equation is called the Lattice Boltzmann equation (LBE) or the discrete velocity Boltzmann equation with BGK collision operator.

The body force is represented in the BE, Eq (1.2.4), as $\mathbf{g}\cdot\nabla_{\mathbf{c}} f(\mathbf{x},\mathbf{c},t)$ with respect to distribution function f. $\mathbf{g}$ is called the force acceleration [60]. So

$$\partial_t f(\mathbf{x},\mathbf{c},t) + \mathbf{c}\cdot\nabla_{\mathbf{x}} f(\mathbf{x},\mathbf{c},t) + \mathbf{g}\cdot\nabla_{\mathbf{c}} f(\mathbf{x},\mathbf{c},t) = -\frac{1}{\tau}\left(f - f^0\right). \tag{2.1.29}$$

We cannot set the body force in the lattice Boltzmann equation LBE directly, due to the discretization of the particle velocity. There are various ways to set the body force in LBE, for example the approach of Shan, Yuan and Chen [60], which is based on the projection of the Hermite expansion. It is difficult to project the force term directly on the Hermite basis, because there is a gradient with respect to velocity in the forcing term. So, the projection is done by using Eqs (2.1.1) and (2.1.2).

$$\begin{aligned}\nabla_{\mathbf{c}} f(\mathbf{x},\mathbf{c},t) &= \nabla_{\mathbf{c}}\omega(\mathbf{c})\sum_{n=0}^{\infty}\frac{1}{n!}H^n_{\boldsymbol{\alpha}}(\mathbf{c})\,a^n_{\boldsymbol{\alpha}}(\mathbf{x},t) = \sum_{n=0}^{\infty}\frac{1}{n!}a^n_{\boldsymbol{\alpha}}\nabla_{\mathbf{c}}\left(\omega(\mathbf{c})H^n_{\boldsymbol{\alpha}}\right)\\ &= \sum_{n=0}^{\infty}\frac{-1^n}{n!}a^n_{\boldsymbol{\alpha}}\nabla^{n+1}_{\mathbf{c}}\,\omega(\mathbf{c}) = -\omega(\mathbf{c})\sum_{n=0}^{\infty}\frac{1}{n!}a^n_{\boldsymbol{\alpha}}H^{n+1}_{\boldsymbol{\alpha}} = -\omega(\mathbf{c})\sum_{n=1}^{\infty}\frac{1}{n!}a^{n-1}_{\boldsymbol{\alpha}}H^n_{\boldsymbol{\alpha}}.\end{aligned} \tag{2.1.30}$$

By defining the force term as $F(\mathbf{c}) = -\mathbf{g}\cdot\nabla_{\mathbf{c}} f(x,\mathbf{c},t)$, the projection of the force

term can be written as

$$F(\mathbf{c}) = \omega(\mathbf{c}) \sum_{n=0}^{\infty} \frac{1}{n!} \mathbf{g} a_{\boldsymbol{\alpha}}^{n-1} H_{\boldsymbol{\alpha}}^{n}. \tag{2.1.31}$$

By evaluating the force term at $\mathbf{c}_i$ and multiplying it by $\frac{\omega_i}{\omega(\mathbf{c}_i)}$:

$$\frac{\omega_i}{\omega(\mathbf{c}_i)} F(\mathbf{c}_i) = \frac{\omega_i}{\omega(\mathbf{c}_i)} \omega(\mathbf{c}_i) \sum_{n=0}^{\infty} \frac{1}{n!} \mathbf{g} a_{\boldsymbol{i\alpha}}^{n-1} H_{\boldsymbol{\alpha}}^{n}(\mathbf{c}_i). \tag{2.1.32}$$

For simplicity we define the force term as $F_i = \frac{\omega_i}{\omega(\mathbf{c}_i)} F(\mathbf{c}_i)$, so the force term will be

$$F_i = \omega_i \sum_{n=0}^{\infty} \frac{1}{n!} \mathbf{g} a_{\boldsymbol{i\alpha}}^{n-1} H_{\boldsymbol{i\alpha}}^{n}. \tag{2.1.33}$$

We can expand the force term with equilibrium distribution functions, then truncate it at the third term. This is because $a_{0\alpha}^{0} = a_{\alpha}^{0}$, $a_{0\alpha}^{1} = a_{\alpha}^{1}$ and $a_{0\alpha}^{2} = a_{\alpha}^{2}$. So

$$\begin{aligned}
F_i &= \omega_i \sum_{n=0}^{3} \frac{1}{n! c_s^{2n}} \mathbf{g} a_{\boldsymbol{0\alpha}}^{n-1} H_{\boldsymbol{i\alpha}}^{n}, \\
F_i &= \omega_i \rho \left(\frac{\mathbf{c}_i \cdot \mathbf{g}}{c_s^2} + \frac{1}{c_s^2} \left((\mathbf{c}_i \cdot \mathbf{u})(\mathbf{c}_i . \mathbf{g}) - c_s^4 (\mathbf{g} \cdot \mathbf{u}) \right) \right. \\
&+ \frac{1}{6c_s^6} (\Big((\mathbf{c}_i \cdot \mathbf{u})(\mathbf{c}_i \cdot \mathbf{g})^2 + c_s^2 \mathbf{c}_i^2 (\theta - 1) - c_s^2 ((\mathbf{c}_i \cdot \mathbf{g})(2(\mathbf{g} \cdot \mathbf{u})) \\
&\left. + \left(\mathbf{u}^2 + c_s^2 (\theta - 1) D \right) \Big) + 2 c_s^2 (\theta - 1)(\mathbf{c}_i \cdot \mathbf{g})) \right).
\end{aligned} \tag{2.1.34}$$

In the isothermal system $\theta = 1$, so the third force term vanishes. Then, the third order of velocity is neglected and the last properties are used

$$F_i = \omega_i \rho \left(\frac{\mathbf{c}_i \cdot \mathbf{g}}{c_s^2} + \frac{(\mathbf{c}_i \cdot \mathbf{u})(\mathbf{c}_i \cdot \mathbf{g})}{c_s^4} - \frac{(\mathbf{g} \cdot \mathbf{u})}{c_s^2} \right). \tag{2.1.35}$$

So, we can write the Lattice Boltzmann equation with force term as

$$\partial_t f_i + \mathbf{c}_i \cdot \bigtriangledown f_i = -\frac{1}{\tau} \left(f_i - f_i^0 \right) + F_i. \tag{2.1.36}$$

In the Lattice Boltzmann equation the macroscopic thermodynamic variables and

their fluxes are calculated by moment summation, Eq (2.1.22). The truncation of second order is important for moments (density, velocity, temperature, pressure) and their fluxes, while the truncation of the third order is important for heat fluxes, i.e the third moment.

There are various approaches to discretise the BGK model, such as that of Shan and He, who discretise the BGK equation for velocity using an approach which is related to Grad's system of 13 moments [28]. Other approaches have been used to approximate the Boltzmann equation, though, such as that of Lou and He in 1997 [26].

2.1.2 Time and space discretisation: the trapezoidal rule

After discretisation of the Boltzmann equation with respect to velocity we get

$$\partial_t f_i + \mathbf{c}_i \cdot \bigtriangledown f_i = -\frac{1}{\tau}(f_i - f_i^0) + F_i,$$

where F_i is the forcing term. In Lagrangian formulation, this equation is written as

$$D_t f_i = -\frac{1}{\tau}(f_i - f_i^0) + F_i. \tag{2.1.37}$$

The second order approximation has been approximated by using the integration along the characteristic δ_t for the left hand side of Eq (2.1.37) and by using the trapezoidal rule for the right hand side in Eq (2.1.37)

$$f_i(\mathbf{x} + \mathbf{c}_i\delta_t, t + \delta_t) - f_i(\mathbf{x}, t) \simeq \frac{\delta_t}{2}\left[-\frac{1}{\tau}\left(f_i - f_i^0\right) + F_i\right]|_{t+\delta_t} + \frac{\delta_t}{2}\left[-\frac{1}{\tau}\left(f_i - f_i^0\right) + F_i\right]|_t + O(\delta_t^3), \tag{2.1.38}$$

which is an implicit equation for f_i. To write this equation as an explicit formula [28] we define

$$\overline{f}_i = f_i + \frac{\delta_t}{2\tau}\left(f_i - f_i^0\right) - \frac{\delta_t}{2}F_i. \tag{2.1.39}$$

By substituting Eq (2.1.39) into Eq (2.1.38) then doing some algebra operations the Eq (2.1.38) is written as

$$\overline{f}_i(\,\mathbf{x}+\mathbf{c}_i\delta_t,t+\delta_t)-\overline{f}_i(\mathbf{x},t)\simeq-\left[\frac{\delta_t}{\tau}\left(f_i(\mathbf{x},t)-f_i^0(\mathbf{x},t)\right)-\delta_t F_i\right]|_t+O(\delta_t^3). \quad (2.1.40)$$

From Eq (2.1.39) f_i is written as

$$f_i(\mathbf{x},t)=\frac{2\tau}{2\tau+\delta_t}\overline{f}_i(\mathbf{x},t)+\frac{\delta_t}{2\tau+\delta_t}f_i^0(\mathbf{x},t)+\frac{\delta_t\tau}{2\tau+\delta_t}F_i. \quad (2.1.41)$$

By substituting Eq (2.1.41) into Eq (2.1.40), the latter is written as

$$\begin{aligned}\Longrightarrow \overline{f}_i(\mathbf{x}+\mathbf{c}_i\delta_t,t+\delta_t)-\overline{f}_i(\mathbf{x},t)&\simeq-\frac{\delta_t}{\tau+\frac{\delta_t}{2}}\left[\left(\overline{f}_i(\mathbf{x},t)-f_i^0(\mathbf{x},t)\right)-\tau F_i\right],\\ \Longrightarrow \overline{f}_i(\mathbf{x}+\mathbf{c}_i\delta_t,t+\delta_t)-\overline{f}_i(\mathbf{x},t)&=-\frac{1}{\overline{\tau}}\left[\left(\overline{f}_i(\mathbf{x},t)-f_i^0(\mathbf{x},t)\right)-\tau F_i\right], \quad (2.1.42)\end{aligned}$$

where $\overline{\tau}=\dfrac{\tau+0.5\delta_t}{\delta_t}$, $\tau=\overline{\tau}\delta_t-0.5\delta_t$ and the f_i^0 depends on $\mathbf{u}$ in respect of the distribution function $\overline{f}_i$. This equation is called the second order approximation of LBE.

The right hand term of LBE is found using the collision step which represents the exchange of momentum with neighbouring particles where the exchange must be faster than the velocity of the fluid. The left hand term is the streaming step that means the particles move to the neighbouring nodes from time step t to the next time step $t+\delta t$. In other words, the collision step means $\overline{f}_i$ is updated at current location $\mathbf{x}$ and the streaming step means the updated $\overline{f}_i$ propagates to local neighbours.

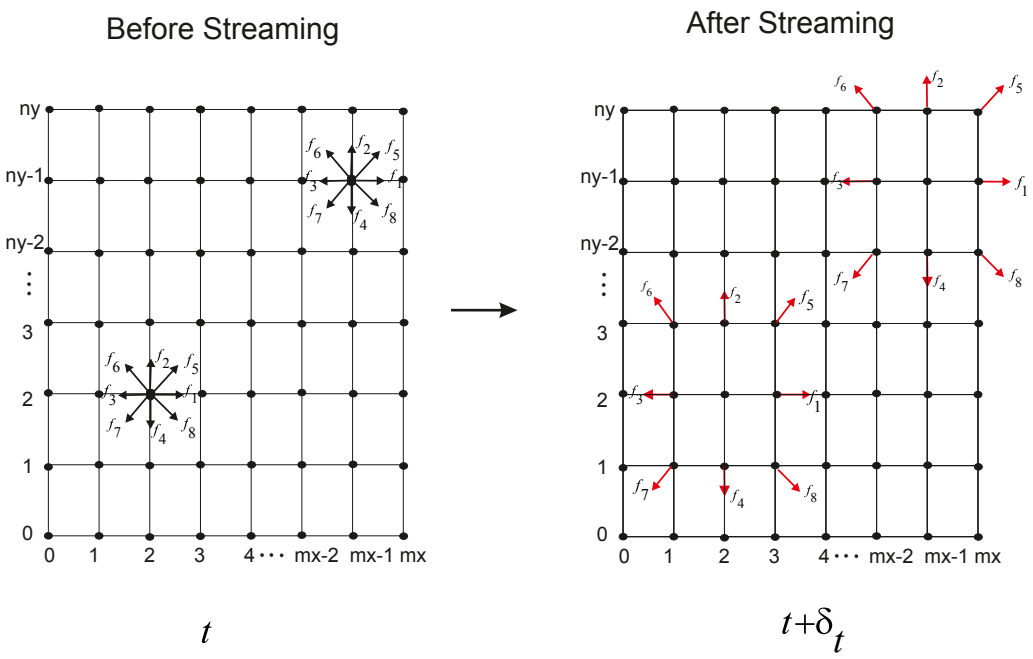

Figure 2.1: The streaming step in two dimensions.

We can derive the macroscopic quantities with body force term in this case as

$$\begin{aligned}
\overline{\rho} &= \sum_i \overline{f}_i = \sum_i \left[f_i + \frac{\delta_t}{2\tau}\left(f_i - f_i^0\right) - \frac{\delta_t}{2} F_i \right] = \rho, \\
\overline{\rho}\ \overline{\mathbf{u}} &= \sum_i \mathbf{c}_i \overline{f}_i = \sum_i \mathbf{c}_i f_i + \frac{\delta_t}{2\tau} \sum_i \mathbf{c}_i \left(f_i - f_i^0\right) - \frac{\delta_t}{2} \sum_i \mathbf{c}_i F_i = \rho \mathbf{u} - \frac{\delta_t}{2}\mathbf{F}, \\
\Longrightarrow \mathbf{u} &= \overline{\mathbf{u}} + \frac{\delta_t}{2}\mathbf{F}, \qquad (2.1.43)
\end{aligned}$$

and

$$\begin{aligned}
\overline{\mathbf{\Pi}} &= \sum_i \mathbf{c}_i \mathbf{c}_i \overline{f}_i, \\
\Longrightarrow \overline{\mathbf{\Pi}} &= \mathbf{\Pi} + \frac{\delta_t}{2\tau}\mathbf{\Pi} - \frac{\delta_t}{2\tau}\mathbf{\Pi}^0 - \frac{\delta_t}{2}\left(\mathbf{F}\mathbf{u} + \mathbf{u}\mathbf{F}\right), \\
\Longrightarrow \mathbf{\Pi} &= \frac{2\tau}{2\tau+\delta_t}\overline{\mathbf{\Pi}} + \frac{2\tau}{2\tau+\delta_t}\mathbf{\Pi}^0 + \frac{\delta_t \tau}{2\tau+\delta_t}\left(\mathbf{F}\mathbf{u} + \mathbf{u}\mathbf{F}\right). \qquad (2.1.44)
\end{aligned}$$

The formula for $\overline{\boldsymbol{Q}}$ is

$$\overline{\boldsymbol{Q}} = \sum_i \mathbf{c}_i \mathbf{c}_i \mathbf{c}_i \overline{f}_i = \boldsymbol{Q} + \frac{\delta_t}{2\tau}\boldsymbol{Q} - \frac{\delta_t}{2\tau}\boldsymbol{Q}^0 - \sum_i \mathbf{c}_i \mathbf{c}_i \mathbf{c}_i F_i, \qquad (2.1.45)$$

where $\sum_i F_i = 0$, $\sum_i \mathbf{c}_i F_i = \mathbf{F}$, $\sum_i \mathbf{c}_i \mathbf{c}_i F_i = \mathbf{F}\mathbf{u} + \mathbf{u}\mathbf{F}$ and $\mathbf{F} = \rho \mathbf{g}$ is body force.

The conserved macroscopic quantities are $\rho = \sum_i f_i = \sum_i f_i^0$, $\rho \mathbf{u} = \sum_{i=1} \mathbf{c}_i f_i = \sum_{i=1} \mathbf{c}_i f_i^0$,

$\mathbf{\Pi} = \sum_{i=1} \mathbf{c}_i \mathbf{c}_i f_i$, $\mathbf{\Pi}^0 = \sum_{i=1} \mathbf{c}_i \mathbf{c}_i f_i^0$ and $\boldsymbol{Q}^0 = \sum_{i=1} \mathbf{c}_i \mathbf{c}_i \mathbf{c}_i f_i^0$.

2.2 Lattice Boltzmann units

The scaling for Lattice Boltzmann is implemented in two steps [37]. The first of these involves converting the physical system to the dimensionless system, which does not depend on physical scales or simulation parameters. The second involves converting the dimensionless system to Lattice Boltzmann or a discrete simulation. The subscripts p, d and lb indicate the physical, dimensionless system and Lattice Boltzmann units, respectively. The conversion from the physical system to the dimensionless system is made by choosing two characteristics, namely length scale l_0 and time scale t_0. The length scale l_0 describes the length or size of something in the system, such as the obstacle size. The time scale t_0 is the time which is required in the system. The characteristic velocity is $u_0 = \frac{l_0}{t_0}$. The space discrete δ_x and time discrete δ_t are chosen to make the conversion from the dimensionless system to Lattice Boltzmann.

In the physical system, the momentum equation is

$$\frac{\partial \mathbf{u}_p}{\partial t_p} + (\mathbf{u}_p \cdot \bigtriangledown_p)\mathbf{u}_p = -\frac{1}{\rho_{0,p}} \bigtriangledown_p p_p + \nu_p \bigtriangledown_p^2 \cdot \mathbf{u}_p, \tag{2.2.1}$$

and the flow is considered incompressible when $\bigtriangledown \cdot \mathbf{u}_p = 0$. The physical time and space in the system are t_p and x_p and the dimensionless time and space in the system are

$$t_d = \frac{t_p}{t_{0,p}},\ x_d = \frac{x_p}{x_{0,p}}. \tag{2.2.2}$$

Other physical quantities on the dimensionless system will be

$$u_p = \frac{l_{0,p}}{t_{0,p}} u_d,\ \partial_{t_p} = \frac{1}{t_{0,p}} \partial_{t_d},\ \bigtriangledown_p = \frac{1}{l_{0,p}} \bigtriangledown_d,\ p_p = \rho_{0,p} \frac{l_{0,p}^2}{t_{0,p}^2} p_d. \tag{2.2.3}$$

By substituting Eq (2.2.2) and Eq (2.2.3) into momentum equation Eq (2.2.1), the

dimensionless momentum equation is

$$\frac{\partial \mathbf{u}_d}{\partial t_d} + (\mathbf{u}_d \cdot \bigtriangledown_d)\,\mathbf{u}_d = -\bigtriangledown_d p_d + \frac{1}{Re}\bigtriangledown_d^2 \cdot \mathbf{u}_d, \tag{2.2.4}$$

and $\bigtriangledown \cdot \mathbf{u}_d = 0$ where $Re = \dfrac{l_0^2}{t_0 \nu}$ is the dimensionless Reynolds number and the Kinematic viscosity in the dimensionless system is $\nu_d = \dfrac{1}{Re}$. Now the first step of conversion is complete and the second step is implemented as follows. The space discrete is defined as $\delta_x = \dfrac{1}{n_x}$, where n_x is the number of cells which is used to discretise the length, while time discrete is defined as $\delta_t = \dfrac{1}{n_{iter}}$, where the n_{iter} is the number of iteration steps within the reference time. The dimensionless velocity and Kinematic viscosity which are based on the lattice Boltzmann method are

$$u_d = \frac{\delta_x}{\delta_t} u_{lb},\ \nu_d = \frac{\delta_{x^2}}{\delta_t} \nu_{lb}, \tag{2.2.5}$$

so, the LB velocity and Kinematic viscosity are

$$u_{lb} = \frac{\delta_t}{\delta_x} u_d,\ \nu_{lb} = \frac{\delta_t}{\delta_{x^2}} \frac{1}{Re}. \tag{2.2.6}$$

2.2.1 The convergence and accuracy of the Lattice Boltzmann method

The convergence and accuracy of the Lattice Boltzmann method is examined by two types of scaling, namely acoustic and diffusive [70]. In acoustic scaling $\delta_t \sim \delta_x$, where $c = \dfrac{\delta_x}{\delta_t}$ is the lattice speed velocity. The Reynolds number and the characteristic velocity U are fixed in this kind of scaling. Thus, the Mach number $Ma = \dfrac{U}{c_s} \ll 1$ is fixed in acoustic scaling, and the Reynolds number is proportional to the Mach number and Knudsen number *i.e.* ($Re = \dfrac{Ma}{K_n}$). The definition of the Reynolds number $Re = \dfrac{UL}{\nu}$ allows us to specify the Kinematic viscosity ν and gives the relaxation time $\tau = 3\nu$ where L is the characteristic length of flow. In diffusive scaling, $\delta_t \sim \delta_x^2$ and the relaxation time τ is fixed, which leads to ν also being fixed. In order to fix the Reynolds number $Re = \dfrac{UL}{\nu}$ in this kind of scaling

we have to vary the characteristic velocity U when we double the space discrete. Thus, the Mach number in this scaling is reduced by a resolution for the grid size and tends to zero, and the errors in the Mach number are reduced. Thus, the incompressible Navier-Stokes equations are directly obtained using diffusive scaling.

Chapter 3

Lattice Boltzmann model

3.1 D_dQ_q model

A lattice is defined mathematically as a collection of nodes distributed regularly on a grid, where velocity connects the nodes together. In the LBE, the lattice is defined as D_dQ_q, where d is the number of dimensions and q is the number of links. D_dQ_q contains a zero velocity which means a rest situation for particles [72]. Some lattices such as D_1Q_2 do not have a zero in rest position. In the following section, we will explain how we can apply the Chapman-Enskog approach to LBE to obtain the Navier-Stokes equations in two-dimensional lattices such as D_2Q_9 and three-dimensional ones such as D_3Q_{19}.

3.1.1 D_2Q_9 lattice

The D_2Q_9 lattice is a square symmetrical lattice that contains nodes, each of which has nine lattice velocities and nine distribution functions corresponding to it:

$$\mathbf{c}_i = \begin{cases} (0,0) & i = 0, \\ (\cos\left[(i-1)\frac{\pi}{2}\right], sin\left[(i-1)\frac{\pi}{2}\right])c & i = 1,2,3,4, \\ (\cos\left[(i-5)\frac{\pi}{2}+\frac{\pi}{4}\right], sin\left[(i-5)\frac{\pi}{2}+\frac{\pi}{4}\right])\sqrt{2}c & i = 5,6,7,8, \end{cases}$$

where $c = \frac{\delta_x}{\delta_t}$, δ_x is the unit space step and δ_t is the unit time step.

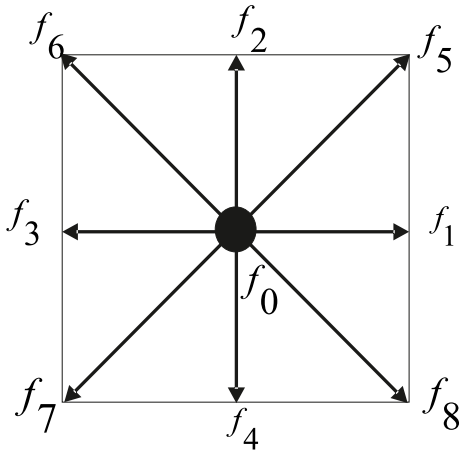

Figure 3.1: D_2Q_9 Lattice [25].

The D_2Q_9 has nine weight values, grouped as: ω_a, which corresponds to stationary velocity; ω_b, to horizontal and vertical velocities $i = 1,2,3,4$; and ω_c to diagonal velocities $i = 5,6,7,8$.

From the orthogonal basis of Hermite polynomials, see section (2.1) of chapter (2), we can find the weight functions as follows

$$\sum_i \omega_i c_{i\alpha} = 1,$$

$$\sum_i \omega_i c_{i\alpha} c_{i\beta} = c_s^2 \delta_{\alpha\beta},$$

$$\sum_i \omega_i c_{i\alpha} c_{i\beta} c_{i\gamma} c_{i\delta} = c_s^4 \left(\delta_{\alpha\gamma}\delta_{\beta\delta} + \delta_{\alpha\gamma}\delta_{\beta\delta}\right),$$

$$\sum_i \omega_i c_{i\alpha} c_{i\beta} c_{i\gamma} c_{i\delta} c_{i\theta} c_{i\varepsilon} = c_s^6 \left(\delta_{\alpha\delta}\left(\delta_{\beta\varepsilon}\delta_{\gamma\zeta} + \delta_{\beta\zeta}\delta_{\gamma\varepsilon}\right)\right. \tag{3.1.1}$$

$$\left. + \delta_{\alpha\varepsilon}\left(\delta_{\beta\delta}\delta_{\gamma\zeta} + \delta_{\beta\zeta}\delta_{\gamma\delta}\right) + \delta_{\alpha\zeta}\left(\delta_{\beta\delta}\delta_{\gamma\varepsilon} + \delta_{\beta\varepsilon}\delta_{\gamma\delta}\right)\right), \tag{3.1.2}$$

We can use the Wolf-method [74] to find weight functions. In Wolf-method, the isotropic tensor is defined as

$$T_{\alpha_1\alpha_2\ldots\alpha_n} = \sum_{i=1} \omega_i c_{i\alpha_1} c_{i\alpha_2} \ldots c_{i\alpha_n}. \tag{3.1.3}$$

The isotropic tensor depends on the symmetry and the orthogonality between the velocities and weights set in the lattice tensor. In D_2Q_9, the lattice tensor of rank

zero is

$$\sum_{i=0}^{9} \omega_i = 1. \tag{3.1.4}$$

The lattice tensors of ranks one, three and five, respectively, are

$$\sum_{i=0}^{9} \omega_i c_{i\alpha} = \sum_{i=1}^{9} \omega_i c_{i\alpha} c_{i\beta} c_{i\gamma} = \sum_{i=0}^{9} \omega_i c_{i\alpha} c_{i\beta} c_{i\gamma} c_{i\delta} c_{i\theta} = 0. \tag{3.1.5}$$

The lattice tensor of rank two is

$$\sum_{i=0}^{9} \omega_i c_{i\alpha} c_{i\beta} = c_s^2 \delta_{\alpha\beta} = c_s^2 = \frac{1}{3}\delta_{\alpha\beta}, \tag{3.1.6}$$

and of rank four is

$$\sum_{i=0}^{9} \omega_i c_{i\alpha} c_{i\beta} c_{i\gamma} c_{i\delta} = \Delta_{\alpha\beta\gamma\delta}, \tag{3.1.7}$$

where $\Delta_{\alpha\beta\gamma\delta} = \left(c_s^2\right)^2 (\delta_{\alpha\beta}\delta_{\gamma\delta} + \delta_{\alpha\gamma}\delta_{\beta\delta} + \delta_{\alpha\delta}\delta_{\gamma\beta})$

1. if

$$\alpha = \beta = \gamma = \delta \Longrightarrow \sum_{i=0}^{9} \omega_i c_{i\alpha} c_{i\beta} c_{i\gamma} c_{i\delta} = 3\left(c_s^2\right)^2, \tag{3.1.8}$$

2. if

$$\alpha = \beta \neq \gamma = \delta \Longrightarrow \sum_{i=0}^{9} \omega_i c_{i\alpha} c_{i\beta} c_{i\gamma} c_{i\delta} = \left(c_s^2\right)^2, \tag{3.1.9}$$

where $c_s = \dfrac{c}{\sqrt{3}}$ and $\delta_{\alpha\beta}$ is the Kronecker delta function:

$$\delta_{\alpha\beta} = \begin{cases} 1 & \alpha = \beta, \\ 0 & \text{else.} \end{cases}$$

These equations lead to

$$\begin{aligned} \omega_a + 4\omega_b + 4\omega_c &= 1, \\ 2\omega_b c^4 + 4\omega_c c^4 &= 3\left(c_s^2\right)^2, \\ 4\omega_c c^4 &= \left(c_s^2\right)^2, \end{aligned} \tag{3.1.10}$$

and by solving this system of equations we obtain $\omega_a = \frac{4}{9}$, $\omega_b = \frac{1}{9}$ and $\omega_c = \frac{1}{36}$. The D_2Q_9 lattice satisfies the Navier-Stokes equations, which will be proven in the next section.

3.1.2 D_3Q_{19} lattice

The D_3Q_{19} lattice is a cubic symmetrical lattice which contains nodes, each of which has 19 lattice velocities $\mathbf{c}_i$ and 19 distribution functions $\{f_i\}$ corresponding to it. The D_3Q_{19} consists of one distribution function at the stationary centre, 6 at the faces and twelve at the edges. The 19 velocities $\mathbf{c}_i$ are

$$\mathbf{c}_i = \begin{cases} \mathbf{c}_0 = (0,0,0) \\ \mathbf{c}_{1,2}, \mathbf{c}_{3,4}, \mathbf{c}_{5,6} = (\pm,1,0),(0,\pm1,0),(0,0,\pm1) \\ \mathbf{c}_{7,8,9,10}, \mathbf{c}_{11,12,13,14}, \mathbf{c}_{15,16,17,18} = (\pm1,\pm1,0),(\pm1,0,\pm1),(0,\pm1,\pm1). \end{cases}$$

There are 19 weight functions corresponding to these velocities, which are defined as

$$\omega_i = \begin{cases} \frac{2}{9} & i = 0 \\ \frac{1}{18} & i = 1,2,3,4,5,6 \\ \frac{1}{36} & i = 7,8,...,18. \end{cases}$$

where ω_a corresponds to stationary velocity, ω_b for $i = 1,2,3,4,5,6$ to horizontal and vertical velocities and ω_c for $i = 7,8,...,18$ to diagonal velocities. We can find these weight functions from the orthogonality basis of Hermite polynomials, see section (2.1) of chapter (2), by using the Wolf-method [74], to define the isotropic tensor in three dimensions. Thus, the weights function can be found by solving

the following system

$$\begin{aligned} \omega_a + 6\omega_b + 12\omega_c &= 1, \\ 2\omega_b c^4 + 8\omega_c c^4 &= 3\left(c_s^2\right)^2, \\ 4\omega_c c^4 &= \left(c_s^2\right)^2, \end{aligned} \tag{3.1.11}$$

from which we obtain $\omega_a = \frac{2}{9}, \omega_b = \frac{1}{18}$ and $\omega_c = \frac{1}{36}$.

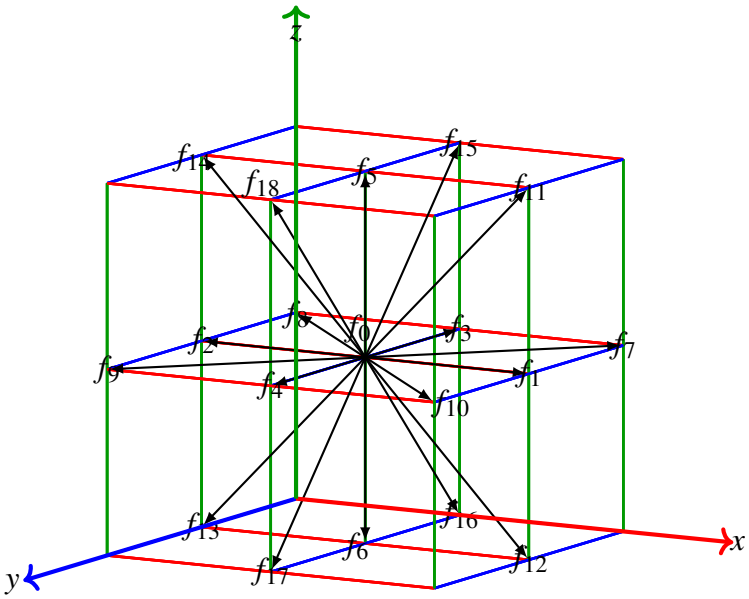

Figure 3.2: D_3Q_{19} lattice.

The D_3Q_{19} lattice also satisfies the Navier-Stokes equations, as we will prove in the next section.

3.2 The Chapman-Enskog to derive the Navier-Stokes equations

The Chapman-Enskog procedure is dependent on expanding the non-conserved moments and the time derivative as a combination or series in the collision term τ, because the solution of the discrete Boltzmann equation, Eq (2.1.28), changes slowly over time scales much longer than the collision time τ. The procedure is done by taking the summation over i with different powers of lattice velocity for Eq (2.1.28), then substituting the moment velocity in these equations which contain

the combinations or series, then expanding the ∂_t,$\mathbf{\Pi}$ and Q and substituting these expansions into these equations which contain the combinations or series, and finally gathering all terms of the same powers of τ. The approximation of the zero order yields the flow at equilibrium state, whereas the first order approximation leads to the Navier-Stokes equations. We can explain this approach to find the Navier-Stokes equations mathematically, applying the Chapman-Enskog expansion approach to the BGK-Boltzmann equation (3.2.1) in D_2Q_9 and D_3Q_{19}, using the following steps: The discrete version of the BGK-Boltzmann equation is

$$\partial_t f_i + \mathbf{c}_i \cdot \bigtriangledown f_i = -\frac{1}{\tau}(f_i - f_i^0). \tag{3.2.1}$$

When we take Eq (3.2.1) and sum over i (velocity), then

$$\partial_t \sum_i f_i + \bigtriangledown \cdot \sum_i \mathbf{c}_i f_i = -\frac{1}{\tau}\left(\sum_i f_i - \sum_i f_i^0\right),$$

where the conserved macroscopic quantities are

$$\rho = \sum_i f_i = \sum_i f_i^0, \quad \rho\mathbf{u} = \sum_i \mathbf{c}_i f_i = \sum_i \mathbf{c}_i f_i^0,$$

$$\partial_t \rho + \nabla \cdot \rho\mathbf{u} = 0. \tag{3.2.2}$$

Then we take Eq (3.2.1) and multiply it by $\mathbf{c}_i$, and sum over i, then

$$\partial_t \sum_i \mathbf{c}_i f_i + \nabla \cdot \sum_i \mathbf{c}_i \mathbf{c}_i f_i = -\frac{1}{\tau}\left(\sum_i \mathbf{c}_i f_i - \sum_i \mathbf{c}_i f_i^0\right).$$

The macroscopic quantities in this last equation are $\mathbf{\Pi} = \sum_i \mathbf{c}_i \mathbf{c}_i f_i, \mathbf{Q} = \sum_i \mathbf{c}_i \mathbf{c}_i \mathbf{c}_i f_i$, so

$$\partial_t(\rho\mathbf{u}) + \nabla \cdot \mathbf{\Pi} = -\frac{1}{\tau}(\rho\mathbf{u} - \rho^0\mathbf{u}^0) = 0,$$

$$\partial_t(\rho\mathbf{u}) + \nabla \cdot \mathbf{\Pi} = 0. \tag{3.2.3}$$

Then we take Eq (3.2.1) and multiply it by $\mathbf{c}_i\mathbf{c}_i$, then

$$\sum_i \mathbf{c}_i\mathbf{c}_i f_i + \nabla\cdot\sum_i \mathbf{c}_i\mathbf{c}_i\mathbf{c}_i f_i = -\frac{1}{\tau}(\sum_i \mathbf{c}_i\mathbf{c}_i f_i - \sum_i \mathbf{c}_i\mathbf{c}_i f_i^0),$$
$$\Longrightarrow \partial_t\mathbf{\Pi} + \nabla\cdot\mathbf{Q} = -\frac{1}{\tau}(\mathbf{\Pi} - \mathbf{\Pi}^0). \tag{3.2.4}$$

Then we take Eq (3.2.1) and multiply it by $\mathbf{c}_i\mathbf{c}_i\mathbf{c}_i$, then

$$\sum_i \mathbf{c}_i\mathbf{c}_i\mathbf{c}_i f_i + \nabla\cdot\sum_i \mathbf{c}_i\mathbf{c}_i\mathbf{c}_i\mathbf{c}_i f_i = -\frac{1}{\tau}(\sum_i \mathbf{c}_i\mathbf{c}_i\mathbf{c}_i f_i - \sum_i \mathbf{c}_i\mathbf{c}_i\mathbf{c}_i f_i^0),$$
$$\Longrightarrow \partial_t\mathbf{Q} + \nabla\cdot\mathbf{R} = -\frac{1}{\tau}(\mathbf{Q} - \mathbf{Q}^0). \tag{3.2.5}$$

We will now expand ∂_t, Π, $\mathbf{Q}$ and $\mathbf{R}$ using the Chapman-Enskog as follows:

$$\mathbf{\Pi} = \mathbf{\Pi}^0 + \tau\mathbf{\Pi}^1 + O(\tau^2), \quad \mathbf{Q} = \mathbf{Q}^0 + \tau\mathbf{Q}^1 + O(\tau^2), \quad \mathbf{R} = \mathbf{R}^0 + \tau\mathbf{R}^1 + O(\tau^2),$$
$$\partial_t = \partial_{t_0} + \tau\partial_{t_1} + O(\tau^2), \tag{3.2.6}$$

where $\mathbf{\Pi}^0 = \sum_i \mathbf{c}_i\mathbf{c}_i f_i^0$, $\mathbf{Q}^0 = \sum_i \mathbf{c}_i\mathbf{c}_i\mathbf{c}_i f_i^0$, $\mathbf{R}^0 = \sum_i \mathbf{c}_i\mathbf{c}_i\mathbf{c}_i\mathbf{c}_i f_i^0$.

The expansion in Eq (3.2.6) are truncated to the first order of τ and substituted into Eqs (3.2.2), (3.2.3), (3.2.4) and Eq (3.2.5), so, the above equations will become

$$\partial_{t_0}\rho + \tau\partial_{t_1}\rho + \nabla\cdot(\rho\mathbf{u}) = 0,$$

$$\partial_{t_0}\rho\mathbf{u} + \nabla\cdot\mathbf{\Pi}^0 + \tau(\partial_{t_1}\rho\mathbf{u} + \nabla\cdot\mathbf{\Pi}^1) = 0,$$

$$\partial_{t_0}\mathbf{\Pi}^0 + \nabla\cdot\mathbf{Q}^0 + \tau\partial_{t_0}\mathbf{\Pi}^1 + \tau\partial_{t_1}\mathbf{\Pi}^0 + (\nabla\cdot\mathbf{Q}^1)\tau = -\mathbf{\Pi}^1,$$

$$\partial_{t_0}\mathbf{Q}^0 + \nabla\cdot\mathbf{R}^0 + \tau\partial_{t_0}\mathbf{Q}^1 + \tau\partial_{t_1}\mathbf{Q}^0 + \tau^2\partial_{t_1}\mathbf{Q}^1 + (\nabla\cdot\mathbf{R}^1)\tau = -\mathbf{Q}^1.$$

By gathering all the terms of order τ^0, τ^1 and τ^2, we will obtain the following equations:

$$\partial_{t_0}\rho = -\nabla\cdot\rho\mathbf{u}, \tag{3.2.7}$$

$$\partial_{t_0}\rho\mathbf{u} = -\nabla\cdot\mathbf{\Pi}^0, \tag{3.2.8}$$

$$\partial_{t_0}\mathbf{\Pi}^0 + \nabla\cdot\mathbf{Q}^0 = -\mathbf{\Pi}^1, \tag{3.2.9}$$

$$\partial_{t_1}\rho = 0, \tag{3.2.10}$$

$$\partial_{t_1}\rho\mathbf{u} = -\nabla\cdot\mathbf{\Pi}^1, \tag{3.2.11}$$

$$\partial_{t_0}\mathbf{\Pi}^1 + \partial_{t_1}\mathbf{\Pi}^0 + (\nabla\cdot\mathbf{Q}^1) = 0, \tag{3.2.12}$$

$$\partial_{t_0}\mathbf{Q}^0 + \nabla\cdot\mathbf{R}^0 = -\mathbf{Q}^1, \tag{3.2.13}$$

$$\partial_{t_0}\mathbf{Q}^1 + \nabla\cdot\mathbf{R}^1 + \partial_{t_1}\mathbf{Q}^0 = 0, \tag{3.2.14}$$

$$\partial_{t_1}\mathbf{Q}^1 = 0. \tag{3.2.15}$$

Now we will find the continuity equation. We know that $\partial_{t_1}\rho = 0$, therefore $\partial_t = \partial_{t_0}$. Now we substitute these equations into

$$\partial_{t_0}\rho + \tau\partial_{t_1}\rho + \nabla\cdot\rho\mathbf{u} = 0,$$

$$\implies \partial_t\rho + \nabla\cdot\rho\mathbf{u} = 0.$$

We need to calculate $\partial_{t_0}\mathbf{\Pi}^0$ and $\nabla\cdot\mathbf{Q}^0$ to obtain $\mathbf{\Pi}^1$. We know that

$$\Pi^0_{\alpha\beta} = \sum_i c_{i\alpha}c_{i\beta}f_i^0,$$

where

$$f_i^0 = \rho\omega_i[1 + \frac{c_{i\alpha}u_\alpha}{c_s^2} - \frac{u^2}{2c_s^2} + \frac{c_{i\alpha}c_{i\beta}u_\alpha u_\beta}{2(c_s^2)^2}],$$

and $u = |\mathbf{u}|$. In the D_2Q_9 and D_3Q_{19} lattices $c_s^2 = \frac{c}{3}$, where c is lattice speed and $c = 1$, α and β are vectors in two dimensions for D_2Q_9 and in three dimensions

for D_3Q_{19}. The equilibrium distribution function f^0 will therefore be

$$f_i^0 = \rho\omega_i\left[1+3c_{i\alpha}u_\alpha - \frac{3}{2}u_\alpha u_\alpha + \frac{9}{2}c_{i\alpha}c_{i\beta}u_\alpha u_\beta\right].$$

We then distribute ω_i on summation terms, using n^{th} rank generalized lattice tensor results from Wolf [74], so that

$$\begin{aligned}\Pi^0_{\alpha\beta} &= \sum_i c_{i\alpha}c_{i\beta}f_i^0,\\ &= \frac{\rho}{3}\delta_{\alpha\beta} + \frac{\rho}{2}(u_\alpha u_\beta + u_\alpha u_\beta).\end{aligned}$$

Thus,

$$\Pi^0_{\alpha\beta} = \frac{\rho}{3}\delta_{\alpha\beta} + \rho u_\alpha u_\beta,\ \mathbf{\Pi}^0 = PI + \rho\mathbf{uu},$$

where $P = \frac{\rho}{3}$ and I is the identity matrix. To calculate $\nabla\cdot\mathbf{Q}^0$ we will follow this process:

$$Q^0_{\alpha\beta\gamma} = \sum_i c_{i\alpha}c_{i\beta}c_{i\gamma}f_i^0,$$

$$\begin{aligned}Q^0_{\alpha\beta\gamma} = \rho\Bigg[&\sum_i w_i c_{i\alpha}c_{i\beta}c_{i\gamma} + 3\sum_i w_i c_{i\alpha}c_{i\beta}c_{i\gamma}c_{i\delta}u_\delta - \frac{3}{2}\sum_i w_i c_{i\alpha}c_{i\beta}c_{i\gamma}u_\delta u_\delta\\ &+\frac{9}{2}\sum_i w_i c_{i\alpha}c_{i\beta}c_{i\gamma}c_{i\delta}c_{i\theta}u_\delta u_\theta\Bigg],\end{aligned}$$

where the lattice tensor of zero rank is

$$\sum_i^9 \omega_i = 1. \tag{3.2.16}$$

The lattice tensor of ranks one, three and five, respectively, are

$$\sum_i \omega_i c_{i\alpha} = \sum_i \omega_i c_{i\alpha}c_{i\beta}c_{i\gamma} = \sum_i \omega_i c_{i\alpha}c_{i\beta}c_{i\gamma}c_{i\delta}c_{i\theta} = 0. \tag{3.2.17}$$

The lattice tensor of rank two is

$$\sum_i \omega_i c_{i\alpha} c_{i\beta} = c_s^2 \delta_{\alpha\beta} = c_s^2 = \frac{1}{3}\delta_{\alpha\beta}, \tag{3.2.18}$$

and of rank four is

$$\sum_i \omega_i c_{i\alpha} c_{i\beta} c_{i\gamma} c_{i\delta} = \Delta_{\alpha\beta\gamma\delta}, \tag{3.2.19}$$

where $\Delta_{\alpha\beta\gamma\delta} = \left(c_s^2\right)^2 (\delta_{\alpha\beta}\delta_{\gamma\delta} + \delta_{\alpha\gamma}\delta_{\beta\delta} + \delta_{\alpha\delta}\delta_{\gamma\beta})$

1. if

$$\alpha = \beta = \gamma = \delta \Longrightarrow \sum_i \omega_i c_{i\alpha} c_{i\beta} c_{i\gamma} c_{i\delta} = 3\left(c_s^2\right)^2, \tag{3.2.20}$$

2. if

$$\alpha = \beta \neq \gamma = \delta \Longrightarrow \sum_i \omega_i c_{i\alpha} c_{i\beta} c_{i\gamma} c_{i\delta} = \left(c_s^2\right)^2, \tag{3.2.21}$$

where $c_s = \dfrac{c}{\sqrt{3}}$ in two and three dimensions and $\delta_{\alpha\beta}$ is the Kronecker delta function

$$\delta_{\alpha\beta} = \begin{cases} 1 & \alpha = \beta, \\ 0 & \text{else.} \end{cases}$$

Now we use the n^{th} rank generalized lattice tensor results, Eqs (3.2.16), (3.2.17), (3.2.18) and (3.2.19), then

$$Q^0_{\alpha\beta\gamma} = \rho \frac{1}{3}\Delta_{\alpha\beta\gamma\delta} u_\delta, \tag{3.2.22}$$

$$= \frac{1}{3}\rho(u_\gamma \delta_{\alpha\beta} + u_\beta \delta_{\alpha\gamma} + u_\alpha \delta_{\gamma\beta}), \tag{3.2.23}$$

$$\Longrightarrow \partial_\gamma Q^0_{\alpha\beta\gamma} = \frac{1}{3}(\partial_\gamma \rho u_\gamma \delta_{\alpha\beta} + \partial_\gamma \rho u_\beta \delta_{\alpha\gamma} + \partial_\gamma \rho u_\alpha \delta_{\gamma\beta}), \tag{3.2.24}$$

$$\Longrightarrow \bigtriangledown \cdot \mathbf{Q}_0 = [(\bigtriangledown \cdot \rho\mathbf{u})I + (\bigtriangledown \rho\mathbf{u}) + (\bigtriangledown \rho\mathbf{u})^T]. \tag{3.2.25}$$

To find $\partial_{t_0}\mathbf{\Pi}^0$ we use the following process. We know that

$$\partial_{t_0}\mathbf{\Pi}^0 = \frac{1}{3}\partial_{t_0}\rho I + \partial_{t_0}\rho\mathbf{uu}.$$

First, we must find $\partial_{t_0}\rho\mathbf{uu}$. To find it we will apply the product rule which is

$$\partial_t\rho\mathbf{uu} = (\partial_t\rho\mathbf{u})\mathbf{u} + \mathbf{u}\partial_t(\rho\mathbf{u}) - (\partial_t\rho)\mathbf{uu},$$

then substitute Eq (3.2.7) and Eq (3.2.8) into $\partial_{t_0}\rho\mathbf{uu}$ after the application of the product rule, so $\partial_{t_0}\rho\mathbf{uu} = (-\nabla\cdot\mathbf{\Pi}^0)\mathbf{u} + \mathbf{u}(-\nabla\cdot\mathbf{\Pi}^0) + (\nabla\cdot\rho\mathbf{u})\mathbf{uu}$.
We will neglect the third term in $\mathbf{u}$ because $M_a \ll 1$ where $M_a = \dfrac{\mathbf{u}}{c} \ll 1$. We will use the definition of Π^0, so

$$\nabla\cdot\mathbf{\Pi}^0 = \frac{1}{3}(\nabla\cdot\rho I) + \nabla\cdot\rho\mathbf{uu},$$

then

$$\begin{aligned}\partial_{t_0}\rho\mathbf{uu} &= -\frac{1}{3}(\nabla\cdot\rho I)\mathbf{u} - (\bigtriangledown\cdot\rho\mathbf{uu})\,\mathbf{u} - \frac{1}{3}\mathbf{u}(\nabla\cdot\rho I) - \mathbf{u}\,(\bigtriangledown\cdot\rho\mathbf{uu}) \\ &= -\frac{1}{3}(\nabla\cdot\rho I)\mathbf{u} - \frac{1}{3}\mathbf{u}(\nabla\cdot\rho I)\end{aligned}$$

because we neglected the term of third order. Then

$$\partial_{t_0}\mathbf{\Pi}^0 = -\frac{1}{3}(\nabla\cdot\rho\mathbf{u})I - \frac{1}{3}(\nabla\cdot\rho I)\mathbf{u} - \frac{1}{3}\mathbf{u}(\nabla\cdot\rho I) \tag{3.2.26}$$

$$= -\frac{1}{3}(\nabla\cdot\rho\mathbf{u})I - \frac{1}{3}(\nabla\rho)\mathbf{u} - \frac{1}{3}\mathbf{u}(\nabla\rho). \tag{3.2.27}$$

From Eq (3.2.9) we know that

$$\mathbf{\Pi}^1 = -\partial_{t_0}\mathbf{\Pi}^0 - \nabla\cdot\mathbf{Q}^0, \tag{3.2.28}$$

so

$$\begin{aligned}\mathbf{\Pi}^1 &= +\frac{1}{3}(\nabla\cdot\rho\mathbf{u})I+\frac{1}{3}(\nabla\cdot\rho I)\mathbf{u}+\frac{1}{3}\mathbf{u}(\nabla\cdot\rho I)-\frac{1}{3}\left[(\nabla\cdot\rho\mathbf{u})I+(\nabla\rho\mathbf{u})+(\nabla\rho\mathbf{u})^T\right]\\ &= \frac{1}{3}\left[(\partial_\alpha\rho)u_\beta+u_\alpha(\partial_\beta\rho)-\partial_\alpha(\rho u_\beta)-\partial_\beta(\rho u_\alpha)\right]. \qquad (3.2.29)\end{aligned}$$

We know that

$$\partial_\alpha(\rho u_\beta)=\rho(\partial_\alpha u_\beta)+(\partial_\alpha\rho)u_\beta,$$

$$\partial_\beta(\rho u_\alpha)=\rho(\partial_\beta u_\alpha)+u_\alpha(\partial_\beta\rho).$$

When we substitute these equations into (3.2.29), so

$$\begin{aligned}\mathbf{\Pi}^1 &= -\frac{1}{3}\left[\rho(\partial_\alpha u_\beta)+\rho(\partial_\beta u_\alpha)\right],\\ \mathbf{\Pi}^1 &= -\frac{1}{3}\rho[(\nabla\mathbf{u})+(\nabla\mathbf{u})^T].\end{aligned}$$

Further substitution is then done, of $\mathbf{\Pi}^0$, $\partial_{t_1}\rho=0$ and $\mathbf{\Pi}^1$ into

$$\partial_{t_0}\rho\mathbf{u}+\nabla\cdot\mathbf{\Pi}^0+\tau(\partial_{t_1}\rho\mathbf{u}+\nabla\cdot\mathbf{\Pi}^1)=0,$$

to find that

$$\partial_t(\rho\mathbf{u})+\nabla\cdot\left(\frac{\rho}{3}I+\rho\mathbf{u}\mathbf{u}\right)-\nabla\cdot\frac{\tau\rho}{3}\left[(\nabla\mathbf{u})+(\nabla\mathbf{u})^T\right]=0,$$

$$\partial_t(\rho\mathbf{u})+\nabla\cdot\left(\frac{\rho}{3}I+\rho\mathbf{u}\mathbf{u}\right)-\nabla\cdot\mu\left[(\nabla\mathbf{u})+(\nabla\mathbf{u})^T\right]=0,$$

where $(\mu=\frac{\tau\rho}{3})$ is the dynamic viscosity and $(\nu=\frac{\tau}{3})$ is kinematic viscosity. This equation is the momentum equation.

With small Mach numbers the hydrodynamic equations will lead to the incom-

pressible Navier-Stokes equations, indicated by the following:

$$\begin{aligned} D_t\rho = \partial_t\rho + \nabla\cdot\rho\mathbf{u} = 0,\\ \frac{\partial}{\partial t} + \mathbf{u}\cdot\nabla = 0,\\ \nabla\cdot\mathbf{u} = 0,\\ \partial_t(\mathbf{u}) + \mathbf{u}\cdot\nabla\mathbf{u} = -\frac{1}{\rho}\nabla p + \nu(\nabla^2\mathbf{u}). \end{aligned} \tag{3.2.30}$$

where $D_t\rho$ is continuity equation and Eq (3.2.30) is momentum equation.

To find $\mathbf{Q}^1$ we have to calculate this equation, where: $-\partial_{t_0}\mathbf{Q}^0 - \nabla\cdot\mathbf{R}^0 = \mathbf{Q}^1$

$$Q^0_{\alpha\beta\gamma} = \frac{1}{3}(\rho u_\gamma\delta_{\alpha\beta} + \rho u_\beta\delta_{\alpha\gamma} + \rho u_\alpha\delta_{\gamma\beta}), \tag{3.2.31}$$

$$\partial_{t_0}Q^0_{\alpha\beta\gamma} = \frac{1}{3}(\partial_{t_0}\rho u_\gamma\delta_{\alpha\beta} + \partial_{t_0}\rho u_\beta\delta_{\alpha\gamma} + \partial_{t_0}\rho u_\alpha\delta_{\gamma\beta}), \tag{3.2.32}$$

and also the following, from equation (3.2.8), where we see that

$$\partial_{t_0}\rho u_\gamma = -\nabla_\delta\cdot\Pi^0_{\gamma\delta}, \tag{3.2.33}$$

$$\partial_{t_0}\rho u_\beta = -\nabla_\delta\cdot\Pi^0_{\beta\delta}, \tag{3.2.34}$$

$$\partial_{t_0}\rho u_\alpha = -\nabla_\delta\cdot\Pi^0_{\alpha\delta}, \tag{3.2.35}$$

so,

$$\begin{aligned} \partial_{t_0}Q^0_{\alpha\beta\gamma} = \frac{1}{3}(-\nabla_\delta\cdot\Pi^0_{\gamma\delta}\delta_{\alpha\beta} + -\nabla_\delta\cdot\Pi^0_{\beta\delta}\delta_{\alpha\gamma} + -\nabla_\delta\cdot\Pi^0_{\alpha\delta}\delta_{\gamma\beta}),\\ = \frac{1}{3}\left[-\partial_\delta\left(\frac{\rho}{3}\delta_{\gamma\delta} + \rho u_\gamma u_\delta\right)\delta_{\alpha\beta} - \partial_\delta\left(\frac{\rho}{3}\delta_{\beta\delta} + \rho u_\beta u_\delta\right)\delta_{\alpha\gamma} - \partial_\delta\left(\frac{\rho}{3}\delta_{\alpha\delta} + \rho u_\alpha u_\delta\right)\delta_{\gamma\beta}\right],\\ \partial_{t_0}Q^0_{\alpha\beta\gamma} = -\frac{\rho}{9}\left[\partial_\gamma\delta_{\alpha\beta} + \partial_\beta\delta_{\alpha\gamma} + \partial_\alpha\delta_{\gamma\beta}\right] - \frac{1}{3}\left[\rho u_\gamma\delta_{\alpha\beta} + \rho u_\beta\delta_{\alpha\gamma} + \rho u_\alpha\delta_{\beta\gamma}\right]\partial_\delta u_\delta. \end{aligned} \tag{3.2.36}$$

Now we want to find $\nabla\cdot\mathbf{R}^0$, starting with $R^0_{\alpha\beta\gamma\delta} = \sum_i c_{i\alpha}c_{i\beta}c_{i\gamma}c_{i\delta}f^0_i$, which is done

by

$$
\begin{aligned}
&= \rho \left[\sum_i w_i c_{i\alpha} c_{i\beta} c_{i\gamma} c_{i\delta} + 3 \sum_i w_i c_{i\alpha} c_{i\beta} c_{i\gamma} c_{i\delta} c_{i\theta} u_\theta - \frac{3}{2} \sum_i w_i c_{i\alpha} c_{i\beta} c_{i\gamma} c_{i\delta} u_\theta u_\theta \right. \\
&\qquad \left. + \frac{9}{2} \sum_i w_i c_{i\alpha} c_{i\beta} c_{i\gamma} c_{i\delta} c_{i\theta} c_{i\varepsilon} u_\theta u_\varepsilon \right], \\
&= \rho \left[\sum_i w_i c_{i\alpha} c_{i\beta} c_{i\gamma} c_{i\delta} - \frac{3}{2} \sum_i w_i c_{i\alpha} c_{i\beta} c_{i\gamma} c_{i\delta} u_\theta u_\theta + \frac{9}{2} \sum_i w_i c_{i\alpha} c_{i\beta} c_{i\gamma} c_{i\delta} c_{i\theta} c_{i\varepsilon} u_\theta u_\varepsilon \right], \\
&= \rho \left[\frac{1}{9} \left[\delta_{\alpha\beta}\delta_{\gamma\delta} + \delta_{\alpha\gamma}\delta_{\beta\delta} + \delta_{\alpha\delta}\delta_{\gamma\beta} \right] - \frac{1}{6} \left[\delta_{\alpha\beta}\delta_{\gamma\delta} + \delta_{\alpha\gamma}\delta_{\beta\delta} + \delta_{\alpha\delta}\delta_{\gamma\beta} \right] u_\theta u_\theta \right. \\
&\left. + \frac{1}{6} \left[\delta_{\alpha\delta} \left(\delta_{\beta\theta}\delta_{\gamma\varepsilon} + \delta_{\beta\varepsilon}\delta_{\gamma\theta} \right) + \delta_{\alpha\theta} \left(\delta_{\beta\delta}\delta_{\gamma\varepsilon} + \delta_{\beta\varepsilon}\delta_{\gamma\delta} \right) + \delta_{\alpha\varepsilon} \left(\delta_{\beta\delta}\delta_{\gamma\theta} + \delta_{\beta\theta}\delta_{\gamma\delta} \right) \right] u_\theta u_\varepsilon \right],
\end{aligned}
\tag{3.2.37}
$$

where

$$
\begin{aligned}
\sum_i w_i c_{i\alpha} c_{i\beta} c_{i\gamma} c_{i\delta} c_{i\theta} c_{i\varepsilon} &= c_s^6 \left[\delta_{\alpha\delta} \left(\delta_{\beta\theta}\delta_{\gamma\varepsilon} + \delta_{\beta\varepsilon}\delta_{\gamma\theta} \right) \right. \\
&\left. + \delta_{\alpha\theta} \left(\delta_{\beta\delta}\delta_{\gamma\varepsilon} + \delta_{\beta\varepsilon}\delta_{\gamma\delta} \right) + \delta_{\alpha\varepsilon} \left(\delta_{\beta\delta}\delta_{\gamma\theta} + \delta_{\beta\theta}\delta_{\gamma\delta} \right) \right],
\end{aligned}
\tag{3.2.38}
$$

and

$$
\begin{aligned}
\nabla_\delta \cdot R^0_{\alpha\beta\gamma\delta} &= \nabla_\delta \cdot \rho \left[\frac{1}{9} \left[\delta_{\alpha\beta}\delta_{\gamma\delta} + \delta_{\alpha\gamma}\delta_{\beta\delta} + \delta_{\alpha\delta}\delta_{\gamma\beta} \right] - \nabla_\delta \cdot \frac{1}{6} \left[\delta_{\alpha\beta}\delta_{\gamma\delta} + \delta_{\alpha\gamma}\delta_{\beta\delta} + \delta_{\alpha\delta}\delta_{\gamma\beta} \right] u_\theta u_\theta \right. \\
&\left. + \nabla_\delta \cdot \frac{1}{6} \left[\delta_{\alpha\delta} \left(\delta_{\beta\theta}\delta_{\gamma\varepsilon} + \delta_{\beta\varepsilon}\delta_{\gamma\theta} \right) + \delta_{\alpha\theta} \left(\delta_{\beta\delta}\delta_{\gamma\varepsilon} + \delta_{\beta\varepsilon}\delta_{\gamma\delta} \right) + \delta_{\alpha\varepsilon} \left(\delta_{\beta\delta}\delta_{\gamma\theta} + \delta_{\beta\theta}\delta_{\gamma\delta} \right) \right] u_\theta u_\varepsilon \right], \\
&= \left[\frac{\rho}{9} \left[\delta_{\alpha\beta}\partial_\gamma + \delta_{\alpha\gamma}\partial_\beta + \partial_\alpha\delta_{\gamma\beta} \right] - \frac{\rho}{3} \left[\delta_{\alpha\beta}\partial_\gamma + \delta_{\alpha\gamma}\partial_\beta + \partial_\alpha\delta_{\gamma\beta} \right] u_\theta u_\theta \right. \\
&\left. + \frac{1}{6} \left[u_\alpha \left(\partial_\beta \rho u_\gamma + \partial_\gamma \rho u_\beta \right) + u_\gamma \left(\partial_\alpha \rho u_\beta + \partial_\beta \rho u_\alpha \right) + u_\beta \left(\partial_\alpha \rho u_\gamma + \partial_\gamma \rho u_\alpha \right) \right] \right].
\end{aligned}
\tag{3.2.39}
$$

Then Eqs (3.2.36) and (3.2.39) are substituted into $-\partial_{t_0}\mathbf{Q}^0 - \nabla \cdot \mathbf{R}^0 = \mathbf{Q}^1$

$$
\begin{aligned}
Q^1_{\alpha\beta\gamma} &= \frac{1}{3} \left[\rho u_\gamma \delta_{\alpha\beta} + \rho u_\beta \delta_{\alpha\gamma} + \rho u_\alpha \delta_{\beta\gamma} \right] \partial_\delta u_\delta + \frac{\rho}{3} \left[\delta_{\alpha\beta}\partial_\gamma + \delta_{\alpha\gamma}\partial_\beta + \partial_\alpha\delta_{\gamma\beta} \right] u_\theta u_\theta \\
&\quad + \frac{\rho}{6} \left[u_\alpha \left(\partial_\beta u_\gamma + \partial_\gamma u_\beta \right) + u_\gamma \left(\partial_\alpha u_\beta + \partial_\beta u_\alpha \right) + u_\beta \left(\partial_\alpha u_\gamma + \partial_\gamma u_\alpha \right) \right].
\end{aligned}
\tag{3.2.40}
$$

In D_3Q_{19} the $u_\delta = (u_x, u_y, u_z)$, therefore

$$\begin{aligned} Q^1_{\alpha\beta\gamma} = \frac{1}{3}\left[\rho u_\gamma \delta_{\alpha\beta} + \rho u_\beta \delta_{\alpha\gamma} + \rho u_\alpha \delta_{\beta\gamma}\right](\partial_x u_x + \partial_y u_y + \partial_z u_z) \\ + \frac{\rho}{3}\left[\delta_{\alpha\beta}\partial_\gamma + \delta_{\alpha\gamma}\partial_\beta + \partial_\alpha \delta_{\gamma\beta}\right]\left(u_x^2 + u_y^2 + u_z^2\right) \\ - \frac{\rho}{6}\left[u_\alpha\left(\partial_\beta u_\gamma + \partial_\gamma u_\beta\right) + u_\gamma\left(\partial_\alpha u_\beta + \partial_\beta u_\alpha\right) + u_\beta\left(\partial_\alpha u_\gamma + \partial_\gamma u_\alpha\right)\right]. \end{aligned} \tag{3.2.41}$$

Chapter 4

Boundary conditions

Boundary conditions have an important role in mathematics as they are used to determine the mathematical solutions for many physical problems. In physics, the fluid boundary represents the interaction between fluid molecules and solid wall molecules, so boundary conditions can be defined as special collisions between solid and fluid molecules. Mathematically, boundary conditions are a set of conditions based on a set of differential equations to describe the solution of equations at a wall or domain.

The principle of stating the boundary conditions in the LBM is to determine a set of distribution functions which are used to calculate macroscopic quantities on the boundary nodes. The boundary conditions must be simple and sufficient enough to satisfy a high level of accuracy and stability.

There are many types of boundary conditions. Here we will briefly describe some of them which are used in our simulations, such as periodic and bounce back.

4.1 Periodic boundary condition

The easiest approach to express the boundary condition is using a grid mesh. This contains nodes (i, j) where $i = 0, 1, ..., m_x$ and $j = 0, 1, ..., n_y$ and four directions N, S, W, E which are called North, South, West and East, respectively. These directions represent the sites of the buffers, as can be seen in Figure (4.1) [56].

$$
\begin{aligned}
N &= \{(i, ny) : i = 0, ..., m_x\}, \\
S &= \{(i, 0) : i = 0, ..., m_x\}, \\
W &= \{(0, j) : j = 0, ..., n_y\}, \\
E &= \{(mx, j) : j = 0, ..., n_y\}.
\end{aligned} \tag{4.1.1}
$$

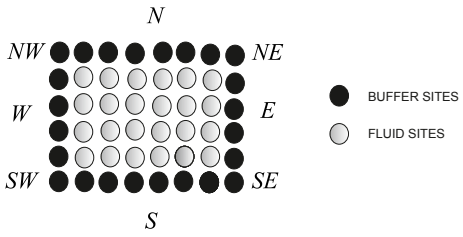

Figure 4.1: Buffer sites for a 8×6 domain [56].

Periodic boundary conditions mean the molecules leave the boundary and return back to the fluid on the opposite side in the same direction and at the same velocity. For example, when the molecules move from the East buffer E with direction $\mathbf{c}_1$ (horizontal direction), the distribution function $f_1(m_x, j)$ at time t streams or transfers to $f_1(0, j)$ at the next time step $t + \delta_t$:

$$\begin{aligned} f_{in,W}(W) &= f_{out,E}(E), \\ f_{in,E}(E) &= f_{out,W}(W), \end{aligned} \tag{4.1.2}$$

$$\begin{aligned} \{in, W\} = \{out, E\}, \quad f_k(0, j) = f_k(m_x, j), \quad k = 1, 5, 8 \\ \{out, W\} = \{in, E\}, \quad f_k(m_x, j) = f_k(0, j), \quad k = 3, 6, 7. \end{aligned} \tag{4.1.3}$$

The subscripts in and out represent the inward and outward population, respectively, as seen in Figure (4.2). For the corner buffer sites we take this treatment

$$\begin{aligned} f_{in}(NW) &= f_{out}(SE), \\ f_{in}(SW) &= f_{out}(NE), \\ f_{in}(NE) &= f_{out}(SW), \\ f_{in}(SE) &= f_{out}(NW), \end{aligned} \tag{4.1.4}$$

which is applied to D_2Q_9 as shown below.

Figure 4.2: Periodic boundary condition for D_2Q_9 [20].

In general, this condition preserves the mass.

4.2 No-slip boundary condition

The no-slip boundary conditions assume that fluid moves with the same velocity as the wall. In bounce back boundary condition, one of the ways of implementing the no-slip boundary condition, the stationary wall standing on the lattice axis reflects the direction of molecules and their velocities to their original location after their collision with the wall. The LGA and LBM have a property which enables the complete bounce back scheme to be performed very easily in a parallel method. However, it is difficult to distinguish the direction of the distribution function after it hits the wall [64].

4.2.1 Bounce back boundary condition

There are several schemes of bounce back boundary conditions such as standard bounce back scheme, modified bounce back scheme, half-way bounce back scheme and on-grid bounce back scheme [64].

4.2.2 Standard Bounce Back Scheme

This scheme is also called bounce back without collision, because the collision process does not happen at the boundary nodes (stationary wall) [64]. For $D2Q9$ the unknown distribution function f_2, f_5 and f_6 are marked in this scheme as

$$\begin{aligned} f_2(i,j) &= f_4(i,j+1), \\ f_5(i,j) &= f_7(i+1,j+1), \\ f_6(i,j) &= f_8(i-1,j+1). \end{aligned} \tag{4.2.1}$$

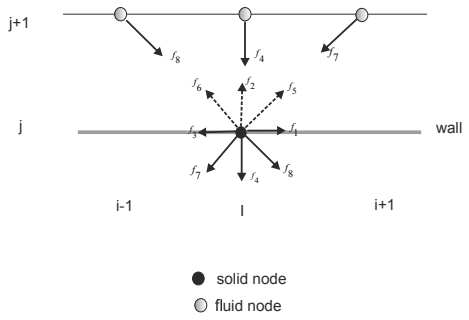

Figure 4.3: Standard bounce back scheme at the bottom of D_2Q_9 [64].

The standard bounce back scheme has first order accuracy.

4.2.3 Modified Bounce Back Scheme or On-Grid Bounce Back Scheme

This scheme is distinguished by imposing a collision process and force on the boundary nodes [64]. For $D2Q9$ the unknown collision distribution function $\overline{f}_2, \overline{f}_5$ and $\overline{f}_6$ are marked in this scheme as

$$\begin{aligned} f_2(i,j) &= f_4(i,j), \\ f_5(i,j) &= f_7(i,j), \\ f_6(i,j) &= f_8(i,j). \end{aligned} \tag{4.2.2}$$

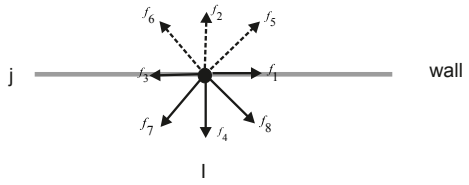

Figure 4.4: Modified bounce back scheme at the bottom of D_2Q_9 [64].

The Modified bounce back scheme is of second order accuracy.

4.2.4 Half-way bounce back scheme

The half-way bounce back scheme is a kind of standard bounce back scheme. Its formulation is the same as the standard bounce back formulation except that the stationary wall is located in the centre of the link between the wall grid point

and fluid grid point, which means in terms of physics that the molecules and their velocities arrive at the stationary wall at time step $\frac{\delta_t}{2}$, then reflect along with their velocities to their original position at time step $\frac{\delta_t}{2}$ [64]. For this reason, the accuracy of the half-way bounce back scheme is of second order.

In the example of D_2Q_9 the unknown collision distribution functions $\overline{f}_2, \overline{f}_5$ and $\overline{f}_6$ are formulated as

$$\begin{aligned} f_2(i,j) &= f_4(i,j+1), \\ f_5(i,j) &= f_7(i+1,j+1), \\ f_6(i,j) &= f_8(i-1,j+1). \end{aligned} \tag{4.2.3}$$

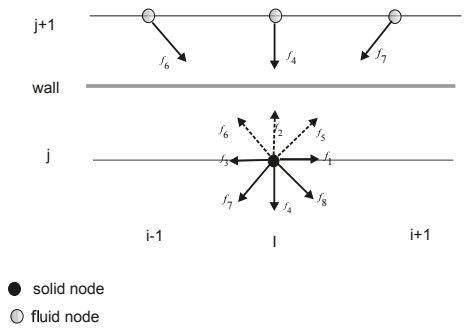

Figure 4.5: Half-way bounce back scheme at the bottom of D_2Q_9 [64].

4.3 Specular boundary condition

The specular boundary condition is used to calculate the slip velocity at the wall. After the collision, the unknown distribution functions are reflected in the same way as light is reflected by a mirror [55]. For $D2Q9$, the unknown distribution functions $\overline{f}_2, \overline{f}_5$ and $\overline{f}_6$ are marked as

$$\begin{aligned} f_2(i,j) &= f_4(i,j), \\ f_5(i,j) &= f_8(i,j), \\ f_6(i,j) &= f_7(i,j). \end{aligned} \tag{4.3.1}$$

This boundary condition has been used by Lim [40] to examine the pressure and shear driven 2-dimensional micro-channel flow.

4.4 The combination of bounce back and specular boundary conditions

In real gas flow in micro-channels, the no-slip bounce-backs and free-slip specular reflections (zero shear stress) is not always able to describe or explain the momentum exchange and friction between the wall and fluid. Hence, the combination of them is often considered a better method to simulate gas flow in micro-channels. This combination of no-slip bounce back and specular boundary conditions has been presented by Tang *et. al*. [66] and formulated as

$$f_i = r f_i^{BB} + (1-r) f_i^{SR}, \tag{4.4.1}$$

where r is the reflection coefficient and $(1-r)$ is the specular reflection. Succi [65] also presented the combination of bounce back and specular boundary condition but with the addition of a slip coefficient $(1-r)$ to a very similar formula to that proposed by Tang *et. al* [68]. An example of this, using modified bounce back combined with specular reflection boundary condition, to find the unknown distribution functions $\overline{f}_2, \overline{f}_5$ and $\overline{f}_6$ at the South wall of D_2Q_9, is formulated as

$$\begin{aligned} f_2(i,j) &= r f_4(i,j), \\ f_5(i,j) &= r f_7(i,j) + (1-r) f_8(i,j), \\ f_6(i,j) &= r f_8(i,j)\,(1-r) f_7(i,j). \end{aligned} \tag{4.4.2}$$

4.5 Slip boundary condition.

The Knudsen number divides flow into four regimes: continuum flow $(k_n \leq 0.001)$; slip flow $(0.001 < k_n \leq 0.1)$; transition flow $(0.1 < k_n \leq 10)$ and free molecular flow $(k_n \geq 10)$. In the slip flow regime the flow is affected by rarefaction, and the Navier-Stokes equations are valid as long as tangential slip velocity is applied along the flow domain walls. The effect of rarefaction is to reduce the density and pressure.

In 1823, Navier suggested a slip boundary condition which supposed that tangential fluid velocity is proportional to the rate of shear stress at the surface [48]. Later in 1823, James Clerk Maxwell applied Navier-slip boundary conditions to the rarefied gas flows over surfaces [43]. He used the Taylor expansion to expand the slip velocity at the surface. We write this expression as

$$u_s = u(y) - u_w = \theta_u \left(\lambda \frac{\partial u}{\partial n} + \frac{\lambda^2}{2} \frac{\partial^2 u}{\partial n^2} + ... \right) |_w, \tag{4.5.1}$$

where u_s is the slip velocity, $u(y)$ is the tangential velocity, u_w is the velocity at the wall, $n \gtrless 0$ is the normal direction to the wall, $\theta_u = \dfrac{2-\sigma_u}{\sigma_u}$ is a streamwise momentum accommodation coefficient, and σ_u is always equal to one in engineering practical or engineering applications. The $\lambda = L_{mfp}$ is the mean free path, which can be replaced in liquid slip by the slip length l_s or molecular interaction length, as the mathematical meaning is the same [41]. Mean free path cannot be satisfactorily defined, because the Boltzmann collision operator is dependent on the velocity of the particles [58]. The first order slip velocity is obtained by truncation of the Taylor expansion to the first term, so, the form for slip velocity of the first order [43] is

$$u_s = \lambda \left(\frac{\partial u}{\partial n} \right) |_w \, . \tag{4.5.2}$$

4.6 Moment-based boundary condition

The lattice Boltzmann equation includes a finite group of distribution functions. These distribution functions can be related to Lattice Boltzmann moments by a linear, invertible transformation. The moment-based boundary condition is distinguished by assuming the boundary conditions on the moments at the boundary, then expressing these as conditions for the unknown variables. The moment-basis boundary condition could be considered to build directly on the method presented by Noble *et. al* [50], who used the hexagonal FHP (D_2Q_7) lattice model and assumed constraint on the velocity to find the two incoming distribution functions. Lattices such as D_2Q_9 and D_3Q_{19}, however, have more than two

incoming distribution functions and the approach will therefore be more complicated. For this reason, the Noble approach has been generalised by Bennett [6], who uses the linear relationship between the distribution functions and moments, imposes conditions on independent moments and then converts these conditions into the unknown (incoming) distribution functions.

The moment-based boundary condition has been applied to several forms of flow in both 2 and 3 dimensions. Examples of two-dimensional applications include: diffusive slip [6], rarefied flow with Navier-Maxwell slip velocity [58], multiphase flow with partially-wetted walls [23] and stress boundary conditions (Burnett order stress) [57]. Their results show that the accuracy of the moment-based boundary conditions to implement velocity and pressure boundary condition is of second order, which coincides with the LBM in this case.

The moment-based boundary conditions in two dimensions have been extended to three dimensions, for example by Kao *et. al* [34]. In this study, Krastins' extension of the moment boundary condition to three dimensions is detailed, in which first order Lattice Boltzmann equation with no-slip and pressure boundary conditions is used to simulate flows such as the convection in dendritic solidification. He also estimates the momentum flux tensor $\mathbf{Q}$ to its equilibrium $\mathbf{Q}^0$, which is used to recover the Navier-Stokes equations up to the second order.

There are many advantages for moment-based conditions. One of the advantages is that it eliminates the viscosity-dependent error associated with bounce-back, and another is that it allows a diversity of hydrodynamic constituents to be put at grid points. A further advantage is the ease of parallelising moment-based conditions to implement period boundary and pressure boundary conditions, because the distribution functions being used come from the boundary nodes or cells. One disadvantage of this approach, however, is that the extension required to work on a curved geometry is difficult.

There are other advantages of the moment-based condition, such as its convenience for continuum flows because boundary conditions located directly for macroscopic quantities (moments) is reasonable, compared with describing ki-

netic theory's virtual interactions between particles and wall. Whereas kinetic boundary conditions can in some instances be used to address the Lattice Boltzmann method, kinetic boundary conditions are not suitable for the D_2Q_9 system [6]. This is because we truncate the infinite moment system to a nine-moment system, and this truncation leads to loss of connection to the continuity of the Boltzmann equation. The moment-based boundary condition, however, is reasonable in this case, as the Navier-Stokes equations (equations used for the macroscopic level) are solved by the LBM such that the macroscopic quantities (moments) must satisfy the set boundary condition.

In this thesis, the extension to three dimensional moment-based boundary condition is of second order accuracy according to LBM, Eq (2.1.42), and the exact value for $\mathbf{Q}$ is found by deriving $\mathbf{Q}^0$, Eq (3.2.23), and $\mathbf{Q}^1$, Eq (3.2.41), where $\mathbf{Q} = \mathbf{Q}^0 + \tau\mathbf{Q}^1$. Also, the moment-based boundary condition is used to implement: a solid boundary, such as no-slip or Navier-slip in either 2 or 3 dimensions; an open boundary, such as pressure in 2 or 3 dimensions or inflow in 3; or one with corners.

4.6.1 Moment Grouping

If we have n independent lattice velocities, it follows that we must have a set number of moments n. For example, for D_2Q_9 we have nine independent moments. Six of them are hydrodynamic moments ρ, ρu_x, ρu_y, Π_{xx}, Π_{yy} and Π_{xy}, and three of them are pseudo-kinetic Q_{xxy}, Q_{xyy} and R_{xxyy}. The moments can be defined as

$\mathbf{m} = M\mathbf{f}$ where, for D_2Q_9, M is square matrix of 9×9:

$$\begin{pmatrix} \rho \\ \rho u_x \\ \rho u_y \\ \Pi_{xx} \\ \Pi_{yy} \\ \Pi_{xy} \\ Q_{xxy} \\ Q_{xyy} \\ R_{xxyy} \end{pmatrix} = \begin{pmatrix} 1 & 1 & 1 & 1 & 1 & 1 & 1 & 1 & 1 \\ 0 & 1 & 0 & -1 & 0 & 1 & -1 & -1 & 1 \\ 0 & 0 & 1 & 0 & -1 & 1 & 1 & -1 & -1 \\ 0 & 1 & 0 & 1 & 0 & 1 & 1 & 1 & 1 \\ 0 & 0 & 1 & 0 & 1 & 1 & 1 & 1 & 1 \\ 0 & 0 & 0 & 0 & 0 & 1 & -1 & 1 & -1 \\ 0 & 0 & 0 & 0 & 0 & 1 & 1 & -1 & -1 \\ 0 & 0 & 0 & 0 & 0 & 1 & -1 & -1 & 1 \\ 0 & 0 & 0 & 0 & 0 & 1 & 1 & 1 & 1 \end{pmatrix} \begin{pmatrix} f_0 \\ f_1 \\ f_2 \\ f_3 \\ f_4 \\ f_5 \\ f_6 \\ f_7 \\ f_8 \end{pmatrix} \tag{4.6.1}$$

i.e.

$$\begin{pmatrix} \rho \\ \rho u_x \\ \rho u_y \\ \Pi_{xx} \\ \Pi_{yy} \\ \Pi_{xy} \\ Q_{xxy} \\ Q_{xyy} \\ R_{xxyy} \end{pmatrix} = \begin{pmatrix} \sum_i f_i \\ \sum_i c_{ix} f_i \\ \sum_i c_{iy} f_i \\ \sum_i c_{ix} c_{ix} f_i \\ \sum_i c_{iy} c_{iy} f_i \\ \sum_i c_{ix} c_{iy} f_i \\ \sum_i c_{ix} c_{ix} c_{iy} f_i \\ \sum_i c_{ix} c_{iy} c_{iy} f_i \\ \sum_i c_{ix} c_{ix} c_{iy} c_{iy} f_i \end{pmatrix} \tag{4.6.2}$$

The equilibrium moments may be ordered as $\mathbf{m}^{eq} = M\mathbf{f}^{eq}$.

For D_3Q_{19} there are 19 independent moments, nine of which are hydrodynamic: ρ, ρu_x, ρu_y, Π_{xx}, Π_{yy}, Π_{zz} and Π_{xy}, Π_{xz} and Π_{yz}; and nine of which are pseudo-kinetic: Q_{xxy}, Q_{xyy}, Q_{xxz}, Q_{xzz}, Q_{yyz}, Q_{yzz} and R_{xxyy}, R_{xxzz} and R_{yyzz}.

The moments grouping for D_3Q_{19} can be expressed as

$$
\begin{pmatrix}
\rho \\ \rho u_x \\ \rho u_y \\ \rho u_z \\ \Pi_{xx} \\ \Pi_{yy} \\ \Pi_{zz} \\ \Pi_{xy} \\ \Pi_{xz} \\ \Pi_{yz} \\ Q_{xxy} \\ Q_{xyy} \\ Q_{xxz} \\ Q_{xzz} \\ Q_{yyz} \\ Q_{yzz} \\ R_{xxyy} \\ R_{xxzz} \\ R_{yyzz}
\end{pmatrix}
=
\begin{pmatrix}
1 & 1 & 1 & 1 & 1 & 1 & 1 & 1 & 1 & 1 & 1 & 1 & 1 & 1 & 1 & 1 & 1 & 1 & 1 \\
0 & 1 & -1 & 0 & 0 & 0 & 0 & 1 & -1 & -1 & 1 & 1 & 1 & -1 & -1 & 0 & 0 & 0 & 0 \\
0 & 0 & 0 & 1 & -1 & 0 & 0 & 1 & 1 & -1 & -1 & 0 & 0 & 0 & 0 & 1 & 1 & -1 & -1 \\
0 & 0 & 0 & 0 & 0 & 1 & -1 & 0 & 0 & 0 & 0 & 1 & -1 & -1 & 1 & 1 & -1 & -1 & 1 \\
0 & 1 & 1 & 0 & 0 & 0 & 0 & 1 & 1 & 1 & 1 & 1 & 1 & 1 & 1 & 0 & 0 & 0 & 0 \\
0 & 0 & 0 & 1 & 1 & 0 & 0 & 1 & 1 & 1 & 1 & 0 & 0 & 0 & 0 & 1 & 1 & 1 & 1 \\
0 & 0 & 0 & 0 & 0 & 1 & 1 & 0 & 0 & 0 & 0 & 1 & 1 & 1 & 1 & 1 & 1 & 1 & 1 \\
0 & 0 & 0 & 0 & 0 & 0 & 0 & 1 & -1 & 1 & -1 & 0 & 0 & 0 & 0 & 0 & 0 & 0 & 0 \\
0 & 0 & 0 & 0 & 0 & 0 & 0 & 0 & 0 & 0 & 0 & 1 & -1 & 1 & -1 & 0 & 0 & 0 & 0 \\
0 & 0 & 0 & 0 & 0 & 0 & 0 & 0 & 0 & 0 & 0 & 0 & 0 & 0 & 0 & 1 & -1 & 1 & -1 \\
0 & 0 & 0 & 0 & 0 & 0 & 0 & 1 & 1 & -1 & -1 & 0 & 0 & 0 & 0 & 0 & 0 & 0 & 0 \\
0 & 0 & 0 & 0 & 0 & 0 & 0 & 1 & -1 & -1 & 1 & 0 & 0 & 0 & 0 & 0 & 0 & 0 & 0 \\
0 & 0 & 0 & 0 & 0 & 0 & 0 & 0 & 0 & 0 & 0 & 1 & -1 & -1 & 1 & 0 & 0 & 0 & 0 \\
0 & 0 & 0 & 0 & 0 & 0 & 0 & 0 & 0 & 0 & 0 & 1 & 1 & -1 & -1 & 0 & 0 & 0 & 0 \\
0 & 0 & 0 & 0 & 0 & 0 & 0 & 0 & 0 & 0 & 0 & 0 & 0 & 0 & 0 & 1 & -1 & -1 & 1 \\
0 & 0 & 0 & 0 & 0 & 0 & 0 & 0 & 0 & 0 & 0 & 0 & 0 & 0 & 0 & 1 & 1 & -1 & -1 \\
0 & 0 & 0 & 0 & 0 & 0 & 0 & 1 & 1 & 1 & 1 & 0 & 0 & 0 & 0 & 0 & 0 & 0 & 0 \\
0 & 0 & 0 & 0 & 0 & 0 & 0 & 0 & 0 & 0 & 0 & 1 & 1 & 1 & 1 & 0 & 0 & 0 & 0 \\
0 & 0 & 0 & 0 & 0 & 0 & 0 & 0 & 0 & 0 & 0 & 0 & 0 & 0 & 0 & 1 & 1 & 1 & 1
\end{pmatrix}
\begin{pmatrix}
f_0 \\ f_1 \\ f_2 \\ f_3 \\ f_4 \\ f_5 \\ f_6 \\ f_7 \\ f_8 \\ f_9 \\ f_{10} \\ f_{11} \\ f_{12} \\ f_{13} \\ f_{14} \\ f_{15} \\ f_{16} \\ f_{17} \\ f_{18}
\end{pmatrix},
$$

i.e.

$$
\begin{pmatrix}
\rho \\
\rho u_x \\
\rho u_y \\
\rho u_z \\
\Pi_{xx} \\
\Pi_{yy} \\
\Pi_{zz} \\
\Pi_{xy} \\
\Pi_{xz} \\
\Pi_{yz} \\
Q_{xxy} \\
Q_{xyy} \\
Q_{xxz} \\
Q_{xzz} \\
Q_{yyz} \\
Q_{yzz} \\
R_{xxyy} \\
R_{xxzz} \\
R_{yyzz}
\end{pmatrix}
=
\begin{pmatrix}
\sum_i f_i \\
\sum_i c_{ix} f_i \\
\sum_i c_{iy} f_i \\
\sum_i c_{iz} f_i \\
\sum_i c_{ix} c_{ix} f_i \\
\sum_i c_{iy} c_{iy} f_i \\
\sum_i c_{iz} c_{iz} f_i \\
\sum_i c_{ix} c_{iy} f_i \\
\sum_i c_{ix} c_{iz} f_i \\
\sum_i c_{iy} c_{iz} f_i \\
\sum_i c_{ix} c_{ix} c_{iy} f_i \\
\sum_i c_{ix} c_{iy} c_{iy} f_i \\
\sum_i c_{ix} c_{ix} c_{iz} f_i \\
\sum_i c_{ix} c_{iz} c_{iz} f_i \\
\sum_i c_{iy} c_{iy} c_{iz} f_i \\
\sum_i c_{iy} c_{iz} c_{iz} f_i \\
\sum_i c_{ix} c_{ix} c_{iy} c_{iy} f_i \\
\sum_i c_{ix} c_{ix} c_{iz} c_{iz} f_i \\
\sum_i c_{iy} c_{iy} c_{iz} c_{iz} f_i
\end{pmatrix}
\tag{4.6.3}
$$

Moreover, the choosing of moments is dependent on the boundary condition to be applied such as no-slip, Navier-slip, pressure and inflow boundary boundary condition, implemented using moment-based boundary condition. The choice of moments of a low order is preferable to a high order, as the latter do not appear in the Navier-Stokes equations and cannot be directly physically interpreted. However, the use of high order moments such as $\mathbf{Q}$ is necessary at edges and

corners.

4.6.2 Moment boundary technique

The scenario for D_2Q_9 is as follows. Consider that we have a solid wall at both the North and South sides of the flow. After the streaming step, the unknown distribution functions at the North boundary are f_4, f_7 and f_8, and at the South are f_2, f_5 and f_6, as illustrated in the table below (4.1).

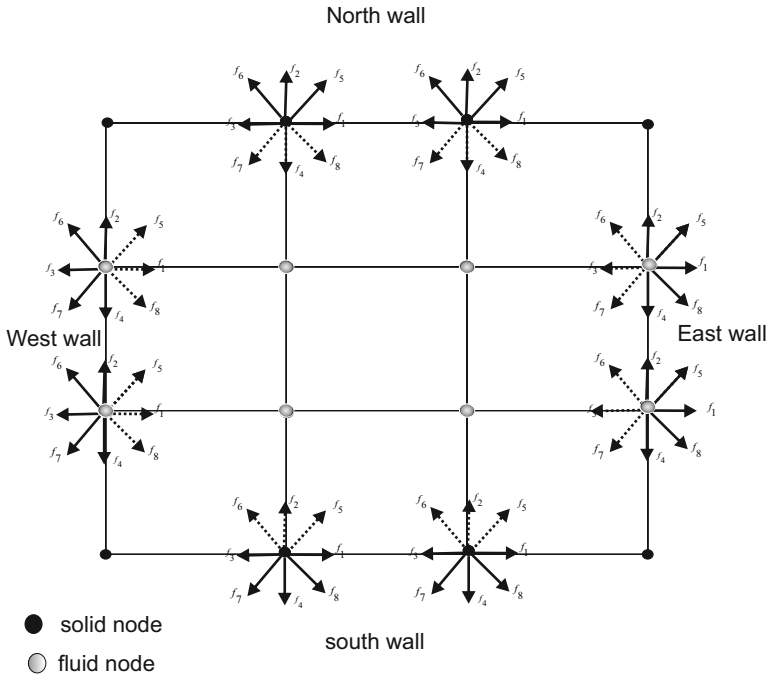

Figure 4.6: The unknown distribution functions after streaming.

The principle of the moment-based boundary condition is to find the three unknown distribution functions using three independent equations. These are obtained using the following steps:

- From section (4.6.1), Eq (4.6.1), every moment is written as a linear combi-

nation of distribution functions and lattice velocities. For example,

$$\begin{aligned}
\rho &= f_0 + f_1 + f_2 + f_3 + f_4 + f_5 + f_6 + f_7 + f_8, \\
\rho u_y &= f_2 - f_4 + f_5 + f_6 - f_7 - f_8, \\
&= f_2 + f_5 + f_6 - (f_4 + f_7 + f_8), \\
\Pi_{yy} &= f_2 + f_5 + f_6 + (f_4 + f_7 + f_8). \qquad (4.6.4)
\end{aligned}$$

- The unknown distribution functions in every linear combination are determined. For instance, at the North wall the unknown distribution functions are f_4, f_7 and f_8 at every moment as demonstrated in Eq (4.6.4).
- All the linear combinations of unknown distribution functions are arranged in Table (4.1) and Table (4.2).
- One moment from every row in the table is chosen. The moments in every row are independent. For this example, the selected moments are: the moment of the zero order (density ρ); the first order moment (momentum $\rho\mathbf{u}$); and the second order moment (momentum flux tensor $\mathbf{\Pi}$).
- The constraints that correspond to the moments are imposed.
- The system which consists of the three unknown distribution functions with three independent equations is solved.

Moments	Combination of unknowns distribution function at the North boundary	Combination of unknowns distribution function at the South boundary
$\rho, \rho u_y, \Pi_{yy}$	$f_4 + f_7 + f_8$	$f_2 + f_5 + f_6$
$\rho u_x, \Pi_{xy}, Q_{xyy}$	$f_8 - f_7$	$f_5 - f_6$
$\Pi_{xx}, Q_{xxy}, R_{xxyy}$	$f_8 + f_7$	$f_5 + f_6$

Table 4.1: Moments at the North and South boundaries.

Moments	Combination of unknowns distribution function at the East boundary	Combination of unknowns distribution function at the West boundary
$\rho, \rho u_x, \Pi_{xx}$	$f_3 + f_6 + f_7$	$f_1 + f_5 + f_8$
$\rho u_y, \Pi_{xy}, Q_{xxy}$	$f_6 - f_7$	$f_5 - f_8$
$\Pi_{yy}, Q_{xyy}, R_{xxyy}$	$f_6 + f_7$	$f_5 + f_8$

Table 4.2: Moments at the East and West boundaries.

The scenario for D_3Q_{19} is similar to that for D_2Q_9. For example, D_3Q_{19} always has five unknown incoming distributions at the faces after LBM post-streaming, which can be found from five linearly independent moment conditions. These unknown incoming distributions are listed in Tables (4.3), (4.4), (4.5) and (4.6). An example of these unknown distribution functions, in this case at the South wall, are f_5, f_{11}, f_{14}, f_{15} and f_{18} and the five linearly independent moments are ρu_x, ρu_y, ρu_z, Π_{xx} and Π_{yy} which are written as linear combinations of distribution functions as follows:

$$\begin{aligned}
\rho u_x &= f_1 - f_2 + f_7 - f_8 - f_9 + f_{10} + f_{11} + f_{12} - f_{13} - f_{14}, \\
\rho u_y &= f_3 - f_4 + f_7 + f_8 - f_9 - f_{10} + f_{15} + f_{16} - f_{17} - f_{18}, \\
\rho u_z &= f_5 - f_6 + f_{11} - f_{12} - f_{13} + f_{14} + f_{15} - f_{16} - f_{17} + f_{18}, \\
\Pi_{xx} &= f_1 + f_2 + f_7 + f_8 + f_9 + f_{10} + f_{11} + f_{12} + f_{13} + f_{14}, \\
\Pi_{yy} &= f_3 + f_4 + f_7 + f_8 + f_9 + f_{10} + f_{15} + f_{16} + f_{17} + f_{18}.
\end{aligned} \tag{4.6.5}$$

We can find the unknown distribution functions by solving system (4.6.5), after assuming the constraints corresponding to them.

Moments	Combination of unknown distribution functions at the South boundary
$\rho u_x, \Pi_{xz}, Q_{xzz}$	$f_{11} - f_{14}$
$\rho u_y, \Pi_{yz}, Q_{yzz}$	$f_{15} - f_{18}$
$\rho, \rho u_z, \Pi_{zz}$	$f_5 + f_{11} + f_{14} + f_{15} + f_{18}$
$\Pi_{xx}, R_{xxzz}, Q_{xxz}$	$f_{11} + f_{14}$
$\Pi_{yy}, R_{yyzz}, Q_{yyz}$	$f_{15} + f_{18}$

Table 4.3: Moments at the South boundary, in 3D.

Moments	Combination of unknown distribution functions at the North boundary
$\rho u_x, -\Pi_{xz}, Q_{xzz}$	$f_{12} - f_{13}$
$\rho u_y, -\Pi_{yz}, Q_{yzz}$	$f_{16} - f_{17}$
$-\rho, \rho u_z, -\Pi_{zz}$	$-f_6 - f_{12} - f_{13} - f_{16} - f_{17}$
$\Pi_{xx}, R_{xxzz}, -Q_{xxz}$	$f_{12} + f_{13}$
$\Pi_{yy}, R_{yyzz}, -Q_{yyz}$	$f_{16} + f_{17}$

Table 4.4: Moments at the North boundary, in 3D.

Moments	Combination of unknown distribution functions at the East boundary
$-\rho, \rho u_x, -\Pi_{xx}$	$-f_2 - f_8 - f_9 - f_{13} - f_{14}$
$\rho u_y, -\Pi_{xy}, Q_{xxy}$	$f_8 - f_9$
$\rho u_z, -\Pi_{xz}, Q_{xxz}$	$-f_{13} + f_{14}$
$\Pi_{yy}, -Q_{xyy}, R_{xxyy}$	$f_8 + f_9$
$\Pi_{zz}, -Q_{xzz}, R_{xxzz}$	$f_{13} + f_{14}$

Table 4.5: Moments at the East boundary, in 3D.

Moments	Combination of unknown distribution functions at the West boundary
$\rho, \rho u_x, \Pi_{xx}$	$f_1 + f_7 + f_{10} + f_{11} + f_{12}$
$\rho u_y, \Pi_{xy}, Q_{xxy}$	$f_7 - f_{10}$
$\rho u_z, \Pi_{xz}, Q_{xxz}$	$f_{11} - f_{12}$
$\Pi_{yy}, Q_{xyy}, R_{xxyy}$	$f_7 + f_{10}$
$\Pi_{zz}, Q_{xzz}, R_{xxzz}$	$f_{11} + f_{12}$

Table 4.6: Moments at the West boundary, in 3D.

Higher order moments such as $\mathbf{Q}$ and $\mathbf{R}$ are used for the edges and corners because we need nine moments at the edge and 12 moments at the corner in order to find the unknown distribution functions. The use of high order moments is reasonable for this because we neglected the third order term when we calculated $\mathbf{\Pi}^1$ Eq (3.2.27) from Eq (3.2.28)

The unknown incoming distribution functions for every moment on the South West edge are listed in Table (4.7). 9 independent moments need to be chosen in order to find 9 unknown distribution functions, which in this example consist of: three momentum, ρu_x, ρu_y and ρu_z; five momentum flux tensor, Π_{xx}, Π_{yy}, Π_{zz}, Π_{xz}

and Π_{xy}; and a third order momentum flux tensor, Q_{xyy}. The choice of moments is based on the symmetry and independence of moments and it is therefore possible to create or choose another group of independent and symmetric moments. By assuming the constraints on the moments and solving the system, which consists of nine moments and nine unknown distribution functions, we will find the unknown distribution functions.

Moments	Combination of unknown distribution functions at the South West edge
ρ	$f_1+f_5+f_7+f_{10}+f_{11}+f_{12}+f_{15}+f_{16}$
$\rho u_x, \Pi_{xx}$	$f_1+f_7+f_{10}+f_{11}+f_{12}$
ρu_y	$f_7-f_{10}+f_{15}-f_{18}$
ρu_z	$f_5+f_{11}-f_{12}+f_{15}+f_{18}$
Π_{yy}	$f_7+f_{10}+f_{15}+f_{18}$
Π_{zz}	$f_5+f_{11}+f_{12}+f_{15}+f_{18}$
Π_{xy}, Q_{xxy}	f_7-f_{10}
Π_{xz}, Q_{xxz}	$f_{11}-f_{12}$
Q_{xyy}	f_7+f_{10}
Π_{yz}, Q_{yzz}	$f_{15}-f_{18}$
Q_{xzz}	$f_{11}+f_{12}$
Q_{yyz}, R_{yyzz}	$f_{15}+f_{18}$
R_{xxyy}	$f_{10}+f_{11}$
R_{xxzz}	$f_{12}+f_{15}$

Table 4.7: Moments at the South West edge, in 3D.

Because there are twelve unknown distribution functions at the corner, we need twelve independent moments at this location. The unknown distribution functions for each moment are listed in Table (4.8) for the South West front corner. The unknown distribution functions are found by using the same procedure used to find them for the faces and edges. The 12 moments in this example are: three momentum, ρu_x, ρu_y and ρu_z, five momentum flux tensor, Π_{xx}, Π_{yy}, Π_{zz}, Π_{xz} and Π_{xy}, and three third order moments, Q_{xyy}, Q_{xxz} and Q_{yzz}. Again the selection is based upon the independence and symmetry of moments.

Moments	Combination of unknown distribution functions at South West front corner
ρ	$f_1+f_3+f_5+f_7+f_8+f_{10}+f_{11}+f_{12}+f_{14}+f_{15}+f_{16}+f_{18}$
ρu_x	$f_1+f_7-f_8-f_9+f_{10}+f_{11}+f_{12}-f_{14}$
ρu_y	$f_3+f_7+f_8-f_{10}+f_{15}+f_{16}-f_{18}$
ρu_z	$f_5+f_{11}-f_{12}+f_{14}+f_{15}-f_{16}+f_{18}$
Π_{xx}	$f_1+f_7+f_8+f_9+f_{10}+f_{11}+f_{12}+f_{14}$
Π_{yy}	$f_3+f_7+f_8+f_{10}+f_{15}+f_{16}+f_{18}$
Π_{zz}	$f_5+f_{11}+f_{12}+f_{14}+f_{15}+f_{16}+f_{18}$
Π_{xy}	$f_7-f_8-f_{10}$
Π_{xz}, Q_{xzz}	$f_{11}-f_{12}-f_{14}$
Π_{yz}	$f_{15}-f_{16}-f_{18}$
Q_{xxy}	$f_7+f_8-f_{10}$
Q_{xyy}	$f_7-f_8+f_{10}$
Q_{yzz}	$f_{15}+f_{16}-f_{18}$
Q_{xxz}	$f_{11}-f_{12}+f_{14}$
Q_{yyz}	$f_{15}-f_{16}+f_{18}$
R_{xxyy}	$f_8+f_{10}+f_{11}$
R_{xxzz}	$f_{12}+f_{14}+f_{15}$
R_{yyzz}	$f_{15}+f_{16}+f_{18}$

Table 4.8: Moments at the South West front corner, in 3D.

4.7 Poiseuille flow

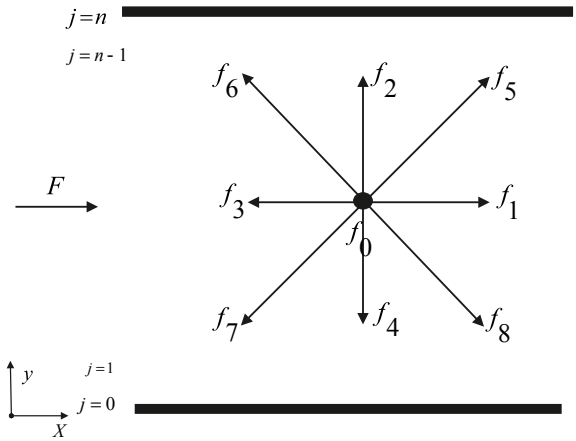

Figure 4.7: Interior flow or Poiseuille flow [29].

The analytical solution of Poiseuille flow for the Lattice Boltzmann model under a condition known as steady state, which means the flow is independent of time [29], is written as $\frac{\partial u}{\partial x} = 0$, $\frac{\partial v}{\partial x} = 0$ and $\rho = const$. The velocity is defined as $\mathbf{u} = (u_x, u_y)$ where u_x and u_y are the velocity in x- and y-direction, respectively. The vertical velocity, u_y, is zero. Thus, the analytical solution is:

$$u_j = \frac{4}{n^2} U_c j\,(n-j) + u_s. \tag{4.7.1}$$

where u_j is the velocity in x-direction and $j = 1,...,n-1$, $j = 0$ and $j = n$ represent the lower and upper boundaries, $U_c = \frac{n^2 \delta_x^2}{8\nu} G_x$ is the centreline velocity and $\mathbf{F} = \rho G_x$ is the body force in x-direction. u_s is the slip velocity, which depends on the boundary conditions at the wall. The slip velocity for the standard bounce back scheme is

$$u_s = \frac{2}{3n^2} U_c \left[(2\tau - 1)(4\tau - 3) - 3n\right], \quad \left(U_c = \frac{n^2 \delta_x^2}{8\nu} G_x\right) \tag{4.7.2}$$

and it has an error of first order $O\left(\frac{1}{n}\right)$.

The velocity profile with slip velocity for Poiseuille flow with modified bounce back scheme is

$$\begin{aligned} u_j &= \frac{4}{n^2} U_c j\,(n-j) + \frac{16\tau\,(2\tau - 1)}{3n^2} U_c \\ u_s &= \frac{16\tau\,(2\tau - 1)}{3n^2} U_c \quad \left(U_c = \frac{n^2 \delta_x^2}{8\nu} G_x\right), \quad \tau \neq 1, \end{aligned} \tag{4.7.3}$$

and is of second order $O\left(\frac{1}{n^2}\right)$, while the velocity profile with slip velocity for Poiseuille flow with halfway wall is

$$\begin{aligned} u_j &= \frac{4}{(n-1)^2} U_c j\,(n-j) + u_s \\ u_s &= \frac{2}{3\,(n-1)^2} U_c \left[(2\tau - 1)(4\tau - 3) - 3n\right], \quad \left(U_c = \frac{(n-1)^2\, \delta_x^2}{8\nu} G_x\right). \end{aligned} \tag{4.7.4}$$

The exact solution for Poiseuille flow is

$$u_j^{'} = \frac{U_c\,(2j-1)\,(2n-2j-1)}{(n-1)^2}, \quad \left(U_c = \frac{(n-1)^2\,\delta_x^2}{8\nu} G_x\right), \tag{4.7.5}$$

and the velocity error from LBM is

$$u_j - u_j^{'} = \frac{U_c\,[4\tau\,(4\tau-5)+3]}{3\,(n-1)^2}. \tag{4.7.6}$$

4.7.1 D_2Q_9 Simulations

4.7.1.1 Poiseuille flow with bounce back boundary conditions

The purpose of this simulation is to verify the analysis for Poiseuille flow with various types of boundary conditions set at the wall and periodic boundary condition at the inlet and outlet. The flow in this simulation is in the x-direction. Figure (4.8) illustrates the velocity profiles for Poiseuille flow u_j which is scaled with $U_c = 0.1$ and various schemes. The size of the system is $n_x \times n_y = 16 \times 6$. The initial condition for the density $\rho = 1$. The result of the slip velocity in every scheme that has been used in this simulation is that of a perfect parabola as demonstrated in Figure (4.8), which shows that the velocity profiles of LBM are in excellent agreement with the analytical solution of Poiseuille flow at each type of bounce back boundary condition, as seen in Eqs (4.7.2), (4.7.3) and (4.7.4). The error between the numerical results and the analytical ones is of order 10^{-16}.

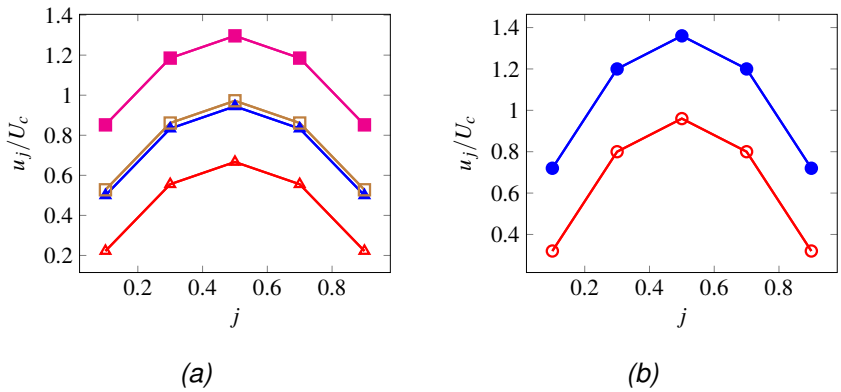

Figure 4.8: Numerical velocities of LBM with slip velocity for (□,■) standard bounce back, (△,▲) modified bounce back scheme and (○,●) halfway scheme with their the normalized velocity profile of Poiseuille flow (−) at relaxation times of 0.75 and 2, respectively.

Different orders of error occur in different schemes. For instance, at $\tau = 0.75$ the error of standard bounce back scheme is 0.333 in this size system, whereas the error of modified bounce back is 2.777 $\times 10^{-2}$, and the exact solution for Poiseuille flow is 44.00 $\times 10^{-2}$. By doubling the grid point n_y in every scheme, the error can be reduced in order to show errors of first order for standard, and second order for both modified bounce back and the exact solution of halfway scheme for Poiseuille flow, all of which can be seen in Figure (4.9).

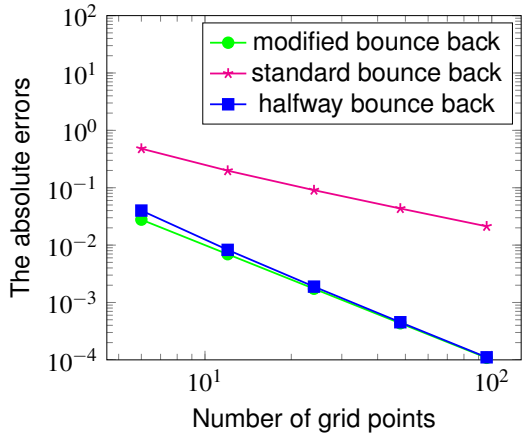

Figure 4.9: The absolute errors.

4.7.1.1.1 Conclusion

Overall, the LBM results using various boundary schemes correspond exactly with the analytical solution of Poiseuille flow at each different scheme of bounce back boundary conditions.

4.7.1.2 Poiseuille flow with moment-based boundary condition and no-slip boundary condition, in 2D

When assessing this flow, the D_2Q_9 model is used and the simulation conducted with the second order approximation of the LBE, Eq (2.1.42), with its macroscopic quantities, Eqs (2.1.43) and (2.1.44). Additionally, the force term (2.1.35) is selected as x-direction and periodic boundary condition is used at the inlet (West) and outlet (East) side (open boundary condition). No-slip boundary condition is applied at the wall in order to identify the constraints of three independent moments, because no-slip boundary condition leads to the tangential and vertical velocity at the wall being zero $u_x = u_y = 0$, which means the tangential

momentum will be zero $(\rho u_x = 0)$, normal momentum will be zero $(\rho u_y = 0)$, and tangential momentum flux tensor will be $\Pi_{xx} = \frac{\rho}{3}$, because $\Pi_{xx} = \Pi^0_{xx} + \tau\Pi^1_{xx} = p + \rho u_x u_x + \tau\partial_x u_x = \frac{\rho}{3}$, where $p = \frac{\rho}{3}$. From the Chapman-Enskog approach section (3.2), we have seen that

$$\tau\Pi^1_{xx} = -\frac{\rho}{3}\tau(\partial_x u_x) - \frac{\rho}{3}\tau(\partial_x u_x) = -\frac{2}{3}\tau\rho(\partial_x u_x) = -2\mu(\partial_x u_x) \simeq (\partial_x u_x). \tag{4.7.7}$$

By following the same process we find that $\Pi_{yy} = \dfrac{\rho}{3}$. We convert these moments to the moments of the second order of LBM

$$\rho\overline{u}_x = \rho u_x - \frac{\delta_t}{2}F_x \Rightarrow \rho\overline{u}_x = -\frac{\delta_t}{2}\rho G_x, \tag{4.7.8}$$

$$\rho\overline{u}_y = \rho u_y - \frac{\delta_t}{2}F_y = 0, \tag{4.7.9}$$

$$\overline{\Pi}_{xx} = \Pi_{xx} + \frac{\delta_t}{2\tau}\Pi_{xx} - \frac{\delta_t}{2\tau}\Pi^0_{xx} - \frac{\delta_t}{2}(F_x u_x + u_x F_x) = \frac{\rho}{3},$$

$$\overline{\Pi}_{xx} = \Pi_{xx} + \frac{\delta_t}{2\tau}\Pi_{xx} - \frac{\delta_t}{2\tau}\Pi^0_{xx} - \frac{\delta_t}{2}\rho(G_x u_x + u_x G_x) = \frac{\rho}{3}, \tag{4.7.10}$$

where the body force is $\mathbf{F} = (F_x, F_y) = \rho(G_x, 0)$. These three moments are written as a combination of distribution functions, as seen in Eq (4.7.11), Eq (4.7.12) and Eq.(4.7.13). Then the constraints corresponding to them are assumed and the three equations are solved to find these unknown distribution functions

$$-\frac{\delta_t}{2}\rho G_x = \overline{f}_1 - \overline{f}_3 + \overline{f}_5 - \overline{f}_6 - \overline{f}_7 + \overline{f}_8, \tag{4.7.11}$$

$$0 = \overline{f}_2 - \overline{f}_4 + \overline{f}_5 + \overline{f}_6 - \overline{f}_7 - \overline{f}_8, \tag{4.7.12}$$

$$\frac{\rho}{3} = \overline{f}_1 + \overline{f}_3 + \overline{f}_5 + \overline{f}_6 + \overline{f}_7 + \overline{f}_8. \tag{4.7.13}$$

At the North wall the unknown distribution functions $\overline{f}_4$, $\overline{f}_7$ and $\overline{f}_8$ are

$$\overline{f}_4 = \overline{f}_1 + \overline{f}_2 + \overline{f}_3 + 2(\overline{f}_5 + \overline{f}_6) - \frac{\rho}{3},$$

$$\overline{f}_7 = -\overline{f}_3 - \overline{f}_6 + \frac{\rho}{6} + \frac{\delta_t}{4}\rho G_x,$$

$$\overline{f}_8 = -\overline{f}_1 - \overline{f}_5 + \frac{\rho}{6} - \frac{\delta_t}{4}\rho G_x, \tag{4.7.14}$$

while at the South wall $\overline{f}_2$, $\overline{f}_5$ and $\overline{f}_6$ are

$$\begin{aligned}
\overline{f}_2 &= \overline{f}_1 + \overline{f}_3 + \overline{f}_4 + 2\left(\overline{f}_7 + \overline{f}_8\right) - \frac{\rho}{3}, \\
\overline{f}_5 &= -\overline{f}_1 - \overline{f}_8 + \frac{\rho}{6} - \frac{\delta_t}{4}\rho G_x, \\
\overline{f}_6 &= -\overline{f}_3 - \overline{f}_7 + \frac{\rho}{6} + \frac{\delta_t}{4}\rho G_x.
\end{aligned} \tag{4.7.15}$$

The density is calculated using the following definition

$$\rho = \overline{f}_0 + \overline{f}_1 + \overline{f}_2 + \overline{f}_3 + \overline{f}_4 + \overline{f}_5 + \overline{f}_6 + \overline{f}_7 + \overline{f}_8,$$

along with Eq (4.7.12), so at the South wall it is

$$\rho = \overline{f}_0 + \overline{f}_1 + \overline{f}_3 + 2\left(\overline{f}_4 + \overline{f}_7 + \overline{f}_8\right) \tag{4.7.16}$$

and at the North wall it is

$$\rho = \overline{f}_0 + \overline{f}_1 + \overline{f}_3 + 2\left(\overline{f}_2 + \overline{f}_5 + \overline{f}_6\right). \tag{4.7.17}$$

The chosen grid point size is $n_x \times n_y = 16 \times 6$, in which the simulation results in a perfect parabola with an error of 10^{-17}. This means the velocity of LBM is in excellent agreement with the analytical solution of Poiseuille flow without slip velocity u_s.

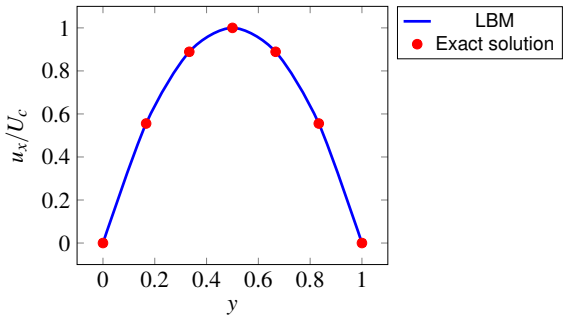

Figure 4.10: The velocity profile of LBM with no-slip boundary conditions, in 2D.

4.7.1.3 Poiseuille Flow with Moment-Based Boundary Condition and Non-slip Boundary Condition in 3D

In this flow simulation, the D_3Q_{19} model is used, with the second order of the LBM, Eq (2.1.42), with its macroscopic quantities, Eq (2.1.43) and Eq (2.1.44). The force term seen in Eq (2.1.35) is in x-direction, and periodic boundary condition is used at the inlet (West) and outlet (East) side (open boundary condition). Also, no-slip boundary condition is applied at the South and North walls to identify the constraints of five independent moments. In the no-slip boundary condition the velocity is zero at every wall. Thus, we assume

$$u_x = u_y = u_z = 0, \tag{4.7.18}$$

so the three moments will be

$$\begin{aligned} \rho u_x = \rho u_y = \rho u_z = 0, \\ \Pi^0_{xx} = \frac{\rho}{3}\delta_{xx} + \rho u_x u_x = \frac{\rho}{3}, \\ \Pi^0_{yy} = \frac{\rho}{3}\delta_{yy} + \rho u_y u_y = \frac{\rho}{3}. \end{aligned} \tag{4.7.19}$$

The form for the body force in three dimensions is written as $\mathbf{F} = (\rho G_x, \rho G_y, \rho G_z) = (\rho G_x, 0, 0)$, the tangential momentum flux tensor is

$$\Pi_{xx} = \Pi^0_{xx} + \tau\Pi^1_{xx} = \frac{\rho}{3} - \tau\frac{2\rho}{3}\partial_x u_x = \frac{\rho}{3}$$

and the vertical momentum flux tensor is

$$\Pi_{yy} = \Pi^0_{yy} + \tau\Pi^1_{yy} = \frac{\rho}{3} - \tau\frac{2\rho}{3}\partial_y u_y = \frac{\rho}{3},$$

so

$$\begin{aligned}
\rho\overline{u}_x &= \rho u_x - \frac{\delta_t}{2}\rho G_x = -\frac{\delta_t}{2}\rho G_x,\\
\rho\overline{u}_y &= \rho u_y - \frac{\delta_t}{2}\rho G_y = 0,\\
\rho\overline{u}_z &= \rho u_z - \frac{\delta_t}{2}\rho G_z = 0,\\
\overline{\Pi}_{xx} &= \Pi_{xx} + \frac{\delta_t}{2\tau}\Pi_{xx} - \frac{\delta_t}{2\tau}\Pi^0_{xx} - \frac{\delta_t}{2}\left(\rho G_x u_x + u_x \rho G_x\right) = \frac{\rho}{3},\\
\overline{\Pi}_{yy} &= \Pi_{yy} + \frac{\delta_t}{2\tau}\Pi_{yy} - \frac{\delta_t}{2\tau}\Pi^0_{yy} - \frac{\delta_t}{2}\left(\rho G_y u_y + u_y \rho G_y\right) = \frac{\rho}{3},
\end{aligned} \tag{4.7.20}$$

and

$$\begin{aligned}
\rho\overline{u}_x &= \overline{f}_1 - \overline{f}_2 + \overline{f}_7 - \overline{f}_8 - \overline{f}_9 + \overline{f}_{10} + \overline{f}_{11} + \overline{f}_{12} - \overline{f}_{13} - \overline{f}_{14} = -\frac{\delta_t}{2}\rho G_x,\\
\rho\overline{u}_y &= \overline{f}_3 - \overline{f}_4 + \overline{f}_7 + \overline{f}_8 - \overline{f}_9 - \overline{f}_{10} + \overline{f}_{15} + \overline{f}_{16} - \overline{f}_{17} - \overline{f}_{18} = 0,\\
\rho\overline{u}_z &= \overline{f}_5 - \overline{f}_6 + \overline{f}_{11} - \overline{f}_{12} - \overline{f}_{13} + \overline{f}_{14} + \overline{f}_{15} - \overline{f}_{16} - \overline{f}_{17} + \overline{f}_{18} = 0,\\
\overline{\Pi}_{xx} &= \overline{f}_1 + \overline{f}_2 + \overline{f}_7 + \overline{f}_8 + \overline{f}_9 + \overline{f}_{10} + \overline{f}_{11} + \overline{f}_{12} + \overline{f}_{13} + \overline{f}_{14} = \frac{\rho}{3},\\
\overline{\Pi}_{yy} &= \overline{f}_3 + \overline{f}_4 + \overline{f}_7 + \overline{f}_8 + \overline{f}_9 + \overline{f}_{10} + \overline{f}_{15} + \overline{f}_{16} + \overline{f}_{17} + \overline{f}_{18} = \frac{\rho}{3}.
\end{aligned} \tag{4.7.21}$$

By solving system (4.7.21) we can find the unknown distribution functions at the South and North walls, as follows. The unknown distribution functions at the South wall are

$$\overline{f}_5, \overline{f}_{11}, \overline{f}_{14}, \overline{f}_{15}, \overline{f}_{18}, \tag{4.7.22}$$

so,

$$\begin{aligned}
\overline{f}_5 &= \overline{f}_1+\overline{f}_2+\overline{f}_3+\overline{f}_4+\overline{f}_6+2\overline{f}_7+2\overline{f}_8+2\overline{f}_9+2\overline{f}_{10}+2\overline{f}_{12}+2\overline{f}_{13}+\\
&\quad 2\overline{f}_{16}+2\overline{f}_{17}-\frac{2}{3}\rho,\\
\overline{f}_{11} &= -\overline{f}_1-\overline{f}_7-\overline{f}_{10}-\overline{f}_{12}+\frac{\rho}{6}-\frac{\delta_t}{4}\rho G_x,\\
\overline{f}_{14} &= -\overline{f}_2-\overline{f}_8-\overline{f}_9-\overline{f}_{13}+\frac{\rho}{6}+\frac{\delta_t}{4}\rho G_x,\\
\overline{f}_{15} &= -\overline{f}_3-\overline{f}_7-\overline{f}_8-\overline{f}_{16}+\frac{\rho}{6},\\
\overline{f}_{18} &= -\overline{f}_4-\overline{f}_9-\overline{f}_{10}-\overline{f}_{17}+\frac{\rho}{6}.
\end{aligned} \tag{4.7.23}$$

The unknown distribution functions at the North wall are

$$\overline{f}_6,\overline{f}_{12},\overline{f}_{13},\overline{f}_{16},\overline{f}_{17}, \tag{4.7.24}$$

so

$$\begin{aligned}
\overline{f}_6 &= \overline{f}_1+\overline{f}_2+\overline{f}_3+\overline{f}_4+\overline{f}_5+2\overline{f}_7+2\overline{f}_8+2\overline{f}_9+2\overline{f}_{10}+2\overline{f}_{11}+2\overline{f}_{14}+\\
&\quad 2\overline{f}_{15}+2\overline{f}_{18}-\frac{2}{3}\rho,\\
\overline{f}_{12} &= -\overline{f}_1-\overline{f}_7-\overline{f}_{10}-\overline{f}_{11}+\frac{\rho}{6}-\frac{\delta_t}{4}\rho G_x,\\
\overline{f}_{13} &= -\overline{f}_2-\overline{f}_8-\overline{f}_9-\overline{f}_{14}+\frac{\rho}{6}+\frac{\delta_t}{4}\rho G_x,\\
\overline{f}_{16} &= -\overline{f}_3-\overline{f}_7-\overline{f}_8-\overline{f}_{15}+\frac{\rho}{6},\\
\overline{f}_{17} &= -\overline{f}_4-\overline{f}_9-\overline{f}_{10}-\overline{f}_{18}+\frac{\rho}{6}.
\end{aligned} \tag{4.7.25}$$

The definition of the density is

$$\begin{aligned}
\rho = \overline{f}_0+\overline{f}_1+\overline{f}_2+\overline{f}_3+\overline{f}_4+\overline{f}_5+\overline{f}_6+\overline{f}_7+\overline{f}_8+\overline{f}_9+\overline{f}_{10}+\overline{f}_{11}\\
+\overline{f}_{12}+\overline{f}_{13}+\overline{f}_{14}+\overline{f}_{15}+\overline{f}_{16}+\overline{f}_{17}+\overline{f}_{18}.
\end{aligned} \tag{4.7.26}$$

From this density equation (4.7.26) and that for momentum $\rho\overline{u}_z$ (4.7.21) we can find the density at the South and North walls. At the South wall it is

$$\rho = \overline{f}_0 + \overline{f}_1 + \overline{f}_2 + \overline{f}_3 + \overline{f}_4 + 2\overline{f}_6 + \overline{f}_7 + \overline{f}_8 + \overline{f}_9 + \overline{f}_{10} + 2\overline{f}_{12} + 2\overline{f}_{13} + 2\overline{f}_{16} + 2\overline{f}_{17}, \tag{4.7.27}$$

and at the North

$$\rho = \overline{f}_0 + \overline{f}_1 + \overline{f}_2 + \overline{f}_3 + \overline{f}_4 + 2\overline{f}_5 + \overline{f}_7 + \overline{f}_8 + \overline{f}_9 + \overline{f}_{10} + 2\overline{f}_{11} + 2\overline{f}_{14} + 2\overline{f}_{15} + 2\overline{f}_{18}. \tag{4.7.28}$$

The selected size of grid points is $n_x \times n_y \times n_z = 6 \times 6 \times 16$, where n_x, n_y and n_z are the grid point or size in x-, y- and z-directions, respectively. At this size the simulation results in a perfect parabola with an error of 10^{-17}. This means the velocity profile of LBM is in excellent agreement with the exact solution of Poiseuille flow without slip velocity u_s, as seen in Eq (4.7.1). The velocity profile is located along the height of the channel H and in the middle of the channel at $n_x/2, n_y/2$

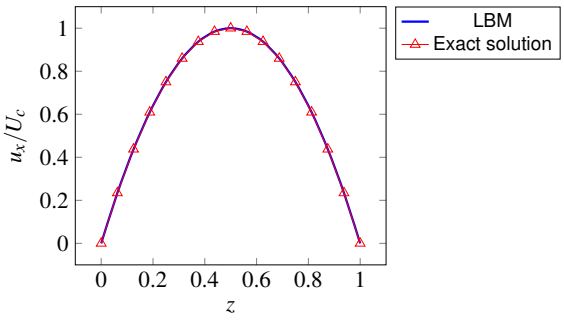

Figure 4.11: The velocity profile of LBM with no-slip boundary conditions, in 3D.

4.7.1.3.1 Conclusion

The velocity of LBM is in excellent agreement with the exact solution in two and three dimensions and in both cases the error is 10^{-17} *i.e.* to machine accuracy.

Chapter 5

2D pulsatile flow with no-slip and Navier-slip boundary conditions

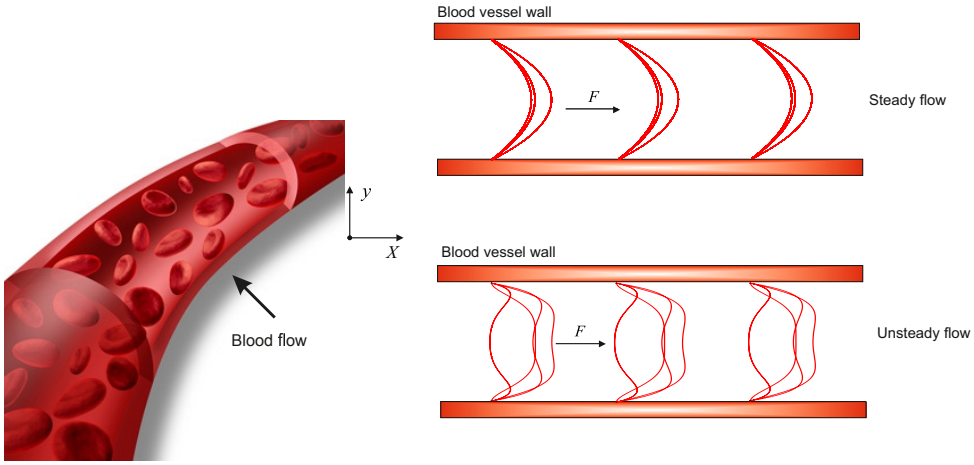

Figure 5.1: Blood flow or pulsatile flow [73] .

5.1 Introduction

The LBM has been developed and is used to simulate fluid flow and it has been applied to various types of steady and unsteady fluid flow problems such as turbulent flows, multiphase flow and blood flow [14]. As an example, the study of blood flow and its properties can give a greater understanding of atherosclerosis and the flow parameters which influence this phenomenon. The blood flow in the vascular system is driven by the pulsating pressure gradient which is produced by the heart. As a simple model of this, we simulate plane channel flow under periodic forcing, thereby avoiding the complexity of the cylindrical coordinates appropriate for blood flow in 2D. This pulsatile flow is essentially the standard Poiseuille flow except that the flow is driven by the periodic forcing term.

It is necessary to conduct experiments and numerical studies to investigate blood flow, and various previous studies can be found on this.
Some of the numerical studies or computational methods of both unsteady and steady flow include analytical solutions. For example, in 2D, He and Lou [25] produced second order accuracy for the error between the numerical and analytical solutions. Cosgrove *et. al*. [14] generated second order accuracy with halfway boundary conditions as well as for the forcing term. Latt [36] found that the error increases with high grid size in some cases. All these authors are examples of very good results which compare well with the analytical solutions.

Artoli [5] presented Womersley flow in two and three dimensions with standard bounce back boundary conditions at the wall. When he fixed the Reynolds number, he was able to produce first order accuracy using modified bounce back boundary conditions and a second order forcing term in 2D. In addition, he obtained first order accuracy when he fixed the Reynolds number corresponding to the range of grid sizes and periods, respectively, to keep the Womersley number a constant in 3D. This method, using a curved boundary condition, results in a range of relaxation time. Later, Artoli *et. al*. [4] studied steady flow in a two dimensional symmetric bifurcation.

In this chapter, moment-based boundary conditions are used with the Lattice Boltzmann method (LBM) to simulate numerically 2D flow driven between two parallel plates by a pulsating pressure gradient. This flow simulation is achieved using a model of single relaxation time under both Navier-slip and no-slip conditions, with two different approaches to the investigation of convergence. The first, which is used for no-slip conditions, employs acoustic scaling in which the Reynolds, Mach and Womersley numbers are fixed whilst the LBM relaxation time is varied. The second approach uses diffusive scaling, for Navier-slip conditions, where the Womersley and Reynolds numbers and relaxation time are fixed, and the Mach number decreases as the grid size increases.

5.2 Moment-based boundary condition

At the planar boundaries aligned with grid points of the D_2Q_9, LBM post-streaming has 3 unknown incoming distributions that can be found using 3 linearly independent moment conditions. Physical constraints are imposed on 3 linearly independent hydrodynamic moments in the moment-based boundary scheme, from which the 3 unknown distribution functions at a boundary are obtained.

In order for this condition to be applied, it is assumed that there is a solid wall at both North and South flow boundaries. When the streaming step is complete, it is apparent that the unknown distribution functions at the North boundary are $\overline{f}_4$, $\overline{f}_7$ and $\overline{f}_8$, and at the South $\overline{f}_2$, $\overline{f}_5$ and $\overline{f}_6$.

Three linearly independent moments chosen from Table (5.1) are used to implement Navier-slip boundary conditions. In this case, these are: vertical velocity momentum ρu_y; tangential momentum ρu_x; and tangential momentum flux tensor Π_{xx} at the wall. These are imposed as $\rho u_x = u_s$, $\rho u_y = 0$, $\Pi_{xx} = \frac{\rho}{3} + \rho u_s^2$, where u_s is the slip velocity (NB: $p = \frac{\rho}{3}$ is the pressure). We define the tangential momentum flux tensor as $\Pi_{xx} = \Pi^0_{xx} + \tau\Pi^1_{xx}$. Also, $\Pi^1_{xx} \simeq \partial_x u_x$, which is zero under either no-slip or slip conditions. Then, at either the North boundary or the South, $\rho\overline{u}_y = 0$, $\rho\overline{u}_x = \rho u_s - \frac{\delta_t}{2}\rho G_x$ and $\overline{\Pi}_{xx} = \frac{\rho}{3} + \rho u_s^2 - \rho G_x u_s$, where $\mathbf{F} = \rho\,(G_x, 0)$ is the body force.

Moments	Combination at the North boundary	Combination at the South boundary
$\rho, \rho u_y, \Pi_{yy}$	$f_4 + f_7 + f_8$	$f_2 + f_5 + f_6$
$\rho u_x, \Pi_{xy}, Q_{xyy}$	$f_8 - f_7$	$f_5 - f_6$
$\Pi_{xx}, Q_{xxy}, R_{xxyy}$	$f_8 + f_7$	$f_5 + f_6$

Table 5.1: Moments at the North and South boundaries.

Now, the system can be solved as shown in equation (5.2.1) to find the three

unknown distribution functions.

$$\begin{aligned}
\rho\overline{u}_x &= \overline{f}_1+\overline{f}_5+\overline{f}_8-\left(\overline{f}_3+\overline{f}_6+\overline{f}_7\right)=\rho u_s-\frac{\delta_t}{2}\rho G_x,\\
\rho\overline{u}_y &= \overline{f}_2+\overline{f}_5+\overline{f}_6-\left(\overline{f}_4+\overline{f}_7+\overline{f}_8\right)=0,\\
\overline{\Pi}_{xx} &= \overline{f}_1+\overline{f}_5+\overline{f}_8+\left(\overline{f}_3+\overline{f}_6+\overline{f}_7\right)=\frac{\rho}{3}+\rho u_s^2-\rho G_x u_s.
\end{aligned} \tag{5.2.1}$$

At the South wall, for example, the unknown distribution functions are $\overline{f}_2$, $\overline{f}_5$ and $\overline{f}_6$

$$\begin{aligned}
\overline{f}_2 &= \overline{f}_1+\overline{f}_3+\overline{f}_4+2\left(\overline{f}_7+\overline{f}_8\right)-\frac{\rho}{3}-\rho u_s^2-\rho G_x u_s,\\
\overline{f}_5 &= -\overline{f}_1-\overline{f}_8+\frac{\rho}{6}-\frac{\delta_t}{4}\rho G_x+\frac{1}{2}\rho u_s+\frac{1}{2}\rho u_s^2-\frac{\delta_t}{2}\rho G_x u_s,\\
\overline{f}_6 &= -\overline{f}_3-\overline{f}_7+\frac{\rho}{6}+\frac{\delta_t}{4}\rho G_x-\frac{1}{2}\rho u_s+\frac{1}{2}\rho u_s^2-\frac{\delta_t}{2}\rho G_x u_s,
\end{aligned} \tag{5.2.2}$$

the density is calculated by using the definition of density which is

$$\rho=\overline{f}_0+\overline{f}_1+\overline{f}_2+\overline{f}_3+\overline{f}_4+\overline{f}_5+\overline{f}_6+\overline{f}_7+\overline{f}_8$$

and $\rho\overline{u}_y$, so the density is

$$\rho=\overline{f}_0+\overline{f}_1+\overline{f}_3+2\left(\overline{f}_4+\overline{f}_7+\overline{f}_8\right), \tag{5.2.3}$$

and at the North $\overline{f}_4$, $\overline{f}_7$ and $\overline{f}_8$

$$\begin{aligned}
\overline{f}_4 &= \overline{f}_1+\overline{f}_2+\overline{f}_3+2\left(\overline{f}_5+\overline{f}_6\right)-\frac{\rho}{3}-\rho u_s^2+\rho G_x u_s,\\
\overline{f}_7 &= -\overline{f}_3-\overline{f}_6+\frac{\rho}{6}+\frac{\delta_t}{4}\rho G_x-\frac{1}{2}\rho u_s+\frac{1}{2}\rho u_s^2-\frac{\delta_t}{2}\rho G_x u_s,\\
\overline{f}_8 &= -\overline{f}_1-\overline{f}_5+\frac{\rho}{6}-\frac{\delta_t}{4}\rho G_x+\frac{1}{2}\rho u_s+\frac{1}{2}\rho u_s^2-\frac{\delta_t}{2}\rho G_x u_s,
\end{aligned} \tag{5.2.4}$$

where $\rho=\overline{f}_0+\overline{f}_1+\overline{f}_3+2\left(\overline{f}_2+\overline{f}_5+\overline{f}_6\right)$ is obtained using the definition of density

along with $\rho\overline{u}_y$. Now, the slip velocity at the wall can be found. We know that

$$\begin{aligned}\overline{\Pi}_{xy} &= \Pi_{xy} + \frac{\delta_t}{2\tau}\Pi_{xy} - \frac{\delta_t}{2\tau}\Pi^0_{xy} - \frac{\delta_t}{2}\rho\left(G_x u_y + u_s G_y\right), \quad u_x = u_s,\\ &= \Pi_{xy} + \frac{\delta_t}{2\tau}\Pi_{xy},\\ \overline{\Pi}_{xy} &= \frac{2\tau+1}{2\tau}\Pi_{xy},\end{aligned} \tag{5.2.5}$$

where $u_y = 0$ and $G_y = 0$, so,

$$\begin{aligned}\Pi_{xy} &= \frac{2\tau}{2\tau+1}\left(\overline{\Pi}_{xy}\right),\\ \Pi_{xy} &= \frac{2\tau}{2\tau+1}\left(\overline{f}_5 - \overline{f}_6 + \overline{f}_7 - \overline{f}_8\right).\end{aligned} \tag{5.2.6}$$

The slip velocity is proportional to the shear stress at the wall as explained in section (4.5), so $u_s = l_s\partial_n u_{wall}$, where $n \gtrless 0$ and l_s is the slip length. From the Chapman-Enskog expansion seen in section (3.2), the shear stress at the wall is defined as

$$\Pi_{xy} = \Pi^0_{xy} + \tau\Pi^1_{xy} = \frac{\rho}{3}\delta_{xy} + \rho u_x u_y + \tau\frac{-\rho}{3}\left(\partial_x u_y + \partial_y u_x\right) = \tau\frac{-\rho}{3}\partial_x u_y = -\mu\partial_x u_y.$$

Therefore, the shear stress is defined as $\Pi_{xy} = -\mu\partial_y u_{wall}$, where $n = y = n \gtrless 0$ and $\mu = \nu\rho = \frac{\tau}{3}\rho$. Also,

$$u_s = -\frac{l_s}{\mu}\Pi_{xy}, \tag{5.2.7}$$

$$\rho u_s = -\rho\frac{-l_s}{\mu}\frac{2\tau}{2\tau+1}\overline{\Pi}_{xy}, \tag{5.2.8}$$

where $\rho\dfrac{-l_s}{\mu}\dfrac{2\tau}{2\tau+1} = \rho\dfrac{-l_s}{\frac{\tau}{3}}\dfrac{2\tau}{\rho\left(2\tau+1\right)} = \dfrac{-6l_s}{\left(2\tau+1\right)}$, so,

$$u_s = \frac{-6l_s}{\rho\left(2\tau+1\right)}\left(\overline{f}_5 - \overline{f}_6 + \overline{f}_7 - \overline{f}_8\right). \tag{5.2.9}$$

At the South wall the shear stress is positive toward the wall, hence $\Pi_{xy} = -\mu\partial_n u_{wall}$, where $n = y > 0$ and the unknown distribution functions are $\overline{f}_2$, $\overline{f}_5$ and $\overline{f}_6$. These

are substituted into Eq (5.2.9), to find that the slip velocity is

$$u_s = \frac{-6l_s}{\rho\,(2\tau+1)}\left(-\overline{f}_1+\overline{f}_3+2\overline{f}_7-2\overline{f}_8+\rho u_s-\frac{1}{2}\rho G_x\right),$$
$$u_s = \frac{-6l_s}{\rho\,(1+2\tau+6l_s)}\left(-\overline{f}_1+\overline{f}_3+2\overline{f}_7-2\overline{f}_8-\frac{1}{2}\rho G_x\right). \tag{5.2.10}$$

At the North wall the shear stress has a negative sign because the shear stress is negative toward the wall, hence

$$(\Pi_{xy}) = -\left(-\mu\partial_y u_{wall}\right), \tag{5.2.11}$$

and

$$u_s = \frac{6l_s}{\rho\,(2\tau+1)}\left(\overline{f}_5-\overline{f}_6+\overline{f}_7-\overline{f}_8\right). \tag{5.2.12}$$

At the North wall the unknown distribution functions are $\overline{f}_4$, $\overline{f}_7$ and $\overline{f}_8$, which we substitute into Eq (5.2.9)

$$u_s = \frac{6l_s}{\rho\,(2\tau+1)}\left(\overline{f}_1-\overline{f}_3+2\overline{f}_5-2\overline{f}_6+\frac{1}{2}\rho G_x-\rho u_s\right),$$
$$u_s = \frac{6l_s}{\rho\,(1+2\tau+6l_s)}\left(\overline{f}_1-\overline{f}_3+2\overline{f}_5-2\overline{f}_6+\frac{1}{2}\rho G_x\right). \tag{5.2.13}$$

Using $u_x = u_s = 0$ the unknown distribution functions with no-slip boundary condition can be found.

5.3 The exact solutions for pulsatile flow

Two-dimensional pulsatile flow, also known as Womersley flow, is driven by a pulsating pressure gradient implemented with an equivalent body force $G_x = \left(2U_c\nu/h^2\right)\cos(wt)$ in the x-direction, where U_c is the centreline speed for the zero frequency case (*i.e.* Poiseuille flow), h is the channel half-width, $\nu = \frac{U_c h}{Re_{cl}}$ is Kinematic viscosity and Re_{cl} is the centreline Reynolds number. Under no-slip boundary conditions, the exact solution at $u_x = 0$ at $y = \pm h$ is

$$\frac{u_x}{U_c} = \Re\left[\frac{-j}{W_0}\left(1-\frac{\cosh\left((1+j)W_0\frac{y}{h}\right)}{\cosh\left((1+j)W_0\right)}\right)e^{\frac{j2\pi t}{P}}\right], \tag{5.3.1}$$

where $W_0 = \sqrt{\frac{w}{2\nu}}h$ is the dimensionless Womersley number in which $w = \frac{2\pi}{P}$ is the pulsation angular frequency, $j = \sqrt{-1}$, t is the time and P is the period.

Under Navier-slip conditions, the exact solution $u_x = u_s = l_s|\frac{du_x}{dy}|$ at $y = \pm h$ is

$$\frac{u_x}{U_c} = \Re\left[\left(\frac{u_s}{U_c}\frac{\cosh\left((1+j)W_0\frac{y}{h}\right)}{\cosh\left((1+j)W_0\right)} + \frac{j}{W_0}\left(1 - \frac{\cosh\left((1+j)W_0\frac{y}{h}\right)}{\cosh\left((1+j)W_0\right)}\right)\right) e^{\frac{j2\pi t}{P}}\right], \quad (5.3.2)$$

$$\frac{u_s}{U_c} = \frac{(j-1)K_n \sinh\left((1+j)W_0\right)}{W_0\left[\cosh\left((1+j)W_0\right) - K_n W_0 (1+j)\sinh\left((1+j)W_0\right)\right]}, \quad (5.3.3)$$

where $K_n = \frac{l_s}{h}$ is the dimensionless slip length. It is evident that both of these exact solutions are independent of the Reynolds number.

5.4 Simulations

The LBM and boundary conditions discussed previously are used in this pulsatile flow simulation, with a horizontally periodic domain. Computational grids of dimensions $n_x \times n_y$ are used, where $n_x = 2$ and $n_y = 16, 32, 64, 128, 256, 512$. The channel half width in the lattice units is $h = \frac{n_y}{2}$. Over a single period, the norm error $\| \overline{L}(p) \|_2$ is

$$\| \overline{L}(p) \|_2 = \sqrt{\frac{1}{n_\theta}\frac{1}{n_x n_y}\sum_{l,r} |\mathbf{u}_{LBM}(l,r,\theta,p) - \mathbf{u}_{Exact}(l,r,\theta,p)|^2}, \quad (5.4.1)$$

where $l = 0, ..., n_x, r = 0, ..., n_y$ and n_θ is the number of angles in a period, which in this case assumes $n_\theta = 8$. We then run the total computation until $t = kP$, where k is the number of periods that are necessary for the computations to achieve a fully-periodic state.

5.4.1 Simulation under no-slip boundary conditions

5.4.1.1 First simulation: acoustic scaling

We fix the centreline velocity in lattice units at $U_c = 0.1$ in this simulation, which fixes the Mach number to $Ma \ll 1$. The centreline Reynolds number $Re_{cl} = \frac{U_c h}{\nu}$ is also fixed, as we vary the grid size. This allows ν to be specified, giving the relaxation time $\tau = 3\nu$. Additionally, the Womersley number is fixed so that the

period $P = \frac{n_y \pi Re_{cl}}{2W_0^2 U_c}$, making the timestep $\delta t = 1/P$ proportional to grid increment $\delta x = 2/ny$, which therefore halves as the grid size doubles. The examination of the convergence is done by altering the grid size n_y as well as correspondingly altering τ and P in order to keep constant the Reynolds and Womersley numbers. Womersley numbers close to the ones used in references [25], [5] and [14] are chosen. These are detailed in Figure (5.2), where Figure (5.2)(a) shows that for the chosen low frequency $W_0 = 0.194$ the velocity is parabolic. These results are maintained across a range of Re_{cl} and grid sizes. In the case of the chosen high-frequency Womersley number, $W_0 = 12.533$, the velocity profile is flattened, a result which is also maintained across a range of Reynolds numbers, in this case from 0.5 to 500. Typical results for grid size 64 are shown in Figures (5.2)(a) and (b).

However, the chosen moderate Womersley number W_0 shows LBM velocity which does not concur with the analytical solution for the low Reynolds number Re_{cl}=0.5 even as grid size increases, as can be seen in Figures (5.2)(c) and (d). Indeed, this simulation seems to converge to a different solution from these parameters' exact one. In this case it is noted that Kinematic viscosity $\nu \approx \frac{n_y}{10}$ increases with the increase of the period $P \approx \frac{50 n_y}{100}$, and that $\lambda = \frac{1}{\tau + 0.5}$ is therefore too small for the LBM to have sufficient reaction time to the changes in the pressure gradient, which remains so even for larger grid sizes. However, with higher Re_{cl} a better agreement is seen between the numerical results and the analytical ones. An example can be seen in Figure (5.2)(e), where the rate of relaxation is $\lambda \geq 0.5$ and the period $P = 50 n_y$, so that the LBM does have enough time to react to the changes in pressure.

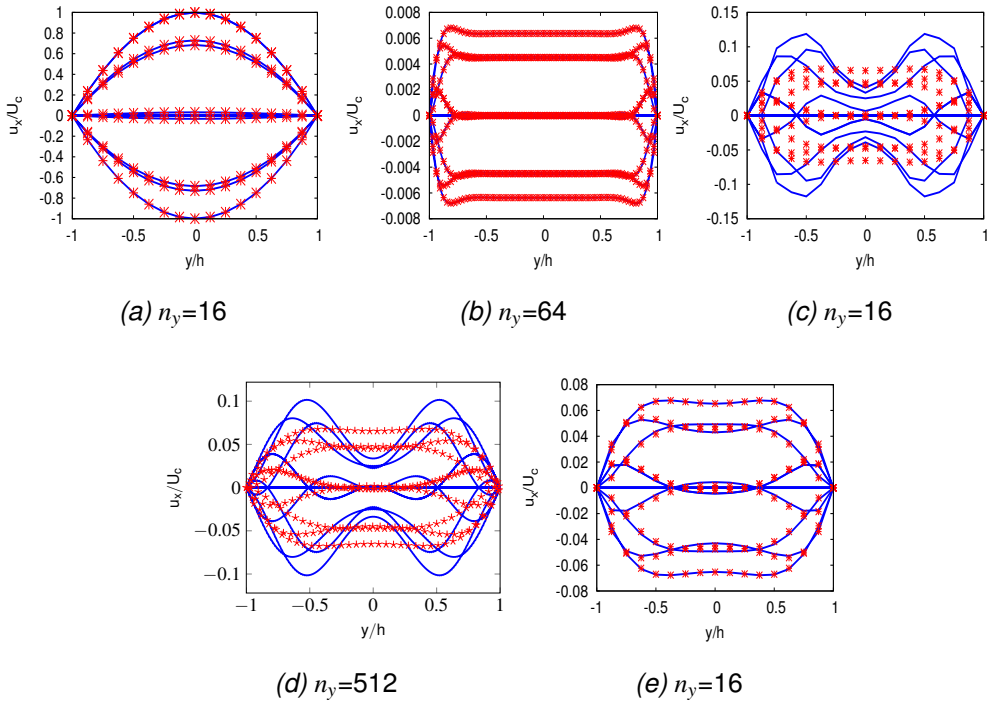

(a) n_y=16 *(b)* n_y=64 *(c)* n_y=16

(d) n_y=512 *(e)* n_y=16

Figure 5.2: (a) $W_0 = 0.194$, $Re_{cl} = 5$ (b) $W_0 = 12.533$ with $Re_{cl} = 50$ (c), (d) $W_0 = 3.963$, $Re_{cl} = 0.5$ and (e) $W_0 = 3.963$, $Re_{cl} = 5$. Blue lines: LBM; $*$: exact solution.

In this simulation, the low Womersley number shows a flattening off of the norm error for every Reynolds number, *i.e.* the method does not converge to the exact solution, as can be seen in Figure (5.3)(a). This behaviour has also been observed by Artoli [5] for $W_0 \approx 15$ and $W_0 \approx 8$ in both 2D and 3D. Latt [36] noticed, furthermore, that in some cases the error is increased with high grid size. The method does converge for higher Reynolds numbers as the Womersley number increases, as shown in Figure (5.3). However, each case shows a convergence of the numerical process as the grid size increases, even though the results do not always converge to the exact results. This is shown in Figure (5.4), in which the error between velocities computed with grid sizes 16 - 256 are contrasted with grid sizes obtained by $n_y = 512$.

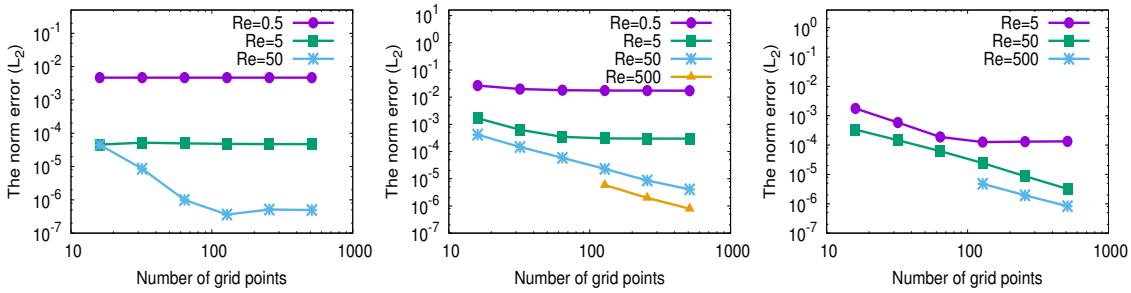

(a) $W_0 = 0.194$ (b) $W_0 = 3.963$ (c) $W_0 = 12.533$

Figure 5.3: Norm error between LBM and exact solutions velocities at $n_y = 16, 32, 64, 128, 256, 512$ for acoustic scaling.

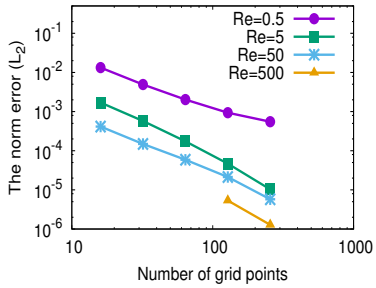

Figure 5.4: Numerical norm error between LBM velocities computed with grid sizes n_y from16 to 256 and compared with fine grid sizes $n_y = 512$ for acoustic scaling and $W_0 = 3.963$.

5.4.1.2 Second simulation: diffusive scaling

Given that in some cases that the approach above results in a lack of convergence to the analytical solutions, this second approach employs diffusive scaling. The relaxation time τ is fixed in this case, and since this determines ν, the centreline Reynolds number is fixed at $Re_{cl} = \frac{U_c n_y}{2\nu}$ by variation of the centreline velocity U_c proportional to grid spacing $\delta x = 2/n_y$. In this case, the fixing of the Womersley number results in period $P = \frac{3\pi(n_y)^2}{4W_0^2\tau}$ and therefore $\delta t \sim \delta x^2$, making the timestep reduce by a factor of 4 as the grid size doubles. Otherwise, this convergence study is similar to the acoustic scaling mentioned above, *i.e.* Re_{cl}, W_0 and τ are fixed as grid size varies, and it is noted that the Mach number in this case is inversely proportional to n_y. This approach has been used by Artoli [5], He and Lou [25], Latt [36] and Cosgrove *et. al* [14]. At the outset $\tau = 0.6$ was chosen, as was done by Artoli [5] and He and Lou [25].

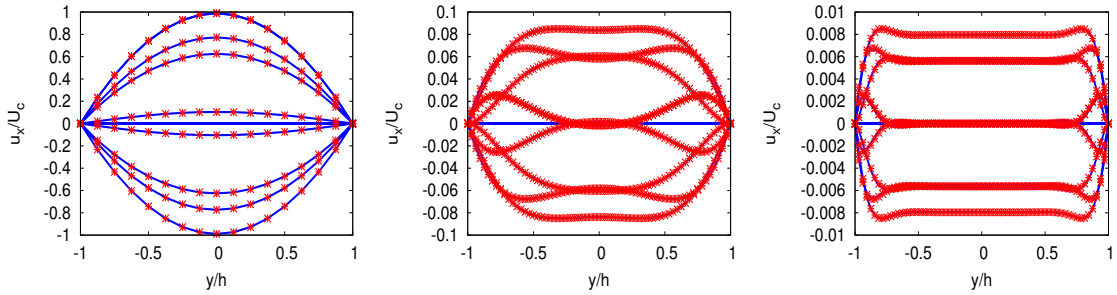

(a) $W_0 = 0.355$ and n_y=16 *(b)* $W_0 = 3.545$ and n_y=64 *(c)* $W_0 = 11.201$ and n_y=64

Figure 5.5: The velocity for τ =0.6. Blue lines: LBM; $*$: exact solution.

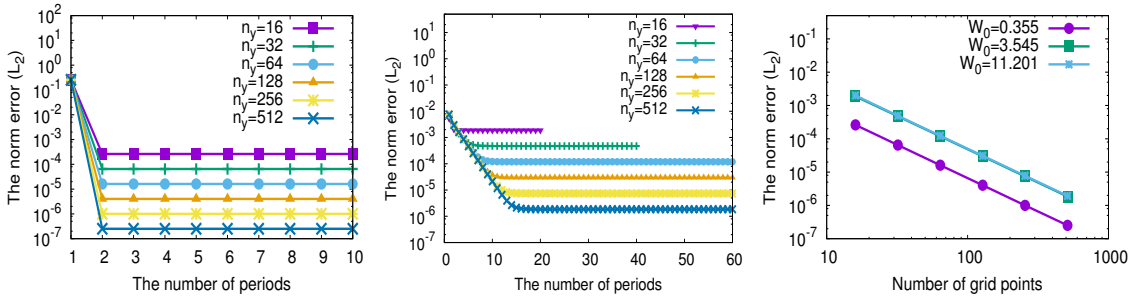

(a) $W_0 = 0.355$ *(b)* $W_0 = 3.545$ *(c)*

Figure 5.6: (a) and (b) are the norm error vs period number, and (c) norm error vs n_y for $\tau = 0.6$.

The comparisons between the exact and the numerical velocity profile solutions for a range of Womersley numbers are successful, as can be seen in Figure (5.5)(a-c). It should be noted that convergence to the final periodic state needs to take place over a number of periods, rather than being instantaneous, and that this number is dependent upon W_0 as well as the grid size, as can be seen in Figure (5.6)(a) and (b).

However, a second-order convergence is found for a range of W_0, as can be seen in Figure (5.6) (c), which is similar convergence behaviour to that found by He and Lou [25], Artoli [5], Latt [36] and Cosgrove *et. al* [14].

5.4.2 Simulation with Navier-slip boundary conditions

Again, this simulation uses diffusive scaling - in other words with fixed relaxation time and $\delta t \sim \delta x^2$ - and a range of slip lengths are investigated for their effects on both the velocity profile and the norm error when different Womersley numbers are used. Figure (5.7) shows a strong agreement between the LBM predictions

and the exact pulsatile flow solution. Slip velocity's effect is evident here. Figure (5.7), for example, shows that different slip velocities exist, and that with $K_n = 0.388$ they are generally larger in magnitude than with $K_n = 0.194$. The same figure also shows that slip velocity is reduced with $K_n = 0.0194$ and the results are nearing no-slip.

This slip velocity behaviour occurs at every Womersley number, as can be seen in Figure (5.7), but slip velocities with high frequency $W_0 = 11.201$ are not as large as slip velocities with low frequency $W_0 = 0.3545$ or middle frequency $W_0 = 3.545$ as is demonstrated in the Figures (5.7).

Each Womersley number has different maximum velocity, the smallest of which is 0.008 at $W_0 = 11.201$, whilst the largest is approximately 1.8 at $W_0 = 0.355$. Second order accuracy is achieved, but not due to this largest maximum velocity. Rather, it is because with $W_0 = 0.355$ and $\tau = 6$ accuracy of second order occurs at all K_n. Therefore, in this case, the relaxation time has a power or effect.

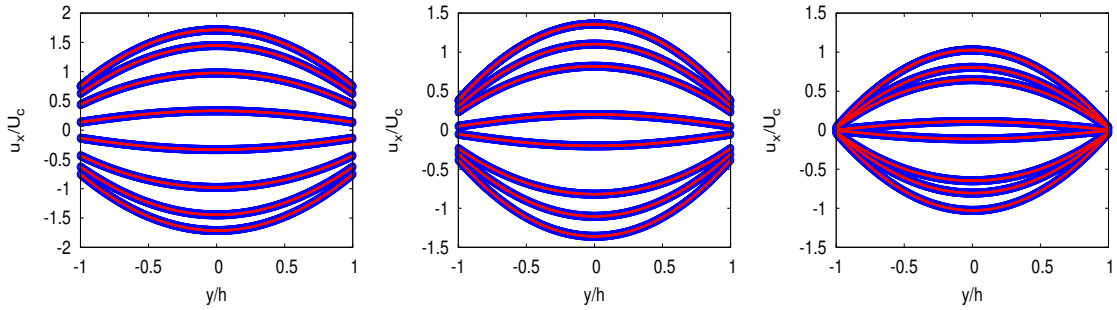

(a) $K_n = 0.388$ *(b)* $K_n = 0.194$ *(c)* $K_n = 0.0194$

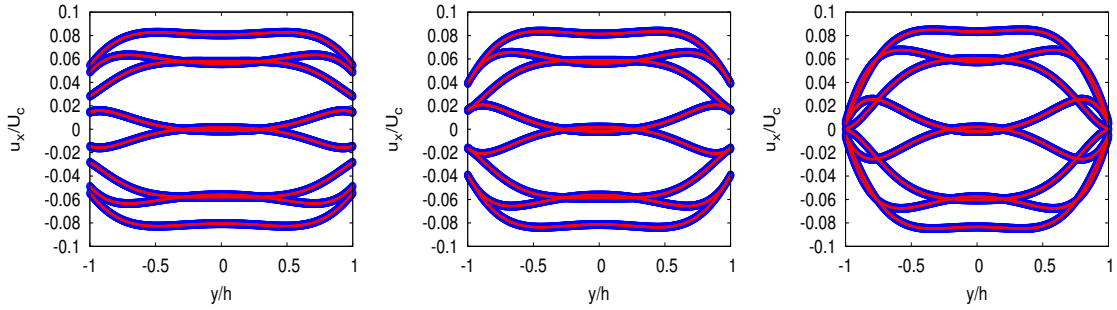

(d) $K_n = 0.388$ *(e)* $K_n = 0.194$ *(f)* $K_n = 0.0194$

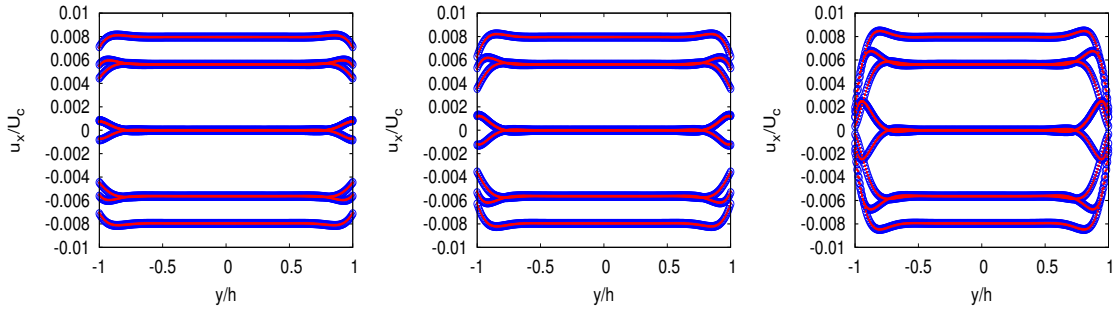

(g) $K_n = 0.388$ *(h)* $K_n = 0.194$ *(i)* $K_n = 0.0194$

Figure 5.7: (a), (b) and (c) $W_0 = 0.3545$, $\tau = 0.6$; (d), (e) and (f) $W_0 = 3.545$, $\tau = 0.6$; (g),(h) and (i) $W_0 = 11.201$, $\tau = 0.6$, $n_y = 512$. Blue: velocity profile of LBM; red: velocity profile of exact solution.

Convergence to the final periodic state must also take place over a number of periods with slip velocity, and this number not only depends upon W_0 and the grid size, but also on K_n and relaxation time τ, as demonstrated in Figures (5.8), (5.9) and (5.10). It is clear that the number of periods with low frequency $W_0 = 0.3545$ is always two for the velocity profile, as seen in Figure (5.8), and more than two with high frequency $W_0 = 11.201$ and middle frequency $W_0 = 3.545$, as shown in Figures (5.9) and (5.10). The number of periods for slip velocity is less than that for velocity profile, in both cases with $\tau = 6, 0.6$ for high frequency $W_0 = 11.201$ and middle frequency $W_0 = 3.545$, while they are larger for slip velocity than for velocity profile when both have small relaxation time $\tau = 0.06$ for $W_0 = 11.201$ and $W_0 = 3.545$ as shown in Table (5.2) (see p.85-86). In addition, the number of periods for slip velocity are less than that for velocity profile, in both cases with $\tau = 6, 0.6$ for high frequency $W_0 = 11.201$ and middle frequency $W_0 = 3.545$, while the converse is true for slip velocity and velocity profile with small relaxation time $\tau = 0.06$ as shown in Table (5.2) (see p.85-86). Furthermore, the increase in relaxation time leads to a decrease in the periods required to reach the convergence state for velocity and slip velocity, as shown in Table (5.2) (see p.85-86). In general, the reduction in K_n leads to a reduction in the number of periods required to reach the convergence state, at both high frequency $W_0 = 11.201$ and middle frequency $W_0 = 3.545$, as seen in Table (5.2) (see p.85-86) and Figures (5.8), (5.9) and (5.10).

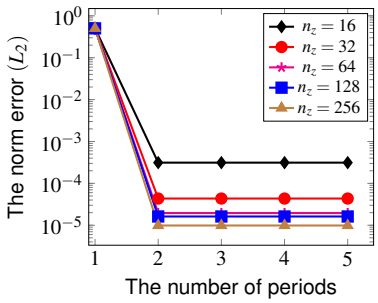

(a) $K_n = 0.388$

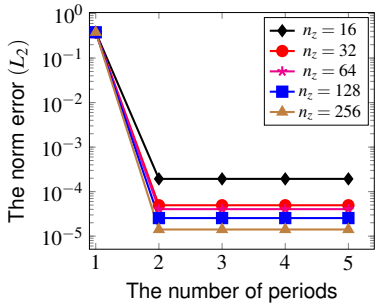

(b) $K_n = 0.194$

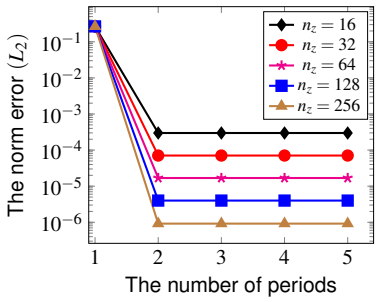

(c) $K_n = 0.0194$

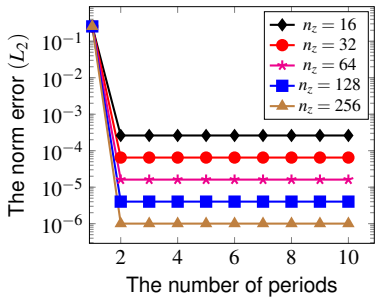

(d) $K_n = 0$

Figure 5.8: The number of periods at $\tau = 0.6$ and $W_0 = 0.354$.

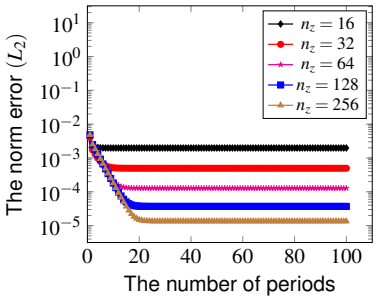

(a) $K_n = 0.388$

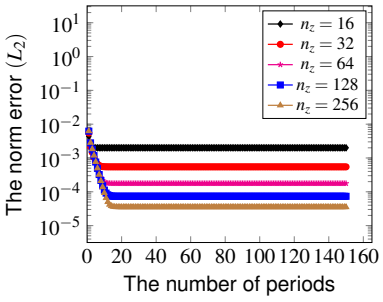

(b) $K_n = 0.194$

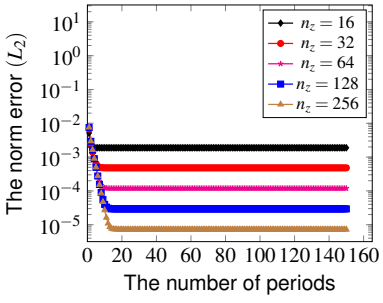

(c) $K_n = 0.0194$

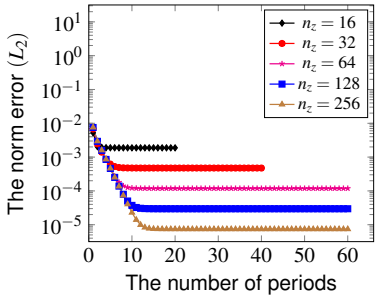

(d) $K_n = 0$

Figure 5.9: The number of periods at τ= 0.6 and $W_0 = 3.545$.

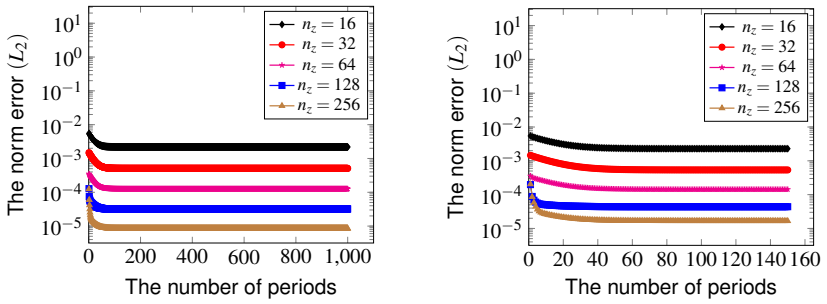

(a) $K_n = 0.388$ *(b)* $K_n = 0.194$

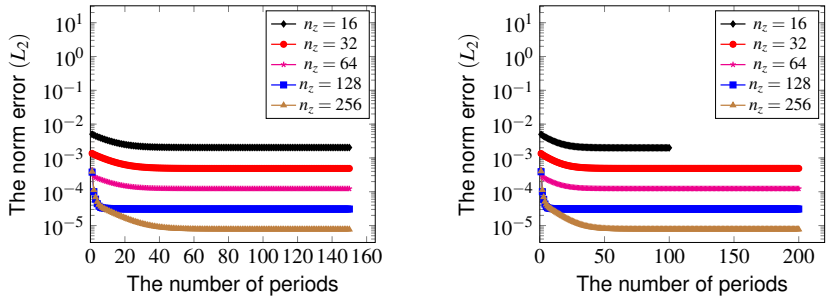

(c) $K_n = 0.0194$ *(d)* $K_n = 0$

Figure 5.10: The number of periods at $\tau = 0.6$ and $W_0 = 11.201$.

The value of the norm error in the velocity is increased by increasing the relaxation time at each Womersley number, K_n, and each grid size. This is demonstrated in in Figure (5.11). The relaxation time for slip velocity also increases in this way, and examples at Womersley number $W_0 = 3.545$ and $W_0 = 0.355$ are shown in Figure (5.12). Additionally, the value of the norm error in the velocity is larger than that in the slip velocity, at each Womersley number, relaxation time, K_n and grid size, which is demonstrated in Figure (5.11) for velocity and in Figure (5.12) for slip velocity. It is also evident that, at relaxation time $\tau = 0.6, 0.06$ with middle and low Womersley numbers, the value of the norm error in the velocity increases when the K_n increases, independent of grid size, as seen in Figure (5.11)(b),(c),(e) and (f). However, at large relaxation times such as $\tau = 6$, a decrease in the K_n does not affect the value of the norm error for velocity, as is clear from Figure (5.11)(a) for $W_0 = 0.355$ and (d) for $W_0 = 3.545$. In addition, the value of the norm error for slip velocity increases as the K_n increases, at every grid size and Womersley number, as seen in Figure (5.12).

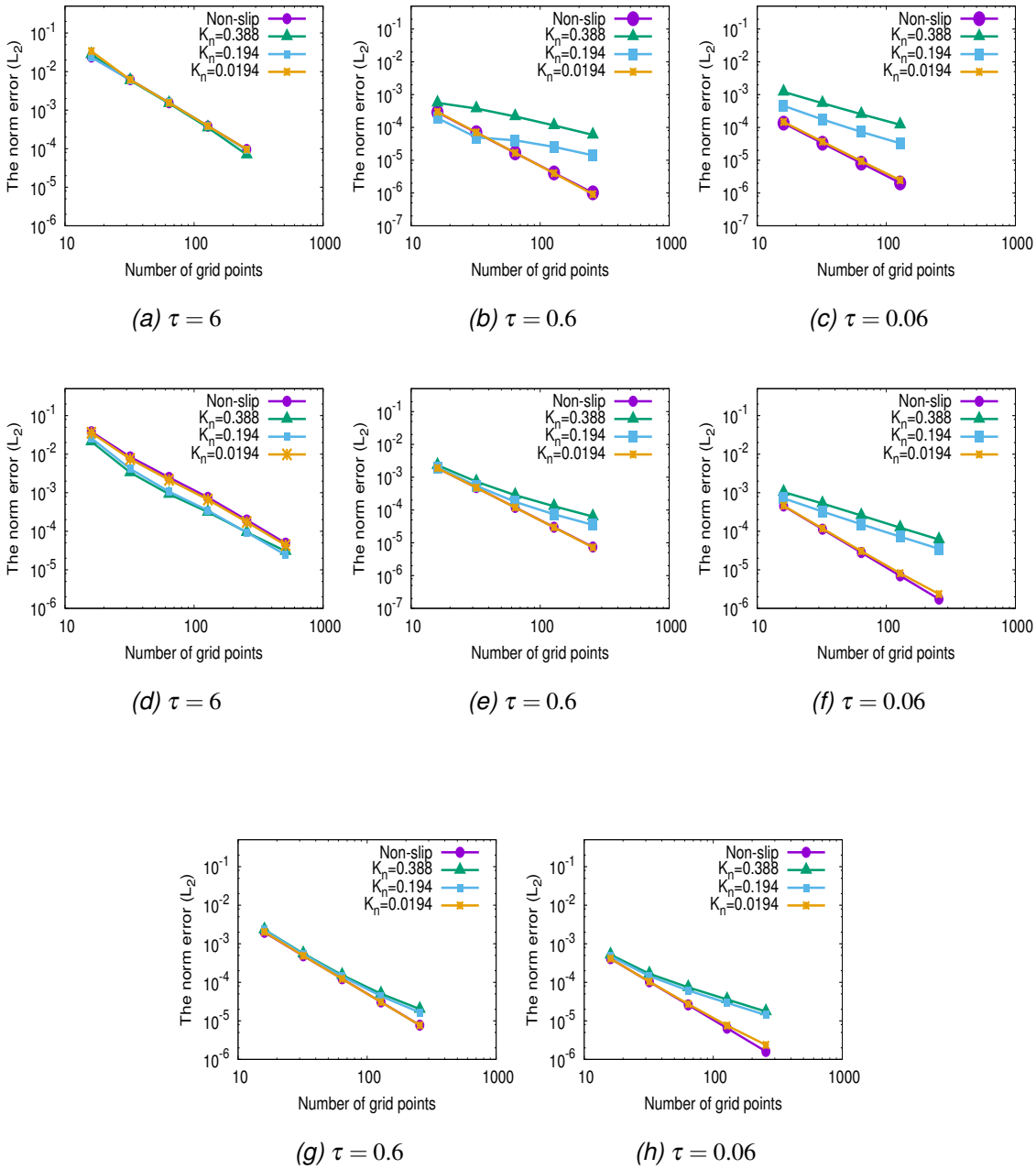

(a) $\tau = 6$ *(b)* $\tau = 0.6$ *(c)* $\tau = 0.06$

(d) $\tau = 6$ *(e)* $\tau = 0.6$ *(f)* $\tau = 0.06$

(g) $\tau = 0.6$ *(h)* $\tau = 0.06$

Figure 5.11: The order of norm error at different K_n with Navier-slip boundary condition. (a), (b), (c) for $W_0 = 0.3545$, (d), (e), (f) for $W_0 = 3.545$ and (g), (h) for $W_0 = 11.201$.

The convergence behaviour found in the Navier-slip simulation is demonstrated in Figure (5.11). It is evident that the numerical results and the error behaviour which follows are, for the given W_0, K_n, determined completely by the value τ. We therefore obtain the norm error by given τ, W_0, K_n, double the grid size n_y and divide U_c by factor 2 in order to fix Re_{cl}. Thus, the Mach number is reduced when the grid size is doubled. For example, at $n_y = 16$ and $U_c = 0.1$ the Mach number will be around $Ma = \dfrac{U_c}{c_s} = 0.172$ and at $n_y = 512$ and $U_c = 0.003125$

the Mach number will be around $Ma = 0.0054$. We can conclude that this kind of scaling is good to use for incompressible flow because the Mach number is reduced and tend to zero. For $\tau = 6$, we see that convergence is of second order, generally, independent of W_0 and K_n. However, for $\tau = 0.6$ and 0.06, it becomes around first order in the case of non-zero K_n as grid sizes increase. Also, errors tend to be larger for high values of K_n, except when the relaxation time is large, such as $\tau = 6$, when the error is small even with large K_n. This can be seen in Figure (5.11)(d). Since the slip velocity is produced as a simulation outcome, investigating how slip velocity error impacts overall error is interesting, and is shown in Figure (5.12). In general, the norm error in the velocity is greater than that in the slip velocity, at every relaxation time, Womersley number, K_n and grid size. This can be seen in Figures (5.11) and (5.12).

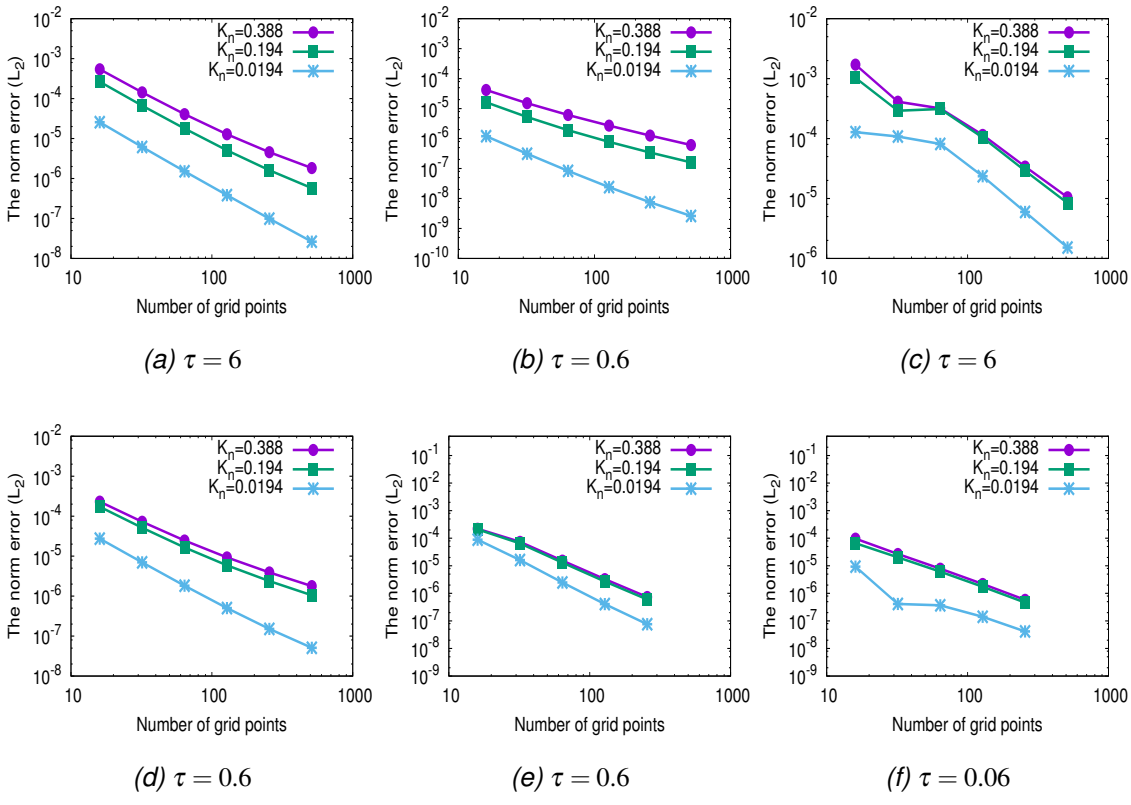

(a) $\tau = 6$ *(b)* $\tau = 0.6$ *(c)* $\tau = 6$

(d) $\tau = 0.6$ *(e)* $\tau = 0.6$ *(f)* $\tau = 0.06$

Figure 5.12: The order of norm error for slip velocity at different K_n with Navier-slip boundary condition. (a), (b) for $W_0 = 0.3545$; (c), (d) for $W_0 = 3.545$; (e), (f) for $W_0 = 11.201$

τ	W_0	k_n	n_y	The number of periods (k)	The number of periods (k) for slip velocity
6,0.6, 0.06	0.355	0.388, 0.194, 0.0194	16	2	2
			32	2	2
			64	2	2
			128	2	2
			256	2	2
			512	2	2
6	3.545	0.388	16	10	9
			32	13	16
			64	15	18
			128	18	20
			256	20	24
			512	25	30
		0.194	16	8	7
			32	12	8
			64	14	10
			128	15	11
			256	22	13
			512	24	18
		0.0194	16	6	6
			32	8	7
			64	10	8
			128	12	9
			256	15	10
			512	18	15
		0	16	5	
			32	5	
			64	8	
			128	10	
			256	13	
			512	15	
0.6	3.545	0.388	16	10	7
			32	20	18
			64	23	20
			128	25	22
			256	30	25
			512	33	29
		0.194	16	10	5
			32	18	13
			64	20	18
			128	23	20
			256	25	24
			512	28	28
		0.0194	16	8	4
			32	18	10
			64	20	13
			128	25	19
			256	28	23
			512	25	20
		0	16	5	
			32	12	
			64	15	
			128	20	
			256	22	
			512	25	

			16	22	28
			32	26	30
			64	39	38
		0.388	128	45	52
			256	56	60
			16	19	24
			32	23	28
			64	33	35
0.06	3.545	0.194	128	40	45
			256	50	58
			16	15	20
			32	18	25
			64	22	29
		0.0194	128	30	34
			256	36	40
			16	12	
			32	15	
			64	19	
		0	128	26	
			256	30	
			16	100	90
			32	110	115
		0.388	64	124	120
			128	137	130
			256	145	140
			16	100	88
			32	125	110
0.6	11.201	0.194	64	132	123
			128	137	129
			256	142	135
			16	72	70
			32	86	80
		0.0194	64	90	86
			128	114	97
			256	125	118
			16	60	
			32	60	
		0	64	60	
			128	60	
			256	80	
			16	100	106
			32	115	118
			64	123	127
		0.388	128	129	136
			256	133	150
			16	90	96
			32	95	100
			64	103	117
0.06	11.201	0.194	128	110	122
			256	120	
			16	64	70
			32	68	80
			64	74	85
		0.0194	128	100	122
			256	120	140
			16	50	
			32	55	
		0	64	60	
			128	72	
			256	90	

Table 5.2: The relation between the Womersley numbers and the number of periods for the norm errors in velocity and slip velocity, at different grid sizes k_n and relaxation times, in two dimensions.

5.5 Conclusion

To conclude, a numerical simulation of pulsatile flow in two dimensions has been performed, in which no slip and Navier-slip conditions were imposed using the lattice Boltzmann method with moment-based boundary conditions. Two approaches have been used to perform grid convergence studies. The first used acoustic scaling in which the Reynolds, Womersley and Mach numbers were fixed. The second used diffusive scaling, in which the lattice relaxation parameter was fixed in addition to the Reynolds and Womersley numbers. Computation of the velocity profile was performed, for comparison with exact solutions. Norm errors were also computed, and the approach was demonstrated to be of second-order accuracy for diffusive scaling in the case of no-slip. This second order accuracy, however, was not shown in the acoustic scaling method. This is because the small relaxation rates due to small Re_{cl} do not allow enough time for the velocity to relax to equilibrium. In the case of Navier-slip, second-order convergence was generally noted for $\tau = 6$, though first-order appeared to be approached for $\tau = 0.6, 0.06$ for non-zero K_n. The errors in the computation of slip length were, in general, less than the errors for velocity overall.

Chapter 6

3D pulsatile flow with no-slip and Navier slip boundary conditions

6.1 Introduction

This chapter details a three-dimensional simulation of the pulsatile flow between parallel plates, driven by a pulsating pressure gradient, using the Lattice Boltzmann method (LBM) with moment-based boundary conditions as before. Once again, the model used is single relaxation time, under both Navier-slip and no-slip boundary conditions. The investigation into convergence uses a diffusive scaling, with a basis of fixed relaxation time and Reynolds and Womersley numbers, while the Mach number reduces as grid size increases. This simulation uses the three dimensional lattice D_3Q_{19} and x-direction flow.

6.2 Moment-based boundary condition in three dimensions

The moment-based boundary condition in two dimensions that we saw previously is now extended to three dimensions. In three dimensions, there are always 5 unknown incoming distributions at the planar boundary faces, aligned with grid points, in D_3Q_{19} LBM post-streaming. In the moment-based boundary approach, five linearly independent moment conditions can be used to find these incoming distributions, by imposing physical constraints on five linearly independent hydrodynamic moments, and using these to obtain the five unknown distribution functions at a boundary.

Moments	Combination of unknown distribution functions at the South boundary
$\rho u_x, \Pi_{xz}, Q_{xzz}$	$f_{11} - f_{14}$
$\rho u_y, \Pi_{yz}, Q_{yzz}$	$f_{15} - f_{18}$
$\rho, \rho u_z, \Pi_{zz}$	$f_5 + f_{11} + f_{14} + f_{15} + f_{18}$
$\Pi_{xx}, R_{xxzz}, Q_{xxz}$	$f_{11} + f_{14}$
$\Pi_{yy}, R_{yyzz}, Q_{yyz}$	$f_{15} + f_{18}$

Table 6.1: Moments at the South boundary, in 3D.

Moments	Combination of unknown distribution functions at the North boundary
$\rho u_x, -\Pi_{xz}, Q_{xzz}$	$f_{12} - f_{13}$
$\rho u_y, -\Pi_{yz}, Q_{yzz}$	$f_{16} - f_{17}$
$-\rho, \rho u_z, -\Pi_{zz}$	$-f_6 - f_{12} - f_{13} - f_{16} - f_{17}$
$\Pi_{xx}, R_{xxzz}, -Q_{xxz}$	$f_{12} + f_{13}$
$\Pi_{yy}, R_{yyzz}, -Q_{yyz}$	$f_{16} + f_{17}$

Table 6.2: Moments at the North boundary, in 3D.

Moments	Combination of unknown distribution functions at the East boundary
$-\rho, \rho u_x, -\Pi_{xx}$	$-f_2 - f_8 - f_9 - f_{13} - f_{14}$
$\rho u_y, -\Pi_{xy}, Q_{xxy}$	$f_8 - f_9$
$\rho u_z, -\Pi_{xz}, Q_{xxz}$	$-f_{13} + f_{14}$
$\Pi_{yy}, -Q_{xyy}, R_{xxyy}$	$f_8 + f_9$
$\Pi_{zz}, -Q_{xzz}, R_{xxzz}$	$f_{13} + f_{14}$

Table 6.3: Moments at the East boundary, in 3D.

Moments	Combination of unknown distribution functions at the West boundary
$\rho, \rho u_x, \Pi_{xx}$	$f_1 + f_7 + f_{10} + f_{11} + f_{12}$
$\rho u_y, \Pi_{xy}, Q_{xxy}$	$f_7 - f_{10}$
$\rho u_z, \Pi_{xz}, Q_{xxz}$	$f_{11} - f_{12}$
$\Pi_{yy}, Q_{xyy}, R_{xxyy}$	$f_7 + f_{10}$
$\Pi_{zz}, Q_{xzz}, R_{xxzz}$	$f_{11} + f_{12}$

Table 6.4: Moments at the West boundary, in 3D.

6.2.1 Pulsatile flow with Navier-slip boundary conditions

In pulsatile flow simulation for three dimensions, moment-based boundary conditions are utilised at the North and South walls to implement no-slip and Navier-slip boundary conditions. The periodic boundary condition is used at the inlet (West side) and outlet (East side) and the flow is in x-direction, is driven using body force which is in x-direction. The slip velocity is specified as x-direction and zero velocity is specified as y- and z-direction. So, the assumption will be

$$u_x = u_{sx},\ u_y = u_z = 0, \tag{6.2.1}$$

and the five independent moments are

$$\begin{aligned}
&\rho u_x = \rho u_{sx},\\
&\rho u_y = \rho u_y = 0,\\
&\rho u_z = \rho u_z = 0,\\
&\Pi^0_{xx} = \frac{\rho}{3}\delta_{xx} + \rho u_x u_x = \frac{\rho}{3} + \rho u_x u_x = \frac{\rho}{3} + \rho u^2_{sx},\\
&\Pi^0_{yy} = \frac{\rho}{3}\delta_{yy} + \rho u_y u_y = \frac{\rho}{3}.
\end{aligned} \tag{6.2.2}$$

Also, the body force in x-direction is $\mathbf{F} = (\rho G_x, \rho G_y, \rho G_z) = (\rho G_x, 0, 0)$, the tangential momentum flux tensor is $\Pi_{xx} = \Pi^0_{xx} + \tau\Pi^1_{xx} = \frac{\rho}{3} - \tau\frac{2\rho}{3}\partial_x u_x = \frac{\rho}{3} + \rho u^2_{sx}$ and $\Pi_{yy} = \Pi^0_{yy} + \tau\Pi^1_{yy} = \frac{\rho}{3} - \tau\frac{2\rho}{3}\partial_y u_y = \frac{\rho}{3}$, so

$$\begin{aligned}
&\rho\overline{u}_x = \rho u_{sx} - \frac{\delta_t}{2}\rho G_x,\\
&\rho\overline{u}_y = \rho u_y - \frac{\delta_t}{2}\rho G_y = 0,\\
&\rho\overline{u}_z = \rho u_z - \frac{\delta_t}{2}\rho G_z = 0,\\
&\overline{\Pi}_{xx} = \Pi_{xx} + \frac{\delta_t}{2\tau}\Pi_{xx} - \frac{\delta_t}{2\tau}\Pi^0_{xx} - \frac{\delta_t}{2}\left(\rho G_x u_x + u_x \rho G_x\right) = \frac{\rho}{3} + \rho u^2_{sx} - \delta_t \rho G_x,\\
&\overline{\Pi}_{yy} = \Pi_{yy} + \frac{\delta_t}{2\tau}\Pi_{yy} - \frac{\delta_t}{2\tau}\Pi^0_{yy} - \frac{\delta_t}{2}\left(\rho G_y u_y + u_y \rho G_y\right) = \frac{\rho}{3},
\end{aligned} \tag{6.2.3}$$

so

$$\begin{aligned}
\rho\overline{u}_x &= \overline{f}_1-\overline{f}_2+\overline{f}_7-\overline{f}_8-\overline{f}_9+\overline{f}_{10}+\overline{f}_{11}+\overline{f}_{12}-\overline{f}_{13}-\overline{f}_{14} = \rho u_{sx}-\frac{\delta_t}{2}\rho G_x,\\
\rho\overline{u}_y &= \overline{f}_3-\overline{f}_4+\overline{f}_7+\overline{f}_8-\overline{f}_9-\overline{f}_{10}+\overline{f}_{15}+\overline{f}_{16}-\overline{f}_{17}-\overline{f}_{18} = 0,\\
\rho\overline{u}_z &= \overline{f}_5-\overline{f}_6+\overline{f}_{11}-\overline{f}_{12}-\overline{f}_{13}+\overline{f}_{14}+\overline{f}_{15}-\overline{f}_{16}-\overline{f}_{17}+\overline{f}_{18} = 0,\\
\overline{\Pi}_{xx} &= \overline{f}_1+\overline{f}_2+\overline{f}_7+\overline{f}_8+\overline{f}_9+\overline{f}_{10}+\overline{f}_{11}+\overline{f}_{12}+\overline{f}_{13}+\overline{f}_{14} = \frac{\rho}{3}+\rho u_{sx}^2-\delta_t\rho G_x,\\
\overline{\Pi}_{yy} &= \overline{f}_3+\overline{f}_4+\overline{f}_7+\overline{f}_8+\overline{f}_9+\overline{f}_{10}+\overline{f}_{15}+\overline{f}_{16}+\overline{f}_{17}+\overline{f}_{18} = \frac{\rho}{3}.
\end{aligned} \tag{6.2.4}$$

The unknown distribution functions at the South wall are

$$\overline{f}_5,\overline{f}_{11},\overline{f}_{14},\overline{f}_{15},\overline{f}_{18}. \tag{6.2.5}$$

By solving system (6.2.4) we can find the unknown distribution function at the South wall which are

$$\begin{aligned}
\overline{f}_5 &= \overline{f}_1+\overline{f}_2+\overline{f}_3+\overline{f}_4+\overline{f}_6+2\overline{f}_7+2\overline{f}_8+2\overline{f}_9+2\overline{f}_{10}+2\overline{f}_{12}+2\overline{f}_{13}+\\
&\quad 2\overline{f}_{16}+2\overline{f}_{17}-\frac{2}{3}\rho+\delta_t\rho G_x u_{sx}-\rho u_{sx}^2,\\
\overline{f}_{11} &= -\overline{f}_1-\overline{f}_7-\overline{f}_{10}-\overline{f}_{12}+\frac{\rho}{6}-\frac{\delta_t}{4}\rho G_x-\frac{\delta_t}{2}\rho G_x u_{sx}+\frac{1}{2}\rho u_{sx}^2+\frac{1}{2}\rho u_{sx},\\
\overline{f}_{14} &= -\overline{f}_2-\overline{f}_8-\overline{f}_9-\overline{f}_{13}+\frac{\rho}{6}+\frac{\delta_t}{4}\rho G_x-\frac{\delta_t}{2}\rho G_x u_{sx}+\frac{1}{2}\rho u_{sx}^2-\frac{1}{2}\rho u_{sx},\\
\overline{f}_{15} &= -\overline{f}_3-\overline{f}_7-\overline{f}_8-\overline{f}_{16}+\frac{\rho}{6},\\
\overline{f}_{18} &= -\overline{f}_4-\overline{f}_9-\overline{f}_{10}-\overline{f}_{17}+\frac{\rho}{6}.
\end{aligned} \tag{6.2.6}$$

The unknown distribution functions at the North wall are

$$\overline{f}_6,\overline{f}_{12},\overline{f}_{13},\overline{f}_{16},\overline{f}_{17}. \tag{6.2.7}$$

Again, by solving system (6.2.4), we can find the unknown distribution functions at the North wall which are

$$\begin{aligned}
\overline{f}_6 &= \overline{f}_1+\overline{f}_2+\overline{f}_3+\overline{f}_4+\overline{f}_5+2\overline{f}_7+2\overline{f}_8+2\overline{f}_9+2\overline{f}_{10}+2\overline{f}_{11}+2\overline{f}_{14}\\
&\quad 2\overline{f}_{15}+2\overline{f}_{18}-\frac{2}{3}\rho+\delta_t\rho G_x u_{sx}-\rho u_{sx}^2,\\
\overline{f}_{12} &= -\overline{f}_1-\overline{f}_7-\overline{f}_{10}-\overline{f}_{11}+\frac{\rho}{6}-\frac{\delta_t}{4}\rho G_x-\frac{\delta_t}{2}\rho G_x u_{sx}+\frac{1}{2}\rho u_{sx}^2+\frac{1}{2}\rho u_{sx},\\
\overline{f}_{13} &= -\overline{f}_2-\overline{f}_8-\overline{f}_9-\overline{f}_{14}+\frac{\rho}{6}+\frac{\delta_t}{4}\rho G_x-\frac{\delta_t}{2}\rho G_x u_{sx}+\frac{1}{2}\rho u_{sx}^2-\frac{1}{2}\rho u_{sx},\\
\overline{f}_{16} &= -\overline{f}_3-\overline{f}_7-\overline{f}_8-\overline{f}_{15}+\frac{\rho}{6},\\
\overline{f}_{17} &= -\overline{f}_4-\overline{f}_9-\overline{f}_{10}-\overline{f}_{18}+\frac{\rho}{6}.
\end{aligned} \tag{6.2.8}$$

Using the definition of density seen in Eq (4.7.26) and $\rho\overline{u}_y$ in system (6.2.4) we can find the density at the South and North walls. At the South wall it is

$$\rho = \overline{f}_0+\overline{f}_1+\overline{f}_2+\overline{f}_3+\overline{f}_4+2\overline{f}_6+\overline{f}_7+\overline{f}_8+\overline{f}_9+\overline{f}_{10}+2\overline{f}_{12}+2\overline{f}_{13}+2\overline{f}_{16}+2\overline{f}_{17}, \tag{6.2.9}$$

and at the North wall

$$\rho = \overline{f}_0+\overline{f}_1+\overline{f}_2+\overline{f}_3+\overline{f}_4+2\overline{f}_5+\overline{f}_7+\overline{f}_8+\overline{f}_9+\overline{f}_{10}+2\overline{f}_{11}+2\overline{f}_{14}+2\overline{f}_{15}+2\overline{f}_{18}. \tag{6.2.10}$$

Now we have to find the slip velocity u_{sx} in the case of $u_x = u_{wall} = u_{sx}$ and $u_y = u_z = 0$. The equilibrium shear stress is

$$\Pi_{xz}^0 = \frac{\rho}{3}\delta_{xz}+\rho u_x u_z = 0, \tag{6.2.11}$$

and

$$\begin{aligned}
\overline{\Pi}_{xz} &= \Pi_{xz} + \frac{\delta_t}{2\tau}\Pi_{xz} - \frac{\delta_t}{2\tau}\Pi^0_{xz} - \frac{\delta_t}{2}\rho\left(G_x u_z + u_x G_z\right), \text{where} \quad u_x = u_{sx}, \\
&= \Pi_{xz} + \frac{\delta_t}{2\tau}\Pi_{xz}, \\
\overline{\Pi}_{xz} &= \frac{2\tau+1}{2\tau}\Pi_{xz}, \\
\left(\overline{f}_{11} - \overline{f}_{12} + \overline{f}_{13} - \overline{f}_{14}\right) &= \frac{2\tau+1}{2\tau}\Pi_{xz}.
\end{aligned} \tag{6.2.12}$$

We know that the slip velocity is proportional to the shear stress at the wall as explained in section (4.5), so $u_s = l_s \partial_n u_{wall}$. From the Chapman-Enskog expansion section (3.2),

$$\Pi_{xz} = \Pi^0_{xz} + \tau\Pi^1_{xz} = \frac{\rho}{3}\delta_{xz} + \rho u_x u_z - \tau\frac{\rho}{3}(\partial_x u_z + \partial_z u_x) = -\mu\partial_z u_x, \tag{6.2.13}$$

so,

$$u_{sx} = -l_s\partial_z u_x = -\partial_z u_{wall}, \tag{6.2.14}$$

and

$$\begin{aligned}
\Pi_{xz} &= \frac{-\mu}{l_s}u_{sx}, \\
\Rightarrow u_{sx} &= \frac{-l_s}{\mu}\Pi_{xz}, \qquad (6.2.15) \\
\Rightarrow u_{sx} &= \frac{-l_s}{\mu}\frac{2\tau}{2\tau+1}\overline{\Pi}_{xz}, \\
\Rightarrow u_{sx} &= \frac{-l_s}{\mu}\frac{2\tau}{2\tau+1}\left(\overline{f}_{11} - \overline{f}_{12} + \overline{f}_{13} - \overline{f}_{14}\right), \\
u_{sx} &= \frac{-6l_s}{\rho(2\tau+1)}\left(\overline{f}_{11} - \overline{f}_{12} + \overline{f}_{13} - \overline{f}_{14}\right). \qquad (6.2.16)
\end{aligned}$$

At the South wall the shear stress is positive toward the wall, so $u_s = -l_s\partial_n u_{wall}$, where $n > 0$ and $u_{sx} = \dfrac{-l_s}{\mu}\Pi_{xz}$. Thus

$$u_{sx} = \left(\frac{-6l_s}{\rho(2\tau+1)}\left(\overline{f}_{11} - \overline{f}_{12} + \overline{f}_{13} - \overline{f}_{14}\right)\right), \tag{6.2.17}$$

while, at the North wall the shear the shear stress is negative, so $u_s = l_s \partial_n u_{wall}$ and $u_{sx} = \frac{l_s}{\mu}\Pi_{xz}$. Hence

$$u_{sx} = -\left(\frac{-6l_s}{\rho(2\tau+1)}\left(\overline{f}_{11}-\overline{f}_{12}+\overline{f}_{13}-\overline{f}_{14}\right)\right) = \frac{6l_s}{\rho(2\tau+1)}\left(\overline{f}_{11}-\overline{f}_{12}+\overline{f}_{13}-\overline{f}_{14}\right)$$
$$= \frac{6l_s}{\rho(6l_s+2\tau+1)}\left(\frac{\delta_t}{2}\rho G_x+\overline{f}_1-\overline{f}_2+\overline{f}_7-\overline{f}_8-\overline{f}_9+\overline{f}_{10}+2\overline{f}_{12}-2\overline{f}_{13}\right). \tag{6.2.18}$$

The moment-based boundary condition with no-slip at the South and North walls is obtained by setting a zero velocity at x-direction as seen in Eq (6.2.1).

6.3 The exact solutions for pulsatile flow

For three-dimensional pulsatile flow, or Womersley flow, the exact solutions are the same as for two dimensions, where the pulsating pressure gradient is implemented with an equivalent body force $G_x = \left(2U_c\nu/h^2\right)\cos(wt)$ in the x-direction where h is the channel half-width, U_c is the centreline speed for the zero frequency case (*i.e.* Poiseuille flow), h is the channel half-width, $\nu = \frac{U_c h}{Re_{cl}}$ Kinematic viscosity and Re_{cl} the centreline Reynolds number. The exact solution under no-slip boundary conditions at $u_x = 0$ and $z = \pm h$ is

$$\frac{u_x}{U_c} = \Re\left[\frac{-j}{W_0}\left(1-\frac{\cosh\left((1+j)W_0\frac{z}{h}\right)}{\cosh\left((1+j)W_0\right)}\right)e^{\frac{j2\pi t}{P}}\right], \tag{6.3.1}$$

where $j=\sqrt{-1}$, $W_0 = \sqrt{\frac{w}{2\nu}}h$ is the dimensionless Womersley number in which $w = \frac{2\pi}{P}$ is the pulsation angular frequency, t is the time and P is the period.
With Navier-slip conditions $u_x = u_s = l_s|\frac{du_x}{dz}|$ at $z = \pm h$, the exact solution is

$$\frac{u_x}{U_c} = \Re\left[\left(\frac{u_s}{U_c}\frac{\cosh\left((1+j)W_0\frac{z}{h}\right)}{\cosh\left((1+j)W_0\right)}+\frac{j}{W_0}\left(1-\frac{\cosh\left((1+j)W_0\frac{z}{h}\right)}{\cosh\left((1+j)W_0\right)}\right)\right)e^{\frac{j2\pi t}{P}}\right], \tag{6.3.2}$$

$$\frac{u_s}{U_c} = \frac{(j-1)K_n\sinh\left((1+j)W_0\right)}{W_0\left[\cosh\left((1+j)W_0\right)-K_nW_0(1+j)\sinh\left((1+j)W_0\right)\right]}, \tag{6.3.3}$$

with $K_n = \frac{l_s}{h}$ being the dimensionless slip length. It is evident that both the exact solutions, for no-slip and for Navier-slip, are independent of the Reynolds number.

6.4 The simulation

This simulation utilises diffusive scaling, *i.e.* with fixed relaxation time and $\delta t \sim \delta x^2$. Similarly to the case in two dimensions, we select a range of different slip lengths.

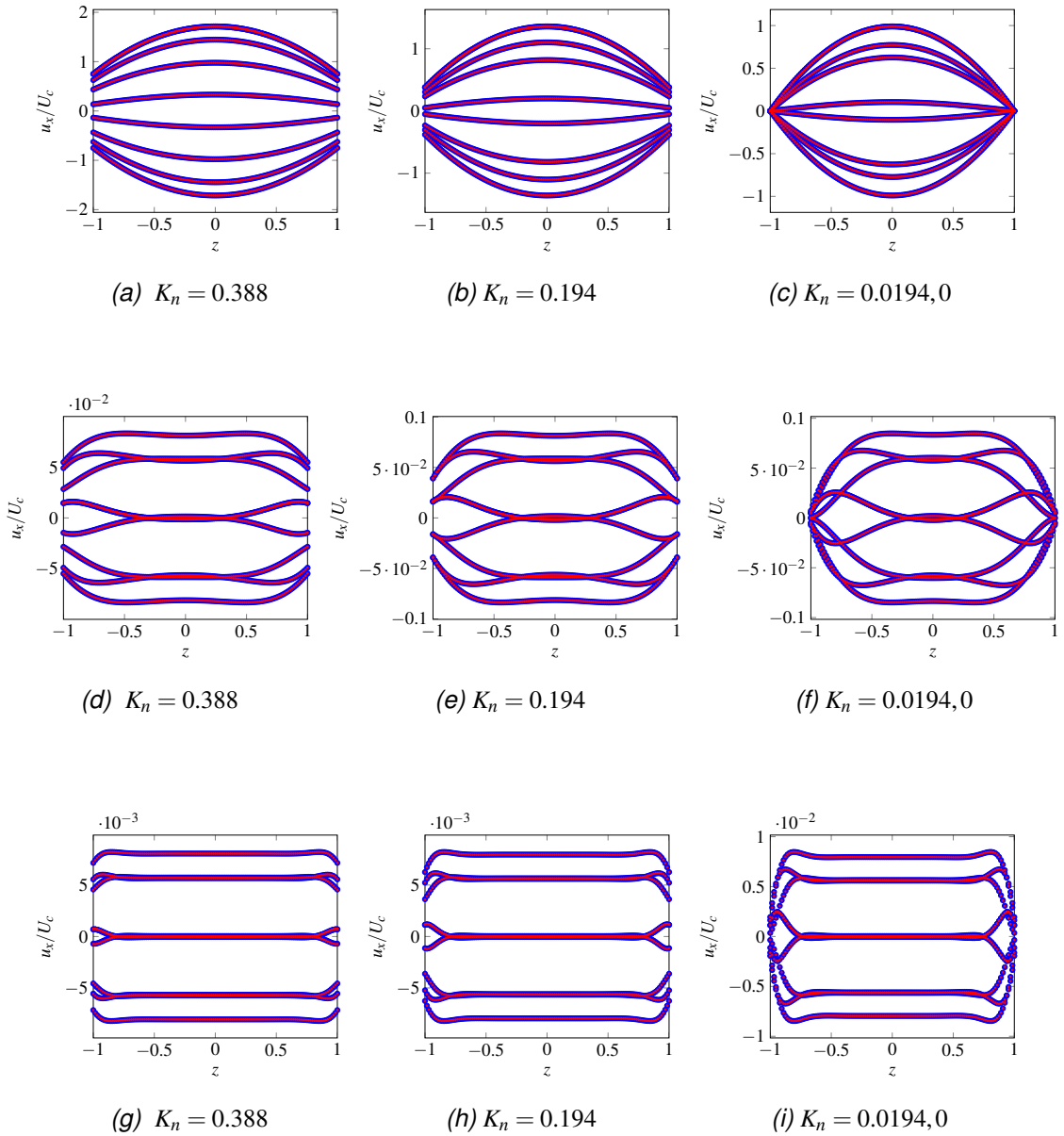

(a) $K_n = 0.388$ *(b)* $K_n = 0.194$ *(c)* $K_n = 0.0194, 0$

(d) $K_n = 0.388$ *(e)* $K_n = 0.194$ *(f)* $K_n = 0.0194, 0$

(g) $K_n = 0.388$ *(h)* $K_n = 0.194$ *(i)* $K_n = 0.0194, 0$

Figure 6.1: Blue: velocity profile of LBM; Red: velocity profile of exact solution at $\tau = 0.6$ and $n_z = 128$. (a), (b) and (c) for $W_0 = 0.3545$; (d), (e) and (f) for $W_0 = 3.545$; (g), (h) and (i) for $W_0 = 11.201$.

Again, as we see in Figure (6.1), there is a strong agreement between the predictions of the LBM and the exact solution of pulsatile flow. The effect of

slip velocity is also the same as for two dimensions, for example in the difference in magnitude of slip velocities. These slip velocities are still reduced with $K_n = 0.0194$, with the results that are very close to those for no-slip in the two-dimensional simulation. It is clear also that the slip velocities with high frequency $W_0 = 11.201$ are still smaller than those with low frequency $W_0 = 0.3545$ or middle frequency $W_0 = 3.545$, as in the 2D simulation. Again, every Womersley number has a different maximum velocity which is the same in both 2D and 3D simulations, so the smallest is again 0.008 at $W_0 = 11.201$ and the largest around 1.8 at $W_0 = 0.355$. The largest maximum velocity still does not have the power to achieve the second order accuracy of the method, which is clear with $W_0 = 0.355$ and $\tau = 6$, where the second order accuracy occurs at all K_n.

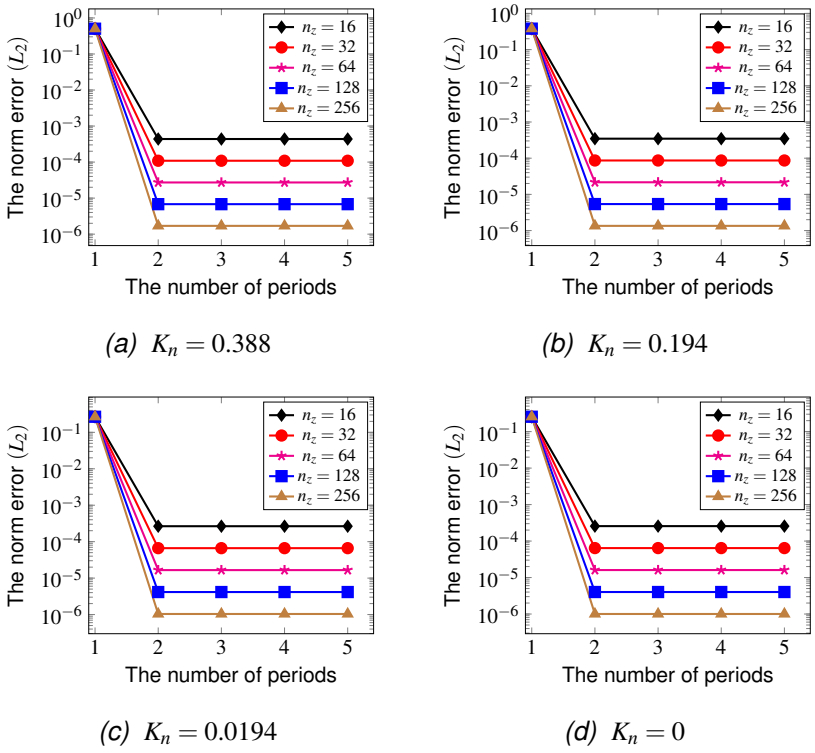

(a) $K_n = 0.388$ *(b)* $K_n = 0.194$

(c) $K_n = 0.0194$ *(d)* $K_n = 0$

Figure 6.2: The number of periods at $\tau = 0.6$ and $W_0 = 0.354$.

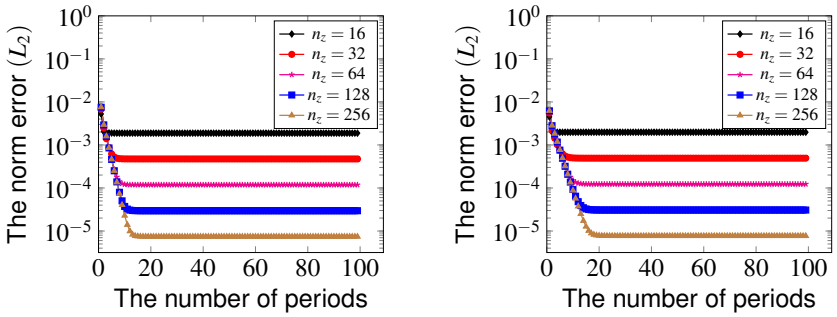

(a) $K_n = 0.388$ *(b)* $K_n = 0.194$

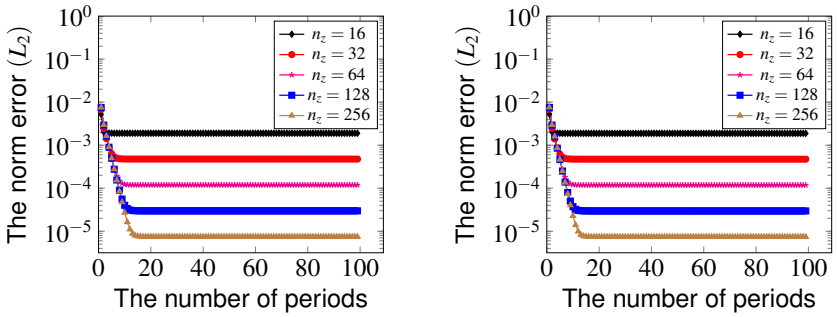

(c) $K_n = 0.0194$ *(d)* $K_n = 0$

Figure 6.3: The number of periods at $\tau = 0.6$ and $W_0 = 3.545$.

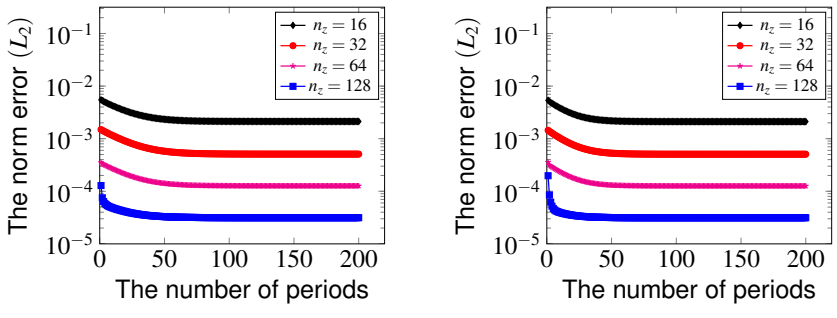

(a) $K_n = 0.388$ *(b)* $K_n = 0.194$

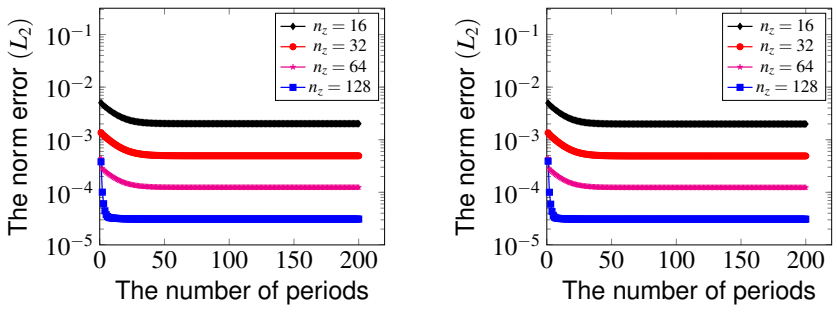

(c) $K_n = 0.0194$ *(d)* $K_n = 0$

Figure 6.4: The number of periods at $\tau = 0.6$ and $W_0 = 11.201$.

Like in two dimensions, in the 3D simulation the convergence state with slip

velocity depends on the number of periods, which is dependent upon W_0, the grid size, K_n and the relaxation time τ, as shown in Figures (6.2), (6.3) and (6.4). The behaviour of the convergence state and the number of periods are the same as in the two dimensional simulation. For example, the number of periods for the velocity profile with low frequency $W_0 = 0.3545$ are again always equal to two, as seen in Figure (6.2), and that there are more than two periods with $W_0 = 11.201$ and $W0 = 3.545$, as shown in Figures (6.3) and (6.4). The number of periods for slip velocity are again less than that for velocity profile when relaxation time $\tau = 6, 0.6$, $W_0 = 11.201$ and $W_0 = 3.545$, while again the number of periods for slip velocity is larger than that for the velocity profile when $\tau = 0.06$ for $W_0 = 11.201$ and $W_0 = 3.545$, as shown in Table (6.5) (see p.101-102).

Furthermore, increase in relaxation time again leads to a decrease in the number of periods required to reach convergence state for velocity and slip velocity, as seen in Table (6.5) (see p.101-102). Once more, at relaxation time $\tau = 0.06$, a decrease in K_n leads to a decrease in required periods to reach convergence state in the case of velocity profile at $W_0 = 11.201$ and $W_0 = 3.545$, as seen in Table (6.5) (see p.101-102) and Figures (6.2), (6.3) and (6.4).

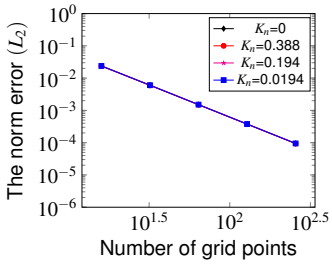

(a) $\tau = 6$

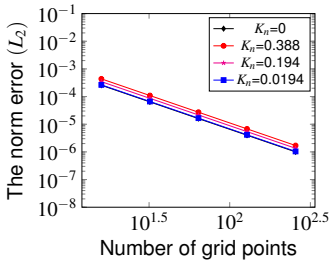

(b) $\tau = 0.6$

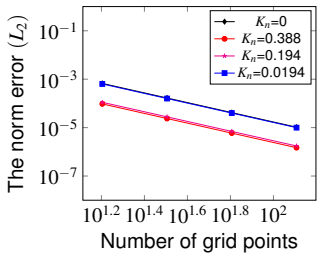

(c) $\tau = 0.06$

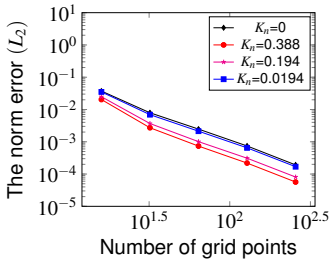

(d) $\tau = 6$

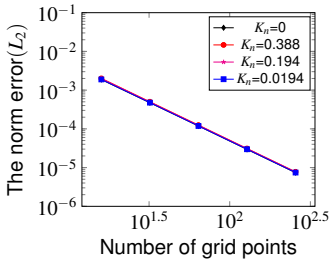

(e) $\tau = 0.6$

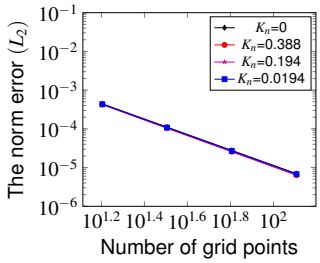

(f) $\tau = 0.06$

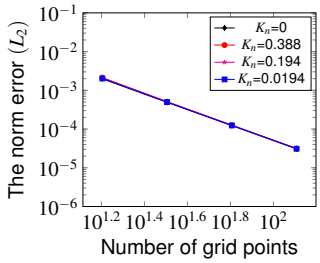

(g) $\tau = 0.6$

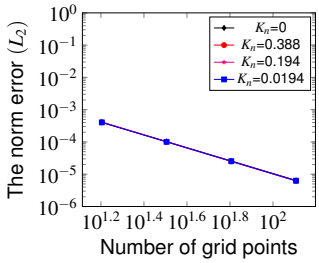

(h) $\tau = 0.06$

Figure 6.5: The norm error in 3D. (a), (b), (c) for $W_0 = 0.3545$ and (d), (e), (f) for $W_0 = 3.545$ and (g), (h) for $W_0 = 11.201$.

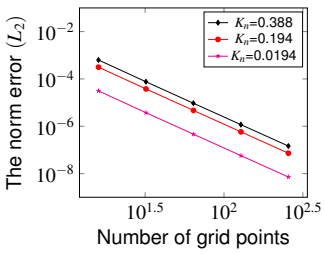

(a) $\tau = 6$

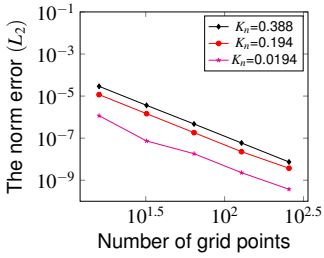

(b) $\tau = 0.6$

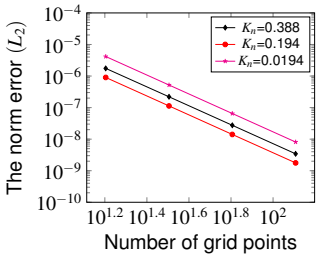

(c) $\tau = 0.06$

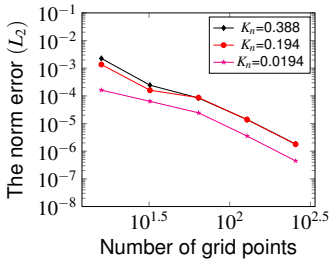

(d) $\tau = 6$

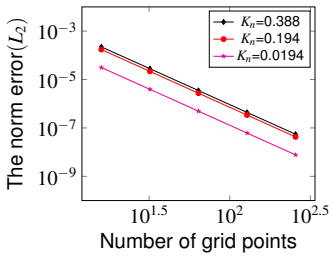

(e) $\tau = 0.6$

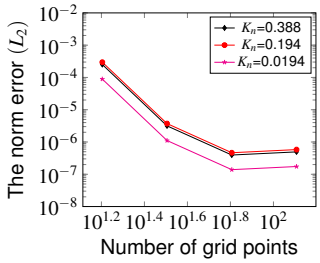

(f) $\tau = 0.06$

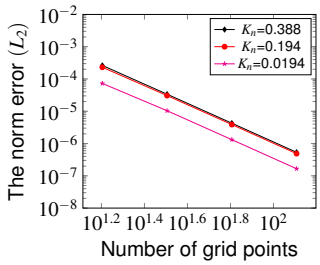

(g) $\tau = 0.6$

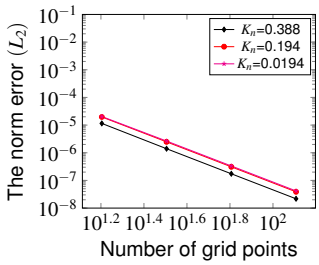

(h) $\tau = 0.06$

Figure 6.6: The norm error for slip velocity in 3D. (a), (b), (c) for $W_0 = 0.3545$ and (d), (e), (f) for $W_0 = 3.545$ and (g), (h) for $W_0 = 11.201$.

In three dimensions, the numerical results and resulting error behaviour for given W_0, K_n are completely determined by the τ value. The examination of the

error uses the same method as for two dimensions. Second-order convergence is generally achieved, independent of W_0 and K_n and τ and errors are in general the same for large values of K_n and small relaxation time $\tau = 0.06, 0.6$ with low or middle frequency, as seen Figure (6.5)(b), (c), (e) and (f). The errors are also the same for each K_n and $\tau = 0.06, 0.6$ with $W_0 = 11.201$ as shown in Figure (6.5)(g) and (f).

Convergence behaviour for velocity profile in this three-dimensional Navier-slip simulation is shown in Figure (6.5) and for slip velocity in Figure (6.6) for slip velocity. The behaviour of the norm error in both is similar in 3D to in 2D, as demonstrated the same Figures (6.5) for velocity profile and (6.6) for slip velocity. For example, the value of the norm error in the velocity profile and slip velocity is increased by increasing the relaxation time at each Womersley number, K_n and grid size, as seen in those same Figures (6.5) and (6.6). Generally, the value of the velocity norm error is larger than that in slip velocity at each relaxation time, Womersley number, K_n and grid size, as shown in Figure (6.5) and Figure (6.6). At relaxation time $\tau = 0.6$ and low Womersley numbers the value of the norm error for the velocity increases when the K_n increases, independent of grid size, as shown in Figure (6.5)(a) and (b). For the slip velocities with the same relaxation time range, it is noted that the norm error increases regardless of the K_n and grid size, in the case of middle and high Womersley numbers, as shown (6.6)(e) and (g). However, with large relaxation times such as $\tau = 6$ with $W_0 = 0.3545$, a decrease in the K_n no longer affects the norm error for velocity, as demonstrated in Figure (6.5)(a), whereas it does affect that in slip velocity, as seen in Figure (6.6)(a).

τ	W_0	K_n	n_y	The number of periods (k)	The number of periods (k) for slip velocity
6,0.6, 0.06,0	0.355	0.388, 0.194, 0.0194	16	2	2
			32	2	2
			64	2	2
			128	2	2
			256	2	2
			512	2	2
6	3.545	0.388	16	10	9
			32	16	30
			64	18	49
			128	20	50
			256	22	69
		0.194	16	29	18
			32	32	26
			64	34	30
			128	42	40
			256	47	44
		0.0194	16	25	19
			32	26	21
			64	27	23
			128	32	25
			256	35	28
		0	16	25	
			32	28	
			64	29	
			128	33	
			256	35	
0.6	3.545	0.388	16	35	17
			32	39	18
			64	50	20
			128	59	23
			256	85	24
		0.194	16	19	17
			32	22	19
			64	26	19
			128	29	21
			256	33	35
		0.0194	16	28	18
			32	40	19
			64	51	20
			128	62	22
			256	85	23
		0	16	15	
			32	18	
			64	20	
			128	21	
			256	22	

			16	22	28
			32	32	35
			64	38	46
		0.388	128	44	55
			16	18	33
			32	24	40
			64	30	42
0.06	3.545	0.194	128	37	46
			16	15	17
			32	18	19
			64	22	26
		0.0194	128	31	37
			16	13	
			32	16	
			64	22	
		0	128	26	
			16	100	60
			32	126	70
			64	133	80
		0.388	128	146	100
			16	70	62
			32	90	68
			64	95	75
0.6	11.201	0.194	128	100	80
			16	55	58
			32	58	60
			64	60	70
		0.0194	128	64	80
			16	50	
		0	32	55	
			64	60	
			128	65	
			16	68	80
			32	70	90
		0.388	64	100	125
			128	150	160
			16	65	75
			32	67	80
0.06	11.201	0.194	64	80	90
			128	140	148
			16	54	47
			32	59	61
		0.0194	64	77	80
			128	107	115
			16	44	
			32	57	
		0	64	58	
			128	90	

Table 6.5: The relation between the Womersley numbers and the number of periods for the norm error of velocity and slip velocity at different grid sizes, L_n and relaxation times in 3D.

6.5 Conclusion

To conclude, the numerical simulation of pulsatile flow in three dimensions has been performed using the lattice Boltzmann method with moment-based boundary conditions to implement no slip as well as Navier-slip conditions. Studies of the grid convergence employed a diffusive scaling method, and the velocity profile was computed for comparison with analytical solutions which are, in general, excellent. Norm errors were also computed which showed that the method is second-order for diffusive scaling in both no-slip and slip cases. Errors in the computation of slip length were in general less than for the velocity overall.

Chapter 7

Fully-developed flow in a three-dimensional square duct

7.1 Introduction

Now we move on to consider duct flow in three dimensions, starting with fully-developed flow which is driven by the body force in y-direction. The velocity profile for this flow is examined and compared with the exact solutions for two dimensions. In this model, no-slip and Navier-slip boundary conditions are applied at the South, North, East and West walls using moment-based boundary conditions, and at the inlet and outlet by periodic boundary conditions, in a square cross-section duct. These are used with second-order LBM in a three dimensional square duct, in order to simulate laminar flow which is incompressible in two regimes: the slip regime, where the dimensionless length slip is $0.001 < K_n < 0.1$ and the transition regime, where $0.1 < K_n < 0.2$. The convergence study is then performed using a single relaxation time and by performing resolution for the grid sizes.

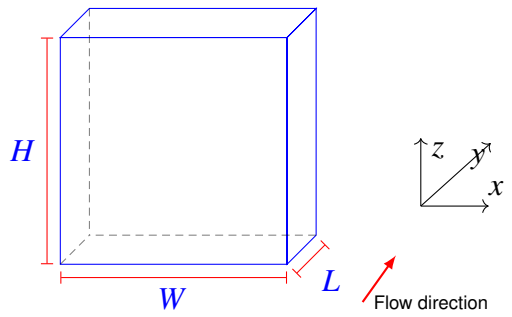

Figure 7.1: The square duct.

7.2 The exact solutions for duct flow

7.2.1 The exact solution under no-slip boundary conditions

The exact solution with no-slip boundary condition [30] at the South, North, East and West walls is

$$u_y = \frac{U_c}{4}\left(\frac{1}{2}(1-z^2) - \frac{16}{\pi^3}\frac{\sum_{n=1}^{\infty}(-1)^n \cosh\left(((2n+1)\pi x/2)\right)\cos\left(((2n+1)\pi z/2)\right)}{(2n+1)^3\cosh\left(((2n+1)\pi/2)\right)}\right), \tag{7.2.1}$$

where $G_y = (2U_c\nu\pi^3/16H^2)$ in which $H = n_z$ is the height of the channel or computational grid size at z-direction, $W = n_x$ is the width of the channel or computational grid size at x-direction and $x = (2i/n_x) - 1$, $z = (2l/n_z) - 1$ where $i = 0,...,n_x$ and $l = 0,...,n_z$.

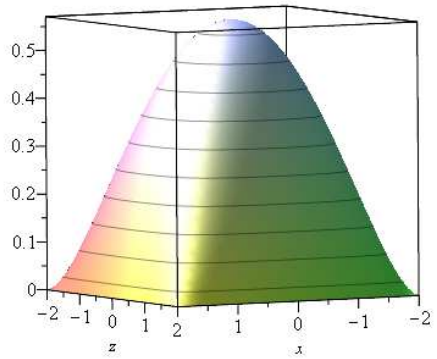

Figure 7.2: The exact solution u_y with no-slip boundary conditions.

7.2.2 The exact solution under Navier-slip boundary conditions

The general exact solution with Navier-slip boundary conditions at these four same walls is

$$u_y = U_c\left[\sum_{n=1}^{\infty} D_n \cosh(A_4\beta_n z)\cos(\beta_n x) - \frac{4x^2 - 1 - 4A_1\theta_u K_n}{A_1^2 8}\right], \tag{7.2.2}$$

where z is defined as $z = (l/n_z) - 0.5$, $l = 0,...,n_z$, $x = (i/n_x) - 0.5$, $i = 0,...,n_x$, $A_1 = \frac{D_h}{H}$, $A_2 = \frac{D_h}{W}$, $A_4 = \frac{A_1}{A_2}$, $Re = \frac{\rho_0 U_c D_h}{\mu}$ in which $D_h = \frac{2WH}{W+H}$ is the hydrodynamic diameter, $\theta_u = \frac{2-\sigma_u}{\sigma_u}$, $\sigma_u = 1$ is a momentum accommodation coefficient, the

dimensionless slip length is $K_n = \frac{l_s}{D_h}$ in which the length slip or mean free path is $l_s = D_h K_n$ and

$$D_n = \frac{4\sin(\frac{1}{2}\beta_n)}{A_1^2\beta_n^2\left[A_1\beta_n\theta_u K_n\sinh(\frac{1}{2}A_4\beta_n)+\cosh(\frac{1}{2}A_4\beta_n)\right]}\frac{1}{\sin(\beta_n)+\beta_n}, \tag{7.2.3}$$

where β_n are roots for $\beta_n\tan(\beta_n) = \frac{1}{A_1\beta_n K_n}$. The body force is $G_y = (U_c\nu {D_h}^2)$. The exact solution is similar to the exact solution in Khasawneh *et. al* [1].

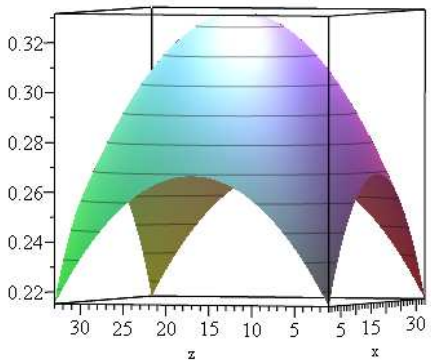

Figure 7.3: The exact solution u_y with Navier-slip boundary conditions.

The exact solution under no-slip and Navier-slip boundary conditions is in two dimensions due to it being based only on x- and z-direction. Note that the exact solution under no-slip and Navier-slip boundary conditions is independent of the Reynolds number Re.

7.2.3 Duct flow under Navier-slip boundary conditions

In this application, moment-based boundary conditions are used on the four walls at West, East, South and North to execute Navier-slip boundary conditions. Periodic boundary conditions are applied at the inlet and outlet, and the flow is driven by body force in y-direction. On the walls, the velocity in y-direction is assumed to be slip velocity and to be zero velocity in the x- and z-direction, so

$$u_x = u_z = 0, u_y = u_{sy}. \tag{7.2.4}$$

The body force is in y-direction $\mathbf{F} = (\rho G_x, \rho G_y, \rho G_z) = (0, \rho G_y, 0)$, so,

$$\begin{aligned}
\rho u_x &= \rho u_z = 0, \\
\rho u_y &= \rho u_{sy}, \\
\Pi^0_{xx} &= \frac{\rho}{3}\delta_{xx} + \rho u_x u_x = \frac{\rho}{3}, \\
\Pi^0_{yy} &= \frac{\rho}{3}\delta_{yy} + \rho u_y u_y = \frac{\rho}{3} + \rho u^2_{sy}, \\
\Pi^0_{zz} &= \frac{\rho}{3}\delta_{zz} + \rho u_z u_z = \frac{\rho}{3}.
\end{aligned} \tag{7.2.5}$$

In addition, from the Chapman-Enskog expansion in section (3.2) we know that

$$\Pi_{xx} = \Pi^0_{xx} + \tau\Pi^1_{xx} = \frac{\rho}{3} - \tau\frac{2\rho}{3}\partial_x u_x = \frac{\rho}{3},$$

$$\Pi_{yy} = \Pi^0_{yy} + \tau\Pi^1_{yy} = \frac{\rho}{3} + \rho u^2_{sy} - \tau\frac{2\rho}{3}\partial_y u_y = \frac{\rho}{3} + \rho u^2_{sy},$$

$$\Pi_{zz} = \Pi^0_{zz} + \tau\Pi^1_{zz} = \frac{\rho}{3} - \tau\frac{2\rho}{3}\partial_z u_z = \frac{\rho}{3},$$

so,

$$\begin{aligned}
\rho\overline{u}_x &= \rho u_x - \frac{\delta_t}{2}\rho G_x = 0, \\
\rho\overline{u}_y &= \rho u_y - \frac{\delta_t}{2}\rho G_y = \rho u_{sy} - \frac{\delta_t}{2}\rho G_y, \\
\rho\overline{u}_z &= \rho u_z - \frac{\delta_t}{2}\rho G_z = 0, \\
\overline{\Pi}_{xx} &= \Pi_{xx} + \frac{\delta_t}{2\tau}\Pi_{xx} - \frac{\delta_t}{2\tau}\Pi^0_{xx} - \frac{\delta_t}{2}(\rho G_x u_x + u_x \rho G_x) = \frac{\rho}{3}, \\
\overline{\Pi}_{yy} &= \Pi_{yy} + \frac{\delta_t}{2\tau}\Pi_{yy} - \frac{\delta_t}{2\tau}\Pi^0_{yy} - \frac{\delta_t}{2}(\rho G_y u_y + u_y \rho G_y) = \frac{\rho}{3} + \rho u^2_{sy} - \delta_t \rho G_y, \\
\overline{\Pi}_{zz} &= \Pi_{zz} + \frac{\delta_t}{2\tau}\Pi_{zz} - \frac{\delta_t}{2\tau}\Pi^0_{zz} - \frac{\delta_t}{2}(\rho G_z u_z + u_z \rho G_z) = \frac{\rho}{3}.
\end{aligned} \tag{7.2.6}$$

To find the unknown distribution functions at the South and North faces we

use five moments which are:

$$\begin{aligned}
\rho\overline{u}_x &= \overline{f}_1-\overline{f}_2+\overline{f}_7-\overline{f}_8-\overline{f}_9+\overline{f}_{10}+\overline{f}_{11}+\overline{f}_{12}-\overline{f}_{13}-\overline{f}_{14}=0,\\
\rho\overline{u}_y &= \overline{f}_3-\overline{f}_4+\overline{f}_7+\overline{f}_8-\overline{f}_9-\overline{f}_{10}+\overline{f}_{15}+\overline{f}_{16}-\overline{f}_{17}-\overline{f}_{18}=\rho u_{sy}-\frac{\delta_t}{2}\rho G_y,\\
\rho\overline{u}_z &= \overline{f}_5-\overline{f}_6+\overline{f}_{11}-\overline{f}_{12}-\overline{f}_{13}+\overline{f}_{14}+\overline{f}_{15}-\overline{f}_{16}-\overline{f}_{17}+\overline{f}_{18}=0,\\
\overline{\Pi}_{xx} &= \overline{f}_1+\overline{f}_2+\overline{f}_7+\overline{f}_8+\overline{f}_9+\overline{f}_{10}+\overline{f}_{11}+\overline{f}_{12}+\overline{f}_{13}+\overline{f}_{14}=\frac{\rho}{3},\\
\overline{\Pi}_{yy} &= \overline{f}_3+\overline{f}_4+\overline{f}_7+\overline{f}_8+\overline{f}_9+\overline{f}_{10}+\overline{f}_{15}+\overline{f}_{16}+\overline{f}_{17}+\overline{f}_{18}=\frac{\rho}{3}+\rho u_{sy}^2-\delta_t\rho G_y,
\end{aligned} \tag{7.2.7}$$

and the unknown distribution functions at the South face are

$$\overline{f}_5,\overline{f}_{11},\overline{f}_{14},\overline{f}_{15},\overline{f}_{18}. \tag{7.2.8}$$

This system (7.2.7) is solved to find the unknown distribution functions at the South face, which are

$$\begin{aligned}
\overline{f}_5 &= \overline{f}_1+\overline{f}_2+\overline{f}_3+\overline{f}_4+\overline{f}_6+2\overline{f}_7+2\overline{f}_8+2\overline{f}_9+2\overline{f}_{10}+2\overline{f}_{12}+2\overline{f}_{13}+\\
&\quad 2\overline{f}_{16}+2\overline{f}_{17}-\frac{2}{3}\rho+\delta_t\rho G_y u_{sy}-\rho u_{sy}^2,\\
\overline{f}_{11} &= -\overline{f}_1-\overline{f}_7-\overline{f}_{10}-\overline{f}_{12}+\frac{\rho}{6},\\
\overline{f}_{14} &= -\overline{f}_2-\overline{f}_8-\overline{f}_9-\overline{f}_{13}+\frac{\rho}{6},\\
\overline{f}_{15} &= -\overline{f}_3-\overline{f}_7-\overline{f}_8-\overline{f}_{16}+\frac{\rho}{6}-\frac{\delta_t}{4}\rho G_y-\frac{\delta_t}{2}\rho G_y u_{sy}+\frac{1}{2}\rho u_{sy}+\frac{1}{2}\rho u_{sy}^2,\\
\overline{f}_{18} &= -\overline{f}_4-\overline{f}_9-\overline{f}_{10}-\overline{f}_{17}+\frac{\rho}{6}+\frac{\delta_t}{4}\rho G_y-\frac{\delta_t}{2}\rho G_y u_{sy}-\frac{1}{2}\rho u_{sy}+\frac{1}{2}\rho u_{sy}^2,
\end{aligned} \tag{7.2.9}$$

and the density is found from the known distribution functions

$$\rho=\overline{f}_0+\overline{f}_1+\overline{f}_2+\overline{f}_3+\overline{f}_4+2\overline{f}_6+\overline{f}_7+\overline{f}_8+\overline{f}_9+\overline{f}_{10}+2\overline{f}_{12}+2\overline{f}_{13}+2\overline{f}_{16}+2\overline{f}_{17}. \tag{7.2.10}$$

Now we have to find the slip velocity u_{sy} in the case of $u_y=u_{wall}=u_{sy}$ and

$u_x = u_z = 0$. The equilibrium shear stress is

$$\Pi^0_{yz} = \frac{\rho}{3}\delta_{yz} + \rho u_y u_z = 0 \tag{7.2.11}$$

and

$$\begin{aligned}
\overline{\Pi}_{yz} &= \Pi_{yz} + \frac{\delta_t}{2\tau}\Pi_{yz} - \frac{\delta_t}{2\tau}\Pi^0_{yz} - \frac{\delta_t}{2}\rho\left(G_y u_z + u_y G_z\right) \text{ in which } u_y = u_{sy}, \\
&= \Pi_{yz} + \frac{\delta_t}{2\tau}\Pi_{yz}, \\
\overline{\Pi}_{yz} &= \frac{2\tau+1}{2\tau}\Pi_{yz}, \\
\left(\overline{f}_{15} - \overline{f}_{16} + \overline{f}_{17} - \overline{f}_{18}\right) &= \frac{2\tau+1}{2\tau}\Pi_{yz}.
\end{aligned} \tag{7.2.12}$$

We know that the slip velocity is proportional to the shear stress at the south wall as explained in section (4.5), so $u_s = l_s \partial_n u_{wall}$ $n \lesseqgtr 0$, and using the Chapman-Enskog expansion in section (3.2),

$$\Pi_{yz} = \Pi^0_{yz} + \tau\Pi^1_{yz} = \frac{\rho}{3}\delta_{yz} + \rho u_y u_z - \tau\frac{\rho}{3}(\partial_y u_z + \partial_z u_y) = -\mu\partial_z u_y, \tag{7.2.13}$$

so,

$$u_{sy} = -l_s\partial_z u_y = -\partial_z u_{wall} \tag{7.2.14}$$

and

$$\begin{aligned}
\Pi_{yz} &= \frac{-\mu}{l_s}u_{sy}, \\
u_{sy} &= \frac{-l_s}{\mu}\Pi_{yz}, \\
u_{sy} &= \frac{-l_s}{\mu}\frac{2\tau}{2\tau+1}\overline{\Pi}_{yz}, \\
u_{sy} &= \frac{-l_s}{\mu}\frac{2\tau}{2\tau+1}\left(\overline{f}_{15} - \overline{f}_{16} + \overline{f}_{17} - \overline{f}_{18}\right), \\
u_{sy} &= \frac{-6l_s}{\rho(2\tau+1)}\left(\overline{f}_{15} - \overline{f}_{16} + \overline{f}_{17} - \overline{f}_{18}\right).
\end{aligned} \tag{7.2.15, 7.2.16}$$

At the South wall the shear stress is positive, so $u_s = -l_s\partial_n u_{wall}$, $n > 0$ and $u_{sy} =$

$\frac{-l_s}{\mu}\Pi_{yz}$. Thus

$$u_{sy} = \left(\frac{-6l_s}{\rho(2\tau+1)}\right)\left(\overline{f}_{15} - \overline{f}_{16} + \overline{f}_{17} - \overline{f}_{18}\right), \tag{7.2.17}$$

and by substituting the distribution functions $\overline{f}_{15}$ and $\overline{f}_{18}$ into Eq (7.2.17), the final form for the slip velocity will be

$$u_{sy} = \frac{6l_s}{\rho(6l_s+2\tau+1)}\left(-\frac{\delta_t}{2}\rho G_y - \overline{f}_3 + \overline{f}_4 - \overline{f}_7 - \overline{f}_8 + \overline{f}_9 + \overline{f}_{10} - 2\overline{f}_{16} + 2\overline{f}_{17}\right). \tag{7.2.18}$$

The unknown distribution functions at the North face are found by again solving system (7.2.7). The slip velocity requires the use of the relations $u_s = l_s\partial_n u_{wall}$ and $u_{sy} = \frac{l_s}{\mu}\Pi_{yz}$, because shear stress is negative toward the North wall.

To find the unknown distribution functions at the East and West faces we use another five moments which are

$$\begin{aligned}
&\rho\overline{u}_x = \overline{f}_1 - \overline{f}_2 + \overline{f}_7 - \overline{f}_8 - \overline{f}_9 + \overline{f}_{10} + \overline{f}_{11} + \overline{f}_{12} - \overline{f}_{13} - \overline{f}_{14} = 0,\\
&\rho\overline{u}_y = \overline{f}_3 - \overline{f}_4 + \overline{f}_7 + \overline{f}_8 - \overline{f}_9 - \overline{f}_{10} + \overline{f}_{15} + \overline{f}_{16} - \overline{f}_{17} - \overline{f}_{18} = \rho u_{sy} - \frac{\delta_t}{2}\rho G_y,\\
&\rho\overline{u}_z = \overline{f}_5 - \overline{f}_6 + \overline{f}_{11} - \overline{f}_{12} - \overline{f}_{13} + \overline{f}_{14} + \overline{f}_{15} - \overline{f}_{16} - \overline{f}_{17} + \overline{f}_{18} = 0,\\
&\overline{\Pi}_{yy} = \overline{f}_3 + \overline{f}_4 + \overline{f}_7 + \overline{f}_8 + \overline{f}_9 + \overline{f}_{10} + \overline{f}_{15} + \overline{f}_{16} + \overline{f}_{17} + \overline{f}_{18} = \frac{\rho}{3} + \rho u_{sy}^2 - \delta_t\rho G_y,\\
&\overline{\Pi}_{zz} = \overline{f}_5 + \overline{f}_6 + \overline{f}_{11} + \overline{f}_{12} + \overline{f}_{13} + \overline{f}_{14} + \overline{f}_{15} + \overline{f}_{16} + \overline{f}_{17} + \overline{f}_{18} = \frac{\rho}{3}.
\end{aligned} \tag{7.2.19}$$

The unknown distribution functions at the West face are

$$\overline{f}_1, \overline{f}_7, \overline{f}_{10}, \overline{f}_{11}, \overline{f}_{12} \tag{7.2.20}$$

which are found by solving system (7.2.19)

$$\begin{aligned}
\overline{f}_1 &= \overline{f}_2+\overline{f}_3+\overline{f}_4+\overline{f}_5+\overline{f}_6+2\overline{f}_8+2\overline{f}_9+2\overline{f}_{13}+2\overline{f}_{14}+2\overline{f}_{15}\\
&\quad +2\overline{f}_{16}+2\overline{f}_{17}+\overline{f}_{18}-\frac{2}{3}\rho+\delta_t\rho G_y u_{sy}-\rho u_{sy}^2,\\
\overline{f}_7 &= -\overline{f}_3-\overline{f}_8-\overline{f}_{15}-\overline{f}_{16}+\frac{\rho}{6}-\frac{\delta_t}{4}\rho G_y-\frac{\delta_t}{2}\rho G_y u_{sy}+\frac{1}{2}\rho u_{sy}+\frac{1}{2}\rho u_{sy}^2,\\
\overline{f}_{10} &= -\overline{f}_4-\overline{f}_9-\overline{f}_{17}-\overline{f}_{18}+\frac{\rho}{6}+\frac{\delta_t}{4}\rho G_y-\frac{\delta_t}{2}\rho G_y u_{sy}-\frac{1}{2}\rho u_{sy}+\frac{1}{2}\rho u_{sy}^2,\\
\overline{f}_{11} &= -\overline{f}_5-\overline{f}_{14}-\overline{f}_{15}-\overline{f}_{18}+\frac{\rho}{6},\\
\overline{f}_{12} &= -\overline{f}_6-\overline{f}_{13}-\overline{f}_{16}-\overline{f}_{17}+\frac{\rho}{6},
\end{aligned} \tag{7.2.21}$$

and the density is found from the known distribution functions

$$\rho = \overline{f}_0+2\overline{f}_2+\overline{f}_3+\overline{f}_4+\overline{f}_5+\overline{f}_6+2\overline{f}_8+2\overline{f}_9+2\overline{f}_{13}+2\overline{f}_{14}+\overline{f}_{15}+\overline{f}_{16}+\overline{f}_{17}+\overline{f}_{18}. \tag{7.2.22}$$

The slip velocity at the West wall is again found by using the shear stress Π_{xy} and the relations $\Pi_{xy}=-\mu\partial_y u_{wall}$ and $u_s=-\frac{l_s}{\mu}\Pi_{xy}$, because shear stress Π_{xy} increases toward the West wall. From Chapman-Enskog the shear stress is defined as

$$\Pi_{xy}=\Pi_{xy}^0+\tau\Pi_{xy}^1=\frac{\rho}{3}\delta_{xy}+\rho u_x u_y+\tau\frac{-\rho}{3}\left(\partial_x u_y+\partial_y u_x\right)=\tau\frac{-\rho}{3}\partial_x u_y=-\mu\partial_x u_y.$$

Thus

$$\begin{aligned}
u_s &= -\frac{l_s}{\mu}\Pi_{xy},\\
u_{sy} &= \frac{-l_s}{\mu}\frac{2\tau}{2\tau+1}\overline{\Pi}_{xy},\\
u_{sy} &= \frac{-l_s}{\mu}\frac{2\tau}{2\tau+1}\left(\overline{f}_7-\overline{f}_8+\overline{f}_9-\overline{f}_{10}\right),\\
u_{sy} &= \frac{-6l_s}{\rho(2\tau+1)}\left(\overline{f}_7-\overline{f}_8+\overline{f}_9-\overline{f}_{10}\right).
\end{aligned} \tag{7.2.23}$$

By substituting the distribution functions $\overline{f}_7$ and $\overline{f}_{10}$ into Eq (7.2.23), the final form

for the slip velocity will be

$$u_{sy} = \frac{6l_s}{\rho(6l_s+2\tau+1)}\left(\frac{\delta_t}{2}\rho G_y + \overline{f}_3 - \overline{f}_4 + 2\overline{f}_8 - 2\overline{f}_9 + \overline{f}_{15} + \overline{f}_{16} - \overline{f}_{17} - \overline{f}_{18}\right). \tag{7.2.24}$$

The unknown distribution functions at the East face are found by solving system 7.2.19. The slip velocity is found by using Π_{xy} and the relations $\Pi_{xy} = \mu\partial_y u_{wall}$ and $u_s = \frac{l_s}{\mu}\Pi_{xy}$, because shear stress Π_{xy} decreases toward the East wall.

To find the unknown distribution functions at the four edges, under moment boundary conditions, we choose nine moments which in this case are

$$\begin{aligned}
\rho\overline{u}_x &= \rho u_x - \frac{\delta_t}{2}\rho G_x = 0,\\
\rho\overline{u}_y &= \rho u_y - \frac{\delta_t}{2}\rho G_y = \rho u_{sy} - \frac{\delta_t}{2}\rho G_y,\\
\rho\overline{u}_z &= \rho u_z - \frac{\delta_t}{2}\rho G_z = 0,\\
\overline{\Pi}_{xx} &= \Pi_{xx} + \frac{\delta_t}{2\tau}\Pi_{xx} - \frac{\delta_t}{2\tau}\Pi^0_{xx} - \frac{\delta_t}{2}\left(\rho G_x u_x + u_x\rho G_x\right) = \frac{\rho}{3},\\
\overline{\Pi}_{yy} &= \Pi_{yy} + \frac{\delta_t}{2\tau}\Pi_{yy} - \frac{\delta_t}{2\tau}\Pi^0_{yy} - \frac{\delta_t}{2}\left(\rho G_y u_y + u_y\rho G_y\right) = \frac{\rho}{3} + \rho u_{sy}^2 - \delta_t\rho G_y,\\
\overline{\Pi}_{zz} &= \Pi_{zz} + \frac{\delta_t}{2\tau}\Pi_{zz} - \frac{\delta_t}{2\tau}\Pi^0_{zz} - \frac{\delta_t}{2}\left(\rho G_z u_z + u_z\rho G_z\right) = \frac{\rho}{3},\\
\overline{\Pi}_{xz} &= \Pi_{xz} + \frac{\delta_t}{2\tau}\Pi_{xz} - \frac{\delta_t}{2\tau}\Pi^0_{xz} - \frac{\delta_t}{2}\left(\rho G_z u_x + u_z\rho G_x\right) = 0,\\
\overline{\Pi}_{xy} &= \Pi_{xy} + \frac{\delta_t}{2\tau}\Pi_{xy} - \frac{\delta_t}{2\tau}\Pi^0_{xy} - \frac{\delta_t}{2}\left(\rho G_y u_x + u_y\rho G_x\right) = \frac{-\rho}{3}\left(\frac{2\tau+\delta_t}{2}\right)\partial_x u_y\\
&= \frac{-\rho}{3}\left(\frac{2\tau+\delta_t}{2}\right)\frac{\pm u_{sy}}{l_s},\\
\overline{Q}_{xyy} &= Q_{xyy} + \frac{\delta_t}{2\tau}Q_{xyy} - \frac{\delta_t}{2\tau}Q^0_{xyy} - \frac{\delta_t}{2}\frac{\rho}{3}G_x = \frac{\rho}{3}\left(\frac{2\tau+\delta_t}{2}\right)\left(\left(\partial_x u_y\right)u_y\right)\\
&= \overline{\Pi}_{xy}u_{sy},
\end{aligned} \tag{7.2.25}$$

where the shear stress Π_{xy} and Π_{xz} is defined as

$$\Pi_{xy} = \Pi^0_{xy} + \tau\Pi^1_{xy} = \frac{\rho}{3}\delta_{xy} + \rho u_x u_y + \tau\frac{-\rho}{3}\left(\partial_x u_y + \partial_y u_x\right) = \tau\frac{-\rho}{3}\partial_x u_y, \tag{7.2.26}$$

$$\Pi_{xz} = \Pi^0_{xz} + \tau\Pi^1_{xz} = \frac{\rho}{3}\delta_{xz} + \rho u_x u_z + \tau\frac{-\rho}{3}\left(\partial_x u_z + \partial_z u_x\right) = 0, \tag{7.2.27}$$

and equilibrium third moment Q^0_{xyy} and the third moment Q_{xyy} are defined as

$$Q^0_{xyy} = \frac{\rho}{3}u_x = 0, Q^1_{xyy} = \frac{\rho}{3}\left(\partial_x u_y^2 - u_y \partial_x u_y\right) = \frac{\rho}{3}\left(\left(\partial_x u_y\right) u_y\right), \tag{7.2.28}$$

$$Q_{xyy} = Q^0_{xyy} + \tau Q^1_{xyy} = \tau\frac{\rho}{3}\left(\left(\partial_x u_y\right) u_y\right), \sum_0^{18} c_{ix}c_{iy}c_{iy}F_i = \frac{\rho}{3}G_x = 0, \tag{7.2.29}$$

for more detail how we calculate the $\overline{Q}_{xyy}$ see the Appendix (A). So, the nine-moment system for the four edges will be

$$\begin{aligned}
&\rho\overline{u}_x = \overline{f}_1 - \overline{f}_2 + \overline{f}_7 - \overline{f}_8 - \overline{f}_9 + \overline{f}_{10} + \overline{f}_{11} + \overline{f}_{12} - \overline{f}_{13} - \overline{f}_{14} = 0,\\
&\rho\overline{u}_y = \overline{f}_3 - \overline{f}_4 + \overline{f}_7 + \overline{f}_8 - \overline{f}_9 - \overline{f}_{10} + \overline{f}_{15} + \overline{f}_{16} - \overline{f}_{17} - \overline{f}_{18} = \rho u_{sy} - \frac{\delta_t}{2}\rho G_y,\\
&\rho\overline{u}_z = \overline{f}_5 - \overline{f}_6 + \overline{f}_{11} - \overline{f}_{12} - \overline{f}_{13} + \overline{f}_{14} + \overline{f}_{15} - \overline{f}_{16} - \overline{f}_{17} + \overline{f}_{18} = 0,\\
&\overline{\Pi}_{xx} = \overline{f}_1 + \overline{f}_2 + \overline{f}_7 + \overline{f}_8 + \overline{f}_9 + \overline{f}_{10} + \overline{f}_{11} + \overline{f}_{12} + \overline{f}_{13} + \overline{f}_{14} = \frac{\rho}{3},\\
&\overline{\Pi}_{yy} = \overline{f}_3 + \overline{f}_4 + \overline{f}_7 + \overline{f}_8 + \overline{f}_9 + \overline{f}_{10} + \overline{f}_{15} + \overline{f}_{16} + \overline{f}_{17} + \overline{f}_{18} = \frac{\rho}{3} + \rho u_{sy}^2 - \delta_t\rho G_y,\\
&\overline{\Pi}_{zz} = \overline{f}_5 + \overline{f}_6 + \overline{f}_{11} + \overline{f}_{12} + \overline{f}_{13} + \overline{f}_{14} + \overline{f}_{15} + \overline{f}_{16} + \overline{f}_{17} + \overline{f}_{18} = \frac{\rho}{3},\\
&\overline{\Pi}_{xz} = \overline{f}_{11} - \overline{f}_{12} + \overline{f}_{13} - \overline{f}_{14} = 0,\\
&\overline{\Pi}_{xy} = \overline{f}_7 - \overline{f}_8 + \overline{f}_9 - \overline{f}_{10} = \frac{-\rho}{3}\left(\frac{2\tau + \delta_t}{2}\right)\frac{\pm u_{sy}}{l_s},\\
&\overline{Q}_{xyy} = \overline{f}_7 - \overline{f}_8 - \overline{f}_9 + \overline{f}_{10} = \overline{\Pi}_{xy}u_{sy}.
\end{aligned} \tag{7.2.30}$$

As the example below uses the South West edge, we must note that at the West wall the shear stress Π_{xy} increases toward the wall, and thus,

$$\overline{\Pi}_{xy} = \frac{-\rho}{3}\left(\frac{2\tau + \delta_t}{2}\right)\frac{u_{sy}}{l_s}. \tag{7.2.31}$$

Then, by solving the above system Eq (7.2.30) using Eq (7.2.31), the unknown distribution functions at the either the South West or North West edges can be found. For example, at the South West these are

$$\overline{f}_1, \overline{f}_5, \overline{f}_7, \overline{f}_{10}, \overline{f}_{11}, \overline{f}_{12}, \overline{f}_{14}, \overline{f}_{15}, \overline{f}_{18}, \tag{7.2.32}$$

so using Eqs (7.2.30) and (7.2.31), we find that the unknown distribution functions

at the South West edge are

$$
\begin{aligned}
\overline{f}_1 &= \overline{f}_2 + 2\overline{f}_6 + 4\overline{f}_{13} + 2\overline{f}_{16} + 2\overline{f}_{17} - \frac{\rho}{3} - \frac{\rho\,(2\tau+1)}{6}\frac{u_{sy}^2}{l_s},\\
\overline{f}_5 &= 2\overline{f}_2 + \overline{f}_3 + \overline{f}_4 + \overline{f}_6 + 4\overline{f}_8 + 4\overline{f}_9 + 4\overline{f}_{13} + 2\overline{f}_{16} + 2\overline{f}_{17} - \frac{2}{3}\rho\\
&\quad + \delta_t \rho G_y u_{sy} - \rho u_{sy}^2 + \frac{\rho\,(2\tau+1)}{6}\frac{u_{sy}^2}{l_s},\\
\overline{f}_7 &= \overline{f}_8 + \frac{\rho\,(2\tau+1)}{12}\frac{u_{sy}^2}{l_s} - \frac{\rho\,(2\tau+1)}{12}\frac{u_{sy}}{l_s},\\
\overline{f}_{10} &= \overline{f}_9 + \frac{\rho\,(2\tau+1)}{12}\frac{u_{sy}^2}{l_s} + \frac{\rho\,(2\tau+1)}{12}\frac{u_{sy}}{l_s},\\
\overline{f}_{11} &= -\overline{f}_2 - \overline{f}_6 - \overline{f}_8 - \overline{f}_9 - 3\overline{f}_{13} - \overline{f}_{16} - \overline{f}_{17} + \frac{\rho}{3},\\
\overline{f}_{12} &= -\overline{f}_6 - \overline{f}_{13} - \overline{f}_{16} - \overline{f}_{17} + \frac{\rho}{6},\\
\overline{f}_{14} &= -\overline{f}_2 - \overline{f}_8 - \overline{f}_9 - \overline{f}_{13} + \frac{\rho}{6},\\
\overline{f}_{15} &= -\overline{f}_3 - 2\overline{f}_8 - \overline{f}_{16} + \frac{\rho}{6} - \frac{\delta_t}{4}\rho G_y - \frac{\delta_t}{2}\rho G_y u_{sy} + \frac{1}{2}\rho u_{sy} + \frac{1}{2}\rho u_{sy}^2,\\
&\quad - \frac{\rho\,(2\tau+1)}{12}\frac{u_{sy}^2}{l_s} + \frac{\rho\,(2\tau+1)}{12}\frac{u_{sy}}{l_s},\\
\overline{f}_{18} &= -\overline{f}_4 - 2\overline{f}_9 - \overline{f}_{17} + \frac{\rho}{6} + \frac{\delta_t}{4}\rho G_y - \frac{\delta_t}{2}\rho G_y u_{sy} - \frac{1}{2}\rho u_{sy} + \frac{1}{2}\rho u_{sy}^2,\\
&\quad - \frac{\rho\,(2\tau+1)}{12}\frac{u_{sy}^2}{l_s} - \frac{\rho\,(2\tau+1)}{12}\frac{u_{sy}}{l_s}.
\end{aligned}
\tag{7.2.33}
$$

The density is found from the known distribution functions

$$
\rho = \overline{f}_0 + 2\overline{f}_2 + \overline{f}_3 + \overline{f}_4 + 2\overline{f}_6 + 2\overline{f}_8 + 2\overline{f}_9 + 4\overline{f}_{13} + 2\overline{f}_{16} + 2\overline{f}_{17}, \tag{7.2.34}
$$

and the slip velocity at the South wall is once again found using the shear stress Π_{yz} and the relations $\Pi_{yz} = -\mu\partial_y u_{wall}$ and $u_s = -\dfrac{l_s}{\mu}\Pi_{yz}$, because again the shear stress Π_{yz} increases toward the South wall. The same procedure seen in the example for the South face, Eq (7.2.17), is used to find the slip velocity for the South West edge

$$
u_{sy} = \frac{6l_s}{\rho(6l_s + 4\tau + 2)}\left(\frac{\delta_t}{2}\rho G_y + \overline{f}_3 - \overline{f}_4 + 2\overline{f}_8 - 2\overline{f}_9 + 2\overline{f}_{16} - 2\overline{f}_{17}\right). \tag{7.2.35}
$$

Moving on to the South East and North East edges, we now note again that at

the East wall the shear stress Π_{xy} is decreased toward the East wall thus,

$$\overline{\Pi}_{xy} = \frac{\rho}{3}\left(\frac{2\tau+\delta_t}{2}\right)\frac{u_{sy}}{l_s}. \tag{7.2.36}$$

By solving the system of Eq (7.2.30) but now with Eq (7.2.36) we can find the unknown distribution functions at either the South East or North East edges. For example, the unknown distribution functions at South East edge are

$$\overline{f}_2, \overline{f}_5, \overline{f}_8, \overline{f}_9, \overline{f}_{11}, \overline{f}_{13}, \overline{f}_{14}, \overline{f}_{15}, \overline{f}_{18}. \tag{7.2.37}$$

which we solve using Eqs (7.2.30) and (7.2.36) to give the unknown distribution functions at South East edge, which are

$$\begin{aligned}
\overline{f}_2 &= \overline{f}_1 + 2\overline{f}_6 + 4\overline{f}_{12} + 2\overline{f}_{16} + 2\overline{f}_{17} - \frac{\rho}{3} + \frac{\rho\,(2\tau+1)}{6}\frac{u_{sy}^2}{l_s},\\
\overline{f}_5 &= 2\overline{f}_1 + \overline{f}_3 + \overline{f}_4 + \overline{f}_6 + 4\overline{f}_7 + 4\overline{f}_{10} + 4\overline{f}_{12} + 2\overline{f}_{16} + 2\overline{f}_{17} - \frac{2}{3}\rho\\
&\quad + \delta_t\rho G_y u_{sy} - \rho u_{sy}^2 - \frac{\rho\,(2\tau+1)}{6}\frac{u_{sy}^2}{l_s},\\
\overline{f}_8 &= \overline{f}_7 - \frac{\rho\,(2\tau+1)}{12}\frac{u_{sy}^2}{l_s} - \frac{\rho\,(2\tau+1)}{12}\frac{u_{sy}}{l_s},\\
\overline{f}_9 &= \overline{f}_{10} - \frac{\rho\,(2\tau+1)}{12}\frac{u_{sy}^2}{l_s} + \frac{\rho\,(2\tau+1)}{12}\frac{u_{sy}}{l_s},\\
\overline{f}_{11} &= -\overline{f}_1 - \overline{f}_7 - \overline{f}_{10} - \overline{f}_{12} + \frac{\rho}{6},\\
\overline{f}_{13} &= -\overline{f}_6 - \overline{f}_{12} - \overline{f}_{16} - \overline{f}_{17} + \frac{\rho}{6},\\
\overline{f}_{14} &= -\overline{f}_1 - \overline{f}_6 - \overline{f}_7 - \overline{f}_{10} - 3\overline{f}_{12} - \overline{f}_{16} - \overline{f}_{17} + \frac{\rho}{3},\\
\overline{f}_{15} &= -\overline{f}_3 - 2\overline{f}_7 - \overline{f}_{16} + \frac{\rho}{6} - \frac{\delta_t}{4}\rho G_y - \frac{\delta_t}{2}\rho G_y u_{sy} + \frac{1}{2}\rho u_{sy} + \frac{1}{2}\rho u_{sy}^2\\
&\quad + \frac{\rho\,(2\tau+1)}{12}\frac{u_{sy}^2}{l_s} + \frac{\rho\,(2\tau+1)}{12}\frac{u_{sy}}{l_s},\\
\overline{f}_{18} &= -\overline{f}_4 - 2\overline{f}_{10} - \overline{f}_{17} + \frac{\rho}{6} + \frac{\delta_t}{4}\rho G_y - \frac{\delta_t}{2}\rho G_y u_{sy} - \frac{1}{2}\rho u_{sy} + \frac{1}{2}\rho u_{sy}^2\\
&\quad + \frac{\rho\,(2\tau+1)}{12}\frac{u_{sy}^2}{l_s} - \frac{\rho\,(2\tau+1)}{12}\frac{u_{sy}}{l_s}.
\end{aligned} \tag{7.2.38}$$

The density is found from known distribution functions,

$$\rho = \overline{f}_0 + 2\overline{f}_1 + \overline{f}_3 + \overline{f}_4 + 2\overline{f}_6 + 2\overline{f}_7 + 2\overline{f}_{10} + 4\overline{f}_{12} + 2\overline{f}_{16} + 2\overline{f}_{17}, \tag{7.2.39}$$

and the slip velocity is found by following the same procedure used previously, but now using the shear stress Π_{yz} with the relations $\Pi_{yz} = -\mu\partial_y u_{wall}$ and $u_s = -\frac{l_s}{\mu}\Pi_{yz}$ because the shear stress Π_{yz} increases toward the South wall, hence

$$u_{sy} = \frac{-6l_s}{\rho(6l_s + 4\tau + 2)}\left(-\frac{\delta_t}{2}\rho G_y - \overline{f}_3 + \overline{f}_4 - 2\overline{f}_7 + 2\overline{f}_{10} - 2\overline{f}_{16} + 2\overline{f}_{17}\right). \tag{7.2.40}$$

The moment boundary conditions under no-slip boundary conditions are again obtained by set $u_x = u_y = u_z = 0$ and following the same steps for moment boundary conditions under Navier-slip boundary condition.

7.3 Simulation

In this simulation, we use diffusive scaling where the centreline velocity is $U_c = 0.1$. The choice of grid sizes in x- and z-direction are $n_x = n_z = 16, 32, 64, 128$ and the grid sizes in y-direction is $n_y = 2$. The aspect ratio is $Ar = 1$, so the hydrodynamic diameter is $D_h = H$, and the flow is in y-direction. The velocity profile is examined at the centreline of the channel *i.e.* at $n_x/2$ and $n_z/2$.

The convergence is then examined by calculating the norm error between the velocity profile of the LBM and the velocity of the exact solution. A single relaxation time method is used in this examination, for which three different relaxation times are selected, namely: $\tau = 0.1, 0.6, 6$. The norm error is defined as

$$\| \overline{L}(y) \|_2 \quad = \quad \sqrt{\frac{1}{n_z}\sum |\mathbf{u}_{LBM}(x,y,z) - \mathbf{u}_{Exact}(x,y,z)|^2}, \tag{7.3.1}$$

where the grid sizes in y-direction is $n_y = 2$.

7.3.1 The results under no-slip boundary conditions

The velocity profile u_y of the LBM agrees well with the exact solution detailed in Eq (7.2.1) for various relaxation times as shown in Figures (7.4) to (7.6). At small relaxation times the convergence starts at the small grid size of 32 as seen in Fig-

ures (7.4) and (7.5), whereas at large relaxation times the convergence between the velocity profile of the LBM u_y and the exact solution needs a large grid size, as shown in Figure (7.6). Also, the velocity profile u_y shows zero velocity at the boundary, which supports our assumption of no-slip boundary conditions at the wall, as seen in Figures (7.4), (7.5) and (7.6).

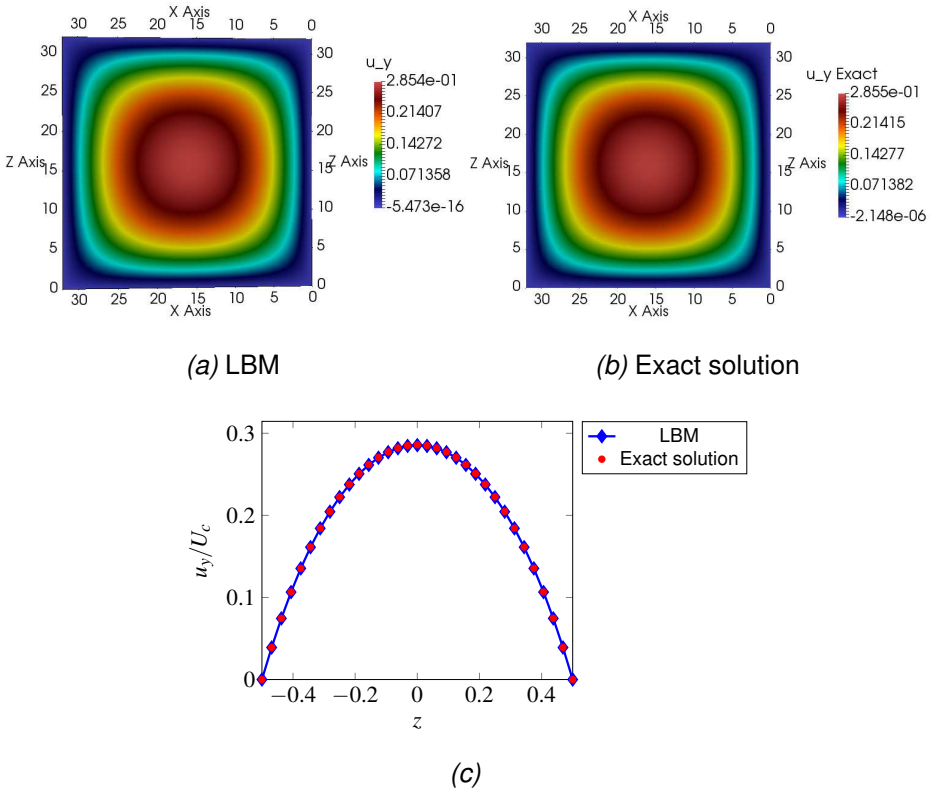

(a) LBM *(b)* Exact solution

(c)

Figure 7.4: The velocity profile u_y at $\tau = 0.1$ and $n_x = n_z = 32$.

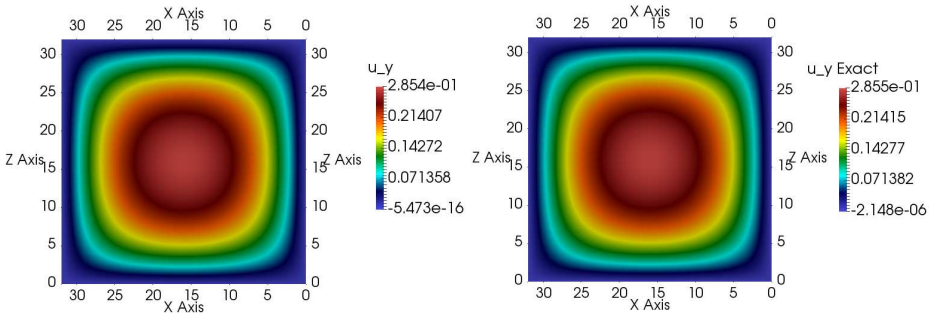

(a) LBM *(b)* Exact solution

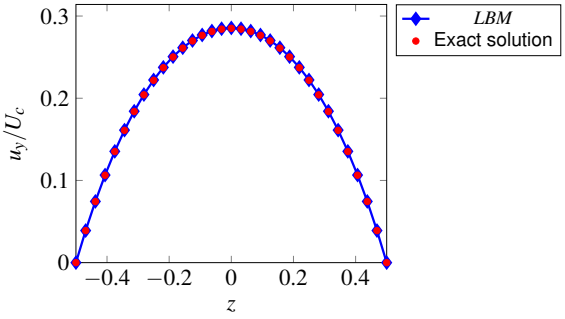

(c)

Figure 7.5: The velocity profile u_y at $\tau = 0.6$ and $n_x = n_z = 32$.

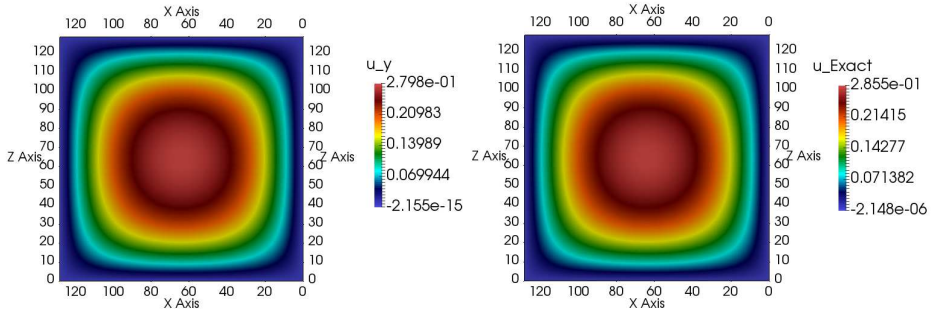

(a) LBM *(b)* Exact solution

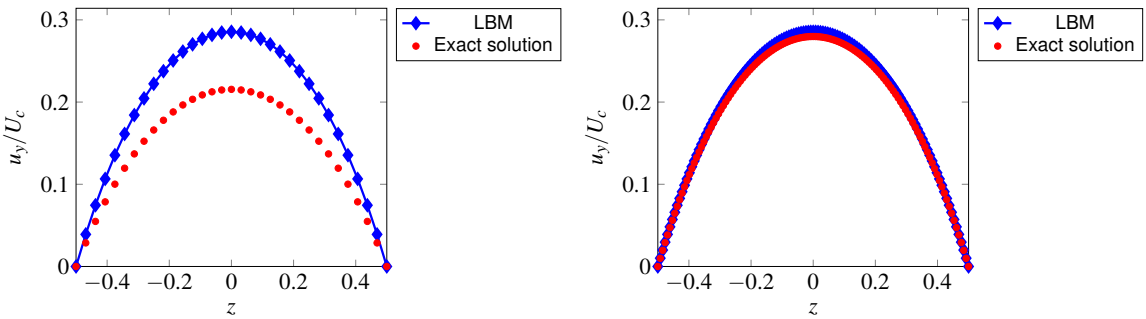

(c) $n_x = n_z = 32$ *(d)* $n_x = n_z = 128$

Figure 7.6: The velocity u_y at $\tau = 6$.

Changes in the relaxation time do not affect the peak or value of the velocity

profile, which is clear from Figures (7.4), (7.5) and (7.6). As the relaxation time indicates the Reynolds number, and therefore when changing the relaxation time we are also changing the Reynolds number, and changes in the relaxation time do not affect the velocity profile, the results are independent of Reynolds number as the exact solution shows.

The velocity profile u_x at the $n_z/2$, $n_y/2$ in x-direction and u_z at the $n_x/2$, $n_y/2$ in z-direction are very small and symmetrical at each relaxation time, and closely match the assumption that the velocity in x- and z-directions is zero. As an example, Figures (7.7) and (7.8) show a very small velocity profile with u_x and u_z at $\tau = 0.6$, respectively. Moreover, Figures (7.7)(a) and (7.8)(a) do indicate weak secondary flows and show similarity in z- and x-directions.

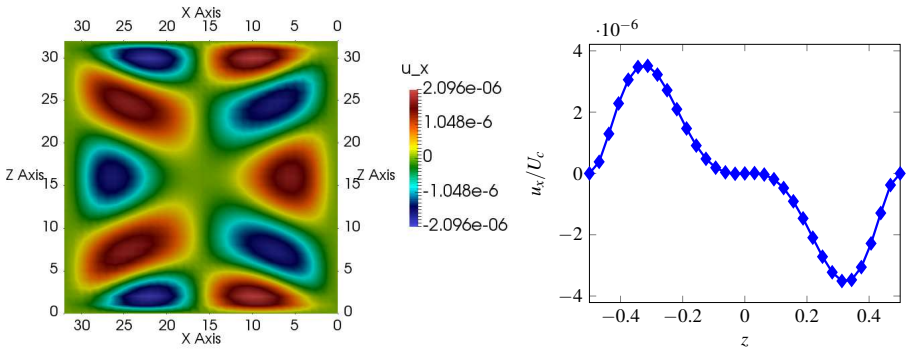

(a) LBM *(b)* LBM

Figure 7.7: The velocity profile u_x at $\tau = 0.6$, $n_z/2$, $n_y/2$ and $n_y = 2$, $n_z = 32$.

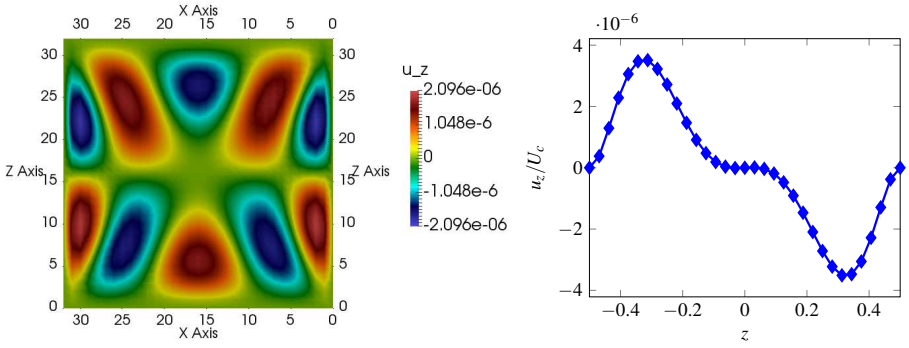

(a) LBM *(b)*

Figure 7.8: The velocity profile u_z at $\tau = 0.6$, $n_x/2$, $n_y/2$ and $n_y = 2$, $n_x = 32$.

By doubling the grid sizes n_z and n_x and using diffusive scaling, we reduce the norm error between the velocity profile of the LBM and the exact solution, at each

relaxation time, as demonstrated in Figure (7.9). In general, at various relaxation times, the accuracy of the norm error is of second-order, which agrees with the accuracy of moment-based boundary conditions. Furthermore, decreases in relaxation time lead to a decrease in the value of the norm error.

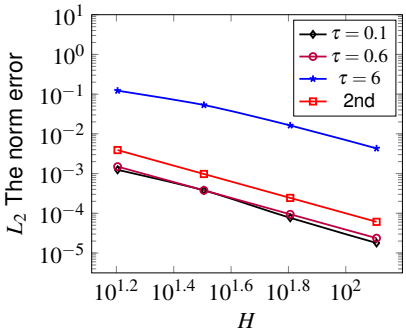

(a)

Figure 7.9: The norm error between the velocity profile of LBM and the exact solution at different relaxation time τ with no-slip boundary condition.

7.3.2 The results under Navier-slip boundary condition

The velocity profile of the LBM u_y closely matches the exact solution obtained from Eq (7.2.2) under Navier-slip boundary conditions, at different relaxation times and K_n, as seen in Figures (7.10), (7.11) and (7.12). At each K_n the velocity profile u_y of the LBM with a small relaxation time $\tau = 0.1, 0.6$ needs a grid size of around $n_z = n_x = 32$ to be in agreement with the exact solution, while with a large relaxation time $\tau = 6$ a grid size around $n_z = 128$ is required as seen in Figures (7.10), (7.11) and (7.12). Thus, the velocity profile u_y of the LBM with a small relaxation time $\tau = 0.1, 0.6$ converges to the the exact solution faster than it does with a large relaxation time $\tau = 6$.

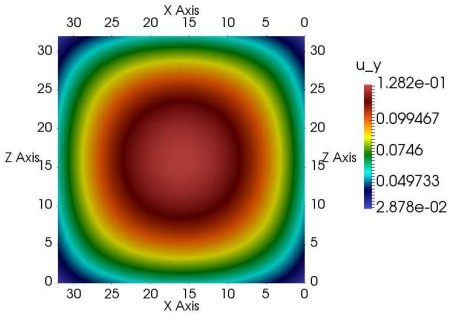

(a) LBM, $K_n = 0.2$

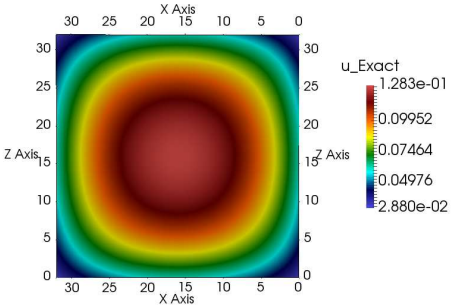

(b) Exact solution, $K_n = 0.2$

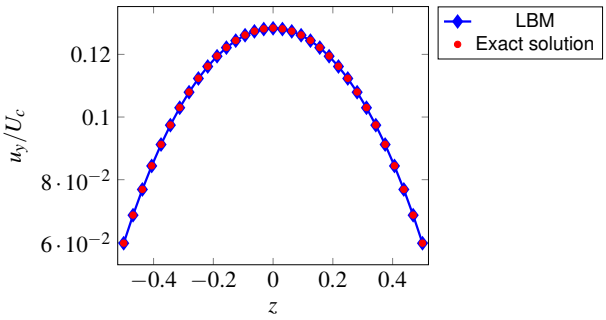

(c) $K_n = 0.2$

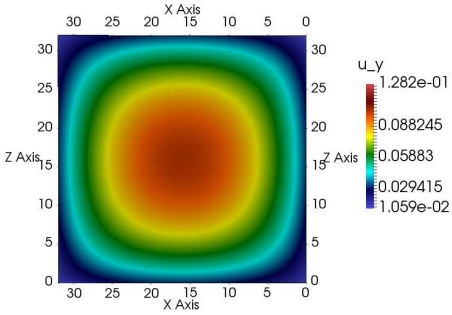

(a) LBM, $K_n = 0.1$

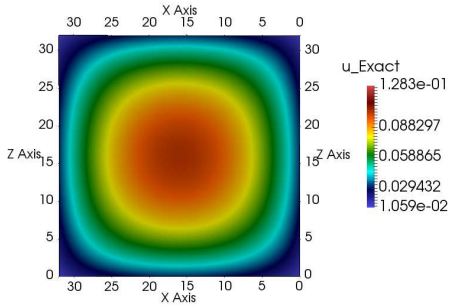

(b) Exact solution, $K_n = 0.1$

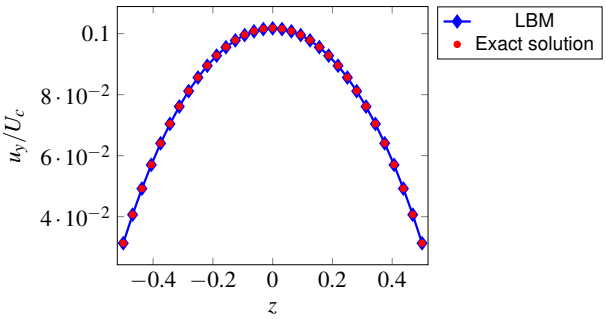

(c) $K_n = 0.1$

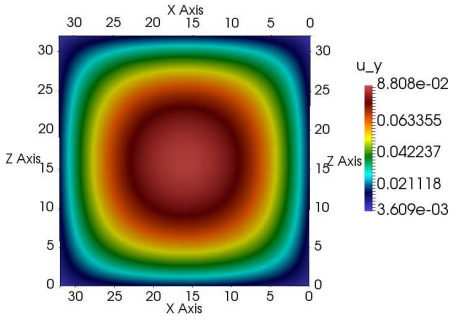

(d) LBM, $K_n = 0.05$

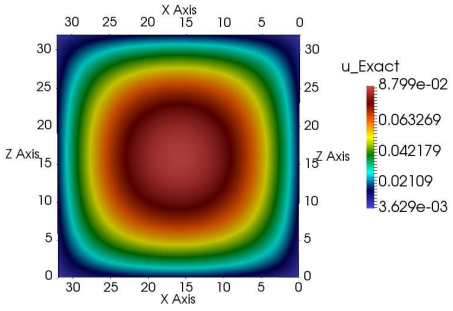

(e) Exact solution, $K_n = 0.05$

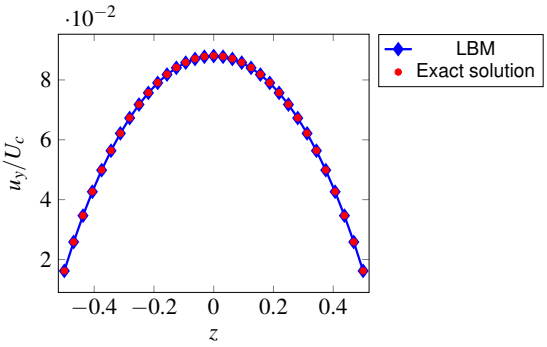

(f) $K_n = 0.05$

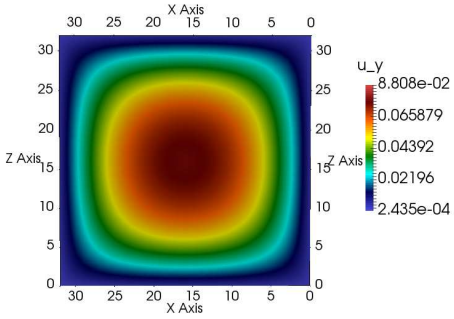

(g) LBM, $K_n = 0.01$

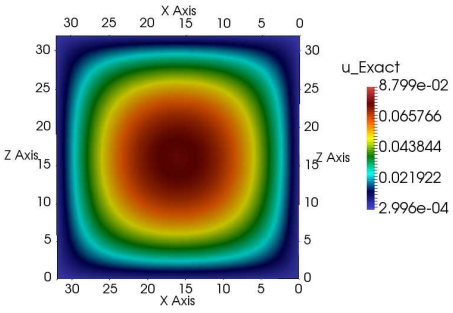

(h) Exact solution, K_n=0.01

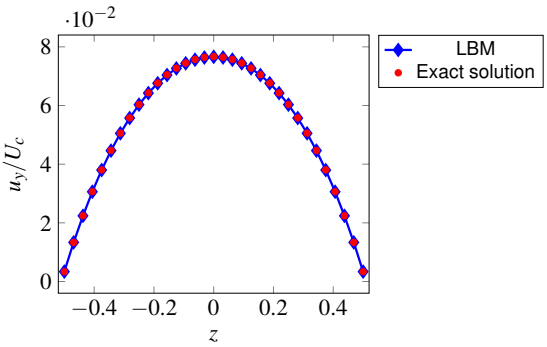

(i) $K_n = 0.01$

Figure 7.10: The velocity profile u_y at $\tau = 0.1$ and $n_z = n_x$=32.

The influence of the dimensionless length slip K_n is clear in Figure (7.10) where the decrease in K_n leads to a decrease in the slip velocity at the wall and

the peak or maximum velocity profile, which happens at each relaxation time and K_n, as shown in Figures (7.11) and (7.12).

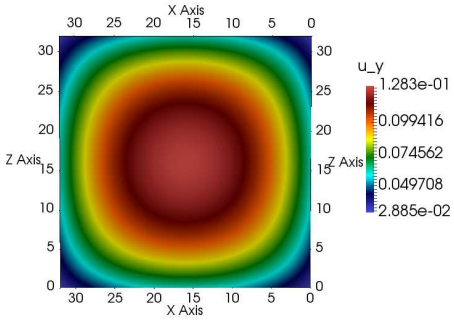

(a) LBM, $K_n = 0.2$

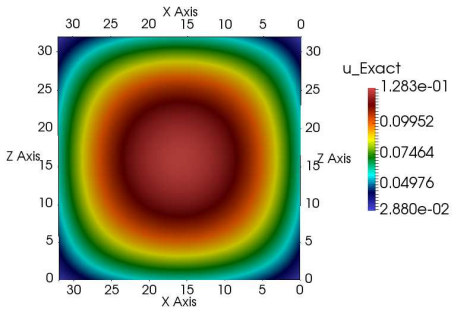

(b) Exact solution, K_n=0.2

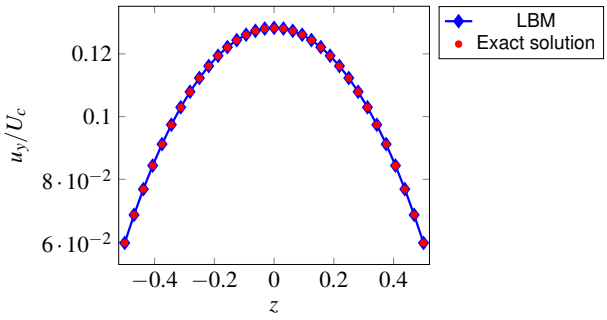

(c) $K_n = 0.2$

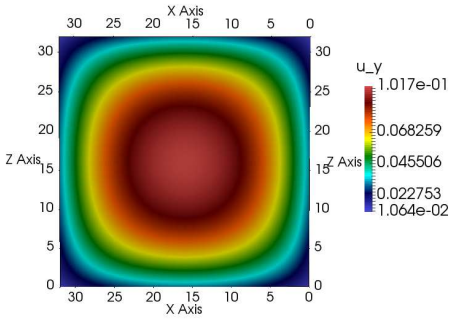

(d) LBM, $K_n = 0.1$

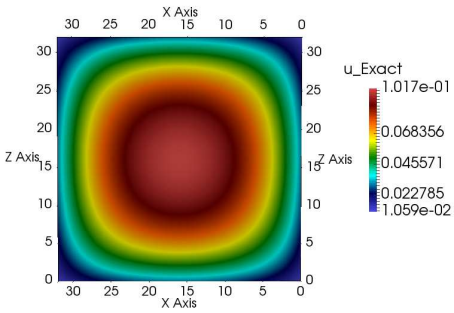

(e) Exact solution, $K_n = 0.1$

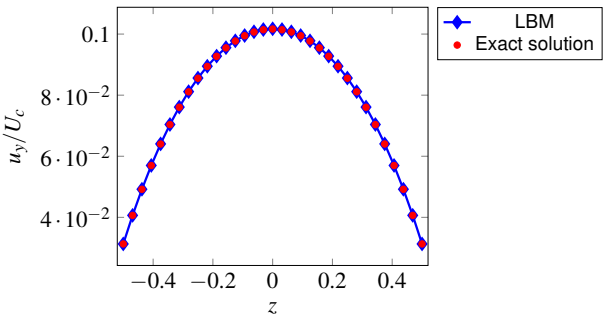

(f) $K_n = 0.1$

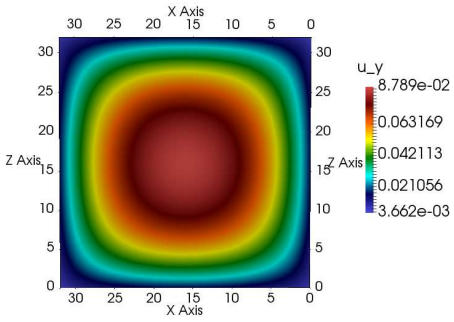

(g) LBM, $K_n = 0.05$

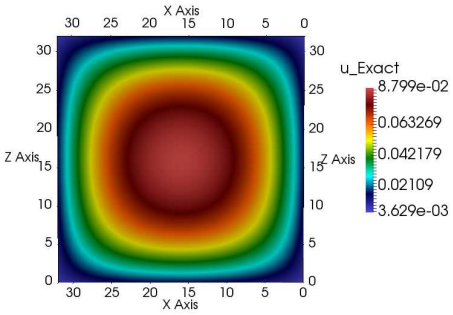

(h) Exact solution, $K_n = 0.05$

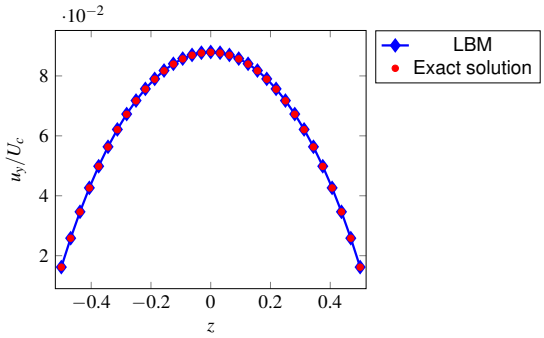

(i) $K_n = 0.05$

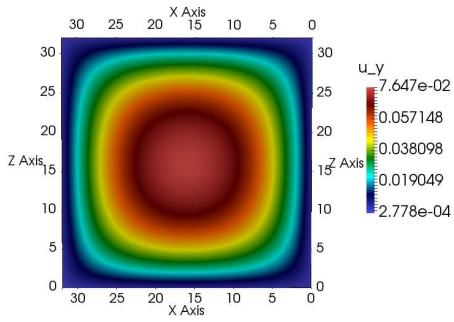

(j) LBM, $K_n = 0.01$

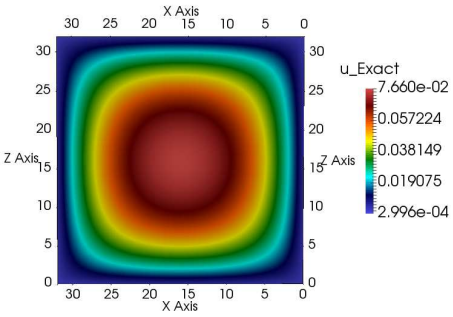

(k) Exact solution, $K_n = 0.01$

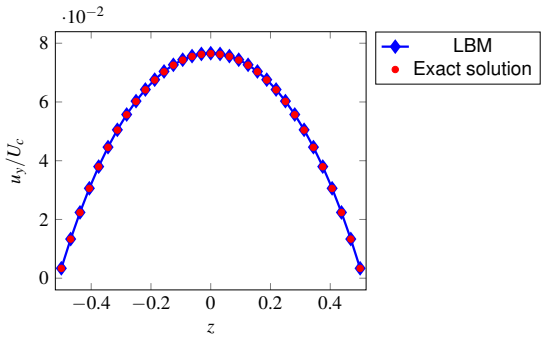

(l) $K_n = 0.01$

Figure 7.11: The velocity profile u_y at $\tau = 0.6$ and $n_x = n_z = 32$.

Variation of the relaxation time does not change the value of velocity profile at each K_n *i.e.* the value of velocity profile is the same at different relaxation time

$\tau = 0.1, 0.6, 6$. This confirms that the results or velocity profiles are independent of the Reynolds number, because the relaxation time is related to the Reynolds number Re and a change in relaxation time therefore leads to a change in the Reynolds number Re. This is noticeable in Figures (7.10), (7.11) and (7.12).

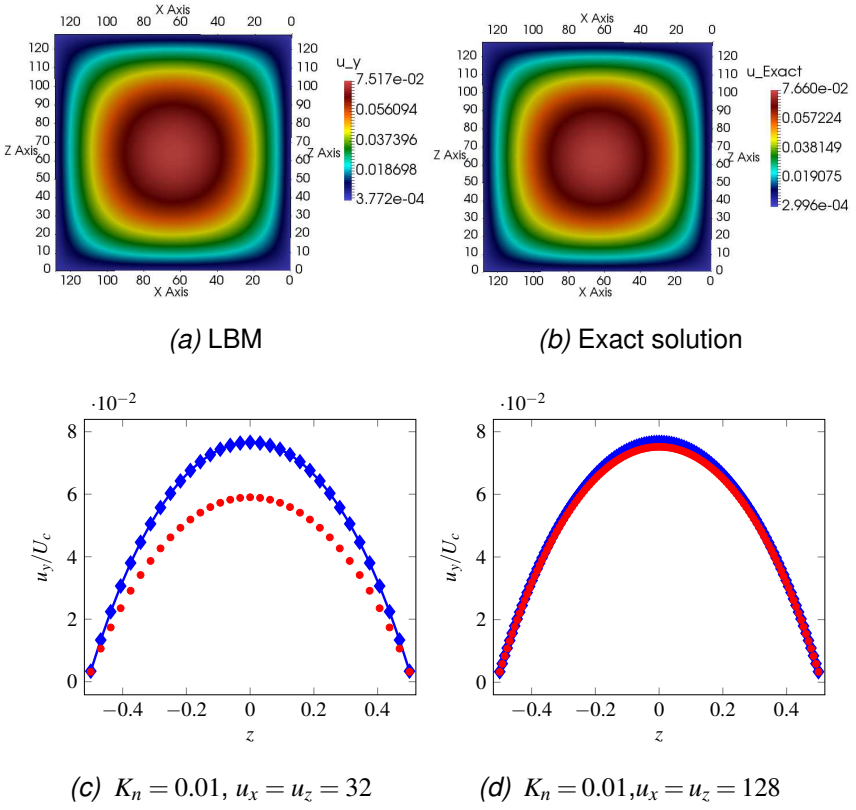

(a) LBM *(b)* Exact solution

(c) $K_n = 0.01$, $u_x = u_z = 32$ *(d)* $K_n = 0.01$,$u_x = u_z = 128$

Figure 7.12: The velocity profile u_y at $\tau = 6$ and $K_n = 0.01$.

The velocity u_x and u_z are very small and symmetrical at each relaxation time and K_n. They closely match the assumption that the velocity in x- and z-direction is zero. For instance, u_x at the $n_z/2$, $n_y/2$ in the x-direction and u_z at the $n_x/2$, $n_y/2$ in the z-direction are both very small at each relaxation time and K_n, such as at $\tau = 0.6$ and $K_n = 0.1$, as seen in Figures (7.13) and (7.14). The velocity u_x and u_z under Navier-slip boundary conditions are smaller than the velocity u_x and u_z under no-slip boundary conditions, as shown in Figures (7.13) and (7.14), and Figures (7.7) and (7.8), respectively. Again, Figures (7.13) (a) and (7.14) (a) indicate weak secondary flows and show similarity in x- and z- directions. The K_n only has a slight effect on u_x and u_z, shown by the closeness of values of u_x and u_z at $K_n = 0.1$ are those at $K_n = 0.01$, as seen in Figures (7.13)(b) and (7.14)(b) for $K_n = 0.1$ and Figures (7.15)(b) and (7.16)(b) for $K_n = 0.01$.

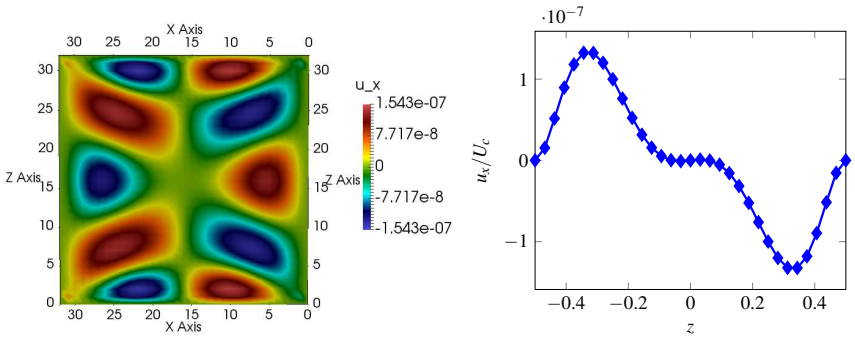

(a) LBM *(b)* $K_n = 0.1$

Figure 7.13: The velocity u_x at $\tau = 0.6$, $K_n = 0.1$, $n_z/2$, $n_y/2$ and $n_y = 2$,$n_z = 32$.

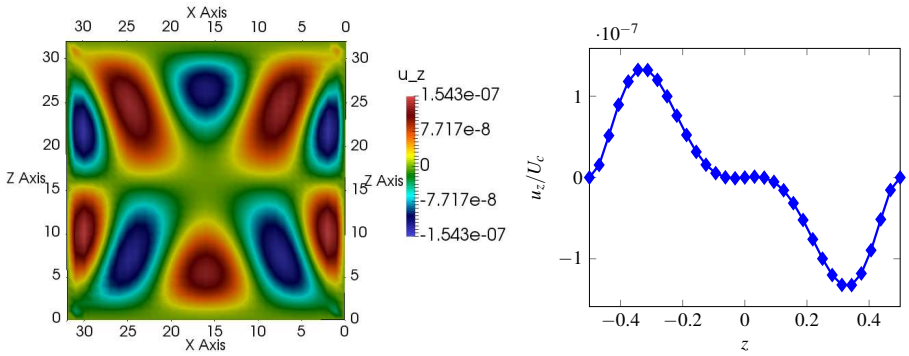

(a) LBM *(b)* $K_n = 0.1$

Figure 7.14: The velocity u_z at $\tau = 0.6$, $K_n = 0.1$, $n_x/2$, $n_y/2$ and $n_y = 2$,$n_x = 32$.

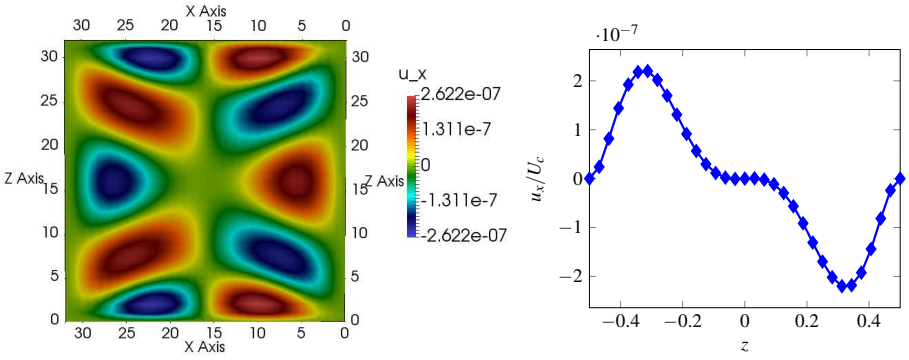

(a) LBM *(b)* $K_n = 0.01$

Figure 7.15: The velocity profile u_x at $\tau = 0.6$, $K_n = 0.01$ $n_z/2$, $n_y/2$ and $n_y = 2$,$n_z = 32$.

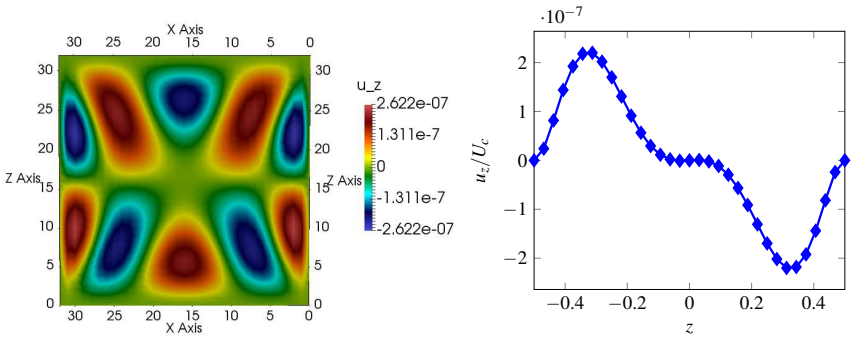

(a) LBM *(b)* $K_n = 0.01$

Figure 7.16: The velocity u_z at $\tau = 0.6$, $K_n = 0.01$, $n_x/2$, $n_y/2$ and $n_y = 2$,$n_x = 32$.

Using a single relaxation time with diffusive scaling gives a second order accuracy for the norm error at different τ and K_n, and agrees well with the accuracy of moment boundary conditions with the second order of LBM, as seen in Figure (7.17). The value of the norm error is affected by two factors, τ and K_n. A change in K_n leads to a change in the value of the norm error at each τ, as seen in Figure (7.17). A decrease in τ produces a decrease in the norm error at each K_n as seen in Figure (7.17)(a) and (b). Note also that the norm errors are the same with small $\tau = 0.1$ and small grid sizes, as shown in Figure (7.17) (c).

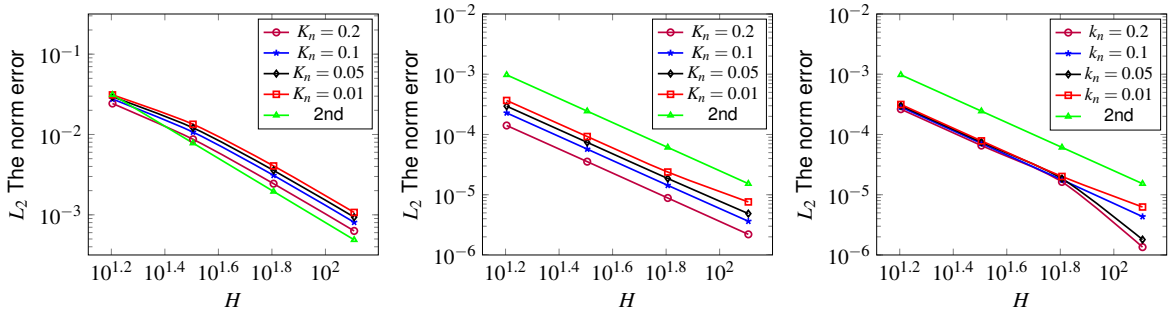

(a) $\tau = 6$ *(b)* $\tau = 0.6$ *(c)* $\tau = 0.1$

Figure 7.17: The norm error at different τ and K_n.

7.4 Conclusion

In conclusion, the numerical simulation of duct flow in three dimensions has been presented using the lattice Boltzmann method with moment-based boundary conditions, which were used to implement two conditions at the wall: no-slip and Navier-slip. Grid convergence studies were performed using diffusive scaling.

Here, the Reynolds and the lattice relaxation parameters were all kept constant. The velocity profile was evaluated and compared with the analytical solutions. Also, norm errors were calculated and the method was shown to be of second order for diffusive scaling for both no-slip and Navier-slip conditions. This model or simulation concludes that the velocity profile of LBM and the exact solution are independent of the Reynolds number Re under both no-slip and Navier-slip boundary conditions. This simulation represents the first stage of the validation of a three dimensional model of duct flow.

Chapter 8

Pressure-driven 2D and 3D flows in micro-channels.

8.1 Literature review for Lattice Boltzmann method and micro-channels.

Micro-channels or micro devices are channels where the fluid flow channels have internal dimensions in the range of 1mm and 1μm. The fluid flow in macro devices is diverse from micro devices, because in macro devices the Navier-Stokes equations are founded on a continuum flow model and derived for small Knudsen numbers k_n which are defined as the ratio of the molecular mean free path to characteristic length. This means the Navier-Stokes equations are founded with generally no-slip boundary conditions. Whilst, in micro devices the phenomenon of rarefaction is important and indicated by the Knudsen number. As the k_n increases, this phenomenon becomes more apparent, resulting in a situation when flow rate and other parameters cannot be predicted using the continuum flow model [33].

Also, diverse flow phenomena has been noticed on micro scales, including compressibility and slip flow. The compressibility effect is clear and particularly apparent with high pressure. The compression occurs when the particles press or squeeze together and the rarefaction happens when the particles expand and have extra space. Thus, the rarefaction is the opposite, leading to a reduction in density and pressure.

The presence of slip velocity at the wall or the boundary causes a high flow rate in micro devices and this flow rate is higher than flow rate with no-slip boundary condition. Previously, slip velocity was described by Maxwell [43] who defined

it as proportional to the rate of shear stress at the wall. The transition from continuum regime to slip or transition regime happens by increasing the Knudsen number. Hence, the Knudsen number divided the fluid regime into four regimes (continuum, slip, transition and free molecular regime). The slip regime is located in the regime which Knudsen number is between $0.001 < k_n < 0.1$.

The Micro-Electro-Mechanical System (MEMS) is one which uses equipment that has a length of between 1mm and 1μm. MEMSs have many applications in different areas [32], [17], [35], [61].

Among the various available methods, the LBM is considered attractive to study micro-flows because of its kinetic origin, its simple structure and its low-cost computation. In addition, the lattice Boltzmann method is easily performed on a parallel computer. There are many authors who have studied fluid or gas flow in micro-channels, as well as the effects of rarefaction and compressibility on the velocity, pressure, temperature and friction factor, using many types of boundary condition at various Knudsen numbers and aspect ratios. Some of these authors have used the lattice Boltzmann method, and some of them other methods. Some examples of these studies are discussed below.

The LBM to simulate rarefied gas flow in micro-channels between two parallel plates has been studied by Nie [49] *et. al* using halfway bounce back boundary condition. When they compared their simulation results with the experiments they found that the nonlinear pressure and the slip velocity have quadratic dependent on the Knudsen number. Also, they applied LBM to simulate micro-cavity flow. They used the non-dimensional relationship between the relaxation time and Knudsen number, $k_n = a\dfrac{\tau - 0.5}{\rho H}$, where H is the height of the channel and is equal to 10 and a is a constant which is chosen as a best constant or value to compare the numerical results with the experiment data. ρ is the density of fluid and 0.5 comes from the Boltzmann equation discretisation by using finite difference scheme. Arkilic [3] *et. al* executed studies for gaseous flow in a 2D long micro-channel with a little rarefaction through the micro-channel and presented an analytical solution of the Navier-Stokes equations with first-order slip bound-

ary condition, pressure and velocity profiles at low Knudsen numbers. Their studies show the compressibility and non continuum effects in long micro-channels. Also, they compared their analytical solutions with the experimental data and the agreement was good.

Lim [40] performed a study for 2D isothermal micro-channel flow driven by pressure using specular bounce back boundary condition and the extrapolation boundary condition at the wall. The extrapolation boundary condition is based on the assumption that the unknown distribution functions at the wall are estimated to their equilibrium distribution functions *i.e.* $f_i = f_i^0$. To calculate f_i^0 they used second order polynomial extrapolation to calculate or find the density and the velocity. Also, they used equilibrium boundary condition to calculate or estimate the unknown distribution functions at the inlet and outlet by fixing the density and extrapolating the velocity *i.e.* $f_i = f_i^0$. Their results for the pressure distribution and slip velocity profiles agree better with the experimental data than with Arkilic's results for analytical solutions.

Lee and Lin [38] simulated the rarefaction and compressibility effects of gas flow in two dimensional micro-channels using second order LBM and derived the relationship between the Knudsen number and relaxation time. They used equilibrium boundary condition which is similar to diffusive boundary condition which was presented by Ansumali and Karlin [2]. Lee and Lin assume the distribution functions to their equilibrium values at boundary $f_i = f_i^0$ for all i. They evaluated the equilibrium distribution functions using a bounce-back boundary condition, the velocity of the wall and density at the grid point which is obtained by giving zero mass flux over the boundary. These boundary conditions leads to set the tangential and normal velocities to zero.And they obtained slip velocity from half-way bounce back boundary condition, their slip length equal to $\delta_x/2$. This means they do not have explicit constraint or form for slip velocity at the wall. Also, they used the Knudsen number based upon the pressure, which is called local Knudsen number, and the well-known relationship between Knudsen number and relaxation time in micro-flow. Their pressure deviation and slip velocity showed good

agreement with Arkilic *et. al* [3].

Jeong *et. al* [33] used the second order LBM model to study the rarefaction and the compressibility for slip flow in a three dimensional rectangular micro-channel. They used local Knudsen number and the relationship between the Knudsen number and relaxation time. Additionally, they used the equilibrium boundary condition and applied the same method or procedure which was presented by Lee and Lin [38] to obtain equilibrium distribution functions without any particular treatment for slip velocity at the wall. They studied the effect of slip velocity, aspect ratio and Knudsen number on pressure deviation. The aspect ratio was between one and seven and three values of Knudsen number were used (0.025, 0.05 and 0.1). Their limited case agreed well with analytical solutions for flow between two parallel plates.

Some authors used a combination of bounce back and specular-reflection conditions, a combination based on the reflection coefficient r to determine the slip velocity at the wall rather than determine specific form for slip velocity. For instance, Succi [65] studied the effects of slip motion on a solid wall using a combination of bounce back and specular-reflection conditions and clarified that slip velocity is affected by the bounce back coefficient Knudsen number. A reflection coefficient range of was used $0 \leq r \leq 0.01$ and it was reported that the slip motion takes place at reflection coefficient of $r < 0.01$. Sbragaglia and Succi [59] applied gas flow in micro channels and studied the rarefaction and compressibility effects using bounce back scheme with $r = 0.95$, centre channel velocity 0.01 and $0 < K_n < 0.8$ range. They accomplished a simulation in three dimensions with D_3Q_{19} lattice and their analytical results matched perfectly with experimental data in range $0.1 < r < 1$. They produced a form of kinetic boundary conditions based on accommodation coefficient, reflection and slip.

Tang *et. al*. [68] related the relaxation time with Knudsen number. Also, they used kinetic boundary conditions, specifically modified bounce back, to get no-slip boundary condition, as well as a combination of kinetic boundary conditions, specifically bounce back, and the specular reflection boundary condition to get

slip velocity which was also used in their 2004 study [67] in which they found that the best value of a reflection coefficient r to get excellent agreement with Arkilic's solutions for velocity, pressure and slip is 0.7. They simulated Poiseuille, Couette and cavity flow in two dimensional micro-channels between two parallel plates. In the Poiseuille simulation the velocity at the inlet was 0.001, the aspect ratio between the height and width was 10 and the friction constant was from the first and second orders. In general, their numerical results are in good agreement with the analytical solutions.

Gou *et. al* [21] studied the physical symmetry, special accuracy and relaxation time on LBGK model for micro-gas channels in slip and transition regime, using Maxwell's diffuse boundary condition. They discussed and reported that the wall effects should be considered when looking at relaxation time in the LBE model for gas flow in micro-channels. Guo and Zheng *et. al* [22] proposed a multiple relaxation time (MRT) lattice Boltzmann model to simulate the Poiseuille and Couette in two dimensional micro-channels using a combination of bounce back and specular-reflection conditions at the the wall and periodic boundary condition at the inlet and outlet. They found out the relaxation time has to relate to the boundary condition to get the generalise solution for the Navier-Stokes equations. This relation is similar to the known relation which is between the relaxation time with Knudsen number.

Verhaeghe [71] *et. al* displayed a simulation using MRT lattice Boltzmann model for micro channels where the gas flow is in slip and transition regime. They used first order slip boundary conditions at the walls and pressure boundary condition at the inlet and outlet to simulate a Poiseuille flow. They used a linear combination of bounce-back and diffusive boundary conditions, which is based on the diffusive scattering term $\beta \in [0,1]$ in order to determine the slip velocity. In addition, they needed to know the wall velocity in the analytical solution of the lattice Boltzmann model to adjust the diffusive scattering term β. Their results are in close agreement with the information-preservation direction simulation Monte Carlo (IP-DSMC) and direction simulation Monte Carlo (DSMC) and Navier-slip

velocity in slip regime. However, these results are in disagreement with IP-DSMC and DSMC in the transition regime although they do still in agreement with Navier-slip velocity in the transition regime. As a result, this combination of boundary conditions does not set an exact value for slip velocity.

Reis and Deller [58] simulate two dimensional rarefied flow between two parallel plate in slip and transition regimes. They used second order lattice Boltzmann Method with moment based boundary conditions to implement Navier-slip boundary condition at the wall in order to determine the exact value of first order slip velocity with fixed slip length. Also, they used pressure boundary conditions at the inlet and outlet. They examined the velocity profile and pressure deviation at aspect ratio $= 0.01$ and various Knudsen number (0.388,0.194,0.0194), and pressure ratio (2,1.4,1.01). Their results is in excellent agreement with the analytical solution and the error was approximately of second order at Knudsen number 0.194, and pressure ratio 2.

Other authors have analysed the fully developed velocity profiles and friction factor of the hydrodynamic entrance region of micro-channels in the slip regime. Some of these used non Lattice Boltzmann Method and are detailed as follows. Moroni and Spiga [46] investigated slip flow in two-dimensional rectangular micro-channels to examine flow which is laminar, steady-state and hydro-dynamically developed, for Newtonian fluids in slip regime. Moroni *et. al* [47] studied the rarefaction effect of gas flow and the impact of Knudsen number and aspect ratio on the friction factor. Additionally, they examined the effect of rarefaction on pressure drop in rectangular, trapezoidal and double trapezoidal silicon micro-channels, for incompressible flow in slip regime. They pointed out the rarefaction effect on the friction factor is stronger for small aspect ratios because the definition of Knudsen number is based on the hydraulic diameter D_h.

Li *et. al*. [39] used experimental and numerical study to examine entrance effects for flow characteristic in micro-channels. They reported that the the friction constant becomes larger in short channels, when the entrance effect becomes an interesting factor.

Duan and Muzychka [15], [16] proposed a model to examine apparent friction factor and Reynolds number product in non-circular micro-channels for fully developed and developing slip flow. This was created based on the accommodation coefficient, cross section of the channel, Knudsen number and channel geometry, which together presents 10 percent accuracy for the most common duct shapes. They reported that the $f_{app}Re$ is a finite value. Moreover, they suggested a model for the prediction of pressure distribution and mass flow rate based on their study of the effect of compressibility on slip flow within non-circular micro-channels [15]. They also constructed a further model for $f_{app}Re$ in non-circular micro-channels for the development of continuum flow and slip flow. This model is dependent on accommodation coefficient and Knudsen number, rather than the cross section of the channel or aspect ratio ε [16]. These models are considered available data for use in engineering the laminar entrance region of rectangular micro-channel.

Other authors have used the Lattice Boltzmann method such as Niya *et. al* [41] to study numerically the fully-developed velocity profiles and friction factor, presenting the fully developed velocity profiles at the entrance of rectangular duct micro-channels in three dimensions. They used incompressible lattice Boltzmann LBGK model with a combination of bounce back and reflection boundary conditions at the wall to determine the slip velocity, using a reflection coefficient equal to $r = 0.7$. They applied velocity boundary condition at the inlet, and pressure boundary condition at the outlet implemented by non-equilibrium extrapolation scheme. They used Knudsen number, Reynolds number and aspect ratio ranges to study the effect of these parameters on the fully developed velocity profiles as well as the apparent friction factor and Reynolds number product $(f_{app}Re)$ at the hydrodynamic entrance length in slip regime. Additionally, they compared the numerical results of $f_{app}Re$ from LBM with the exact solution [15] and finite volume methods. They concluded that the apparent friction factor and Reynolds number product has a finite value at the entrance and decreases with the increase of Knudsen number.

8.2 Overview of this chapter

In this chapter, we present results obtained using a Lattice Boltzmann model (LBM) to simulate rarefaction and compressibility effects for two and three-dimensional flows in micro-channels. Moment-based boundary conditions are used to implement Navier-slip boundary conditions on the walls and pressure boundaries are used to drive the flow. The results are compared with the results which are displayed in the literature above, some of which were obtained using the lattice Boltzmann model with boundary conditions such as the combination of bounce back and reflection boundary condition based on estimation of some parameters in order to determine the slip velocity at the wall. In contrast to these studies mentioned, the moment based boundary conditions work on a determination of the exact value of slip velocity, in order to implement Navier-slip boundary condition.

For the simulations, we use a second-order single relaxation time model and investigate convergence behaviour of the model. The effect of the Knudsen number k_{n_0}, aspect ratio ε between the height and length, aspect ratio Ar between the height and width and pressure ratio Λ_{pr} between the inlet and outlet on velocity, slip velocity, pressure deviation and the mass flow are all investigated.

In these simulations we use second order LBM. Relaxation time is generally defined as $\tau = \nu/c_s^2 = 3\nu$, but in micro-flow the relaxation time is related to the Knudsen number. The slip length is related to the relaxation time as $l_s = \tau c$ where $c = \dfrac{\delta_x}{\delta_t}$ is the speed lattice, and slip length or mean free path is related to the Knudsen number as relation $k_n = \dfrac{l_s}{H}$, so the slip length is $l_s = Hk_n$. These relations lead to a definition of the Knudsen number as $k_n = \dfrac{\tau c}{H}$. In this case the dynamic viscosity is defined as $\mu = \nu\rho$ and $\nu = \tau/3$, so, $\mu = \dfrac{\tau}{3}\rho = \dfrac{1}{3}\rho H k_n$. In LBM simulation, the Mach number Ma should be kept small and the macroscopic relation between k_n, Ma and Re is $k_n \propto \dfrac{Ma}{Re}$. The LBM accuracy is second order with regards to Mach number and also time and space and the reference velocity is the centreline velocity for viscous flow between parallel plates with constant pressure gradient $U_c = \frac{H^2}{8\mu}\frac{p_0 - p_{in}}{L}$ and it is fixed at $U_c = 0.0625$ where L is the length of the channel. The density at the outlet ρ_0 is 1.

8.2.1 The exact solution for 2D and 3D

The exact solution under Navier-slip conditions at $u_x = u_s = l_s|\frac{du_x}{dy}|$ at $y = 0, H$ was presented by Arkilic *et. al* [3]:

$$U_x = -\frac{H^2}{2\mu}\frac{d\overline{p}}{dx}\left(\frac{y}{H} - \frac{y^2}{H^2} + \theta_n k_{n_{Local}}\right), \tag{8.2.1}$$

where $\theta_n = \dfrac{2-\sigma_u}{\sigma_u}$ in which $\sigma_u = 1$ is a momentum accommodation coefficient, the local Knudsen number is $k_{n_{Local}} = k_{n_0}\dfrac{p_0}{p}$, $p = \dfrac{\rho}{3}$ is the pressure, $p_0 = \dfrac{\rho_0}{3}$ is the pressure at the outlet and H is the height of the channel. To keep the viscosity dynamic constant we defined $\mu = \dfrac{\tau}{3}\rho = \dfrac{1}{3}\rho H k_n$. The pressure distribution is given by

$$\overline{p}(x) = -6\sigma_u k_{n_0} + \left(\left(-6\sigma_u k_{n_0}\right)^2 + \left(1 + 12\sigma_u k_{n_0}\right)x + \left(\Lambda_{pr}^2 + 12\sigma_u k_{n_0}\Lambda_{pr}\right)(1-x)\right)^2, \tag{8.2.2}$$

where $\overline{p} = \dfrac{p}{p_0}$, $\Lambda_{pr} = \dfrac{p_{in}}{p_0}$ and $p_{in} = \dfrac{\rho_{in}}{3}$ is the pressure at the inlet. The normalized pressure deviation is $\delta_p = \dfrac{(p - p_{lin})}{p}$, where $p_{lin} = p_0 + (1-x)(p_{in} - p_0)$ is the linear pressure corresponding to constant pressure gradient.

8.3 2D micro-channel

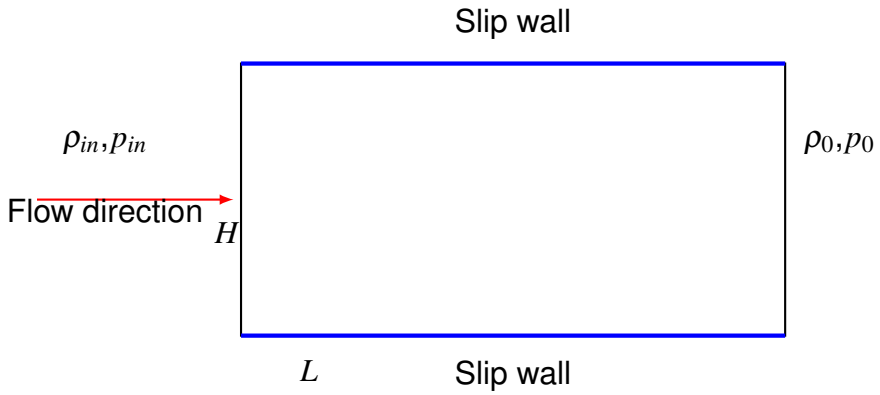

Figure 8.1: 2D pressure-driven flow where H is the height and L is the length of the channel.

8.3.1 The boundary conditions in two dimensions

In this simulation, moment-based boundary conditions are used to implement Navier-slip boundary conditions on the South and North walls and pressure boundary conditions at the inlet and outlet as seen in Figure (8.1) and follows

8.3.1.1 Navier-Slip boundary condition

At the outset we assume the slip velocity u_s is tangential velocity which is in x-direction and the vertical velocity is zero, so, $u_y = 0, u_x = u_s$. The tangential momentum flux tensor is $\Pi_{xx} = \Pi^0_{xx} + \tau\Pi^1_{xx}$, $\Pi^1_{xx} \simeq \partial_x u_x = 0$, $\rho\overline{u}_y = 0$, $\rho\overline{u}_x = \rho u_s$ and $\overline{\Pi}_{xx} = \frac{\rho}{3} + \rho u_s^2$. In pressure-driven slip flow, the non-equilibrium tangential momentum flux tensor $\Pi^1_{xx} \simeq \partial_x u_x$ is not zero at the wall due to changes in the pressure gradient, streamwise [58]. However, Π^1_{xx} is approximated as zero under small Mach number conditions because we neglected the third term of Π^1_{xx}: see section (3.2) for clarification. The system is created by selecting three independent moments from Table (8.1) and assuming the constraints so that $\rho u_x = \rho u_s$, $\rho u_y = 0$, $\Pi_{yy} = \frac{\rho}{3}$ and the bar moments are $\overline{\rho} u_x = \rho u_s$, $\overline{\rho} u_y = 0$, $\overline{\Pi}_{xx} = \frac{\rho}{3} + \rho u_s^2$.

Moments	Combination at the North boundary	Combination at the South boundary
$\rho, \rho u_y, \Pi_{yy}$	$f_4 + f_7 + f_8$	$f_2 + f_5 + f_6$
$\rho u_x, \Pi_{xy}, Q_{xyy}$	$f_8 - f_7$	$f_5 - f_6$
$\Pi_{xx}, Q_{xxy}, R_{xxyy}$	$f_8 + f_7$	$f_5 + f_6$

Table 8.1: Moments at the North and South boundaries.

The system is

$$\begin{aligned}
\rho\overline{u}_x &= \overline{f}_1 + \overline{f}_5 + \overline{f}_8 - \left(\overline{f}_3 + \overline{f}_6 + \overline{f}_7\right) = \rho u_s, \\
\rho\overline{u}_y &= \overline{f}_2 + \overline{f}_5 + \overline{f}_6 - \left(\overline{f}_4 + \overline{f}_7 + \overline{f}_8\right) = 0, \\
\overline{\Pi}_{xx} &= \overline{f}_1 + \overline{f}_5 + \overline{f}_8 + \left(\overline{f}_3 + \overline{f}_6 + \overline{f}_7\right) = \frac{\rho}{3} + \rho u_s^2.
\end{aligned} \tag{8.3.1}$$

The unknown distribution functions at the South wall are $\overline{f}_2$, $\overline{f}_6$ and $\overline{f}_5$. Solving system (8.3.1) then gives

$$\overline{f}_2 = \overline{f}_1 + \overline{f}_3 + \overline{f}_4 + 2\left(\overline{f}_7 + \overline{f}_8\right) - \frac{\rho}{3} - \rho u_s^2, \tag{8.3.2}$$

$$\overline{f}_5 = -\overline{f}_1 - \overline{f}_8 + \frac{\rho}{6} + \frac{1}{2}\rho u_s + \frac{1}{2}\rho u_s^2, \tag{8.3.3}$$

$$\overline{f}_6 = -\overline{f}_3 - \overline{f}_7 + \frac{\rho}{6} - \frac{1}{2}\rho u_s + \frac{1}{2}\rho u_s^2. \tag{8.3.4}$$

Again, as defined in previous chapters, the slip velocity is proportional to the shear stress at the wall $\Pi_{xy} = -\mu\partial_y u_{wall},\ n = y = n \gtrless 0$ and the momentum flux tensor Π_{xy} consists of equilibrium momentum flux Π^0_{xy} tensor and viscous stress Π^1_{xy}:

$$\Pi_{xy} = \Pi^0_{xy} + \tau\Pi^1_{xy} = -\mu\partial_x u_y.$$

Therefore, $\Pi_{xy} = -\mu\partial_y u_{wall}, n = y = n \gtrless 0$ and $u_s = -\frac{l_s}{\mu}\Pi_{xy}$. So, the slip velocity will defined as

$$\rho u_s = \rho\frac{-l_s}{\mu}\frac{2\tau}{2\tau+1}\overline{\Pi}_{xy}, \tag{8.3.5}$$

where $\rho\frac{-l_s}{\mu}\frac{2\tau}{2\tau+1} = \frac{-6l_s}{(2\tau+1)}$, so,

$$u_s = \frac{-6l_s}{\rho\,(2\tau+1)}\left(\overline{f}_5 - \overline{f}_6 + \overline{f}_7 - \overline{f}_8\right). \tag{8.3.6}$$

The slip velocity at the South wall is found by substituting the unknown distribution functions in Eq (8.3.6) and using the relation $u_s = -\frac{l_s}{\mu}\Pi_{xy}$ because the shear stress is positive toward the south wall, hence

$$u_s = \frac{6l_s}{\rho\,(1+2\tau+6l_s)}\left(\overline{f}_1 - \overline{f}_3 + 2\overline{f}_8 - 2\overline{f}_7\right) \tag{8.3.7}$$

where l_s is the slip length.

The unknown distribution functions at the North wall are $\overline{f}_4$, $\overline{f}_7$ and $\overline{f}_8$. Solving system (8.3.1) we get

$$\overline{f}_4 = \overline{f}_1 + \overline{f}_2 + \overline{f}_3 + 2\left(\overline{f}_5 + \overline{f}_6\right) - \frac{\rho}{3} - \rho u_s^2, \tag{8.3.8}$$

$$\overline{f}_7 = -\overline{f}_3 - \overline{f}_6 + \frac{\rho}{6} - \frac{1}{2}\rho u_s + \frac{1}{2}\rho u_s^2, \tag{8.3.9}$$

$$\overline{f}_8 = -\overline{f}_1 - \overline{f}_5 + \frac{\rho}{6} + \frac{1}{2}\rho u_s + \frac{1}{2}\rho u_s^2, \tag{8.3.10}$$

where $\rho = \overline{f}_0 + \overline{f}_1 + \overline{f}_3 + 2\left(\overline{f}_2 + \overline{f}_5 + \overline{f}_6\right)$ is found from the definition of the density and $\rho\overline{u}_y$. As defined in previous chapters, the slip velocity is proportional to the shear stress at the wall $u_s = l_s \partial_y u_{wall}$ thus, $u_s = -\frac{l_s}{\mu}\Pi_{xy}$, and from Chapman-Enskog the shear stress is defined as

$$\Pi_{xy} = \Pi^0_{xy} + \tau\Pi^1_{xy} = \frac{\rho}{3}\delta_{xy} + \rho u_x u_y + \tau\frac{-\rho}{3}\left(\partial_x u_y + \partial_y u_x\right) = \tau\frac{-\rho}{3}\partial_x u_y = -\mu\partial_x u_y.$$

Thus,

$$u_s = -\frac{l_s}{\mu}\Pi_{xy}, \tag{8.3.11}$$

and

$$u_s = \frac{6l_s}{\rho\left(1 + 2\tau + 6l_s\right)}\left(\overline{f}_1 - \overline{f}_3 + 2\overline{f}_5 - 2\overline{f}_6\right), \tag{8.3.12}$$

where l_s is the slip length.

8.3.1.2 Pressure boundary conditions

The unknown distribution functions for the West and East boundaries are found by solving a system determined by three independents moments which are selected from Table (8.2). Here we have chosen the three independent moments ρ, ρu_y and Π_{yy}, with the corresponding assumptions being $\rho\overline{u}_y = 0, \overline{\Pi}_{yy} = \frac{\rho}{3}$.

Moments	Combination at the West boundary	Combination at the East boundary
$\rho, \rho u_x, \Pi_{xx}$	$f_1+f_5+f_8$	$f_3+f_6+f_7$
$\rho u_y, Q_{xxy}, \Pi_{xy}$	f_5-f_8	f_6-f_7
$\Pi_{yy}, Q_{xyy}, R_{xxyy}$	f_8+f_8	f_6+f_7

Table 8.2: Moments at the West and East boundaries.

The system is therefore:

$$\begin{aligned}
\rho &= \overline{f}_0+\overline{f}_2+\overline{f}_3+\overline{f}_4+\overline{f}_6+\overline{f}_7+\left(\overline{f}_1+\overline{f}_5+\overline{f}_8\right),\\
\rho\overline{u}_y &= \overline{f}_2+\overline{f}_5+\overline{f}_6-\left(\overline{f}_4+\overline{f}_7+\overline{f}_8\right)=0,\\
\overline{\Pi}_{yy} &= \overline{f}_2+\overline{f}_5+\overline{f}_6+\left(\overline{f}_4+\overline{f}_7+\overline{f}_8\right)=\frac{\rho}{3}.
\end{aligned} \tag{8.3.13}$$

The unknown distribution functions at the West boundary are $\overline{f}_1$, $\overline{f}_5$ and $\overline{f}_8$. So, system (8.3.13) is solved thus

$$\begin{aligned}
\overline{f}_1 &= -\overline{f}_0-\overline{f}_3+\frac{2\rho_{in}}{3},\\
\overline{f}_5 &= -\overline{f}_2-\overline{f}_6+\frac{\rho_{in}}{6},\\
\overline{f}_8 &= -\overline{f}_4-\overline{f}_7+\frac{\rho_{in}}{6}.
\end{aligned} \tag{8.3.14}$$

where ρ_{in} is the density at the inlet. The unknown distribution functions at the East boundary are $\overline{f}_3$, $\overline{f}_6$ and $\overline{f}_7$. Again we solve system (8.3.13), to get

$$\begin{aligned}
\overline{f}_3 &= -\overline{f}_0-\overline{f}_1+\frac{2\rho_0}{3},\\
\overline{f}_6 &= -\overline{f}_2-\overline{f}_5+\frac{\rho_0}{6},\\
\overline{f}_7 &= -\overline{f}_4-\overline{f}_8+\frac{\rho_0}{6}.
\end{aligned} \tag{8.3.15}$$

where ρ_0 is the density at the outlet. There are five unknown distribution functions at the corner, thus we need to choose five independent moments. Here we have chosen the following: ρ, $\rho\overline{u}_x=\rho u_s$, $\rho\overline{u}_y=0$, $\overline{\Pi}_{xx}=\frac{\rho}{3}+\rho u_s^2, \overline{\Pi}_{yy}=\frac{\rho}{3}$. The system is

$$
\begin{aligned}
\rho &= \overline{f}_0+\overline{f}_2+\overline{f}_3+\overline{f}_4+\overline{f}_6+\overline{f}_7+\left(\overline{f}_1+\overline{f}_5+\overline{f}_8\right),\\
\rho\overline{u}_x &= \overline{f}_1+\overline{f}_5+\overline{f}_8-\left(\overline{f}_3+\overline{f}_6+\overline{f}_7\right)=\rho u_s,\\
\rho\overline{u}_y &= \overline{f}_2+\overline{f}_5+\overline{f}_6-\left(\overline{f}_4+\overline{f}_7+\overline{f}_8\right)=0,\\
\overline{\Pi}_{xx} &= \overline{f}_1+\overline{f}_5+\overline{f}_8+\left(\overline{f}_3+\overline{f}_6+\overline{f}_7\right)=\frac{\rho}{3}+\rho u_s^2,\\
\overline{\Pi}_{yy} &= \overline{f}_2+\overline{f}_5+\overline{f}_6+\left(\overline{f}_4+\overline{f}_7+\overline{f}_8\right)=\frac{\rho}{3}.
\end{aligned}
\tag{8.3.16}
$$

By solving this system the unknown distribution functions at the South West corner $\overline{f}_1,\overline{f}_2,\overline{f}_5,\overline{f}_6,\overline{f}_8$ will be

$$
\begin{aligned}
\overline{f}_1 &= -\overline{f}_0-\overline{f}_3+\frac{2\rho_{in}}{3},\\
\overline{f}_2 &= -\overline{f}_0-\overline{f}_4+\frac{2\rho_{in}}{3}-\rho u_s^2,\\
\overline{f}_5 &= \overline{f}_0+\overline{f}_3+\overline{f}_4+\overline{f}_7-\frac{2\rho_{in}}{3}+\frac{1}{2}\rho_{in}u_s+\frac{1}{2}\rho u_s^2,\\
\overline{f}_6 &= -\overline{f}_3-\overline{f}_7+\frac{\rho_{in}}{6}-\frac{1}{2}\rho_{in}u_s+\frac{1}{2}\rho u_s^2,\\
\overline{f}_8 &= -\overline{f}_4-\overline{f}_7+\frac{\rho_{in}}{6}.
\end{aligned}
\tag{8.3.17}
$$

The slip velocity is found using the relations $\Pi_{xy}=-\mu\partial_y u_{wall}$ and $u_s=-\frac{l_s}{\mu}\Pi_{xy}$ because the shear stress is positive toward the South wall as explained in section (8.3.1.1). Consequently, the slip velocity will defined as

$$
\rho u_s = \rho\frac{-l_s}{\mu}\frac{2\tau}{2\tau+1}\overline{\Pi}_{xy},
\tag{8.3.18}
$$

where $\rho\dfrac{-l_s}{\mu}\dfrac{2\tau}{2\tau+1}=\dfrac{-6l_s}{(2\tau+1)}$,

$$
\begin{aligned}
u_s &= \frac{-6l_s}{\rho\left(1+2\tau\right)}\left(\overline{f}_5-\overline{f}_6+\overline{f}_7-\overline{f}_8\right)\\
&= -\frac{6l_s}{\rho\left(1+2\tau+6l_s\right)}\left(\overline{f}_0+2\overline{f}_3+2\overline{f}_4+4\overline{f}_7-\rho\right).
\end{aligned}
\tag{8.3.19}
$$

The unknown distribution functions at the South East corner are found by solving

system (8.3.16) and using the relations $\Pi_{xy} = -\mu\partial_y u_{wall}$ and $u_s = -\frac{l_s}{\mu}\Pi_{xy}$, as explained in section (8.3.1.1), because the shear stress is positive toward the South wall . The unknown distribution functions at the North West corner are found by solving system (8.3.16) to get

$$\begin{aligned}
\overline{f}_1 &= -\overline{f}_0 - \overline{f}_3 + \frac{2\rho}{3}, \\
\overline{f}_4 &= -\overline{f}_0 - \overline{f}_2 + \frac{2\rho}{3} - \rho u_s^2, \\
\overline{f}_8 &= \overline{f}_0 + \overline{f}_2 + \overline{f}_3 + \overline{f}_6 - \frac{2\rho}{3} + \frac{1}{2}\rho u_s + \frac{1}{2}\rho u_s^2, \\
\overline{f}_7 &= -\overline{f}_3 - \overline{f}_6 + \frac{\rho}{6} - \frac{1}{2}\rho u_s + \frac{1}{2}\rho u_s^2, \\
\overline{f}_5 &= -\overline{f}_2 - \overline{f}_6 + \frac{\rho}{6}.
\end{aligned} \tag{8.3.20}$$

The slip velocity is found by using the relations $\Pi_{xy} = -(-\mu\partial_y u_{wall})$ and $u_s = \frac{l_s}{\mu}\Pi_{xy}$ because the shear stress is negative toward the North wall so,

$$\begin{aligned}
u_s &= \frac{6l_s}{\rho(1+2\tau)}\left(\overline{f}_5 - \overline{f}_6 + \overline{f}_7 - \overline{f}_8\right), \\
&= \frac{-6l_s}{\rho(1+2\tau+6l_s)}\left(\overline{f}_0 + 2\overline{f}_2 + 2\overline{f}_3 + 4\overline{f}_6 - \rho\right).
\end{aligned} \tag{8.3.21}$$

The unknown distribution functions at the North East corner $\overline{f}_3, \overline{f}_4, \overline{f}_6, \overline{f}_7, \overline{f}_8$ are found by again solving system (8.3.16) and the slip velocity is calculated using the relations $\Pi_{xy} = -(-\mu\partial_y u_{wall})$ and $u_s = \frac{l_s}{\mu}\Pi_{xy}$ because the shear stress is negative toward the North wall.

8.3.2 Simulation

8.3.2.1 The velocity profile

Figures (8.2) to (8.5) show an excellent agreement between the velocity profiles and the exact solutions at different heights H, Knudsen numbers k_{n_0}, aspect ratios $\varepsilon = L/H$ and Λ_{pr}. Moreover, the velocity profiles are convergent with exact solutions from $H = 20$ at each Knudsen number k_{n_0}. However, a change in the Knudsen number k_{n_0} and aspect ratio ε does have an effect at each height where the decrease of Knudsen number k_{n_0} leads to a decrease in both the slip velocity

and the maximum velocity. Also, increasing the pressure ratio leads to an increase in the slip velocity and maximum velocity as shown in Figures (8.3) and (8.5).

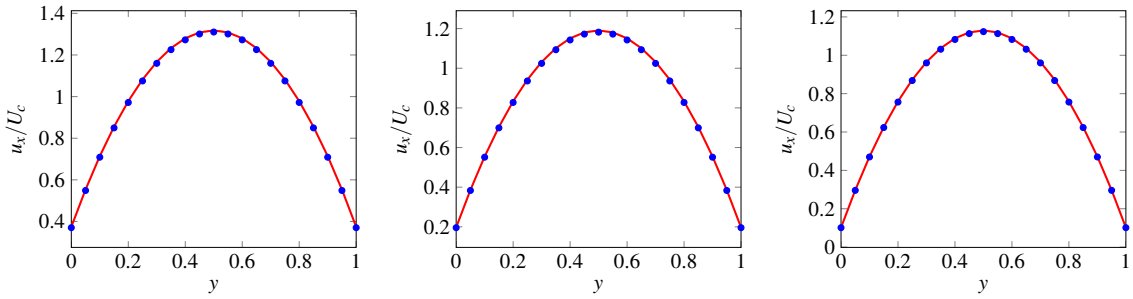

(a) $k_{n_0} = 0.1$ and $L/H = 20$ *(b)* $k_{n_0} = 0.05$ and $L/H = 40$ *(c)* $k_{n_0} = 0.025$ and $L/H = 80$

Figure 8.2: The velocity profiles at $H = 20$ and $\Lambda_{pr} = 2$ in 2D. Blue circle: velocity profiles of LBM; Red line: exact solution.

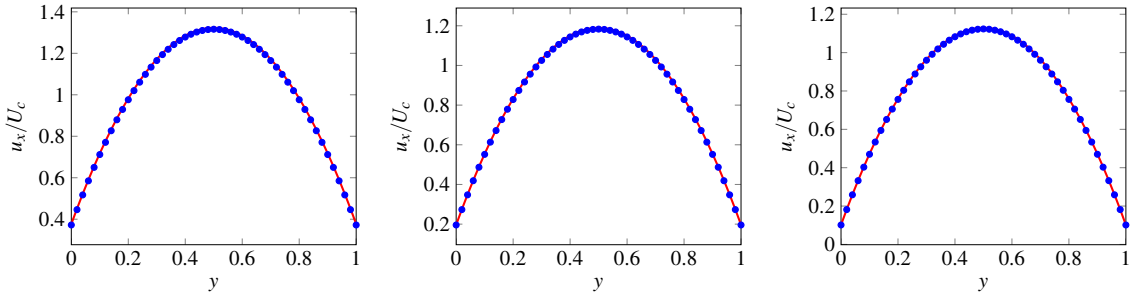

(a) $k_{n_0} = 0.1$ and $L/H = 20$ *(b)* $k_{n_0} = 0.05$ and $L/H = 40$ *(c)* $k_{n_0} = 0.025$ and $L/H = 80$

Figure 8.3: The velocity profiles at $H = 50$ and $\Lambda_{pr} = 2$ in 2D. Blue circle: velocity profiles of LBM; Red line: exact solution.

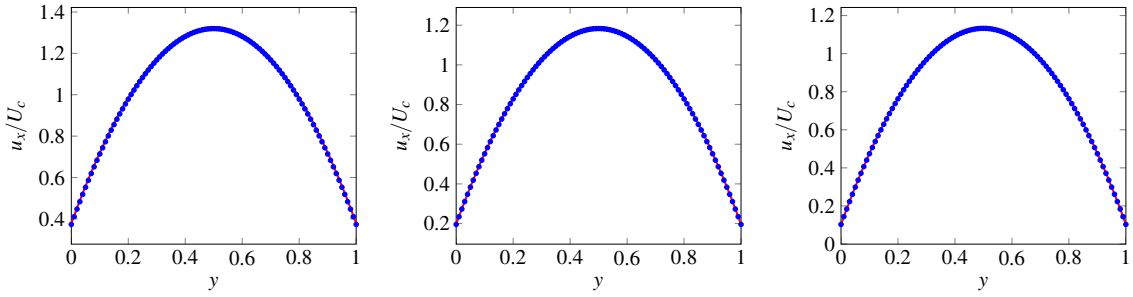

(a) $k_{n_0} = 0.1$ and $L/H = 20$ *(b)* $k_{n_0} = 0.05$ and $L/H = 40$ *(c)* $k_{n_0} = 0.025$ and $L/H = 80$

Figure 8.4: The velocity profiles at $H = 100$ and $\Lambda_{pr} = 2$ in 2D. Blue circle: the velocity profiles of LBM; Red line: the exact solution.

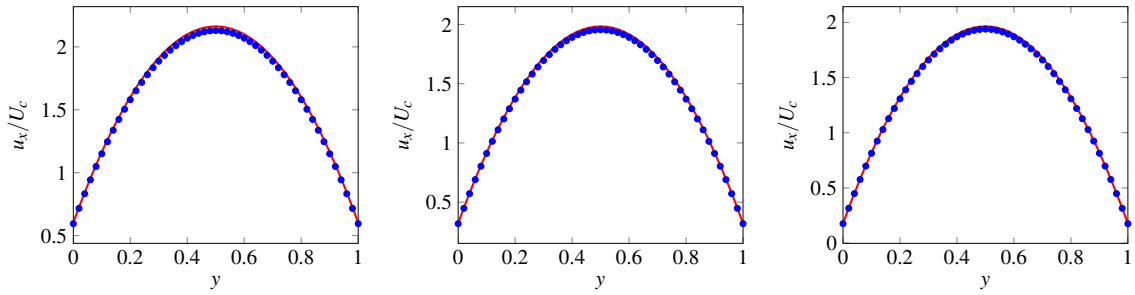

(a) $k_{n_0} = 0.1$ and $L/H = 20$

(b) $k_{n_0} = 0.05$ and $L/H = 40$

(c) $k_{n_0} = 0.025$ and $L/H = 80$

Figure 8.5: The velocity profiles at $H = 50$ and $\Lambda_{pr} = 2.5$, in 2D. Blue circle: the velocity profiles of LBM; Red line: the exact solution.

8.3.2.2 The pressure deviation

Figure (8.6) shows that rarefaction increases exactly as Arkilic's exact solution suggests [3] and there is also good agreement between the pressure deviation of the LBM and Arkilic's exact solution [3] with $\Lambda_{pr} = 2$ and aspect ratio $L/H = 20$, $L/H = 40$ and $L/H = 80$ for $k_{n_0} = 0.1$, $k_{n_0} = 0.05$ and $k_{n_0} = 0.025$, respectively. However, rarefaction increases slightly compared with the exact solution from Arkilic [3] with $\Lambda_{pr} = 2.5$ and aspect ratio $L/H = 20$, $L/H = 40$ and $L/H = 80$ for $k_{n_0} = 0.1$, $k_{n_0} = 0.05$ and $k_{n_0} = 0.025$, respectively, but matches exactly with his solution [3] with $\Lambda_{pr} = 2.5$ and aspect ratio $L/H = 40$, $L/H = 80$ and $L/H = 160$ for $k_{n_0} = 0.1$, $k_{n_0} = 0.05$ and $k_{n_0} = 0.025$ respectively, as seen in Figures (8.7) and (8.8). The value of the pressure deviation is increased by increasing the pressure ratio as shown in Figures (8.6)(b) and (8.7). The change of height does not affect the agreement or rarefaction between the pressure deviation of the LBM and the exact solution with $\Lambda_{pr} = 2$, and this means $H = 20$ is enough to obtain the convergence between the pressure deviation of the LBM and the exact solution $\Lambda_{pr} = 2$ as shown in Figure (8.6), while a decrease in k_{n_0} leads to a increase in the maximum of the pressure deviation as seen in Figure (8.6), Figure (8.7) and Figure (8.8).

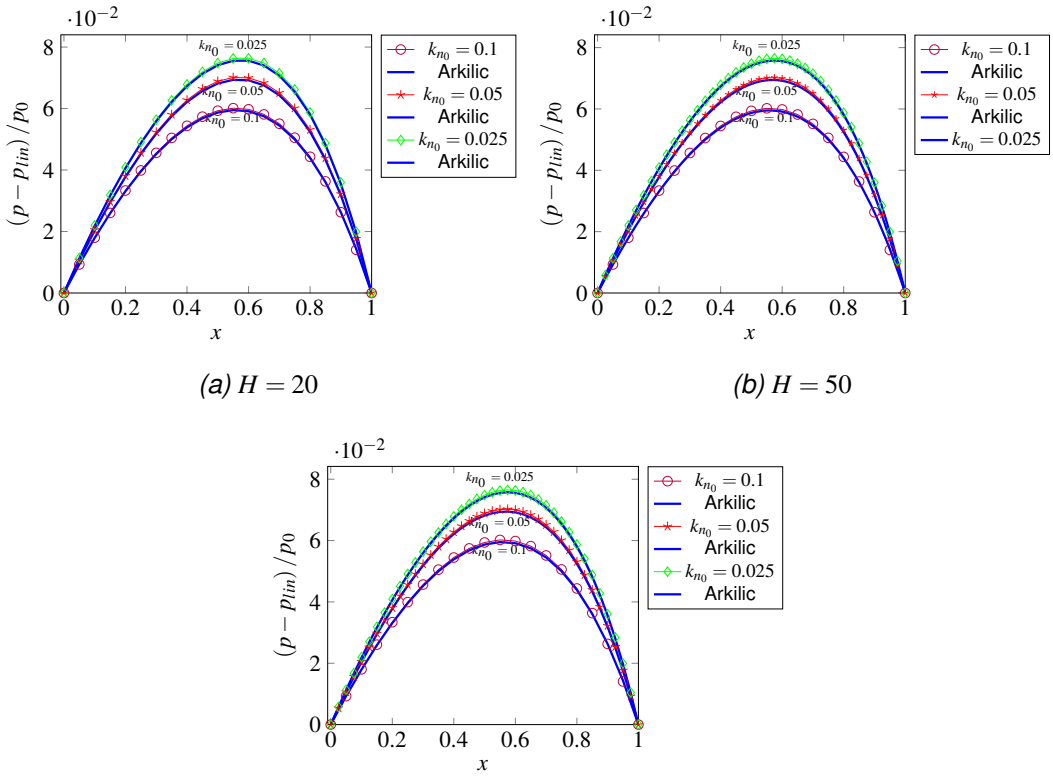

(a) $H = 20$ *(b)* $H = 50$

(c) $H = 100$

Figure 8.6: The pressure deviation at $\Lambda_{pr} = 2$, $k_{n_0} = 0.1$ with $L/H = 20$, $k_{n_0} = 0.05$ and $L/H = 40$, $k_{n_0} = 0.025$ and $L/H = 80$ in 2D.

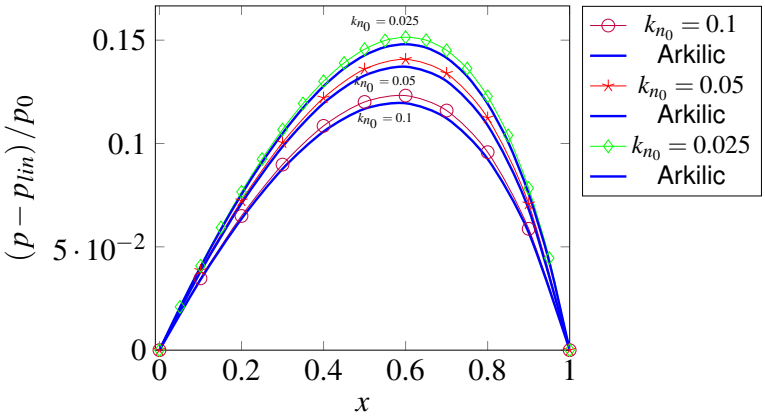

(a) $H = 50$

Figure 8.7: The pressure deviation at $\Lambda_{pr} = 2.5$, $k_{n_0} = 0.1$ with $L/H = 20$, $k_{n_0} = 0.05$ and $L/H = 40$, $k_{n_0} = 0.025$ and $L/H = 80$, in 2D.

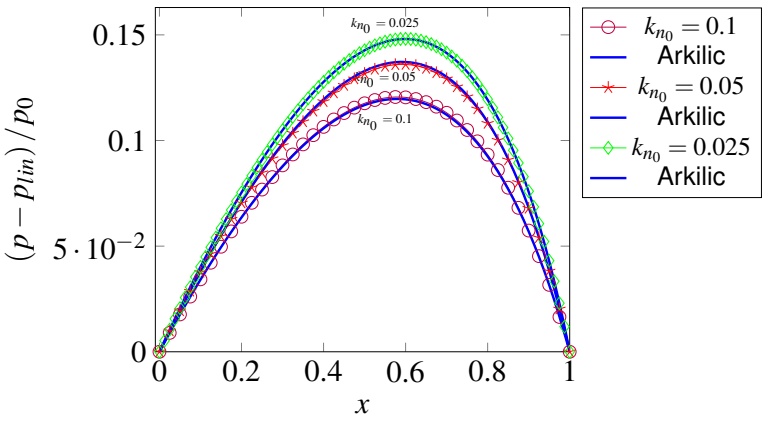

(a) $H = 50$,$\Lambda_{pr} = 2.5$ L/H start from 40

Figure 8.8: The pressure deviation at $\Lambda_{pr} = 2.5$, $k_{n_0} = 0.1$ with $L/H = 40$, $k_{n_0} = 0.05$ and $L/H = 80$, $k_{n_0} = 0.025$ and $L/H = 160$, in 2D.

It is clear from Figure (8.9)(a) that the pressure deviation in this present work, which is based on moment boundary conditions, agrees well with the analytical solution of Arkilic at $H = 50$, $k_{n_0} = 0.1$, $k_{n_0} = 0.05$ and $k_{n_0} = 0.025$ with $\Lambda_{pr} = 2$. Lee and Lin [38] presented that rarefaction is slightly decreased at $k_{n_0} = 0.1$ with $L/H = 20$ and is slightly increased at $k_{n_0} = 0.025$ with $L/H = 80$ with $\Lambda_{pr} = 2$, using wall equilibrium boundary condition. Figure (8.9)(b) and (c) illustrates that the present pressure deviation at $k_{n_0} = 0.05, 0.1$ has a stronger agreement with the analytical solution of Arkilic at $H = 50$ than that presented by Lim *et. al* [40] using two kinds of boundary conditions: specular and extrapolation. Furthermore, their peak of pressure deviation was deviated at the outlet more than Arkilic's because they were interested "in a more rarefied sense" *et. al* [40] (p.2304) and they compare their results with experimental results, whilst Arkilic used the first order of slip velocity.

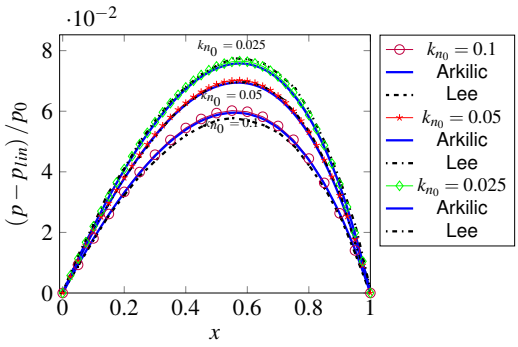

(a) $H = 50$

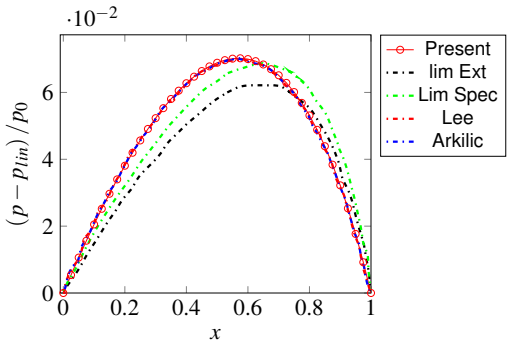

(b) $H = 50$, $k_{n_0} = 0.05$

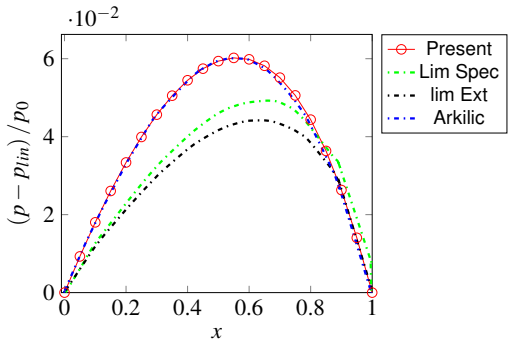

(c) $H = 50$, $k_{n_0} = 0.1$

Figure 8.9: Comparison of the pressure deviation between the present work and the other authors at $\Lambda_{pr} = 2$, in 2D.

8.3.2.3 Slip velocity

Figures (8.10) and (8.11) demonstrate that slip velocity with $H = 20$ is very close to the slip velocity with $H = 50$. The present slip velocity with $H = 50$ accords with that of Arkilic at different k_{n_0} and at $k_{n_0} = 0.1$ and it accords with slip velocity of Arkilic more than that of Lee. Moreover, the slip velocities obtained by Lim *et. al* are much lower than those obtained by either Arkilic, Lee or the present work at $k_{n_0} = 0.05$ as seen in Figure (8.12). The excellent agreement of the present study is due to the moment boundary condition used in this model and its consequent determination of the exact value of slip velocity. A decrease in the k_{n_0} causes a decrease in the slip velocity. In addition, slip velocity is increased by increasing the pressure, and this is shown in Figures (8.10)(b) and (8.11).

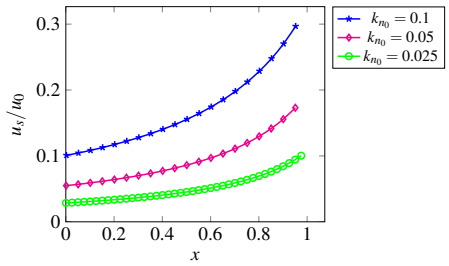

(a) $H = 20$

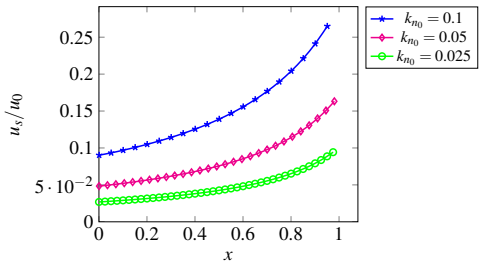

(b) $H = 50$

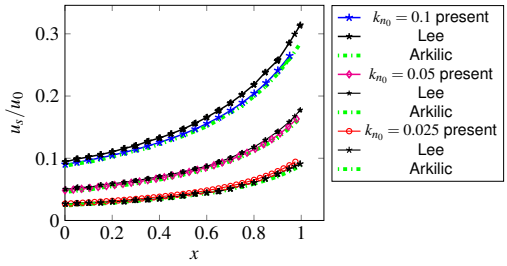

(c) $H = 50$ Lee and Arkilic

Figure 8.10: The slip velocity at $\Lambda_{pr} = 2$ with $k_{n_0} = 0.1$ for $L/H = 20$, $k_{n_0} = 0.05$ for $L/H = 40$ and $k_{n_0} = 0.025$ for $L/H = 80$,in 2D, (c) red: Arkilic and black: Lee.

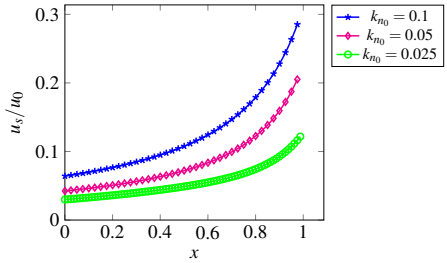

(a) $H = 50$

Figure 8.11: The slip velocity at $\Lambda_{pr} = 2.5$ with $k_{n_0} = 0.1$ for $L/H = 40$, $k_{n_0} = 0.05$ for $L/H = 80$ and $k_{n_0} = 0.025$ for $L/H = 160$, in 2D.

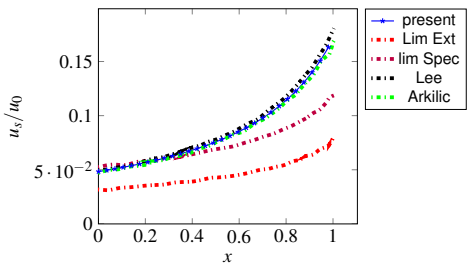

(a) $k_{n_0} = 0.05$

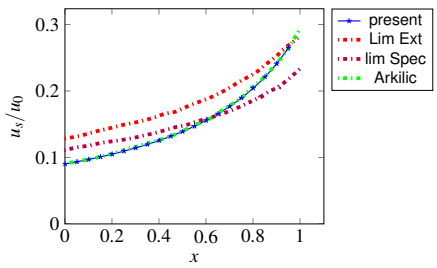

(b) $k_{n_0} = 0.1$

Figure 8.12: Comparison of the slip velocity between our present work and the other authors, at $\Lambda_{pr} = 2$.

8.3.2.4 Mass flow

The mass flow of the LBM with moment-based boundary conditions is conserved and is the same at both the inlet and the outlet at each H, k_{n_0}, Λ_{pr} and ε. The mass flow is not greatly affected by changing the height H at each k_{n_0}, as is illustrated in Table (8.3). However, it is affected by changing the k_{n_0} at each H and Λ_{pr} as Table(8.3) shows, in addition to showing that changes in pressure reduce mass flow.

The height H and pressure ratio Λ_{pr}	Mass flow	k_{n_0}
$H = 20$, $\Lambda_{pr} = 2$	0.0627 0.05388 0.0494	0.1 0.05 0.025
$H = 50$, $\Lambda_{pr} = 2$	0.0629 0.05396 0.04948	0.1 0.05 0.025
$H = 50$, $\Lambda_{pr} = 2.5$	0.0529 0.04596 0.0427	0.1 0.05 0.025

Table 8.3: The relation between mass flow and k_{n_0} in 2D.

8.3.2.5 Norm error L_2

The numerical norm error for velocity profile at the outlet is first order $\Lambda_{pr} = 2$ with $k_{n_0} = 0.1$ for $L/H = 20$, $k_{n_0} = 0.05$ for $L/H = 40$ and $k_{n_0} = 0.025$ for $L/H = 80$. For slip velocity, the numerical norm error is also second order with $k_{n_0} = 0.1, 0.05$ and small grid size, and first order with large grid size, $k_{n_0} = 0.1, 0.05$ and $k_{n_0} = 0.025$ at $\Lambda_{pr} = 2$. Thus, we estimate the error to be first order at various Λ_{pr}, H, k_{n_0} and ε. The convergence study is based on a calculation of the numerical norm error between $H = 20, 40, 80, 160$ with $H_{fine} = 320$. The error for slip velocity is decreased by decreasing k_{n_0} as seen in Figure (8.13)(b).

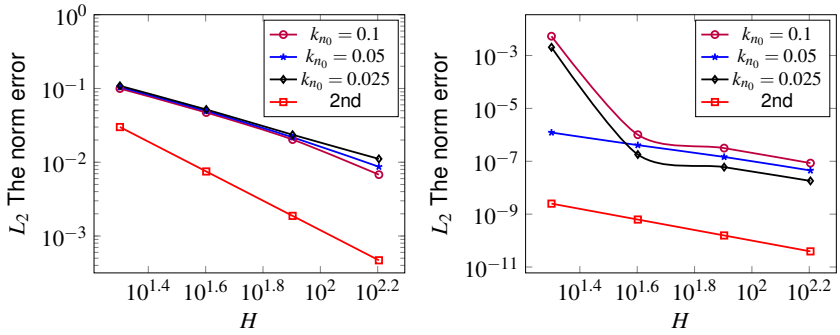

(a) velocity profile u_x *(b)* slip velocity profile u_s

Figure 8.13: The norm error at $\Lambda_{pr} = 2$, $H = 20$ and fine grid point of $n_x = 320$, with $k_{n_0} = 0.1$ for $L/H = 20$, $k_{n_0} = 0.05$ for $L/H = 40$ and $k_{n_0} = 0.025$ for $L/H = 80$, in 2D.

8.4 3D narrow micro-duct

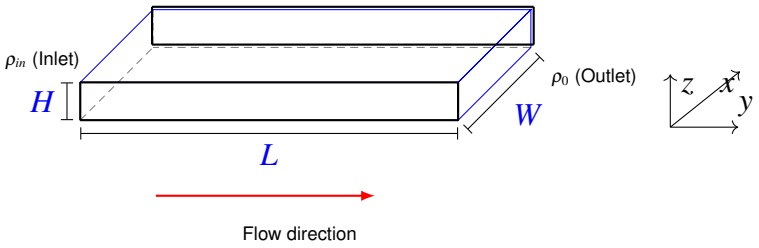

Figure 8.14: 3D narrow micro-duct.

8.4.1 Moment boundary conditions with Navier-slip and pressure gradient in three dimensions

In this simulation, moment-based boundary conditions are used to implement Navier-slip boundary conditions on the West, East, South and North walls and pressure boundary conditions at the inlet and outlet, as follows.

8.4.1.1 Pressure boundary conditions

The slip velocity is assumed at y-direction, and zero velocity assumed for the x, z-direction, thus

$$u_x = u_z = 0, u_y = u_{sy}. \tag{8.4.1}$$

The moments will be:

$$\begin{aligned}
\rho u_x = \rho u_z = 0,\\
\rho u_y = \rho u_{sy},\\
\Pi^0_{xx} = \frac{\rho}{3}\delta_{xx} + \rho u_x u_x = \frac{\rho}{3},\\
\Pi^0_{yy} = \frac{\rho}{3}\delta_{yy} + \rho u_y u_y = \frac{\rho}{3} + \rho u^2_{sy},\\
\Pi^0_{zz} = \frac{\rho}{3}\delta_{zz} + \rho u_z u_z = \frac{\rho}{3}.
\end{aligned} \tag{8.4.2}$$

From the Chapman-Enskog expansion the momentum flux tensor in x,y- and z-direction is defined as

$$\Pi_{xx} = \Pi^0_{xx} + \tau\Pi^1_{xx} = \frac{\rho}{3} - \tau\frac{2\rho}{3}\partial_x u_x = \frac{\rho}{3},$$

$$\Pi_{yy} = \Pi^0_{yy} + \tau\Pi^1_{yy} = \frac{\rho}{3} + \rho u^2_{sy} - \tau\frac{2\rho}{3}\partial_y u_y = \frac{\rho}{3} + \rho u^2_{sy},$$

and

$$\Pi_{zz} = \Pi^0_{zz} + \tau\Pi^1_{zz} = \frac{\rho}{3} - \tau\frac{2\rho}{3}\partial_z u_z = \frac{\rho}{3}.$$

Consequently, the bar moments are

$$\begin{aligned}
\rho\overline{u}_x = \rho u_x = 0,\\
\rho\overline{u}_y = \rho u_y = \rho u_{sy},\\
\rho\overline{u}_z = \rho u_z = 0,\\
\overline{\Pi}_{xx} = \Pi_{xx} + \frac{\delta_t}{2\tau}\Pi_{xx} - \frac{\delta_t}{2\tau}\Pi^0_{xx} = \frac{\rho}{3},\\
\overline{\Pi}_{yy} = \Pi_{yy} + \frac{\delta_t}{2\tau}\Pi_{yy} - \frac{\delta_t}{2\tau}\Pi^0_{yy} = \frac{\rho}{3} + \rho u^2_{sy},\\
\overline{\Pi}_{zz} = \Pi_{zz} + \frac{\delta_t}{2\tau}\Pi_{zz} - \frac{\delta_t}{2\tau}\Pi^0_{zz} = \frac{\rho}{3}.
\end{aligned} \tag{8.4.3}$$

To find the unknown distribution functions at the inlet pressure boundary we use five moments which are

$$\begin{aligned}
\rho &= \overline{f}_0+\overline{f}_1+\overline{f}_2+\overline{f}_3+\overline{f}_4+\overline{f}_5+\overline{f}_6+\overline{f}_7+\overline{f}_8+\overline{f}_9+\overline{f}_{10}+\overline{f}_{11}+\overline{f}_{12}+\overline{f}_{13}+\overline{f}_{14} \\
&\quad +\overline{f}_{15}+\overline{f}_{16}+\overline{f}_{17}+\overline{f}_{18}, \\
\rho\overline{u}_x &= \overline{f}_1-\overline{f}_2+\overline{f}_7-\overline{f}_8-\overline{f}_9+\overline{f}_{10}+\overline{f}_{11}+\overline{f}_{12}-\overline{f}_{13}-\overline{f}_{14}=0, \\
\rho\overline{u}_z &= \overline{f}_5-\overline{f}_6+\overline{f}_{11}-\overline{f}_{12}-\overline{f}_{13}+\overline{f}_{14}+\overline{f}_{15}-\overline{f}_{16}-\overline{f}_{17}+\overline{f}_{18}=0, \\
\overline{\Pi}_{xx} &= \overline{f}_1+\overline{f}_2+\overline{f}_7+\overline{f}_8+\overline{f}_9+\overline{f}_{10}+\overline{f}_{11}+\overline{f}_{12}+\overline{f}_{13}+\overline{f}_{14}=\frac{\rho}{3}, \\
\overline{\Pi}_{zz} &= \overline{f}_5+\overline{f}_6+\overline{f}_{11}+\overline{f}_{12}+\overline{f}_{13}+\overline{f}_{14}+\overline{f}_{15}+\overline{f}_{16}+\overline{f}_{17}+\overline{f}_{18}=\frac{\rho}{3}.
\end{aligned} \tag{8.4.4}$$

This system (8.4.4) can then be used to find the unknown distribution functions at the inlet pressure boundary which are

$$\overline{f}_3,\overline{f}_7,\overline{f}_8,\overline{f}_{15},\overline{f}_{16}, \tag{8.4.5}$$

so,

$$\begin{aligned}
\overline{f}_3 &= -\overline{f}_0-\overline{f}_4+\overline{f}_{11}+\overline{f}_{12}+\overline{f}_{13}+\overline{f}_{14}+\frac{\rho_{in}}{3}, \\
\overline{f}_7 &= -\overline{f}_1-\overline{f}_0-\overline{f}_{11}-\overline{f}_{12}+\frac{\rho_{in}}{6}, \\
\overline{f}_8 &= -\overline{f}_2-\overline{f}_9-\overline{f}_{13}-\overline{f}_{14}+\frac{\rho_{in}}{6}, \\
\overline{f}_{15} &= -\overline{f}_5-\overline{f}_{11}-\overline{f}_{14}-\overline{f}_{18}+\frac{\rho_{in}}{6}, \\
\overline{f}_{16} &= -\overline{f}_6-\overline{f}_{12}-\overline{f}_{13}-\overline{f}_{17}+\frac{\rho_{in}}{6}.
\end{aligned} \tag{8.4.6}$$

We also use the same system (8.4.4) to find the unknown distribution functions at the outlet pressure boundary, which are $\overline{f}_4,\overline{f}_9,\overline{f}_{10},\overline{f}_{17},\overline{f}_{18}$.

The system to find the unknown distribution at the South inlet, South outlet,

North inlet and North outlet edges is

$$
\begin{aligned}
\rho &= \overline{f}_0+\overline{f}_1+\overline{f}_2+\overline{f}_3+\overline{f}_4+\overline{f}_5+\overline{f}_6+\overline{f}_7+\overline{f}_8+\overline{f}_9+\overline{f}_{10}+\overline{f}_{11}+\overline{f}_{12}+\overline{f}_{13}+\overline{f}_{14}\\
&\quad+\overline{f}_{15}+\overline{f}_{16}+\overline{f}_{17}+\overline{f}_{18},\\
\rho\overline{u}_x &= \overline{f}_1-\overline{f}_2+\overline{f}_7-\overline{f}_8-\overline{f}_9+\overline{f}_{10}+\overline{f}_{11}+\overline{f}_{12}-\overline{f}_{13}-\overline{f}_{14}=0,\\
\rho\overline{u}_y &= \overline{f}_3-\overline{f}_4+\overline{f}_7+\overline{f}_8-\overline{f}_9-\overline{f}_{10}+\overline{f}_{15}+\overline{f}_{16}-\overline{f}_{17}-\overline{f}_{18}=\rho u_{sy},\\
\rho\overline{u}_z &= \overline{f}_5-\overline{f}_6+\overline{f}_{11}-\overline{f}_{12}-\overline{f}_{13}+\overline{f}_{14}+\overline{f}_{15}-\overline{f}_{16}-\overline{f}_{17}+\overline{f}_{18}=0,\\
\overline{\Pi}_{xx} &= \overline{f}_1+\overline{f}_2+\overline{f}_7+\overline{f}_8+\overline{f}_9+\overline{f}_{10}+\overline{f}_{11}+\overline{f}_{12}+\overline{f}_{13}+\overline{f}_{14}=\frac{\rho}{3},\\
\overline{\Pi}_{yy} &= \overline{f}_3+\overline{f}_4+\overline{f}_7+\overline{f}_8+\overline{f}_9+\overline{f}_{10}+\overline{f}_{15}+\overline{f}_{16}+\overline{f}_{17}+\overline{f}_{18}=\frac{\rho}{3}+\rho u_{sy}^2,\\
\overline{\Pi}_{zz} &= \overline{f}_5+\overline{f}_6+\overline{f}_{11}+\overline{f}_{12}+\overline{f}_{13}+\overline{f}_{14}+\overline{f}_{15}+\overline{f}_{16}+\overline{f}_{17}+\overline{f}_{18}=\frac{\rho}{3},\\
\overline{\Pi}_{xz} &= \overline{f}_{11}-\overline{f}_{12}+\overline{f}_{13}-\overline{f}_{14}=0,\\
\overline{Q}_{xxz} &= \overline{f}_{11}-\overline{f}_{12}-\overline{f}_{13}+\overline{f}_{14}=\frac{-\rho}{3}\left(\frac{2\tau+\delta_t}{2}\right)\frac{2(\pm u_{sy})}{l_s}u_{sy},\\
\overline{Q}_{yzz} &= \overline{f}_{15}+\overline{f}_{16}-\overline{f}_{17}-\overline{f}_{18}=\frac{\rho}{3}u_{sy},
\end{aligned}
\tag{8.4.7}
$$

where

$$
\begin{aligned}
Q_{xxz} &= Q^0_{xxz}+\tau Q^1_{xxz}=\frac{\rho}{3}u_z+\tau\frac{\rho}{3}\partial_z u_y^2=\tau\frac{\rho}{3}\partial_z u_y^2,\\
\overline{Q}_{xxz} &= \frac{-\rho}{3}\left(\frac{2\tau+\delta_t}{2}\right)\left[\partial_z u_y^2\right]=\frac{-\rho}{3}\left(\frac{2\tau+\delta_t}{2}\right)\left[\partial_z u_y\right]u_y,\\
&= \frac{-\rho}{3}\left(\frac{2\tau+\delta_t}{2}\right)\left[u_y\partial_z u_y+\partial_z u_y u_y\right],\\
&= \frac{-\rho}{3}\left(\frac{2\tau+\delta_t}{2}\right)\left[u_{sy}\frac{u_{sy}}{l_s}+\frac{u_{sy}}{l_s}u_{sy}\right],\\
&= \frac{-\rho}{3}\left(\frac{2\tau+\delta_t}{2}\right)\frac{2(\pm u_{sy})}{l_s}u_{sy},\partial_z u_y=\frac{u_{sy}}{l_s},
\end{aligned}
\tag{8.4.8}
$$

or $\overline{Q}_{xxz}=\overline{\Pi}_{yz}2u_{sy}$, where $\overline{\Pi}_{yz}=\frac{-\rho}{3}\left(\frac{2\tau+\delta_t}{2}\right)\frac{(\pm u_{sy})}{l_s}$, for more details how we calculate the $\overline{Q}_{xxz}$ and $\overline{Q}_{yzz}$ see the Appendix (A). At the South inlet edge the shear stress keeps its sign because it is positive toward the South wall, thus $\overline{\Pi}_{yz}=\frac{-\rho}{3}\left(\frac{2\tau+\delta_t}{2}\right)\frac{(u_{sy})}{l_s}$.
Also, $Q_{yzz}=Q^0_{yzz}+\tau Q^1_{yzz}=\frac{\rho}{3}u_y+\tau\left(\frac{\rho}{3}u_y\partial_y u_y+\frac{\rho}{3}\partial_y u_y^2\right)=\frac{\rho}{3}u_y=\frac{\rho}{3}u_{sy}$ so $\overline{Q}_{yzz}=\frac{\rho}{3}u_{sy}$.
By solving system (8.4.7) we find the unknown distribution functions at the South

inlet and outlet edges. The unknown distribution functions at the South inlet edge are

$$\overline{f}_3, \overline{f}_5, \overline{f}_7, \overline{f}_8, \overline{f}_{11}, \overline{f}_{14}, \overline{f}_{15}, \overline{f}_{16}, \overline{f}_{18}. \tag{8.4.9}$$

$$\begin{aligned}
\overline{f}_3 &= -\overline{f}_0 - \overline{f}_4 + 2\left(\overline{f}_{12} + \overline{f}_{13}\right) - \frac{\rho_{in}\left(2\tau+1\right)}{3}\frac{u_{sy}^2}{l_s} + \frac{\rho_{in}}{3}, \\
\overline{f}_5 &= -\left(\overline{f}_0 + \overline{f}_1 + \overline{f}_2\right) - \overline{f}_6 - 2\left(\overline{f}_{12} + \overline{f}_{13}\right) + \frac{\rho_{in}\left(2\tau+1\right)}{3}\frac{u_{sy}^2}{l_s} - \rho_{in}u_{sy}^2 + \frac{2\rho_{in}}{3}, \\
\overline{f}_7 &= -\overline{f}_1 - \overline{f}_{10} - 2\overline{f}_{12} + \frac{\rho_{in}\left(2\tau+1\right)}{6}\frac{u_{sy}^2}{l_s} - \frac{\rho_{in}}{6}, \\
\overline{f}_8 &= -\overline{f}_2 - \overline{f}_9 - 2\overline{f}_{13} + \frac{\rho_{in}\left(2\tau+1\right)}{6}\frac{u_{sy}^2}{l_s} - \frac{\rho_{in}}{6}, \\
\overline{f}_{11} &= \overline{f}_{12} - \frac{\rho\left(2\tau+1\right)}{6}\frac{u_{sy}^2}{l_s}, \\
\overline{f}_{14} &= \overline{f}_{13} - \frac{\rho\left(2\tau+1\right)}{6}\frac{u_{sy}^2}{l_s}, \\
\overline{f}_{15} &= \frac{1}{2}\left(\overline{f}_0 + \overline{f}_1 + \overline{f}_2\right) + \overline{f}_6 + \overline{f}_{12} + \overline{f}_{13} + \overline{f}_{17} + \frac{\rho_{in}}{2}u_{sy}^2 + \frac{\rho_{in}}{6}u_{sy} - \frac{\rho_{in}}{3}, \\
\overline{f}_{16} &= -\overline{f}_6 - \overline{f}_{12} - \overline{f}_{13} - \overline{f}_{17} + \frac{\rho_{in}}{6}, \\
\overline{f}_{18} &= \frac{1}{2}\left(\overline{f}_0 + \overline{f}_1 + \overline{f}_2\right) - \overline{f}_{17} + \frac{\rho_{in}}{2}u_{sy}^2 - \frac{\rho_{in}}{6}u_{sy} - \frac{\rho_{in}}{6}.
\end{aligned} \tag{8.4.10}$$

The slip velocities at the South inlet and outlet edges are calculated by using the momentum flux tensor Π_{yz}, so, using the Chapman-Enskog expansion

$$\Pi_{yz} = \Pi_{yz}^0 + \tau\Pi_{yz}^1 = \frac{\rho}{3}\delta_{yz} + \rho u_y u_z + \tau\frac{-\rho}{3}\left(\partial_y u_z + \partial_z u_y\right) = \tau\frac{-\rho}{3}\partial_z u_y.$$

The slip velocity is defined, like in previous chapters, as proportional to the shear stress at the wall $u_s = l_s\partial_z u_{wall}$, $n \gtrless 0$. Consequently, $\Pi_{yz} = -\mu\partial_y u_{wall}$ and $u_s = -\dfrac{l_s}{\mu}\Pi_{yz}$ because the shear stress is positive toward the South wall. So, the slip velocity is defined as

$$\rho u_s = \rho\frac{-l_s}{\mu}\frac{2\tau}{2\tau+1}\overline{\Pi}_{yz}, \tag{8.4.11}$$

where $\rho\dfrac{-l_s}{\mu}\dfrac{2\tau}{2\tau+1}=\dfrac{-6l_s}{(2\tau+1)}$, so,

$$u_{sy}=\left(\frac{-6l_s}{\rho_{in}(2\tau+1)}\left(\overline{f}_{15}-\overline{f}_{16}+\overline{f}_{17}-\overline{f}_{18}\right)\right) \tag{8.4.12}$$

$$=\left(\frac{-6l_s}{\rho_{in}(2l_s+2\tau+1)}\right)\left(2\overline{f}_{12}-2\overline{f}_{13}+4\overline{f}_{17}+2\overline{f}_{6}-\frac{\rho_{in}}{3}\right). \tag{8.4.13}$$

The unknown distribution functions $\overline{f}_4,\overline{f}_5,\overline{f}_9,\overline{f}_{10},\overline{f}_{11},\overline{f}_{14},\overline{f}_{15},\overline{f}_{17},\overline{f}_{18}$ at the South outlet edge are found by solving system (8.4.7).

By solving system (8.4.7) we also find the unknown distribution functions at the North inlet and outlet edges, with negative sign for the shear stress $-\Pi_{yz}$ toward the North wall. The slip velocity at the North inlet edge is found by using the relations $\Pi_{yz}=\mu\partial_y u_{wall}$ and $u_s=\dfrac{l_s}{\mu}\Pi_{yz}$ because the shear stress is negative toward the North wall.

The system to find the unknown distribution function at the West inlet and outlet edges, and the East inlet and outlet edges is

$$\begin{aligned}
\rho&=\overline{f}_0+\overline{f}_1+\overline{f}_2+\overline{f}_3+\overline{f}_4+\overline{f}_5+\overline{f}_6+\overline{f}_7+\overline{f}_8+\overline{f}_9+\overline{f}_{10}+\overline{f}_{11}+\overline{f}_{12}+\overline{f}_{13}+\overline{f}_{14},\\
&\quad+\overline{f}_{15}+\overline{f}_{16}+\overline{f}_{17}+\overline{f}_{18},\\
\rho\overline{u}_x&=\overline{f}_1-\overline{f}_2+\overline{f}_7-\overline{f}_8-\overline{f}_9+\overline{f}_{10}+\overline{f}_{11}+\overline{f}_{12}-\overline{f}_{13}-\overline{f}_{14}=0,\\
\rho\overline{u}_y&=\overline{f}_3-\overline{f}_4+\overline{f}_7+\overline{f}_8-\overline{f}_9-\overline{f}_{10}+\overline{f}_{15}+\overline{f}_{16}-\overline{f}_{17}-\overline{f}_{18}=\rho u_{sy},\\
\rho\overline{u}_z&=\overline{f}_5-\overline{f}_6+\overline{f}_{11}-\overline{f}_{12}-\overline{f}_{13}+\overline{f}_{14}+\overline{f}_{15}-\overline{f}_{16}-\overline{f}_{17}+\overline{f}_{18}=0,\\
\overline{\Pi}_{xx}&=\overline{f}_1+\overline{f}_2+\overline{f}_7+\overline{f}_8+\overline{f}_9+\overline{f}_{10}+\overline{f}_{11}+\overline{f}_{12}+\overline{f}_{13}+\overline{f}_{14}=\frac{\rho}{3},\\
\overline{\Pi}_{yy}&=\overline{f}_3+\overline{f}_4+\overline{f}_7+\overline{f}_8+\overline{f}_9+\overline{f}_{10}+\overline{f}_{15}+\overline{f}_{16}+\overline{f}_{17}+\overline{f}_{18}=\frac{\rho}{3}+\rho u_{sy}^2,\\
\overline{\Pi}_{zz}&=\overline{f}_5+\overline{f}_6+\overline{f}_{11}+\overline{f}_{12}+\overline{f}_{13}+\overline{f}_{14}+\overline{f}_{15}+\overline{f}_{16}+\overline{f}_{17}+\overline{f}_{18}=\frac{\rho}{3},\\
\overline{\Pi}_{xz}&=\overline{f}_{11}-\overline{f}_{12}+\overline{f}_{13}-\overline{f}_{14}=0,\\
\overline{Q}_{xzz}&=\overline{f}_{11}+\overline{f}_{12}-\overline{f}_{13}-\overline{f}_{14}=\frac{-\rho}{3}\left(\frac{2\tau+\delta_t}{2}\right)\frac{2(\pm u_{sy})}{l_s}u_{sy},\\
\overline{Q}_{xxy}&=\overline{f}_7+\overline{f}_8-\overline{f}_9-\overline{f}_{10}=\frac{\rho}{3}u_{sy},
\end{aligned} \tag{8.4.14}$$

where

$$
\begin{aligned}
Q_{xzz} = Q^0_{xzz} + \tau Q^1_{xzz} = \frac{\rho}{3}u_x + \tau\frac{\rho}{3}\partial_x u_y^2 = \tau\frac{\rho}{3}\partial_x u_y^2,\\
\overline{Q}_{xzz} = \frac{-\rho}{3}\left(\frac{2\tau+\delta_t}{2}\right)\left[\partial_x u_y^2\right] = \frac{-\rho}{3}\left(\frac{2\tau+\delta_t}{2}\right)\left[\partial_x u_y\right]u_y,\\
= \frac{-\rho}{3}\left(\frac{2\tau+\delta_t}{2}\right)\left[u_y\partial_x u_y + \partial_x u_y u_y\right],\\
= \frac{-\rho}{3}\left(\frac{2\tau+\delta_t}{2}\right)\left[u_{sy}\frac{u_{sy}}{l_s} + \frac{u_{sy}}{l_s}u_{sy}\right],\\
= \frac{-\rho}{3}\left(\frac{2\tau+\delta_t}{2}\right)\frac{2\left(\pm u_{sy}\right)}{l_s}u_{sy}, \partial_x u_y = \frac{u_{sy}}{l_s},
\end{aligned}
\tag{8.4.15}
$$

or $\overline{Q}_{xzz} = \overline{\Pi}_{xy}2u_{sy}$, where $\overline{\Pi}_{xy} = \frac{-\rho}{3}\left(\frac{2\tau+\delta_t}{2}\right)\frac{\left(\pm u_{sy}\right)}{l_s}$. In addition, $Q_{xxy} = Q^0_{xxy} + \tau Q^1_{xxy} = \frac{\rho}{3}u_y + \tau\left(\frac{\rho}{3}u_y\partial_y u_y + \frac{\rho}{3}\partial_y u_y^2\right) = \frac{\rho}{3}u_y = \frac{\rho}{3}u_{sy}$ so $\overline{Q}_{xxy} = \frac{\rho}{3}u_{sy}$. At the West inlet and outlet edges the shear stress increases toward the West wall, or it has positive sign, so the shear stress or $\overline{\Pi}_{xy}$ will keep its sign.

By solving system (8.4.14) we find the unknown distribution functions at the West inlet and outlet edges.

The unknown distribution functions at the West inlet edge are

$$
\overline{f}_1, \overline{f}_3, \overline{f}_7, \overline{f}_8, \overline{f}_{10}, \overline{f}_{11}, \overline{f}_{12}, \overline{f}_{15}, \overline{f}_{16},
\tag{8.4.16}
$$

so,

$$
\begin{aligned}
\overline{f}_1 &= -\left(\overline{f}_0+\overline{f}_2+\overline{f}_5+\overline{f}_6\right)-2\left(\overline{f}_{13}+\overline{f}_{14}\right)+\frac{\rho_{in}\left(2\tau+1\right)}{3}\frac{u_{sy}^2}{l_s}-\rho_{in}u_{sy}^2+\frac{2\rho_{in}}{3},\\
\overline{f}_3 &= -\overline{f}_0-\overline{f}_4+2\left(\overline{f}_{13}+\overline{f}_{14}\right)-\frac{\rho_{in}\left(2\tau+1\right)}{3}\frac{u_{sy}^2}{l_s}+\frac{\rho_{in}}{3},\\
\overline{f}_7 &= \frac{1}{2}\left(\overline{f}_0+\overline{f}_5+\overline{f}_6\right)+\overline{f}_2+\overline{f}_9+\overline{f}_{13}+\overline{f}_{14}+\frac{\rho_{in}}{2}u_{sy}^2+\frac{\rho_{in}}{6}u_{sy}-\frac{\rho_{in}}{3},\\
\overline{f}_8 &= -\overline{f}_2-\overline{f}_9-\overline{f}_{14}-\overline{f}_{13}+\frac{\rho_{in}}{6},\\
\overline{f}_{10} &= \frac{1}{2}\left(\overline{f}_0+\overline{f}_5+\overline{f}_6\right)-\overline{f}_9+\frac{\rho_{in}}{2}u_{sy}^2-\frac{\rho_{in}}{6}u_{sy}-\frac{\rho_{in}}{6},\\
\overline{f}_{11} &= \overline{f}_{14}-\frac{\rho\left(2\tau+1\right)}{6}\frac{u_{sy}^2}{l_s},\\
\overline{f}_{12} &= \overline{f}_{13}-\frac{\rho\left(2\tau+1\right)}{6}\frac{u_{sy}^2}{l_s},\\
\overline{f}_{15} &= -\overline{f}_5-2\overline{f}_{14}-\overline{f}_{18}+\frac{\rho_{in}\left(2\tau+1\right)}{6}\frac{u_{sy}^2}{l_s}+\frac{\rho_{in}}{6},\\
\overline{f}_{16} &= -\overline{f}_6-2\overline{f}_{13}-\overline{f}_{17}+\frac{\rho_{in}\left(2\tau+1\right)}{6}\frac{u_{sy}^2}{l_s}+\frac{\rho_{in}}{6}.
\end{aligned}
\tag{8.4.17}
$$

The slip velocity at the West inlet and outlet edges is found by using the relations $\Pi_{xy}=-\mu\partial_y u_{wall}$ and $u_s=-\dfrac{l_s}{\mu}\Pi_{xy}$ because the the shear stress increases, or has a positive sign, toward the West wall. As explained previously in section (8.3.1.1), the slip velocity at the West inlet edge will be

$$
\begin{aligned}
u_{sy} &= \left(-\frac{6l_s}{\rho_{in}(2\tau+1)}\left(\overline{f}_7-\overline{f}_8+\overline{f}_9-\overline{f}_{10}\right)\right).\\
&= \left(\frac{6l_s}{\rho_{in}(2l_s+2\tau+1)}\right)\left(2\overline{f}_{13}+2\overline{f}_{14}+4\overline{f}_9+2\overline{f}_2-\frac{\rho_{in}}{3}\right)
\end{aligned}
\tag{8.4.18}
$$

The unknown distribution functions $\overline{f}_1,\overline{f}_4,\overline{f}_7,\overline{f}_9,\overline{f}_{10},\overline{f}_{11},\overline{f}_{12},\overline{f}_{17},\overline{f}_{18}$ at the West outlet edge are found by solving system (8.4.14), from which we can also find the unknown distribution functions at East inlet and outlet edges if we use a negative sign for the shear stress $-\overline{\Pi}_{xy}$. The slip velocity is calculated using the relations $\Pi_{xy}=\mu\partial_y u_{wall}$ and $u_s=\dfrac{l_s}{\mu}\Pi_{xy}$ because the shear stress decreases, or has a negative sign, toward the East wall.

8.4.1.2 Navier-slip boundary condition

To implement Navier-slip boundary conditions we use the same assumptions described previously for pressure boundary conditions $(u_x = u_z = 0, u_y = u_{sy})$. Consequently, to find the unknown distribution functions at the South and North walls, we need to again choose five moments, which in this case are

$$\begin{aligned}
\rho\overline{u}_x &= \overline{f}_1 - \overline{f}_2 + \overline{f}_7 - \overline{f}_8 - \overline{f}_9 + \overline{f}_{10} + \overline{f}_{11} + \overline{f}_{12} - \overline{f}_{13} - \overline{f}_{14} = 0,\\
\rho\overline{u}_y &= \overline{f}_3 - \overline{f}_4 + \overline{f}_7 + \overline{f}_8 - \overline{f}_9 - \overline{f}_{10} + \overline{f}_{15} + \overline{f}_{16} - \overline{f}_{17} - \overline{f}_{18} = \rho u_{sy},\\
\rho\overline{u}_z &= \overline{f}_5 - \overline{f}_6 + \overline{f}_{11} - \overline{f}_{12} - \overline{f}_{13} + \overline{f}_{14} + \overline{f}_{15} - \overline{f}_{16} - \overline{f}_{17} + \overline{f}_{18} = 0,\\
\overline{\Pi}_{xx} &= \overline{f}_1 + \overline{f}_2 + \overline{f}_7 + \overline{f}_8 + \overline{f}_9 + \overline{f}_{10} + \overline{f}_{11} + \overline{f}_{12} + \overline{f}_{13} + \overline{f}_{14} = \frac{\rho}{3},\\
\overline{\Pi}_{yy} &= \overline{f}_3 + \overline{f}_4 + \overline{f}_7 + \overline{f}_8 + \overline{f}_9 + \overline{f}_{10} + \overline{f}_{15} + \overline{f}_{16} + \overline{f}_{17} + \overline{f}_{18} = \frac{\rho}{3} + \rho u_{sy}^2.
\end{aligned} \tag{8.4.19}$$

By solving this system (8.4.19) we then find the unknown distribution functions at the South face, which are

$$\overline{f}_5, \overline{f}_{11}, \overline{f}_{14}, \overline{f}_{15}, \overline{f}_{18}, \tag{8.4.20}$$

hence,

$$\begin{aligned}
\overline{f}_5 &= \overline{f}_1 + \overline{f}_2 + \overline{f}_3 + \overline{f}_4 + \overline{f}_6 + 2\overline{f}_7 + 2\overline{f}_8 + 2\overline{f}_9 + 2\overline{f}_{10} + 2\overline{f}_{12} + 2\overline{f}_{13} +\\
&\quad 2\overline{f}_{16} + 2\overline{f}_{17} - \frac{2}{3}\rho - \rho u_{sy}^2,\\
\overline{f}_{11} &= -\overline{f}_1 - \overline{f}_7 - \overline{f}_{10} - \overline{f}_{12} + \frac{\rho}{6},\\
\overline{f}_{14} &= -\overline{f}_2 - \overline{f}_8 - \overline{f}_9 - \overline{f}_{13} + \frac{\rho}{6},\\
\overline{f}_{15} &= -\overline{f}_3 - \overline{f}_7 - \overline{f}_8 - \overline{f}_{16} + \frac{\rho}{6} + \frac{1}{2}\rho u_{sy} + \frac{1}{2}\rho u_{sy}^2,\\
\overline{f}_{18} &= -\overline{f}_4 - \overline{f}_9 - \overline{f}_{10} - \overline{f}_{17} + \frac{\rho}{6} - \frac{1}{2}\rho u_{sy} + \frac{1}{2}\rho u_{sy}^2.
\end{aligned} \tag{8.4.21}$$

The density is found from the known distribution functions

$$\rho = \overline{f}_0 + \overline{f}_1 + \overline{f}_2 + \overline{f}_3 + \overline{f}_4 + 2\overline{f}_6 + \overline{f}_7 + \overline{f}_8 + \overline{f}_9 + \overline{f}_{10} + 2\overline{f}_{12} + 2\overline{f}_{13} + 2\overline{f}_{16} + 2\overline{f}_{17}. \tag{8.4.22}$$

The slip velocity at the South face is then found by using the relation $\Pi_{yz} = -\mu\partial_y u_{wall}$ and $u_s = -\frac{l_s}{\mu}\Pi_{yz}$, because the shear stress increases toward the South wall. Thus,

$$u_{sy} = \frac{6l_s}{\rho(6l_s+2\tau+1)}\left(-\overline{f}_3+\overline{f}_4-\overline{f}_7-\overline{f}_8+\overline{f}_9+\overline{f}_{10}-2\overline{f}_{16}+2\overline{f}_{17}\right). \tag{8.4.23}$$

The unknown distribution functions $\overline{f}_6, \overline{f}_{12}, \overline{f}_{13}, \overline{f}_{16}, \overline{f}_{17}$ at the North face is found by using the same (8.4.19) and the slip velocity at the North face is found by using the relation $\Pi_{yz} = \mu\partial_y u_{wall}$ and $u_s = \frac{l_s}{\mu}\Pi_{yz}$ because the shear stress is decreasing toward the North wall.

To find the unknown distribution functions at the East and West faces we use five moments which are

$$\begin{aligned}
\rho\overline{u}_x &= \overline{f}_1-\overline{f}_2+\overline{f}_7-\overline{f}_8-\overline{f}_9+\overline{f}_{10}+\overline{f}_{11}+\overline{f}_{12}-\overline{f}_{13}-\overline{f}_{14} = 0,\\
\rho\overline{u}_y &= \overline{f}_3-\overline{f}_4+\overline{f}_7+\overline{f}_8-\overline{f}_9-\overline{f}_{10}+\overline{f}_{15}+\overline{f}_{16}-\overline{f}_{17}-\overline{f}_{18} = \rho u_{sy},\\
\rho\overline{u}_z &= \overline{f}_5-\overline{f}_6+\overline{f}_{11}-\overline{f}_{12}-\overline{f}_{13}+\overline{f}_{14}+\overline{f}_{15}-\overline{f}_{16}-\overline{f}_{17}+\overline{f}_{18} = 0,\\
\overline{\Pi}_{yy} &= \overline{f}_3+\overline{f}_4+\overline{f}_7+\overline{f}_8+\overline{f}_9+\overline{f}_{10}+\overline{f}_{15}+\overline{f}_{16}+\overline{f}_{17}+\overline{f}_{18} = \frac{\rho}{3}+\rho u_{sy}^2,\\
\overline{\Pi}_{zz} &= \overline{f}_5+\overline{f}_6+\overline{f}_{11}+\overline{f}_{12}+\overline{f}_{13}+\overline{f}_{14}+\overline{f}_{15}+\overline{f}_{16}+\overline{f}_{17}+\overline{f}_{18} = \frac{\rho}{3}.
\end{aligned} \tag{8.4.24}$$

By solving this system (8.4.24) we then find the unknown distribution functions at the West face which are

$$\overline{f}_1, \overline{f}_7, \overline{f}_{10}, \overline{f}_{11}, \overline{f}_{12}, \tag{8.4.25}$$

so,

$$\begin{aligned}
\overline{f}_1 &= \overline{f}_2+\overline{f}_3+\overline{f}_4+\overline{f}_5+\overline{f}_6+2\overline{f}_8+2\overline{f}_9+2\overline{f}_{13}+2\overline{f}_{14}+2\overline{f}_{15}\\
&\quad +2\overline{f}_{16}+2\overline{f}_{17}+\overline{f}_{18}-\frac{2}{3}\rho-\rho u_{sy}^2,\\
\overline{f}_7 &= -\overline{f}_3-\overline{f}_8-\overline{f}_{15}-\overline{f}_{16}+\frac{\rho}{6}+\frac{1}{2}\rho u_{sy}+\frac{1}{2}\rho u_{sy}^2,\\
\overline{f}_{10} &= -\overline{f}_4-\overline{f}_9-\overline{f}_{17}-\overline{f}_{18}+\frac{\rho}{6}-\frac{1}{2}\rho u_{sy}+\frac{1}{2}\rho u_{sy}^2,\\
\overline{f}_{11} &= -\overline{f}_5-\overline{f}_{14}-\overline{f}_{15}-\overline{f}_{18}+\frac{\rho}{6},\\
\overline{f}_{12} &= -\overline{f}_6-\overline{f}_{13}-\overline{f}_{16}-\overline{f}_{17}+\frac{\rho}{6}.
\end{aligned} \tag{8.4.26}$$

The density is found from the known distribution functions

$$\rho = \overline{f}_0+\overline{f}_1+2\overline{f}_2+\overline{f}_3+\overline{f}_4+\overline{f}_5+\overline{f}_6+2\overline{f}_8+2\overline{f}_9+2\overline{f}_{13}+2\overline{f}_{14}+\overline{f}_{15}+\overline{f}_{16}+\overline{f}_{17}+\overline{f}_{18}. \tag{8.4.27}$$

The slip velocity at the West face is found by using the relation $\Pi_{xy} = -\mu\partial_y u_{wall}$ and $u_s = -\frac{l_s}{\mu}\Pi_{xy}$ because the shear stress increases toward the West wall.

$$u_{sy} = \frac{6l_s}{\rho(6l_s+2\tau+1)}\left(\overline{f}_3-\overline{f}_4+2\overline{f}_8-2\overline{f}_9+\overline{f}_{15}+\overline{f}_{16}-\overline{f}_{17}-\overline{f}_{18}\right). \tag{8.4.28}$$

Similarly, the unknown distribution functions $\overline{f}_2, \overline{f}_8, \overline{f}_9, \overline{f}_{13}, \overline{f}_{14}$ at the East face are found by solving system (8.4.24) and the slip velocity is found using the relation $\Pi_{xy} = \mu\partial_y u_{wall}$ and $u_s = \frac{l_s}{\mu}\Pi_{xy}$ because the shear stress decreases toward the East wall.

To find the unknown distribution functions at the four edges to which moment-based boundary conditions have been applied (South West, North West, South

East and North East edges) we choose the following nine moments:

$$
\begin{aligned}
&\rho\overline{u}_x = \rho u_x = 0,\\
&\rho\overline{u}_y = \rho u_y = \rho u_{sy},\\
&\rho\overline{u}_z = \rho u_z = 0,\\
&\overline{\Pi}_{xx} = \Pi_{xx} + \frac{\delta_t}{2\tau}\Pi_{xx} - \frac{\delta_t}{2\tau}\Pi^0_{xx} = \frac{\rho}{3},\\
&\overline{\Pi}_{yy} = \Pi_{yy} + \frac{\delta_t}{2\tau}\Pi_{yy} - \frac{\delta_t}{2\tau}\Pi^0_{yy} = \frac{\rho}{3},\\
&\overline{\Pi}_{zz} = \Pi_{zz} + \frac{\delta_t}{2\tau}\Pi_{zz} - \frac{\delta_t}{2\tau}\Pi^0_{zz} = \frac{\rho}{3},\\
&\overline{\Pi}_{xz} = \Pi_{xz} + \frac{\delta_t}{2\tau}\Pi_{xz} - \frac{\delta_t}{2\tau}\Pi^0_{xz} = 0,\\
&\overline{\Pi}_{xy} = \Pi_{xy} + \frac{\delta_t}{2\tau}\Pi_{xy} - \frac{\delta_t}{2\tau}\Pi^0_{xy} = \frac{-\rho}{3}\left(\frac{2\tau+\delta_t}{2}\right)\partial_x u_y,\\
&\qquad = \frac{-\rho}{3}\left(\frac{2\tau+\delta_t}{2}\right)\frac{(\pm u_{sy})}{l_s},\\
&\overline{Q}_{xyy} = Q_{xyy} + \frac{\delta_t}{2\tau}Q_{xyy} - \frac{\delta_t}{2\tau}Q^0_{xyy} = \frac{\rho}{3}\left(\frac{2\tau+\delta_t}{2}\right)\left(\left(\partial_x u_y\right)u_y\right),\\
&\qquad = \overline{\Pi}_{xy}u_{sy},
\end{aligned}
$$

where

$$
\begin{aligned}
&\Pi_{xy} = \Pi^0_{xy} + \tau\Pi^1_{xy} = \frac{\rho}{3}\delta_{xy} + \rho u_x u_y + \tau\frac{-\rho}{3}\left(\partial_x u_y + \partial_y u_x\right) = \tau\frac{-\rho}{3}\partial_x u_y,\\
&\Pi_{xz} = \Pi^0_{xz} + \tau\Pi^1_{xz} = \frac{\rho}{3}\delta_{xz} + \rho u_x u_z + \tau\frac{-\rho}{3}\left(\partial_x u_z + \partial_z u_x\right) = 0,
\end{aligned}
\tag{8.4.29}
$$

and

$$
\begin{aligned}
&Q^0_{xyy} = \frac{\rho}{3}u_x = 0, Q^1_{xyy} = \frac{\rho}{3}\left(\partial_x u_y^2 - u_y\partial_x u_y\right) = \frac{\rho}{3}\left(\left(\partial_x u_y\right)u_y\right),\\
&Q_{xyy} = Q^0_{xyy} + \tau Q^1_{xyy} = \tau\frac{\rho}{3}\left(\left(\partial_x u_y\right)u_y\right),
\end{aligned}
\tag{8.4.30}
$$

so,

$$
\begin{aligned}
\rho\overline{u}_x &= \overline{f}_1-\overline{f}_2+\overline{f}_7-\overline{f}_8-\overline{f}_9+\overline{f}_{10}+\overline{f}_{11}+\overline{f}_{12}-\overline{f}_{13}-\overline{f}_{14}=0,\\
\rho\overline{u}_y &= \overline{f}_3-\overline{f}_4+\overline{f}_7+\overline{f}_8-\overline{f}_9-\overline{f}_{10}+\overline{f}_{15}+\overline{f}_{16}-\overline{f}_{17}-\overline{f}_{18}=\rho u_{sy},\\
\rho\overline{u}_z &= \overline{f}_5-\overline{f}_6+\overline{f}_{11}-\overline{f}_{12}-\overline{f}_{13}+\overline{f}_{14}+\overline{f}_{15}-\overline{f}_{16}-\overline{f}_{17}+\overline{f}_{18}=0,\\
\overline{\Pi}_{xx} &= \overline{f}_1+\overline{f}_2+\overline{f}_7+\overline{f}_8+\overline{f}_9+\overline{f}_{10}+\overline{f}_{11}+\overline{f}_{12}+\overline{f}_{13}+\overline{f}_{14}=\frac{\rho}{3},\\
\overline{\Pi}_{yy} &= \overline{f}_3+\overline{f}_4+\overline{f}_7+\overline{f}_8+\overline{f}_9+\overline{f}_{10}+\overline{f}_{15}+\overline{f}_{16}+\overline{f}_{17}+\overline{f}_{18}=\frac{\rho}{3}+\rho u_{sy}^2,\\
\overline{\Pi}_{zz} &= \overline{f}_5+\overline{f}_6+\overline{f}_{11}+\overline{f}_{12}+\overline{f}_{13}+\overline{f}_{14}+\overline{f}_{15}+\overline{f}_{16}+\overline{f}_{17}+\overline{f}_{18}=\frac{\rho}{3},\\
\overline{\Pi}_{xz} &= \overline{f}_{11}-\overline{f}_{12}+\overline{f}_{13}-\overline{f}_{14}=0,\\
\overline{\Pi}_{xy} &= \overline{f}_7-\overline{f}_8+\overline{f}_9-\overline{f}_{10}=\frac{-\rho}{3}\left(\frac{2\tau+\delta_t}{2}\right)\frac{(\pm u_{sy})}{l_s},\\
\overline{Q}_{xyy} &= \overline{f}_7-\overline{f}_8-\overline{f}_9+\overline{f}_{10}=\overline{\Pi}_{xy}u_{sy}.
\end{aligned}
\tag{8.4.31}
$$

At the West wall the shear stress $\overline{\Pi}_{xy}$ has a positive sign because it increases toward the wall, thus the momentum flux tensor is

$$
\overline{\Pi}_{xy}=\frac{-\rho}{3}\left(\frac{2\tau+\delta_t}{2}\right).\frac{u_{sy}}{l_s} \tag{8.4.32}
$$

By solving system (8.4.31) and Eq (8.4.32) we get the unknown distribution functions at the South West and North West edges. At the South West, these are The unknown distribution functions at South West edge are

$$
\overline{f}_1,\overline{f}_5,\overline{f}_7,\overline{f}_{10},\overline{f}_{11},\overline{f}_{12},\overline{f}_{14},\overline{f}_{15},\overline{f}_{18}, \tag{8.4.33}
$$

so,

$$
\begin{aligned}
\overline{f}_1 &= \overline{f}_2+2\overline{f}_6+4\overline{f}_{13}+2\overline{f}_{16}+2\overline{f}_{17}-\frac{\rho}{3}-\frac{\rho\,(2\tau+1)}{6}\frac{u_{sy}^2}{l_s},\\
\overline{f}_5 &= 2\overline{f}_2+\overline{f}_3+\overline{f}_4+\overline{f}_6+4\overline{f}_8+4\overline{f}_9+4\overline{f}_{13}+2\overline{f}_{16}+2\overline{f}_{17}-\frac{2}{3}\rho,\\
&\quad -\rho u_{sy}^2+\frac{\rho\,(2\tau+1)}{6}\frac{u_{sy}^2}{l_s},\\
\overline{f}_7 &= \overline{f}_8+\frac{\rho\,(2\tau+1)}{12}\frac{u_{sy}^2}{l_s}-\frac{\rho\,(2\tau+1)}{12}\frac{u_{sy}}{l_s},\\
\overline{f}_{10} &= \overline{f}_9+\frac{\rho\,(2\tau+1)}{12}\frac{u_{sy}^2}{l_s}+\frac{\rho\,(2\tau+1)}{12}\frac{u_{sy}}{l_s},\\
\overline{f}_{11} &= -\overline{f}_2-\overline{f}_6-\overline{f}_8-\overline{f}_9-3\overline{f}_{13}-\overline{f}_{16}-\overline{f}_{17}+\frac{\rho}{3},\\
\overline{f}_{12} &= -\overline{f}_6-\overline{f}_{13}-\overline{f}_{16}-\overline{f}_{17}+\frac{\rho}{6},\\
\overline{f}_{14} &= -\overline{f}_2-\overline{f}_8-\overline{f}_9-\overline{f}_{13}+\frac{\rho}{6},\\
\overline{f}_{15} &= -\overline{f}_3-2\overline{f}_8-\overline{f}_{16}+\frac{\rho}{6}+\frac{1}{2}\rho u_{sy}+\frac{1}{2}\rho u_{sy}^2,\\
&\quad -\frac{\rho\,(2\tau+1)}{12}\frac{u_{sy}^2}{l_s}+\frac{\rho\,(2\tau+1)}{12}\frac{u_{sy}}{l_s},\\
\overline{f}_{18} &= -\overline{f}_4-2\overline{f}_9-\overline{f}_{17}+\frac{\rho}{6}-\frac{1}{2}\rho u_{sy}+\frac{1}{2}\rho u_{sy}^2,\\
&\quad -\frac{\rho\,(2\tau+1)}{12}\frac{u_{sy}^2}{l_s}-\frac{\rho\,(2\tau+1)}{12}\frac{u_{sy}}{l_s}.
\end{aligned}
\tag{8.4.34}
$$

The density is found from the known distribution functions

$$
\rho = \overline{f}_0+2\overline{f}_2+\overline{f}_3+\overline{f}_4+2\overline{f}_6+2\overline{f}_8+2\overline{f}_9+4\overline{f}_{13}+2\overline{f}_{16}+2\overline{f}_{17}, \tag{8.4.35}
$$

and the slip velocity is found using the shear stress $\Pi_{yz}=-\mu\partial_y u_{wall}$ and $u_s=-\dfrac{l_s}{\mu}\Pi_{yz}$ because the shear stress increases toward the South wall, as explained in the previous section, so,

$$
u_{sy}=\frac{6l_s}{\rho(6l_s+4\tau+2)}\left(\overline{f}_3-\overline{f}_4+2\overline{f}_8-2\overline{f}_9+2\overline{f}_{16}-2\overline{f}_{17}\right). \tag{8.4.36}
$$

The unknown distribution functions $\overline{f}_1,\overline{f}_6,\overline{f}_7,\overline{f}_{10},\overline{f}_{11},\overline{f}_{12},\overline{f}_{13},\overline{f}_{16},\overline{f}_{17}$ at the North West edge are found by solving system (8.4.31) and the slip velocity is found by using $\Pi_{yz}=\mu\partial_y u_{wall}$ and $u_s=\dfrac{l_s}{\mu}\Pi_{yz}$ because the shear stress decreases toward

the North wall as discussed in previous chapters.

However, as we know, at the East wall the shear stress Π_{xy} has a negative sign because it decreases toward the East wall. Hence,

$$\overline{\Pi}_{xy} = \frac{\rho}{3}\left(\frac{2\tau+\delta_t}{2}\right)\frac{u_{sy}}{l_s}. \tag{8.4.37}$$

By solving system (8.4.31) and Eq (8.4.37) we find the unknown distribution functions at the South East and North East edges, and the slip velocity is found by using $\Pi_{yz} = \pm\mu\partial_y u_{wall}$ and $u_s = \pm\frac{l_s}{\mu}\Pi_{yz}$.

The system for the corners consists of 12 moments

$$\begin{aligned}
\rho &= \overline{f}_0+\overline{f}_1+\overline{f}_2+\overline{f}_3+\overline{f}_4+\overline{f}_5+\overline{f}_6+\overline{f}_7+\overline{f}_8+\overline{f}_9+\overline{f}_{10}+\overline{f}_{11}+\overline{f}_{12}+\overline{f}_{13}+\overline{f}_{14}\\
&\quad+\overline{f}_{15}+\overline{f}_{16}+\overline{f}_{17}+\overline{f}_{18},\\
\rho\overline{u}_x &= \overline{f}_1-\overline{f}_2+\overline{f}_7-\overline{f}_8-\overline{f}_9+\overline{f}_{10}+\overline{f}_{11}+\overline{f}_{12}-\overline{f}_{13}-\overline{f}_{14} = 0,\\
\rho\overline{u}_y &= \overline{f}_3-\overline{f}_4+\overline{f}_7+\overline{f}_8-\overline{f}_9-\overline{f}_{10}+\overline{f}_{15}+\overline{f}_{16}-\overline{f}_{17}-\overline{f}_{18} = \rho u_{sy},\\
\rho\overline{u}_z &= \overline{f}_5-\overline{f}_6+\overline{f}_{11}-\overline{f}_{12}-\overline{f}_{13}+\overline{f}_{14}+\overline{f}_{15}-\overline{f}_{16}-\overline{f}_{17}+\overline{f}_{18} = 0,\\
\overline{\Pi}_{xx} &= \overline{f}_1+\overline{f}_2+\overline{f}_7+\overline{f}_8+\overline{f}_9+\overline{f}_{10}+\overline{f}_{11}+\overline{f}_{12}+\overline{f}_{13}+\overline{f}_{14} = \frac{\rho}{3},\\
\overline{\Pi}_{yy} &= \overline{f}_3+\overline{f}_4+\overline{f}_7+\overline{f}_8+\overline{f}_9+\overline{f}_{10}+\overline{f}_{15}+\overline{f}_{16}+\overline{f}_{17}+\overline{f}_{18} = \frac{\rho}{3}+\rho u_{sy}^2,\\
\overline{\Pi}_{zz} &= \overline{f}_5+\overline{f}_6+\overline{f}_{11}+\overline{f}_{12}+\overline{f}_{13}+\overline{f}_{14}+\overline{f}_{15}+\overline{f}_{16}+\overline{f}_{17}+\overline{f}_{18} = \frac{\rho}{3},\\
\overline{\Pi}_{xz} &= \overline{f}_{11}-\overline{f}_{12}+\overline{f}_{13}-\overline{f}_{14} = 0,\\
\overline{\Pi}_{xy} &= \overline{f}_7-\overline{f}_8+\overline{f}_9-\overline{f}_{10} = \frac{-\rho}{3}\left(\frac{2\tau+\delta_t}{2}\right)\frac{(\pm u_{sy})}{l_s},\\
\overline{Q}_{xyy} &= \overline{f}_7-\overline{f}_8-\overline{f}_9+\overline{f}_{10} = \overline{\Pi}_{xy}u_{sy},\\
\overline{Q}_{xxz} &= \overline{f}_{11}-\overline{f}_{12}-\overline{f}_{13}+\overline{f}_{14} = \frac{-\rho}{3}\left(\frac{2\tau+\delta_t}{2}\right)\frac{2\,(\pm u_{sy})}{l_s}u_{sy},\\
\overline{Q}_{yzz} &= \overline{f}_{15}+\overline{f}_{16}-\overline{f}_{17}-\overline{f}_{18} = \frac{\rho}{3}u_{sy}.
\end{aligned} \tag{8.4.38}$$

We know that the shear stress $\overline{\Pi}_{yz}$ at the South wall and shear stress $\overline{\Pi}_{xy}$ at West wall increase toward the South and West walls respectively, thus, the sign is kept positive for $\overline{\Pi}_{xy}$ and $\overline{\Pi}_{yz}$. By solving system (8.4.38) we find the unknown distribution functions at South West inlet and outlet corners.

At the South West inlet corner, these are

$$\overline{f}_1,\overline{f}_3,\overline{f}_5,\overline{f}_7,\overline{f}_8,\overline{f}_{10},\overline{f}_{11},\overline{f}_{12},\overline{f}_{14},\overline{f}_{15},\overline{f}_{16},\overline{f}_{18}, \tag{8.4.39}$$

so,

$$\begin{aligned}
\overline{f}_1 &= -\left(\overline{f}_0+\overline{f}_2\right)-2\overline{f}_4-4\overline{f}_9-\frac{\rho\,(2\tau+1)}{6}\frac{u_{sy}^2}{l_s}-\frac{\rho\,(2\tau+1)}{6}\frac{u_{sy}}{l_s}-\frac{2\rho}{3}u_{sy}+\frac{2\rho}{3},\\
\overline{f}_3 &= 2\overline{f}_2+\overline{f}_4+4\left(\overline{f}_9+4\overline{f}_{13}\right)-\frac{\rho\,(2\tau+1)}{3}\frac{u_{sy}^2}{l_s}+\frac{\rho\,(2\tau+1)}{6}\frac{u_{sy}}{l_s}+\frac{2\rho}{3}u_{sy}-\frac{\rho}{3},\\
\overline{f}_5 &= -\overline{f}_0-2\overline{f}_2-\overline{f}_6-4\overline{f}_{13}+\frac{\rho\,(2\tau+1)}{2}\frac{u_{sy}^2}{l_s}-\rho u_{sy}^2+\frac{2\rho}{3},\\
\overline{f}_7 &= -\overline{f}_2-\overline{f}_9-2\overline{f}_{13}+\frac{\rho\,(2\tau+1)}{4}\frac{u_{sy}^2}{l_s}-\frac{\rho\,(2\tau+1)}{12}\frac{u_{sy}}{l_s}+\frac{\rho}{6},\\
\overline{f}_8 &= -\overline{f}_2-\overline{f}_9-2\overline{f}_{13}+\frac{\rho\,(2\tau+1)}{6}\frac{u_{sy}^2}{l_s}+\frac{\rho}{6},\\
\overline{f}_{10} &= \overline{f}_9+\frac{\rho\,(2\tau+1)}{12}\frac{u_{sy}^2}{l_s}+\frac{\rho\,(2\tau+1)}{12}\frac{u_{sy}}{l_s},\\
\overline{f}_{11} &= \frac{1}{2}\overline{f}_0+\left(\overline{f}_2+\overline{f}_4\right)+2\overline{f}_9+\overline{f}_{13}-\frac{\rho\,(2\tau+1)}{6}\frac{u_{sy}^2}{l_s}+\frac{\rho\,(2\tau+1)}{12}\frac{u_{sy}}{l_s}+\frac{\rho}{3}u_{sy}-\frac{\rho}{3},\\
\overline{f}_{12} &= \frac{1}{2}\overline{f}_0+\left(\overline{f}_2+\overline{f}_4\right)+2\overline{f}_9+\overline{f}_{13}+\frac{\rho\,(2\tau+1)}{12}\frac{u_{sy}}{l_s}+\frac{\rho}{3}u_{sy}-\frac{\rho}{3},\\
\overline{f}_{14} &= \overline{f}_{13}-\frac{\rho\,(2\tau+1)}{6}\frac{u_{sy}^2}{l_s},\\
\overline{f}_{15} &= \frac{1}{2}\overline{f}_0+\left(\overline{f}_2+\overline{f}_6+\overline{f}_{17}\right)+2\overline{f}_{13}-\frac{\rho\,(2\tau+1)}{12}\frac{u_{sy}^2}{l_s}+\frac{\rho}{2}u_{sy}^2+\frac{\rho}{6}u_{sy}-\frac{\rho}{3},\\
\overline{f}_{16} &= -\frac{1}{2}\overline{f}_0-\left(\overline{f}_2+\overline{f}_4+\overline{f}_6+\overline{f}_{17}\right)-2(\overline{f}_9+\overline{f}_{13})-\frac{\rho\,(2\tau+1)}{12}\frac{u_{sy}}{l_s}-\frac{\rho}{3}u_{sy}+\frac{\rho}{2},\\
\overline{f}_{18} &= -\overline{f}_4-2\overline{f}_9-\overline{f}_{17}-\frac{\rho\,(2\tau+1)}{12}\frac{u_{sy}^2}{l_s}-\frac{\rho\,(2\tau+1)}{12}\frac{u_{sy}}{l_s}+\frac{\rho}{2}u_{sy}^2-\frac{\rho}{2}u_{sy}+\frac{\rho}{6}.
\end{aligned} \tag{8.4.40}$$

The slip velocity at the South West inlet corner is found using $\Pi_{yz}=-\mu\partial_y u_{wall}$ and $u_s=-\dfrac{l_s}{\mu}\Pi_{yz}$ because, as we have seen, the shear stress at the South and West has a positive sign toward the South and West walls. As explained previously, the

slip velocity will be

$$u_{sy} = \left(-\frac{6l_s}{\rho(2\tau+1)} \left(\overline{f}_{15} - \overline{f}_{16} + \overline{f}_{17} - \overline{f}_{18} \right) \right), \tag{8.4.41}$$

$$= \left(-\frac{6l_s}{\rho(6l_s+4\tau+2)} \right) \left(\overline{f}_0 + 4\overline{f}_{13} + 4\overline{f}_{17} + 2\overline{f}_2 + 2\overline{f}_4 + 2\overline{f}_6 + 4\overline{f}_9 - \frac{\rho}{3} \right). \tag{8.4.42}$$

where $\rho = \rho_{in}$ is the density at the inlet for the inlet corner. The unknown distribution functions at the South West outlet corner are

$$\overline{f}_1, \overline{f}_4, \overline{f}_5, \overline{f}_7, \overline{f}_9, \overline{f}_{10}, \overline{f}_{11}, \overline{f}_{12}, \overline{f}_{14}, \overline{f}_{15}, \overline{f}_{17}, \overline{f}_{18}, \tag{8.4.43}$$

which are then found by solving system (8.4.38).

Similar methods are used to find the unknown distribution functions on the North West, South East and North East inlets and outlets corners.

8.4.2 Simulation

The three dimensional flow is in the y-direction. The exact solution is the same as we saw previously for parallel plates in two dimensions, demonstrated in Eq (8.2.1). This simulation tests micro-ducts of various aspect ratios $\varepsilon = L/H$, the relation between length and height, where H is the height of the micro-duct and L is the length. The aspect ratio $Ar = H/W$, between height and width, is also varied. Here, W is the width of the micro-duct, which is in x-direction. L and H are in y- and z-direction, respectively. We have seen that the height $H = 20$ is enough to obtain the convergence of velocity, pressure deviation and slip velocity, this simulation uses one channel height of $H = 20$ in three dimensions to test the velocity, pressure deviation and slip velocity, which are examined with $\Lambda_{pr} = 2$. The ratio Λ_{pr} is not increased to more than 2 in three dimensions because the momentum flux tensor Π_{yy} is approximated to the equilibrium momentum flux tensor Π^0_{yy} and we have neglected the viscus stress $\Pi^1_{yy} = -\tau\frac{2\rho}{3}\partial_y u_y$ where $\partial_y u_y =$

0. This is clarified in the relation

$$\Pi_{yy} = \Pi^0_{yy} + \tau\Pi^1_{yy} = \frac{\rho}{3} + \rho u^2_{sy} - \tau\frac{2\rho}{3}\partial_y u_y = \frac{\rho}{3} + \rho u^2_{sy}.$$

Previously, in the two-dimensional simulation, we did increase the ratio Λ_{pr} up to 2.5, but this is very close to 2. We did not increase it more than this for the same reason of approximating the tangential momentum flux tensor. This reason is clarified in Tim and Deller [58].

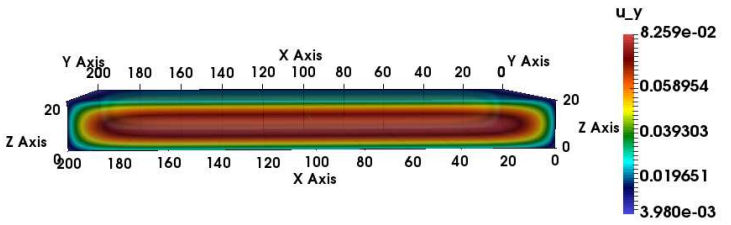

(a) $k_{n_0} = 0.1$

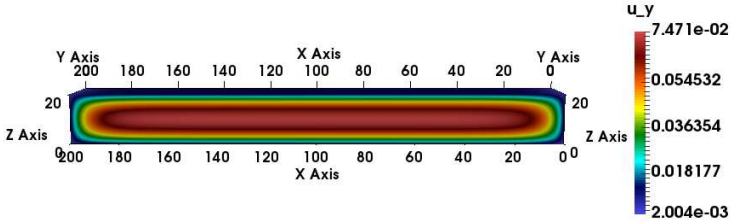

(b) $k_{n_0} = 0.05$

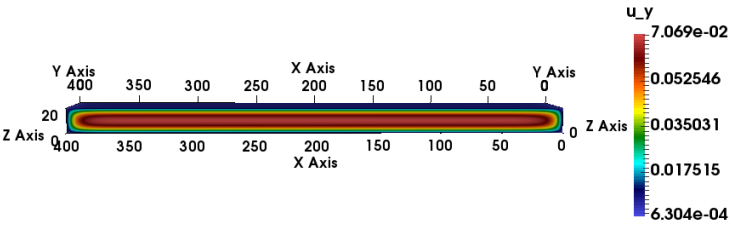

(c) $k_{n_0} = 0.025$

Figure 8.15: The velocity profile at u_y at different k_{n_0} with $n_x = 200$, $n_y = 400$ and $n_z = 20$.

8.4.2.1 The velocity profile in three dimensions

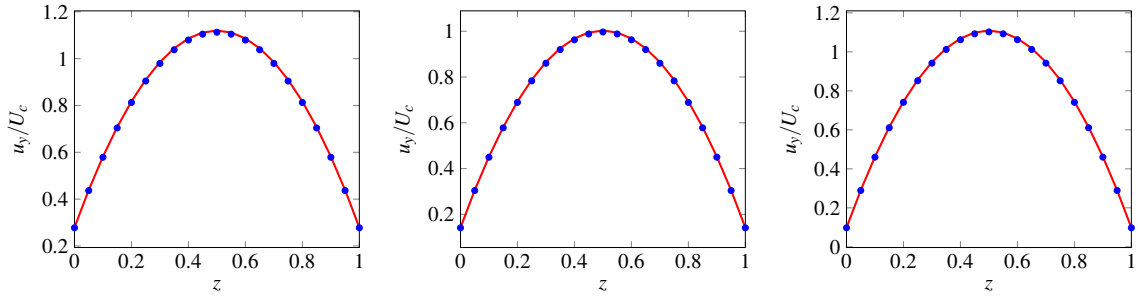

(a) $k_{n_0} = 0.1$ (b) $k_{n_0} = 0.05$ (c) $k_{n_0} = 0.025$

Figure 8.16: The velocity profiles for narrow duct at $H = 20$ and $\Lambda_{pr} = 2$ with $k_{n_0} = 0.1$ for $L/H = 20$, $k_{n_0} = 0.05$ for $L/H = 40$, $k_{n_0} = 0.025$ for $L/H = 80$, $W = n_x = 20$ and $Ar = 7$. Blue circle: the velocity profiles of LBM; Red line: the exact solution.

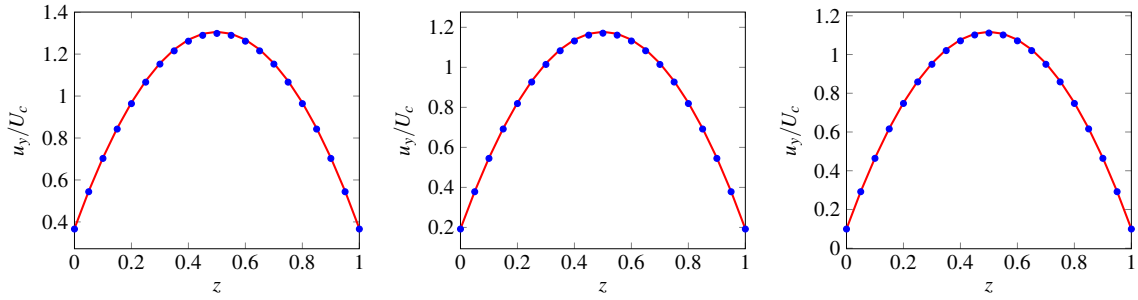

(a) $k_{n_0} = 0.1$ and $L/H = 20$,$H = 20$ (b) $k_{n_0} = 0.05$ and $L/H = 40$ (c) $k_{n_0} = 0.025$ and $L/H = 80$

Figure 8.17: The velocity profile for narrow duct at $H = 20$ and $\Lambda_{pr} = 2$ with k_{n_0}=0.1 for $L/H = 20$, k_{n_0}=0.05 for $L/H = 40$, k_{n_0}=0.025 for $L/H = 80$, $n_x = 200$ and $A_r = 10$. Blue circle: the velocity profiles of LBM; Red line: the exact solution.

In the case of a narrow duct such as ($Ar = H/W = 7, 10$) the velocity of the LBM is in excellent agreement with the exact solution Eq (8.2.1) at each Knudsen number k_{n_0} and aspect ratio ε, as is evident in Figures (8.16) and (8.17). It is clear that changes in the Knudsen number k_{n_0} and aspect ratio ε have an effect on the velocity and the slip velocity at each Ar. For instance, both the maximum velocity and the slip velocity at the wall decrease when the Knudsen number k_{n_0} decrease at each aspect ratio ε and Ar, as shown in Figures (8.16) and (8.17). Additionally, an increase in Ar leads to an increase in the maximum velocity and slip velocity at the wall, which can be seen by comparing Figures (8.16) and (8.17).

8.4.2.2 The pressure deviation

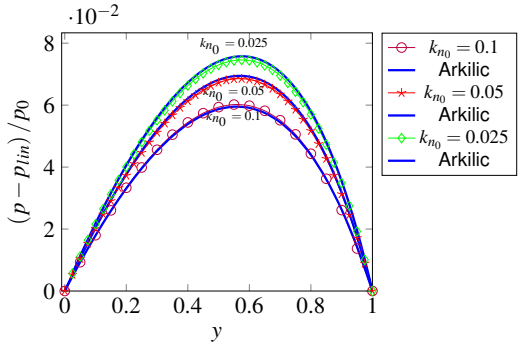

(a) $H = 20$, $Ar = 1$

Figure 8.18: The pressure deviation for square duct at $\Lambda_{pr} = 2$, $Ar = 1$, $k_{n_0} = 0.1$ for $L/H = 20$, $k_{n_0} = 0.05$ for $L/H = 40$, $k_{n_0} = 0.025$ for $L/H = 80$, $W = n_x = 20$.

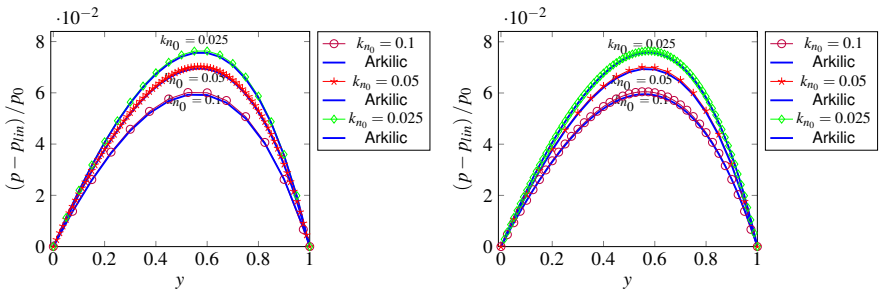

(a) $H = 20$, $Ar = 10$ *(b)* $H = 20$, $Ar = 7$

Figure 8.19: The pressure deviation for narrow duct at $H = 20$, $\Lambda_{pr} = 2$, $k_{n_0} = 0.1$ for $L/H = 20$, $k_{n_0} = 0.05$ for $L/H = 40$, k_{n_0}=0.025 for $L/H = 80$.

Rarefaction increases exactly as Arkilic's analytical solution does [3] and the agreement between the pressure deviation of the LBM and Arkilic's exact solution [3] is very good in the case of $\Lambda_{pr} = 2$, $Ar = 1, 7, 10$, aspect ratio $L/H = 20$, $L/H = 40$ and $L/H = 80$ for $k_{n_0} = 0.1$, $k_{n_0} = 0.05$ and $k_{n_0} = 0.025$, respectively, as seen in Figures (8.18) and (8.19). Decreases in k_{n_0} affect rarefaction and lead to a increase in the maximum pressure deviation, as can be as seen in Figures (8.18) and (8.19).

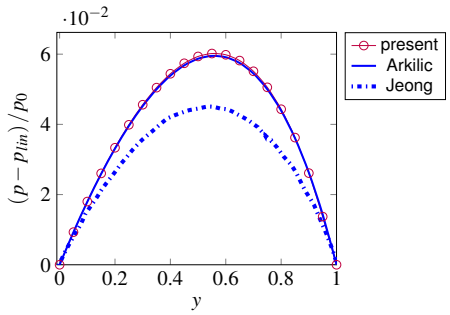

(a) $H = 20, k_{n_0} = 0.1, Ar = 1$

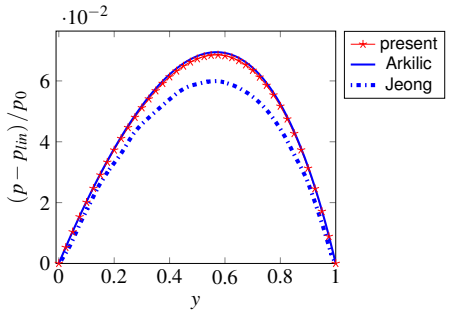

(b) $H = 20, k_{n_0} = 0.05$, $Ar = 1$

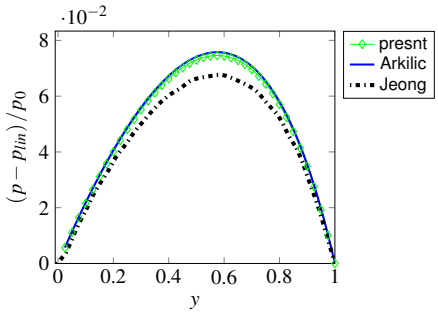

(c) $H = 20, k_{n_0} = 0.025$, $Ar = 1$

Figure 8.20: Comparison of pressure deviation in the present results with those of other authors, in three dimensions, at $\Lambda_{pr} = 2$, $k_{n_0} = 0.1$ for $L/H = 20$, $k_{n_0} = 0.05$ for $L/H = 40$, $k_{n_0} = 0.025$ for $L/H = 80$.

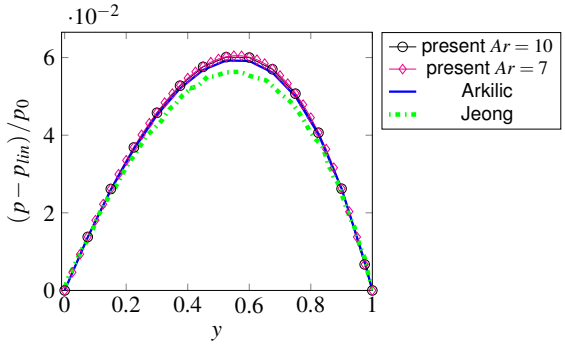

(a) $k_{n_0} = 0.1$,$Ar = 7$

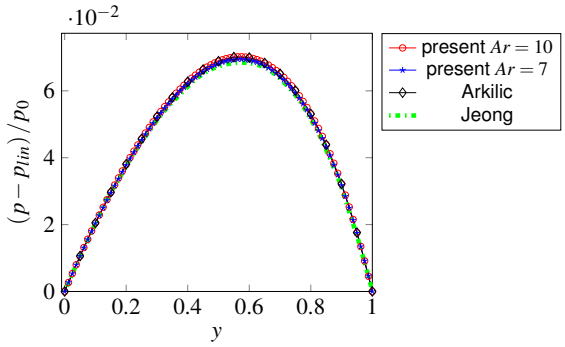

(b) $k_{n_0} = 0.05$,$Ar = 7$

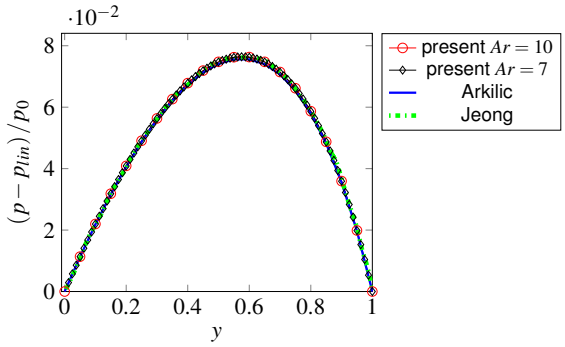

(c) $k_{n_0} = 0.025$,$Ar = 7$

Figure 8.21: Comparison of the pressure deviation in the present results with other authors, in three dimensions, at $\Lambda_{pr} = 2$, $k_{n_0} = 0.1$ for $L/H = 20$, $k_{n_0} = 0.05$ for $L/H = 40$ and $k_{n_0} = 0.025$ for $L/H = 80$.

Because we have seen that height $H = 20$ is enough to obtain the convergence of the pressure deviation and therefore changes in the channel height will not change this, the results of this simulation have been compared with $H = 14,50$ which were presented by Jeong *et. al* [33]. They used equilibrium boundary conditions, and calculated the unknown distribution functions at the inlet and outlet using second order extrapolation. They did not use any particular treatment for the slip velocity at the wall.

Figures (8.18) and (8.19) demonstrate that the pressure deviation in this present work agrees well with the analytical solution of Arkilic. The rarefaction increases exactly as his analytical solution does [3], with our $H = 20$, $k_{n_0} = 0.1$, $k_{n_0} = 0.05$ and $k_{n_0} = 0.025$ with $\Lambda_{pr} = 2$ and $Ar = 1, 7, 10$ in square and narrow ducts. On the other hand, Jeong *et. al* presented greatly reduced rarefaction with $k_{n_0} = 0.1$ and $Ar = 1$, as evidenced in Figure (8.20)(a), with a difference in maximum pressure deviation of about 2% with $Ar = 7$, as shown in Figure (8.21)(a).

The compressibility and rarefaction in the results we present do not have any influence on the pressure deviation maximum at $Ar = 1, 7, 10$, even with small $k_{n_0} = 0.05$ and $k_{n_0} = 0.025$, and the agreement with the analytical solution of Arkilic is again very good, as is clear in Figures (8.18), (8.19) and (8.21). However, the compressibility and rarefaction do decrease the maximum pressure deviation presented by Jeong *et. al* at $Ar = 1$ with $k_{n_0} = 0.05$ and $k_{n_0} = 0.025$ Figure (8.20).

8.4.2.3 Slip velocity

In general, the slip velocity in 3D is less than slip velocity in 2D and this is due to the influence of the edges as seen in Figures (8.22) and (8.23). The slip velocity previously presented by Jeong *et. al* is bigger than that in this present work, as is evidenced in Figures (8.24) and (8.25). These authors did not specify any particular treatment for the slip velocity at the wall. As demonstrated in 2D, the results of slip velocity with $H = 20$ are very close to results for the slip velocity with $H = 50$, and so $H = 20$ was chosen in order to examine the slip velocity. The same behaviour is noticed for slip velocity in this 3D simulation, where a decrease in the k_{n_0} causes a decrease in the slip velocity as demonstrated in Figures (8.22) and (8.23).

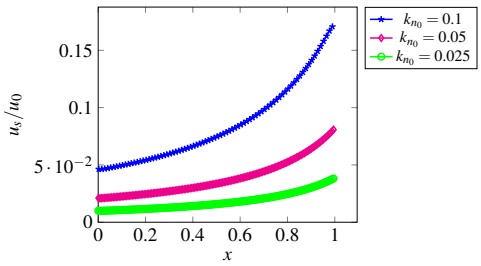

(a) $H = 20, Ar = 1$

Figure 8.22: The slip velocity at $\Lambda_{pr} = 2$ with $k_{n_0} = 0.1$ for $L/H = 20$, $k_{n_0} = 0.05$ for $L/H = 40$ and $k_{n_0} = 0.025$ for $L/H = 80$, $Ar = 1$ duct in 3D.

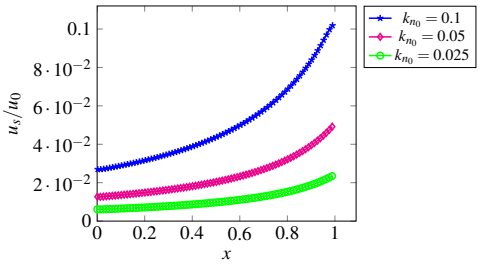

(a) $H = 20, Ar = 7$

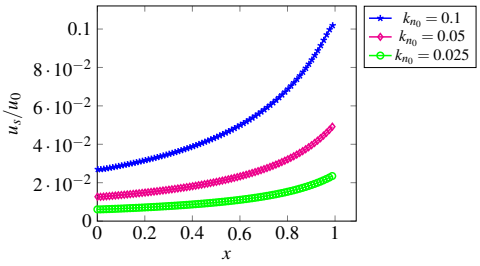

(b) $H = 20, Ar = 10$

Figure 8.23: The slip velocity at $\Lambda_{pr} = 2$ with $k_{n_0} = 0.1$ for $L/H = 20$, $k_{n_0} = 0.05$ for $L/H = 40$ and $k_{n_0} = 0.025$ for $L/H = 80$, $Ar = 10$ Narrow duct in 3D.

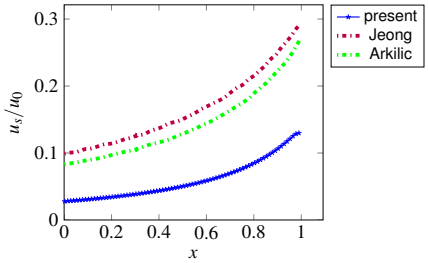

(a) $k_{n_0} = 0.1, Ar = 1$

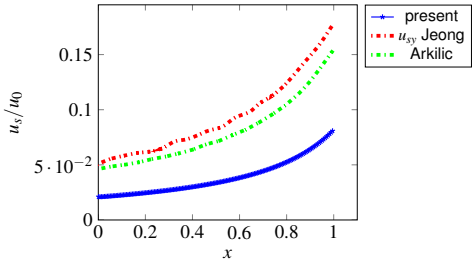

(b) $k_{n_0} = 0.05, Ar = 1$

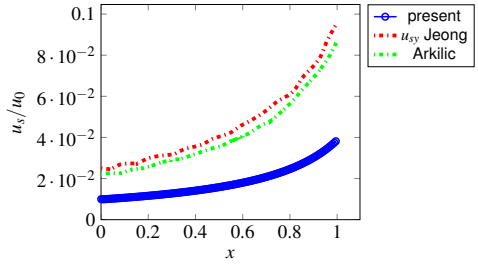

(c) $k_{n_0} = 0.025, Ar = 1$

Figure 8.24: Comparison between the slip velocity in the present work and that of the other authors, at $H = 20$ $\Lambda_{pr} = 2$, in 3D.

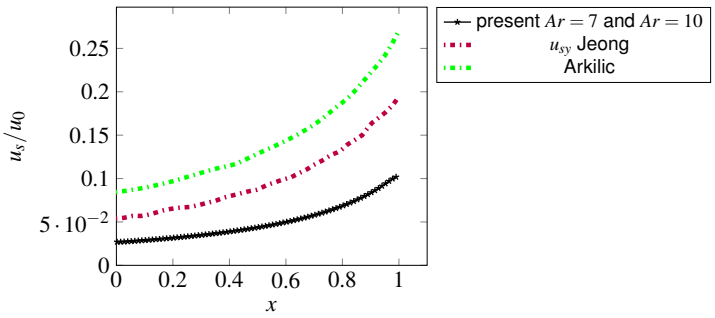

(a) $k_{n_0} = 0.1$

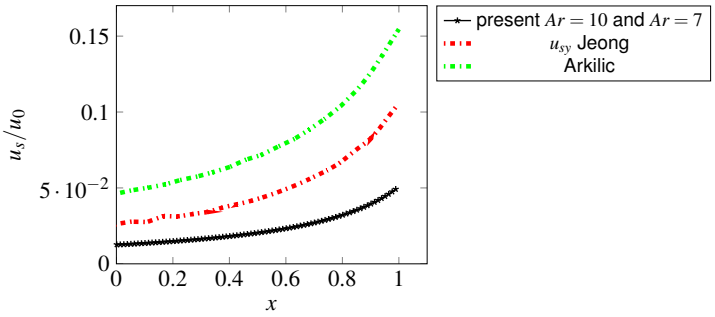

(b) $k_{n_0} = 0.05$

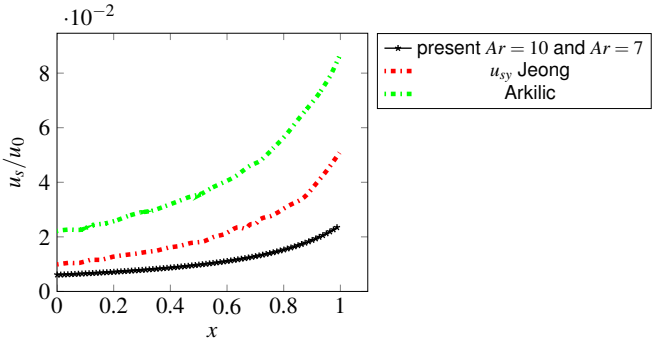

(c) $k_{n_0} = 0.025$

Figure 8.25: Comparison between the slip velocity in the present work and that of the other authors, at $H = 20$ $\Lambda_{pr} = 2$, in 3D.

8.4.2.4 Mass flow

In the 3D simulation, the mass flow of the LBM with moment-based boundary conditions has been conserved, as evidenced by its being the same at the inlet and outlet in each H, k_{n_0}, Ar and ε. Because the mass flow is not greatly affected by changing the height H at each k_{n_0}, the mass flow is just studied at $H = 20$. Variations in the mass flow are slightly affected by changing the k_{n_0} at each Ar as seen in Table (8.4), but seem to have more of an effect at higher aspect ratios Ar. For example, an increase in the Ar in three-dimensional micro-channels leads to an increase in the mass flow as seen in Table (8.4). In general, the mass flow in

three-dimensional micro-channels is less than the mass flow in two-dimensional micro-channels which is due to the presence of edges in three dimensions.

The high H and Ar	Mass flow	k_{n_0}
$H = 20$, $Ar = 1$	0.0277	0.1
	0.02366	0.05
	0.02144	0.025
$H = 20$, $Ar = 7$	0.05718	0.1
	0.04912	0.05
	0.04787	0.025

Table 8.4: The relation between mass flow and k_{n_0}, in 3D, at $\Lambda_{pr} = 2$.

The examination of the norm error order for the velocity profile and the slip velocity has not been performed in three dimensions because it needs a cluster to achieve the required high performance, and the university cluster is limited in size.

8.5 Conclusion

In conclusion, the numerical simulation of laminar flow in two- and three-dimensional micro-channels was presented using the lattice Boltzmann method with moment-based boundary conditions to implement Navier-slip conditions at the wall and pressure boundary conditions at the inlet and outlet. The velocity profile was evaluated and compared with analytical solutions. Grid convergence studies were performed for two dimensions using acoustic scaling. Here, the Reynolds and Mach number were kept constant. The norm errors were also calculated for two dimensions and the method was shown to be first-order for high grid points with acoustic scaling. The mass flow was conserved at each Knudsen number k_{n_0}, height H, aspect ratio Ar and aspect ratio ε. Slip velocity was examined at different k_{n_0}, H, Ar and ε and it was found to agree with other slip velocity seen in the literature. Pressure deviation was compared with exact solutions and results reported in the literature. Our pressure deviation was found to be in excellent agreement with the exact solution at each k_{n_0}, H, Ar and ε.

Chapter 9

Flow in the entrance region of a channel.

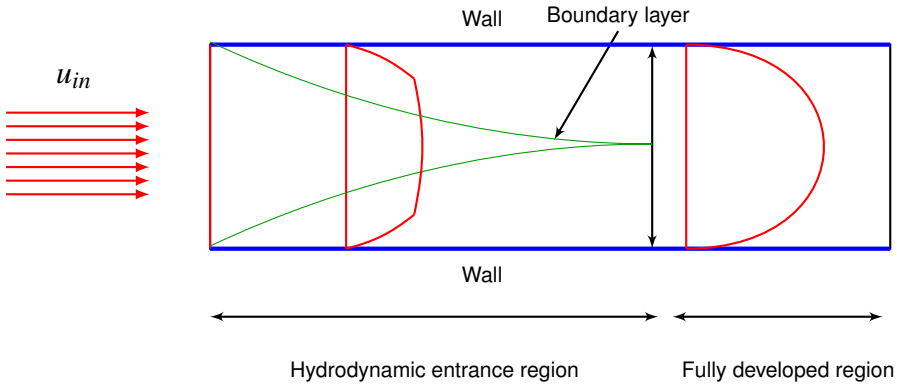

Figure 9.1: Fully developed flow [51].

9.1 Introduction

This chapter will focus on slip flow regime for various reasons. The first of these is that rarefaction has a significant effect and the second is because the slip flow has many practical applications in micro-fluidic devices. Moreover, for the purposes of this study this regime gives the opportunity to examine the efficacy of moment-based boundary conditions with Navier-slip boundary conditions in three dimensions, as well as to determine the exact value of slip velocity. For this simulation, the LBGK D_3Q_{19} model is used with the moment-based boundary conditions to simulate laminar flow at the entrance region of a channel. It has been noted that entrance effects are significant when channel length is the same as hydrodynamic development length. Also examined are the effects on the fully developed profile of the compressibility and rarefaction, which are phenomena that happen if the mean free path is similar to the characteristic length. The flow is

considered fully developed when the velocity profile reaches a position in the axial direction or along the channel where it is not able to change position or location or when the boundary layers merge together, resulting in the velocity profile being a parabola at the fully developed area. We additionally examine the apparent friction factor and Reynolds number product $f_{app}Re$ at the entrance region of the channel with diverse dimensionless slip length K_n, Reynolds numbers, aspect ratios and hydrodynamic entrance lengths, where the hydrodynamic development length is a distance from the channel entrance into a location where the centreline velocity profile becomes 99% fully developed. The behaviour of fully developed profiles and $f_{app}Re$ are compared with those cited in the literature and the value of ($f_{app}Re$) depends on Reynolds number.

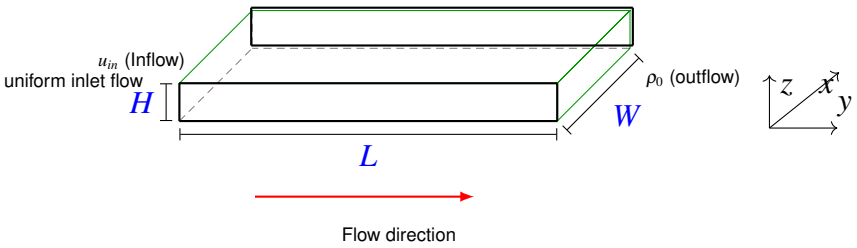

Figure 9.2: 3D inflow inside the duct.

9.2 Inflow boundary condition with Navier-slip boundary condition

In this simulation, Navier-slip boundary conditions are applied at the walls (the South and North faces, the West and East faces, the South and North-West edges and the South and North-East edges) and pressure boundary conditions are implemented at the outlet (the face, the South and North edges, and the West and East edges). Inflow boundary condition are used at the inlet (the face, the South, North, West and East edges at the inlet) and are implemented by assuming a uniform velocity profile at the inlet u_{in}.

The velocity is assumed in y-direction at the inlet $u_y = u_{in}$, $u_x = 0$ and $u_z = 0$. Therefore,

$$
\begin{aligned}
&\rho u_x = \rho u_z = 0,\\
&\rho u_y = \rho u_{in},\\
&\Pi^0_{xx} = \frac{\rho}{3}\delta_{xx} + \rho u_x u_x = \frac{\rho}{3},\\
&\Pi^0_{zz} = \frac{\rho}{3}\delta_{zz} + \rho u_z u_z = \frac{\rho}{3}.
\end{aligned} \tag{9.2.1}
$$

Also, we know that

$$\Pi_{xx} = \Pi^0_{xx} + \tau\Pi^1_{xx} = \frac{\rho}{3} - \tau\frac{2\rho}{3}\partial_x u_x = \frac{\rho}{3},$$

$$\Pi_{yy} = \Pi^0_{yy} + \tau\Pi^1_{yy} = \frac{\rho}{3} + \rho u^2_{in} - \tau\frac{2\rho}{3}\partial_y u_y = \frac{\rho}{3} + \rho u^2_{in},$$

and

$$\Pi_{zz} = \Pi^0_{zz} + \tau\Pi^1_{zz} = \frac{\rho}{3} - \tau\frac{2\rho}{3}\partial_z u_z = \frac{\rho}{3},$$

so,

$$
\begin{aligned}
&\rho\overline{u}_x = \rho u_x = 0,\\
&\rho\overline{u}_y = \rho u_y = \rho u_{in},\\
&\rho\overline{u}_z = \rho u_z = 0,\\
&\overline{\Pi}_{xx} = \Pi_{xx} + \frac{\delta_t}{2\tau}\Pi_{xx} - \frac{\delta_t}{2\tau}\Pi^0_{xx} = \frac{\rho}{3},\\
&\overline{\Pi}_{yy} = \Pi_{yy} + \frac{\delta_t}{2\tau}\Pi_{yy} - \frac{\delta_t}{2\tau}\Pi^0_{yy} = \frac{\rho}{3} + \rho u^2_{in},\\
&\overline{\Pi}_{zz} = \Pi_{zz} + \frac{\delta_t}{2\tau}\Pi_{zz} - \frac{\delta_t}{2\tau}\Pi^0_{zz} = \frac{\rho}{3}.
\end{aligned} \tag{9.2.2}
$$

To find the unknown distribution functions at the inlet wall we have to select five linearly independent moments which in this case are $\rho\overline{u}_x = 0,\ \rho\overline{u}_y = \rho u_{in},\ \rho\overline{u}_z =$

0, $\overline{\Pi}_{xx} = \dfrac{\rho}{3}$, $\overline{\Pi}_{zz} = \dfrac{\rho}{3}$, so

$$\begin{aligned}
\rho\overline{u}_x &= \overline{f}_1 - \overline{f}_2 + \overline{f}_7 - \overline{f}_8 - \overline{f}_9 + \overline{f}_{10} + \overline{f}_{11} + \overline{f}_{12} - \overline{f}_{13} - \overline{f}_{14} = 0,\\
\rho\overline{u}_y &= \overline{f}_3 - \overline{f}_4 + \overline{f}_7 + \overline{f}_8 - \overline{f}_9 - \overline{f}_{10} + \overline{f}_{15} + \overline{f}_{16} - \overline{f}_{17} - \overline{f}_{18} = \rho u_{in},\\
\rho\overline{u}_z &= \overline{f}_5 - \overline{f}_6 + \overline{f}_{11} - \overline{f}_{12} - \overline{f}_{13} + \overline{f}_{14} + \overline{f}_{15} - \overline{f}_{16} - \overline{f}_{17} + \overline{f}_{18} = 0,\\
\overline{\Pi}_{xx} &= \overline{f}_1 + \overline{f}_2 + \overline{f}_7 + \overline{f}_8 + \overline{f}_9 + \overline{f}_{10} + \overline{f}_{11} + \overline{f}_{12} + \overline{f}_{13} + \overline{f}_{14} = \frac{\rho}{3},\\
\overline{\Pi}_{zz} &= \overline{f}_5 + \overline{f}_6 + \overline{f}_{11} + \overline{f}_{12} + \overline{f}_{13} + \overline{f}_{14} + \overline{f}_{15} + \overline{f}_{16} + \overline{f}_{17} + \overline{f}_{18} = \frac{\rho}{3}.
\end{aligned} \tag{9.2.3}$$

The unknown distribution functions at the inlet face are

$$\overline{f}_3, \overline{f}_7, \overline{f}_8, \overline{f}_{15}, \overline{f}_{16}. \tag{9.2.4}$$

By then solving system (9.2.3) we find that the unknown distribution functions at the inlet face are

$$\begin{aligned}
\overline{f}_3 &= \overline{f}_1 + \overline{f}_2 + \overline{f}_4 + \overline{f}_5 + \overline{f}_6 + 2\overline{f}_9 + 2\overline{f}_{10} + 2\overline{f}_{11} + 2\overline{f}_{12}\\
&\quad + 2\overline{f}_{13} + 2\overline{f}_{14} + 2\overline{f}_{17} + 2\overline{f}_{18} - \frac{2\rho}{3} + \rho u_{in},\\
\overline{f}_7 &= -\overline{f}_1 - \overline{f}_{10} - \overline{f}_{11} - \overline{f}_{12} + \frac{\rho}{6},\\
\overline{f}_8 &= -\overline{f}_2 - \overline{f}_9 - \overline{f}_{13} - \overline{f}_{14} + \frac{\rho}{6},\\
\overline{f}_{15} &= -\overline{f}_5 - \overline{f}_{11} - \overline{f}_{14} - \overline{f}_{18} + \frac{\rho}{6},\\
\overline{f}_{16} &= -\overline{f}_6 - \overline{f}_{12} - \overline{f}_{13} - \overline{f}_{17} + \frac{\rho}{6}.
\end{aligned} \tag{9.2.5}$$

To find the unknown distribution functions at the South and North inlet edges

we have to select nine linearly independent moments which in this case are

$$\begin{aligned}
\rho\overline{u}_x &= \overline{f}_1-\overline{f}_2+\overline{f}_7-\overline{f}_8-\overline{f}_9+\overline{f}_{10}+\overline{f}_{11}+\overline{f}_{12}-\overline{f}_{13}-\overline{f}_{14}=0,\\
\rho\overline{u}_y &= \overline{f}_3-\overline{f}_4+\overline{f}_7+\overline{f}_8-\overline{f}_9-\overline{f}_{10}+\overline{f}_{15}+\overline{f}_{16}-\overline{f}_{17}-\overline{f}_{18}=\rho u_{in},\\
\rho\overline{u}_z &= \overline{f}_5-\overline{f}_6+\overline{f}_{11}-\overline{f}_{12}-\overline{f}_{13}+\overline{f}_{14}+\overline{f}_{15}-\overline{f}_{16}-\overline{f}_{17}+\overline{f}_{18}=0,\\
\overline{\Pi}_{xx} &= \overline{f}_1+\overline{f}_2+\overline{f}_7+\overline{f}_8+\overline{f}_9+\overline{f}_{10}+\overline{f}_{11}+\overline{f}_{12}+\overline{f}_{13}+\overline{f}_{14}=\frac{\rho}{3},\\
\overline{\Pi}_{yy} &= \overline{f}_3+\overline{f}_4+\overline{f}_7+\overline{f}_8+\overline{f}_9+\overline{f}_{10}+\overline{f}_{15}+\overline{f}_{16}+\overline{f}_{17}+\overline{f}_{18}=\frac{\rho}{3}+\rho u_{in}^2,\\
\overline{\Pi}_{zz} &= \overline{f}_5+\overline{f}_6+\overline{f}_{11}+\overline{f}_{12}+\overline{f}_{13}+\overline{f}_{14}+\overline{f}_{15}+\overline{f}_{16}+\overline{f}_{17}+\overline{f}_{18}=\frac{\rho}{3},\\
\overline{\Pi}_{xz} &= \overline{f}_{11}-\overline{f}_{12}+\overline{f}_{13}-\overline{f}_{14}=0,\\
\overline{Q}_{xxz} &= \overline{f}_{11}-\overline{f}_{12}-\overline{f}_{13}+\overline{f}_{14}=0,\\
\overline{Q}_{yyz} &= \overline{f}_{15}-\overline{f}_{16}-\overline{f}_{17}+\overline{f}_{18}=0,
\end{aligned} \tag{9.2.6}$$

where $Q_{yyz}=Q^0_{yyz}+\tau Q^1_{yyz}=\frac{\rho}{3}u_z+\tau\frac{\rho}{3}\left[\partial_z u_y^2-u_y\partial_z u_y\right]=\tau\frac{\rho}{3}\left[\partial_z u_y^2-u_y\partial_z u_y\right]$
$\overline{Q}_{yyz}=\frac{-\rho}{3}\left(\frac{2\tau+\delta_t}{2}\right)\left[\partial_z u_y^2-u_y\partial_z u_y\right]=\frac{-\rho}{3}\left(\frac{2\tau+\delta_t}{2}\right)\left[\partial_z u_y\right]u_y=0,\partial_z u_y=0$ because there is no shear stress at the flat wall, only velocity at the inlet.

The unknown distribution functions at the south inlet are

$$\overline{f}_3,\overline{f}_5,\overline{f}_7,\overline{f}_8,\overline{f}_{11},\overline{f}_{14},\overline{f}_{15},\overline{f}_{16},\overline{f}_{18}. \tag{9.2.7}$$

By solving system (9.2.6) we find the unknown distribution functions at the South

inlet which are

$$\begin{aligned}
\overline{f}_3 &= \overline{f}_1 + \overline{f}_2 - \overline{f}_4 + 2\overline{f}_6 + 4\overline{f}_{12} + 4\overline{f}_{13} + \rho u_{in}^2 - \frac{\rho}{3},\\
\overline{f}_5 &= \overline{f}_6,\\
\overline{f}_7 &= -\overline{f}_1 - \overline{f}_{10} - 2\overline{f}_{12} + \frac{\rho}{6},\\
\overline{f}_8 &= -\overline{f}_2 - \overline{f}_9 - 2\overline{f}_{13} + \frac{\rho}{6},\\
\overline{f}_{11} &= \overline{f}_{12},\\
\overline{f}_{14} &= \overline{f}_{13},\\
\overline{f}_{15} &= \overline{f}_{10} - \overline{f}_{12} - \overline{f}_{13} + \overline{f}_{17} + \overline{f}_4 - \overline{f}_6 + \overline{f}_9 + \frac{\rho}{2}u_{in} - \frac{\rho}{2}u_{in}^2,\\
\overline{f}_{16} &= -\overline{f}_6 - \overline{f}_{12} - \overline{f}_{13} - \overline{f}_{17} + \frac{\rho}{6},\\
\overline{f}_{18} &= -\overline{f}_{10} - \overline{f}_4 - \overline{f}_9 - \overline{f}_{17} + \frac{\rho}{2}u_{in}^2 - \frac{\rho}{2}u_{in} + \frac{\rho}{6}.
\end{aligned} \tag{9.2.8}$$

By then solving system (9.2.6) for $\overline{f}_3, \overline{f}_6, \overline{f}_7, \overline{f}_8, \overline{f}_{12}, \overline{f}_{13}, \overline{f}_{15}, \overline{f}_{16}, \overline{f}_{17}$ we find the unknown distribution functions at the North inlet.

The system to find the unknown distribution functions at the West inlet and East inlet edges is

$$\begin{aligned}
\rho\overline{u}_x &= \overline{f}_1 - \overline{f}_2 + \overline{f}_7 - \overline{f}_8 - \overline{f}_9 + \overline{f}_{10} + \overline{f}_{11} + \overline{f}_{12} - \overline{f}_{13} - \overline{f}_{14} = 0,\\
\rho\overline{u}_y &= \overline{f}_3 - \overline{f}_4 + \overline{f}_7 + \overline{f}_8 - \overline{f}_9 - \overline{f}_{10} + \overline{f}_{15} + \overline{f}_{16} - \overline{f}_{17} - \overline{f}_{18} = \rho u_{in},\\
\rho\overline{u}_z &= \overline{f}_5 - \overline{f}_6 + \overline{f}_{11} - \overline{f}_{12} - \overline{f}_{13} + \overline{f}_{14} + \overline{f}_{15} - \overline{f}_{16} - \overline{f}_{17} + \overline{f}_{18} = 0,\\
\overline{\Pi}_{xx} &= \overline{f}_1 + \overline{f}_2 + \overline{f}_7 + \overline{f}_8 + \overline{f}_9 + \overline{f}_{10} + \overline{f}_{11} + \overline{f}_{12} + \overline{f}_{13} + \overline{f}_{14} = \frac{\rho}{3},\\
\overline{\Pi}_{yy} &= \overline{f}_3 + \overline{f}_4 + \overline{f}_7 + \overline{f}_8 + \overline{f}_9 + \overline{f}_{10} + \overline{f}_{15} + \overline{f}_{16} + \overline{f}_{17} + \overline{f}_{18} = \frac{\rho}{3} + \rho u_{in}^2,\\
\overline{\Pi}_{zz} &= \overline{f}_5 + \overline{f}_6 + \overline{f}_{11} + \overline{f}_{12} + \overline{f}_{13} + \overline{f}_{14} + \overline{f}_{15} + \overline{f}_{16} + \overline{f}_{17} + \overline{f}_{18} = \frac{\rho}{3},\\
\overline{\Pi}_{xz} &= \overline{f}_{11} - \overline{f}_{12} + \overline{f}_{13} - \overline{f}_{14} = 0,\\
\overline{Q}_{xzz} &= \overline{f}_{11} + \overline{f}_{12} - \overline{f}_{13} - \overline{f}_{14} = 0,\\
\overline{Q}_{xxy} &= \overline{f}_7 + \overline{f}_8 - \overline{f}_9 - \overline{f}_{10} = \frac{\rho}{3}u_{in},
\end{aligned} \tag{9.2.9}$$

where

$$
\begin{aligned}
Q_{xzz} = Q^0_{xzz} + \tau Q^1_{xzz} = \frac{\rho}{3}u_x + \tau\frac{\rho}{3}\partial_x u_y^2 = \tau\frac{\rho}{3}\partial_x u_y^2,\\
\overline{Q}_{xzz} = \frac{-\rho}{3}\left(\frac{2\tau+\delta_t}{2}\right)\left[\partial_x u_y^2\right] = \frac{-\rho}{3}\left(\frac{2\tau+\delta_t}{2}\right)\left[\partial_x u_y\right]u_y,\\
= \frac{-\rho}{3}\left(\frac{2\tau+\delta_t}{2}\right)\left[u_y\partial_x u_y + \partial_x u_y u_y\right] = 0.
\end{aligned}
\tag{9.2.10}
$$

Also, $Q_{xxy} = Q^0_{xxy} + \tau Q^1_{xxy} = \frac{\rho}{3}u_y + \frac{\rho}{3}\partial_y u_y + \frac{\rho}{3}\partial_y u_y^2 = \frac{\rho}{3}u_y = \frac{\rho}{3}u_{in}$ so $\overline{Q}_{xxy} = \frac{\rho}{3}u_{in}$. By solving system (9.2.9) we find the unknown distribution functions at West inlet, which are

$$
\overline{f}_1, \overline{f}_3, \overline{f}_7, \overline{f}_8, \overline{f}_{10}, \overline{f}_{11}, \overline{f}_{12}, \overline{f}_{15}, \overline{f}_{16},
\tag{9.2.11}
$$

so,

$$
\begin{aligned}
\overline{f}_1 &= -\overline{f}_2 + 2\overline{f}_4 - 2\left(\overline{f}_{13} + \overline{f}_{14}\right) + 2\left(\overline{f}_{17} + \overline{f}_{18}\right) - \rho u_{in}^2 + \frac{2\rho}{3}u_{in},\\
\overline{f}_3 &= \overline{f}_4 + \overline{f}_5 + \overline{f}_6 + 2\left(\overline{f}_{13} + \overline{f}_{14} + \overline{f}_{17} + \overline{f}_{18}\right) + \frac{2\rho}{3}u_{in} - \frac{\rho}{3},\\
\overline{f}_7 &= \overline{f}_2 - \overline{f}_4 + \overline{f}_9 + \overline{f}_{13} + \overline{f}_{14} - \overline{f}_{17} - \overline{f}_{18} + \frac{\rho}{2}u_{in}^2 - \frac{\rho}{6}u_{in},\\
\overline{f}_8 &= -\overline{f}_2 - \overline{f}_9 - \overline{f}_{14} - \overline{f}_{13} + \frac{\rho}{6},\\
\overline{f}_{10} &= -\overline{f}_4 - \overline{f}_9 - \overline{f}_{17} - \overline{f}_{18} + \frac{\rho}{2}u_{in}^2 - \frac{\rho}{2}u_{in} + \frac{\rho}{6}.\\
\overline{f}_{11} &= \overline{f}_{14},\\
\overline{f}_{12} &= \overline{f}_{13},\\
\overline{f}_{15} &= -\overline{f}_5 - 2\overline{f}_{14} - \overline{f}_{18} + \frac{\rho}{6},\\
\overline{f}_{16} &= -\overline{f}_6 - 2\overline{f}_{13} - \overline{f}_{17} + \frac{\rho}{6}.
\end{aligned}
\tag{9.2.12}
$$

By solving system (9.2.9) we find the unknown distribution functions at East inlet.

The system for the corners consists of twelve moments, which are

$$\begin{aligned}
\rho\overline{u}_x &= \overline{f}_1-\overline{f}_2+\overline{f}_7-\overline{f}_8-\overline{f}_9+\overline{f}_{10}+\overline{f}_{11}+\overline{f}_{12}-\overline{f}_{13}-\overline{f}_{14}=0,\\
\rho\overline{u}_y &= \overline{f}_3-\overline{f}_4+\overline{f}_7+\overline{f}_8-\overline{f}_9-\overline{f}_{10}+\overline{f}_{15}+\overline{f}_{16}-\overline{f}_{17}-\overline{f}_{18}=\rho u_{in},\\
\rho\overline{u}_z &= \overline{f}_5-\overline{f}_6+\overline{f}_{11}-\overline{f}_{12}-\overline{f}_{13}+\overline{f}_{14}+\overline{f}_{15}-\overline{f}_{16}-\overline{f}_{17}+\overline{f}_{18}=0,\\
\overline{\Pi}_{xx} &= \overline{f}_1+\overline{f}_2+\overline{f}_7+\overline{f}_8+\overline{f}_9+\overline{f}_{10}+\overline{f}_{11}+\overline{f}_{12}+\overline{f}_{13}+\overline{f}_{14}=\frac{\rho}{3},\\
\overline{\Pi}_{yy} &= \overline{f}_3+\overline{f}_4+\overline{f}_7+\overline{f}_8+\overline{f}_9+\overline{f}_{10}+\overline{f}_{15}+\overline{f}_{16}+\overline{f}_{17}+\overline{f}_{18}=\frac{\rho}{3}+\rho u_{in}^2,\\
\overline{\Pi}_{zz} &= \overline{f}_5+\overline{f}_6+\overline{f}_{11}+\overline{f}_{12}+\overline{f}_{13}+\overline{f}_{14}+\overline{f}_{15}+\overline{f}_{16}+\overline{f}_{17}+\overline{f}_{18}=\frac{\rho}{3},\\
\overline{\Pi}_{xz} &= \overline{f}_{11}-\overline{f}_{12}+\overline{f}_{13}-\overline{f}_{14}=0,\\
\overline{\Pi}_{yz} &= \overline{f}_{15}-\overline{f}_{16}+\overline{f}_{17}-\overline{f}_{18}=0,\\
\overline{\Pi}_{xy} &= \overline{f}_7-\overline{f}_8+\overline{f}_9-\overline{f}_{10}=0,\\
\overline{Q}_{xyy} &= \overline{f}_7-\overline{f}_8-\overline{f}_9+\overline{f}_{10}=\overline{\Pi}_{xy}u_{in},\\
\overline{Q}_{xxz} &= \overline{f}_{11}-\overline{f}_{12}-\overline{f}_{13}+\overline{f}_{14}=0,\\
\overline{Q}_{yzz} &= \overline{f}_{15}+\overline{f}_{16}-\overline{f}_{17}-\overline{f}_{18}=\frac{\rho}{3}u_{in},
\end{aligned} \tag{9.2.13}$$

where

$$\Pi^0_{yz}=\frac{\rho}{3}\delta_{yz}+\rho u_y u_z=0, \tag{9.2.14}$$

from the definition of slip velocity and shear stress,

$$\Pi_{yz}=\Pi^0_{yz}+\tau\Pi^1_{yz}=\frac{\rho}{3}\delta_{yz}+\rho u_y u_z-\tau\frac{\rho}{3}(\partial_y u_z+\partial_z u_y)=-\tau\frac{\rho}{3}\partial_z u_y=-\mu\partial_y u_z, \tag{9.2.15}$$

and

$$\begin{aligned}
\overline{\Pi}_{yz} &= \Pi_{yz}+\frac{\delta_t}{2\tau}\Pi_{yz}-\frac{\delta_t}{2\tau}\Pi^0_{yz}, \quad u_y=u_{sy}=u_{in},\\
&= \Pi_{yz}+\frac{\delta_t}{2\tau}\Pi_{yz}.
\end{aligned} \tag{9.2.16}$$

Thus, $\overline{\Pi}_{yz}=\dfrac{-\rho}{3}\left(\dfrac{2\tau+\delta_t}{2}\right)\partial_z u_y=0, \partial_z u_y=0.$

We define $\overline{\Pi}_{xy}$ in the same way, which will be $\overline{\Pi}_{xy} = \frac{-\rho}{3}\left(\frac{2\tau+\delta_t}{2}\right)\partial_x u_y = 0$, $\partial_x u_y = 0$. By solving system (9.2.13) we find the unknown distribution functions at South West inlet corner, which are

$$\overline{f}_1, \overline{f}_3, \overline{f}_5, \overline{f}_7, \overline{f}_8, \overline{f}_{10}, \overline{f}_{11}, \overline{f}_{12}, \overline{f}_{14}, \overline{f}_{15}, \overline{f}_{16}, \overline{f}_{18}, \tag{9.2.17}$$

so,

$$\begin{aligned}
\overline{f}_1 &= \overline{f}_2 + 2\overline{f}_6 + 4\overline{f}_{13} + 4\overline{f}_{17} + \frac{1\rho}{3}u_{in} - \frac{1\rho}{3},\\
\overline{f}_3 &= 2\overline{f}_2 + \overline{f}_4 + 4\left(\overline{f}_9 + 4\overline{f}_{13}\right) + \frac{2\rho}{3}u_{in} - \frac{\rho}{3},\\
\overline{f}_5 &= 2\overline{f}_4 + \overline{f}_6 + 4\overline{f}_9 + 4\overline{f}_{17} + -\rho u_{in}^2 + \rho u_{in} - \frac{1\rho}{3},\\
\overline{f}_7 &= -\overline{f}_2 - \overline{f}_9 - 2\overline{f}_{13} + \frac{\rho}{6},\\
\overline{f}_8 &= -\overline{f}_2 - \overline{f}_9 - 2\overline{f}_{13} + \frac{\rho}{6},\\
\overline{f}_{10} &= \overline{f}_9,\\
\overline{f}_{11} &= -\overline{f}_6 - \overline{f}_{13} - 2\overline{f}_{17} - \frac{\rho}{6}u_{in} + \frac{\rho}{6},\\
\overline{f}_{12} &= -\overline{f}_6 - \overline{f}_{13}2\overline{f}_{17} - \frac{\rho}{6}u_{in} + \frac{\rho}{6},\\
\overline{f}_{14} &= \overline{f}_{13},\\
\overline{f}_{15} &= -\overline{f}_4 - 2\overline{f}_9 - \overline{f}_{17} + \frac{\rho}{2}u_{in}^2 - \frac{\rho}{3}u_{in} + \frac{\rho}{6},\\
\overline{f}_{16} &= \overline{f}_{17} + \frac{\rho}{6}u_{in},\\
\overline{f}_{18} &= -\overline{f}_4 - 2\overline{f}_9 - \overline{f}_{17} + \frac{\rho}{2}u_{in}^2 - \frac{\rho}{2}u_{in} + \frac{\rho}{6}.
\end{aligned} \tag{9.2.18}$$

By solving system (9.2.13) we find the unknown distribution functions at South East inlet, North West inlet and North East inlet corners. All densities at the inlet including (faces, edges and corners) are calculated from the known distribution functions from the previous time step.

9.3 Simulation

In this simulation, the dimensionless slip length is defined according to the hydraulic diameter of a rectangular channel $D_h = 2HW/(H+W)$, so the definition of

dimensionless slip length K_n is $\frac{l_s}{D_h}$. The dynamic viscosity is defined at the outlet $\mu_0 = \nu_0\rho_0$ in order to keep it constant, and the Kinematic viscosity at the outlet is defined as $\nu_0 = \tau_0/3$. Thus, the definition of the local relaxation time is based on the relaxation time at the outlet

$$\tau = 3\nu = 3\frac{\mu}{\rho} = 3\frac{\mu_0}{\rho} = \frac{\tau_0\rho_0}{\rho}.$$

The local dimensionless slip length used is $K_{n_{Local}} = K_{n_0}\frac{p_0}{p} = K_{n_0}\frac{\rho_0}{\rho}$, where K_{n_0} is the dimensionless slip length at the outlet, the $p_0 = \frac{\rho_0}{3}$ is the pressure at the the outlet, $\rho_0 = 1$ is the density at the outlet and $p = \frac{\rho}{3}$ is the pressure. The Reynolds number $Re = \frac{u_m D_h}{\nu}$ is based on the mean velocity u_m at the cross section of the outlet. The mean velocity is calculated by using the integral of trapezoidal rule. The aspect ratio ε is defined as the ratio between the height H and the width W, or the ratio of the short side to the long side.

A part from the relation between K_n and Reynolds number all important features of micro-channel seem to be there *i.e.* constant dynamic viscosity, slip length and slip velocity depends on the local density ratio. For this reason, we compare our results with the results in literature which are applied in micro-channel. Also, there is von Karaman- type relation between K_n, Reynolds number and Mach number *i.e.* $K_n \propto \frac{Ma}{Re}$ and Mach number is constant and different at each K_n.

9.3.1 Developing velocity profile

The laminar velocity profiles the u_y are set in the width direction, which is in x-direction for $\varepsilon = 1, 0.5$ at different positions of the dimensionless hydrodynamic developed length y^+, where $y^+ = \frac{y}{D_h Re}$, in which y is the dimensionless local position. For $\varepsilon = 0.1$ they are in height direction which is in z-direction at different positions of the dimensionless hydrodynamic developed length. The velocity profiles are normalized by the mean velocity u_m. The developed laminar velocity profiles in the entrance region of the three-dimensional ducts are then examined. The Figures (9.3) to (9.8) show developed laminar velocity profiles for aspect ra-

tio $\varepsilon = 1, 0.5, 0.1$, different $K_{n_0} = 0.001, 0.01, 0.05, 0.1$, different Reynolds numbers Re and different positions y^+.

9.3.1.1 Square Duct $\varepsilon = 1$ and Rectangular Duct $\varepsilon = 0.5$

The laminar velocity profiles at the inlet start as a uniform velocity which have a maximum velocity at the wall and a minimum velocity at the middle or core and they tend to look similar to a parabola at the large y^+ as seen in Figure (9.3). Moreover, the value of the slip velocity reduces when the flow reaches the fully developed region (we can notice this by observing the velocity profiles at different positions of the dimensionless hydrodynamic developed length y^+) at each K_{n_0}. The velocity gradient at the wall caused this reduction in the amount of slip velocity. An example can be seen in Figure (9.3).

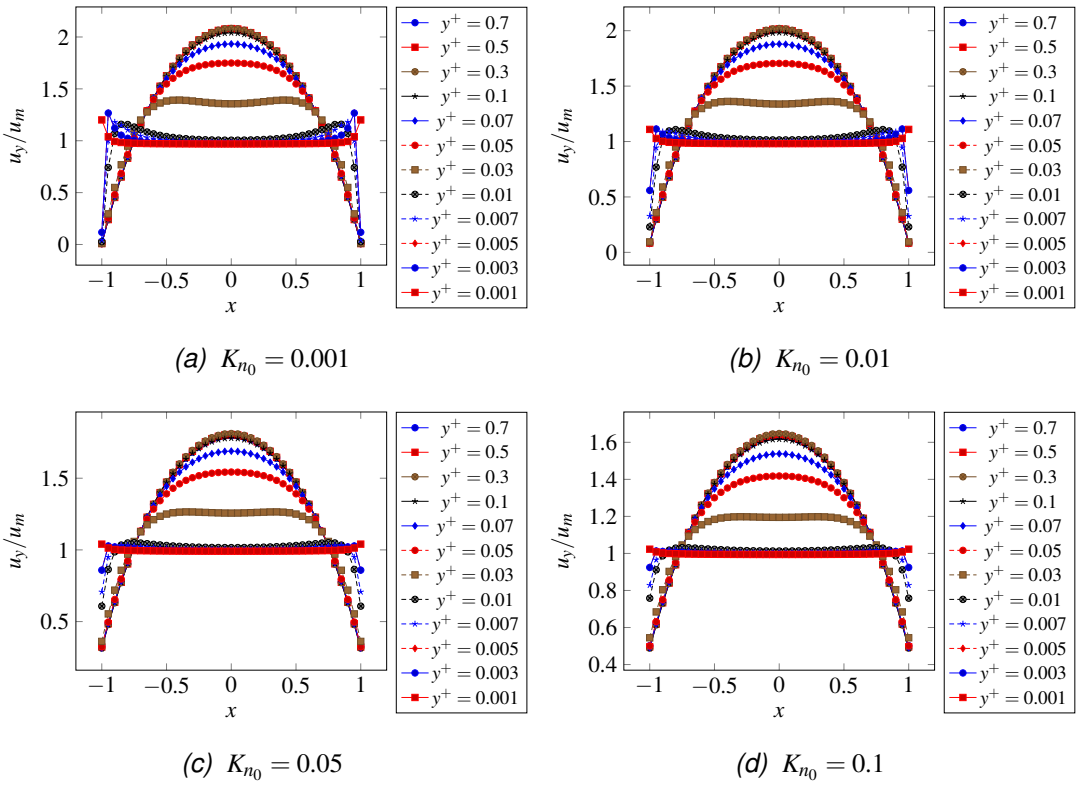

(a) $K_{n_0} = 0.001$ *(b)* $K_{n_0} = 0.01$

(c) $K_{n_0} = 0.05$ *(d)* $K_{n_0} = 0.1$

Figure 9.3: 3D velocity profile at $n_x = 40$,$n_z = 40$, $n_y = 300$, $\varepsilon = 1$, $Re = 10$, $u_{in} = 0.05$ and different K_{n_0}.

The developed velocity profiles at the entrance region are affected by K_{n_0}. For instance, an increase in K_{n_0} produces an increase in the value of slip velocities at the wall and a decrease in the developed velocity profiles in the middle, as seen in Figure (9.3). Furthermore, there are overshoots in the velocity profiles at the axial

location at the inlet even for $K_{n_0} = 0.1$. A reduction in K_{n_0} affects and increases the amount of overshoot, as shown in Figure (9.3). In addition, the velocity profiles at high K_{n_0} are more regular than at low K_{n_0}. See Figure (9.4) for an example.

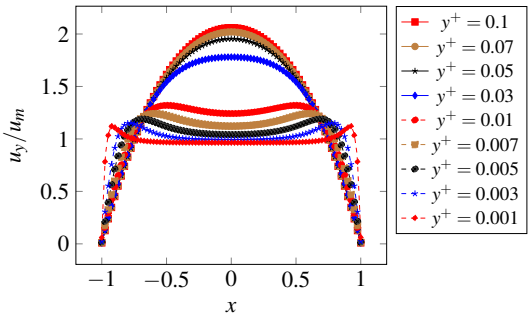

(a) $K_{n_0} = 0.001, n_y = 600$

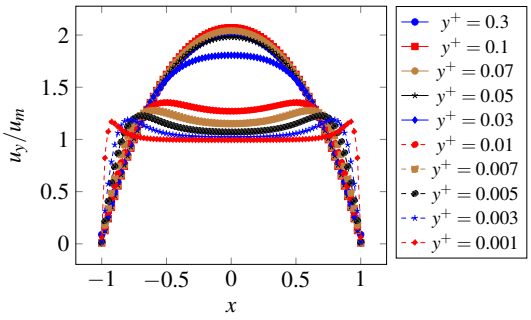

(b) $K_{n_0} = 0.001, n_y = 1000$

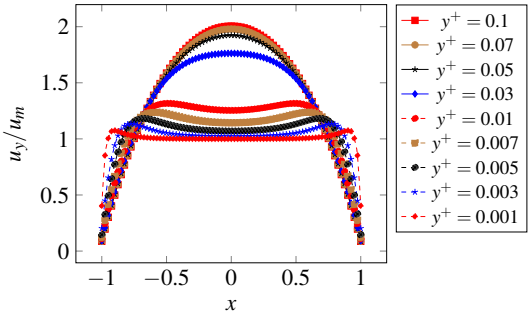

(c) $K_{n_0} = 0.01, n_y = 600$

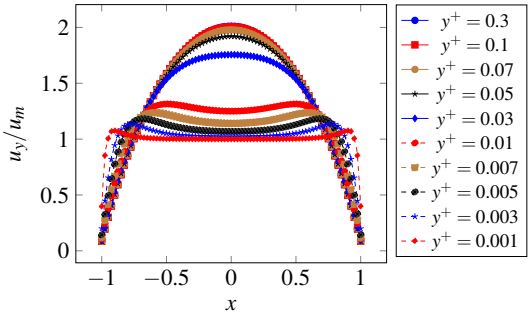

(d) $K_{n_0} = 0.01, n_y = 1000$

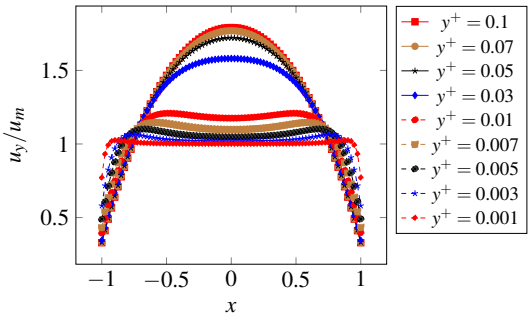

(e) $K_{n_0} = 0.05, n_y = 600$

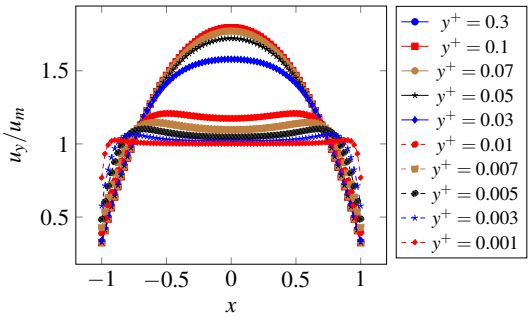

(f) $K_{n_0} = 0.05, n_y = 1000$

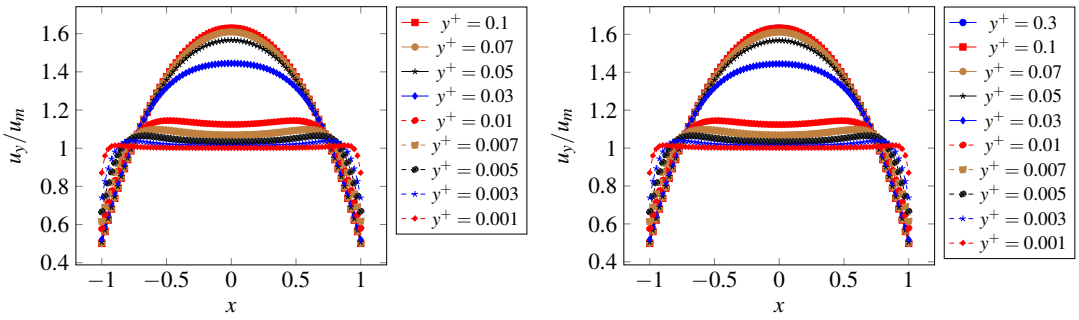

(g) $K_{n_0} = 0.1, n_y = 600$ *(h)* $K_{n_0} = 0.1, n_y = 1000$

Figure 9.4: 3D velocity at $n_x = 80, n_z = 80$, $\varepsilon = 1, Re = 40$, $u_{in} = 0.05$ and different K_{n_0}.

The influence of the Reynolds number is clear in Figure (9.4). An increase in the Reynolds number affects the fully developed velocity profile because it reaches full development with a large Reynolds number Re faster than with a smaller Reynolds number Re. For example, the velocity profile at $y^+ = 0.05$ and $Re = 40$ is fully developed faster than the velocity profile at $y^+ = 0.05$ and $Re = 10$ as seen in Figures (9.3) and (9.4). Further, the velocity profiles are fully developed at $y^+ \geq 0.1$ and this is clear with $Re = 10, 40$ as shown also in Figures (9.3) and (9.4). The increase of the length of the channel shows that the velocity profiles are fully developed at $y^+ \geq 0.1$ because the value of the velocity profile at $y^+ = 0.1$ is the same or quite close to the the value of the velocity profile at $y^+ = 0.3$, as seen in Figure (9.4).

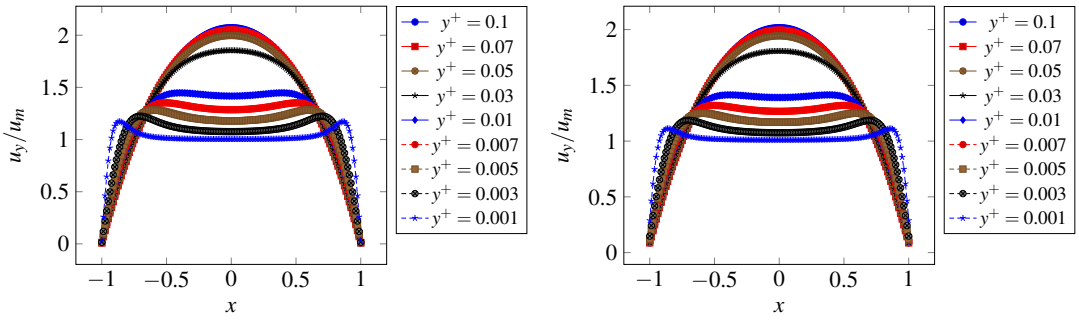

(a) $K_{n_0} = 0.001$ *(b)* $K_{n_0} = 0.01$

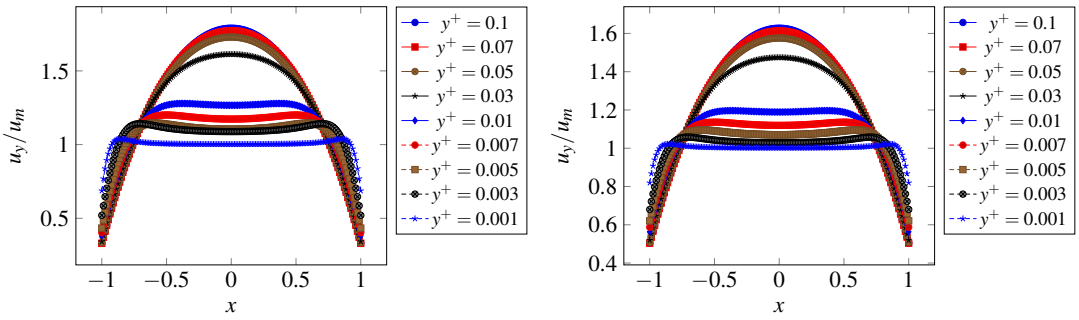

(c) $K_{n_0} = 0.05$ *(d)* $K_{n_0} = 0.1$

Figure 9.5: 3D velocity profiles at $n_x = 160$, $n_z = 160$, $n_y = 2000$, $\varepsilon = 1$, $Re = 80$, $u_{in} = 0.05$ and different K_{n_0}.

The velocity profiles are easily fully developed with large Re at each K_{n_0}. This can be demonstrated by comparing the fully developed velocity profiles in Figures (9.3), (9.4) and (9.5) for $\varepsilon = 1$.

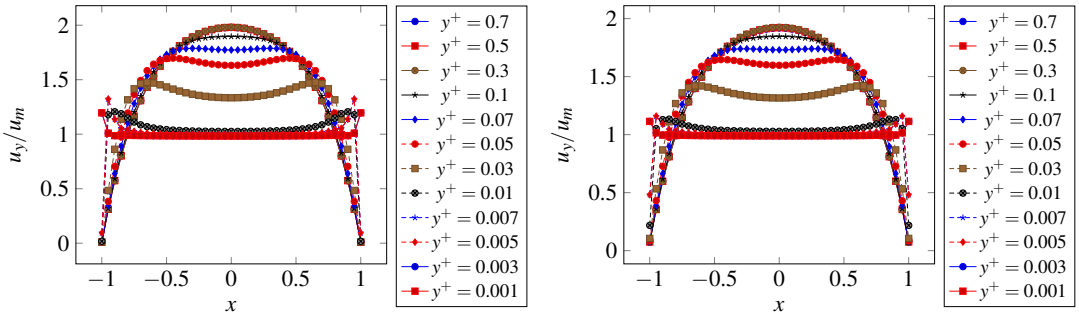

(a) $K_{n_0} = 0.001$ *(b)* $K_{n_0} = 0.01$

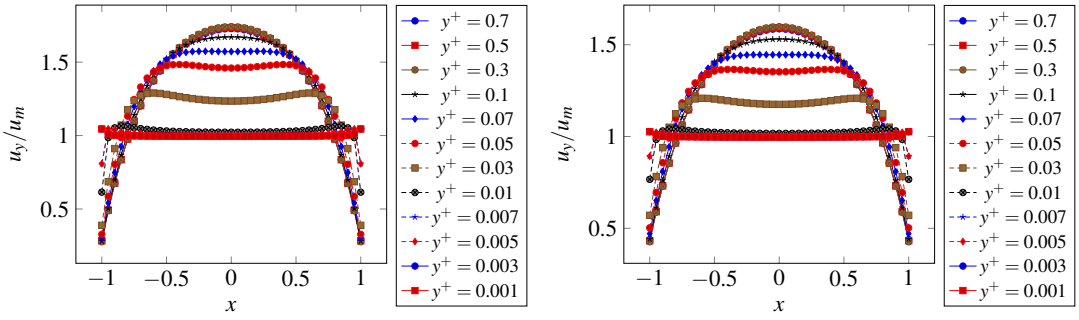

(c) $K_{n_0} = 0.05$ *(d)* $K_{n_0} = 0.1$

Figure 9.6: 3D velocity profiles at $n_x = 40$,$n_z = 20$, $n_y = 200$, $\varepsilon = 0.5$, $Re = 10$, $u_{in} = 0.05$ and different K_{n_0}.

Now we move from aspect ratio $\varepsilon = 1$ to $\varepsilon = 0.5$ to examine the influence of aspect ratio on the fully developed velocity profile at each K_{n_0} and Reynolds

number. The influence of K_{n_0} at $\varepsilon = 0.5$ is shown in Figure (9.6) and is quite similar to the influence of K_{n_0} at $\varepsilon = 1$ as seen in Figure (9.3).

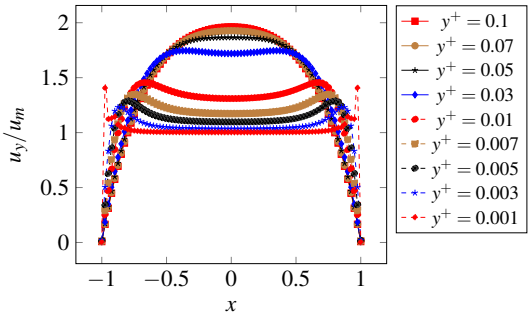

(a) $K_{n_0} = 0.001$, $n_y = 500$

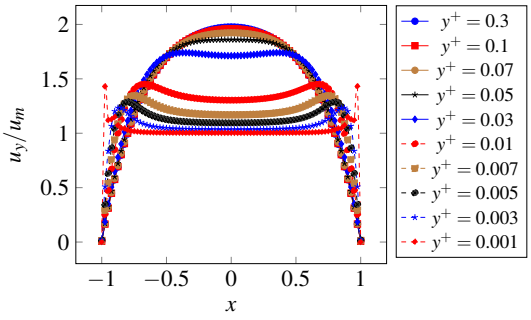

(b) $K_{n_0} = 0.001$, $n_y = 800$

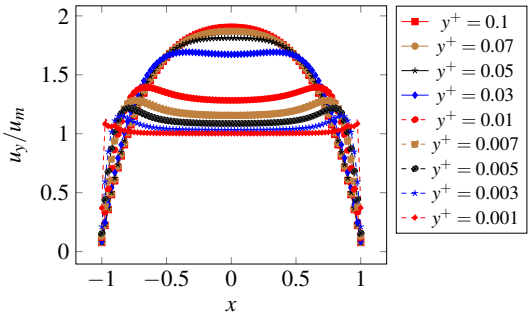

(c) $K_{n_0} = 0.01$, $n_y = 500$

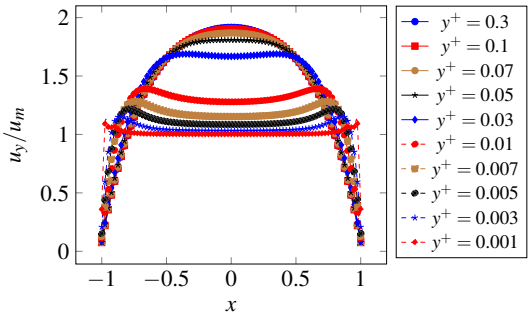

(d) $K_{n_0} = 0.01$, $n_y = 800$

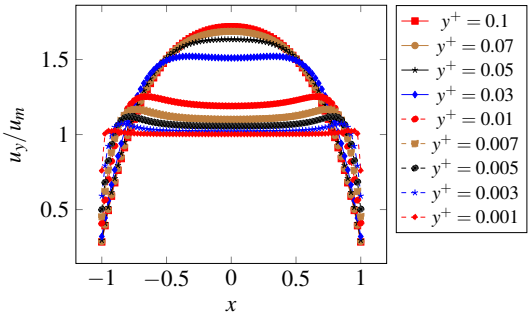

(e) $K_{n_0} = 0.05$,$n_y = 500$

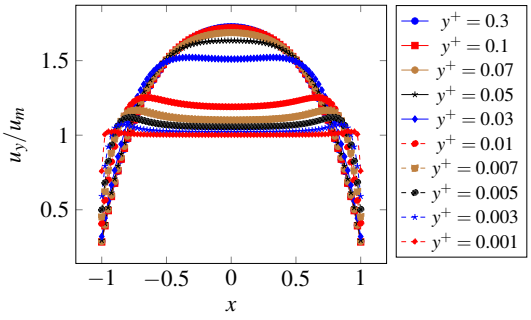

(f) $K_{n_0} = 0.05$,$n_y = 800$

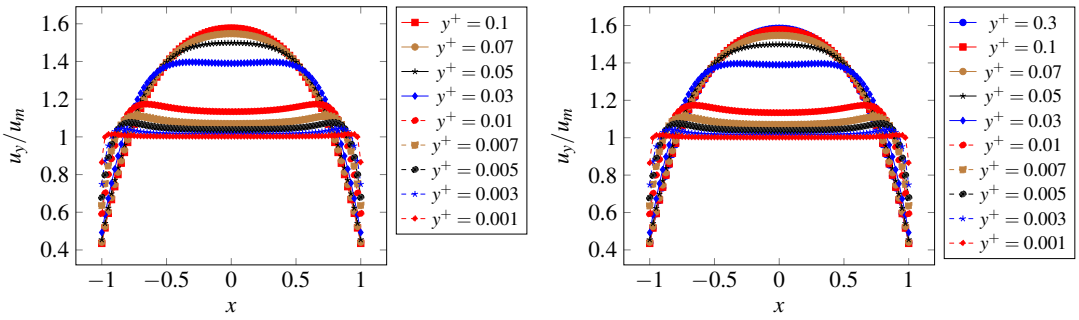

(g) $K_{n_0} = 0.1$, $n_y = 500$ *(h)* $K_{n_0} = 0.1$, $n_y = 800$

Figure 9.7: 3D velocity at $n_x = 80$,$n_z = 40$, $\varepsilon = 0.5$, $Re = 40$, $u_{in} = 0.05$ and different K_{n_0}.

The influence of Reynolds number with $\varepsilon = 0.5$ is similar to the influence of the Reynolds number with $\varepsilon = 1$ at each K_{n_0}. For example, the velocity profile reaches full development with a large Reynolds number Re faster than with a small Reynolds number Re, as in the case of the velocity profiles at $y^+ = 0.03, 0.05$ and $Re = 40$ which fully develop faster than those at $y^+ = 0.03, 0.05$ and $Re = 10$, as seen in Figures (9.7) and (9.6). Additionally, the velocity profiles are fully developed at the dimensionless hydrodynamically developed length y^+ close to or greater than 0.1, which is evident with $Re = 10, 40$, as seen in Figures (9.6) and (9.7). An increase of the length of the channel shows that the velocity profiles are fully developed at hydrodynamically developed length approximated as $y^+ \geq 0.1$ because the value of the velocity profile at $y^+ = 0.1$ is very close to the value of the velocity profile at $y^+ = 0.3$, as seen in Figure (9.7).

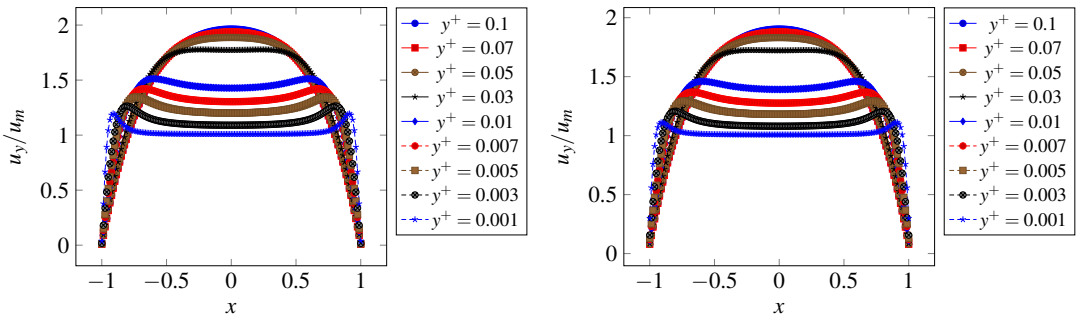

(a) $K_{n_0} = 0.001$ *(b)* $K_{n_0} = 0.01$

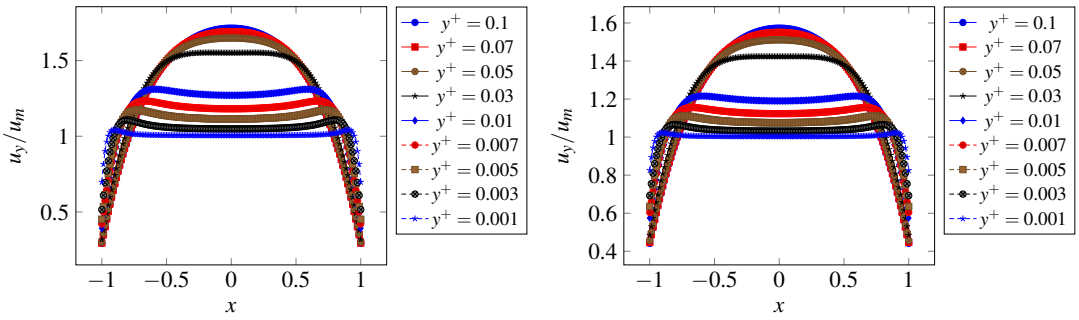

(c) $K_{n_0} = 0.05$ *(d)* $K_{n_0} = 0.1$

Figure 9.8: 3D velocity at $n_x = 160$,$n_z = 80$, $n_y = 1000$, $\varepsilon = 0.5$, $Re = 80$, $u_{in} = 0.05$ and different K_{n_0}.

In addition, the aspect ratio ε's influence on the fully developed velocity profiles is clear to see, because those profiles with $\varepsilon = 0.5$ are slightly flatter than those with $\varepsilon = 1$. This is very noticeable with $Re = 80$ and hydrodynamically developed length $y^+ \geq 0.03$ as seen in Figures (9.5) and (9.8).

The flow seems to be static at the wall close to the entrance region and gradually accelerates toward the centreline for each ε and Re. This happens because the velocity of flow tends to zero near the entrance where particles meet the wall and the viscous friction causes a fast reduction in the velocity until it is zero. The reduction in velocity acceleration at the wall is due to the high pressure gradient, and is seen in all the Figures, for example in (9.5) or (9.8).

In the current model, the fully developed velocity profiles' behaviour with $\varepsilon = 0.5$, provided in Figures (9.5) and (9.8), is similar to that of the profiles which can be seen in Niya *et. al* [41] at various K_{n_0}. Niya *et. al* [41] used a theoretical maximum centreline fully developed velocity in the x-axis (width direction) to normalize the velocity profiles, and this makes a difference in the maximum velocity profile when compared with the profiles in the current model, which are instead normalized using the mean velocity profile at the cross section of the outlet. In this model, the inlet velocity is $u_{in} = 0.05$. Thus, it is reasonable to get a maximum velocity of around 2 with small $K_{n_0} = 0.001$ and around 1.6 with high $K_{n_0} = 0.1$, at each Re and aspect ratio. Moreover, Niya *et. al* [41] used Lattice Boltzmann model (D_3Q_{15}) and a modified K_n which was based on an accommodation coefficient, while the $K_{n_{Local}}$ is used in this model.

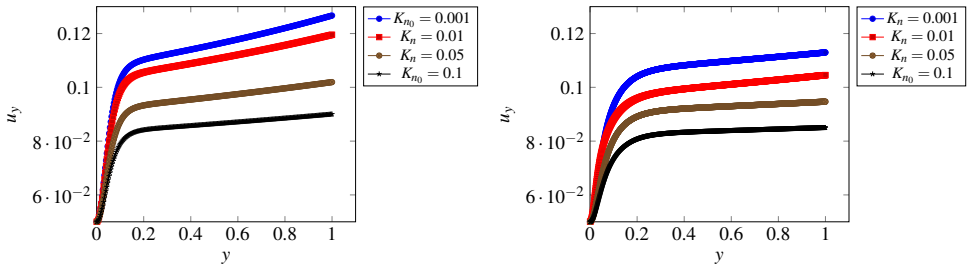

(a) $\varepsilon = 1$ $Re = 10$

(b) $\varepsilon = 1$ $Re = 40$

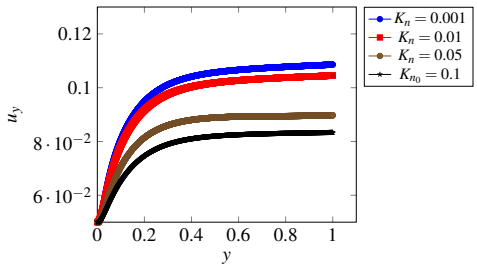

(c) $\varepsilon = 1$ $Re = 80$

Figure 9.9: The velocity u_y at the centreline along the channel.

Overall, Figure (9.9) shows that the velocity profile at the centreline along the channel starts from the inlet velocity of 0.05 and increases sharply to being with, becoming more gradual as it approaches the centreline. Note that with the small Reynolds number, the change in behaviour is more abrupt, at each K_{n_0}, as shown in Figure (9.9)(a), whereas with larger Reynolds numbers the change is more gradual, as seen in Figure (9.9)(c). Furthermore, the value of the velocity profile at the centreline of a channel with a small Reynolds number is slightly larger than the centreline velocity with a large Reynolds number, as shown in Figure (9.9)(a) and (c) for $\varepsilon = 1$. It is clear from Figure (9.9) that the K_{n_0} influences the value of the centreline velocity, where it can be seen that this value is decreased by increasing K_{n_0} at each Reynolds number.

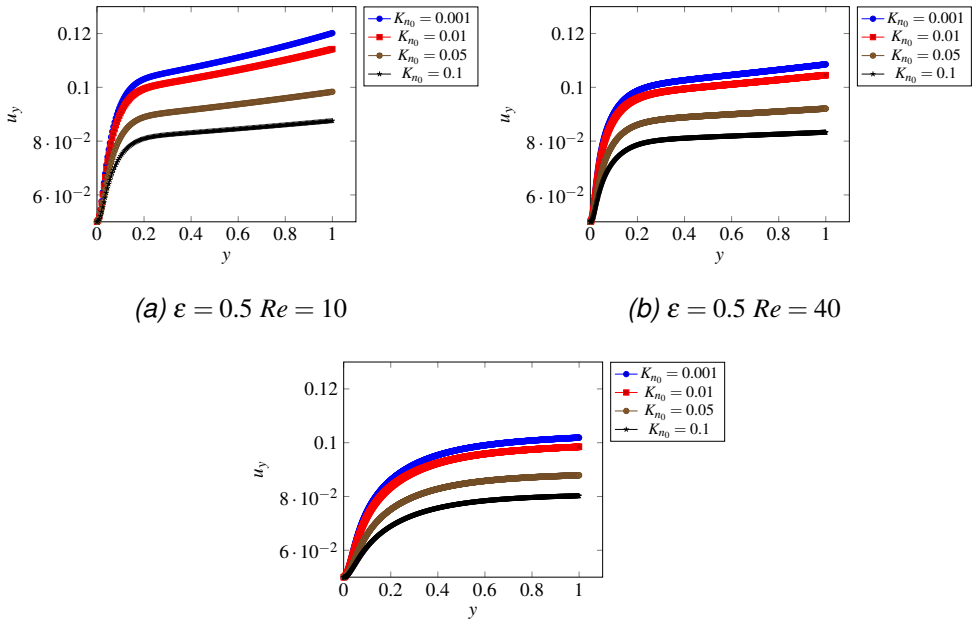

(a) $\varepsilon = 0.5$ $Re = 10$

(b) $\varepsilon = 0.5$ $Re = 40$

(c) $\varepsilon = 0.5$ $Re = 80$

Figure 9.10: The velocity u_y at the centreline along the channel.

The velocity at the centreline along a channel with $\varepsilon = 0.5$ displays similar behaviour to that along a channel with $\varepsilon = 1$ at each K_{n_0} and Reynolds number as seen in Figures (9.10) for $\varepsilon = 0.5$ and (9.9) for $\varepsilon = 1$. However, the velocity value at the centreline along a channel with $\varepsilon = 0.5$ is smaller than that at the centreline along a channel with $\varepsilon = 1$, which may be due to the maximum value of the velocity profiles in each case. In other words, the maximum value of the velocity profile at the centreline along a channel with $\varepsilon = 0.5$ is smaller than the maximum value of the velocity profile at the centreline along a channel with $\varepsilon = 1$.

9.3.1.2 Narrow duct $\varepsilon = 0.1$

The fully developed profiles for a narrow duct of $\varepsilon = 0.1$ are compared with the analytical solution for two parallel plates that was presented by Duan and Muzychka [16]. The exact solution with Navier-slip conditions is at $u_x = u_s = l_s|\frac{du_x}{dy}|$ and at $z = \pm H$, where H is the height of channel. This solution is based on the accommodation coefficient σ_u, K_{n_0} and hydrodynamic development length. The accommodation coefficient σ_u is assumed to be 1, thus the analytical solution will

be

$$u_{Exact}\left(z,y^{+}\right)=\frac{1K_{n_0}}{1+12K_{n_0}}+\frac{1.5}{1+12K_{n_0}}\left(1-\left(y^{+}\right)^{2}\right)+\sum_{i=1}^{\infty}\frac{2\left[\vartheta_i\cos\left(\vartheta_i y^{+}\right)-\sin\left(\vartheta_i\right)\right]exp\left(-16\vartheta_i^{2}y^{+}\right)}{\vartheta_i^{2}\sin\left(\vartheta_i\right)\left[1+12K_{n_0}+16\left(\vartheta_i K_{n_0}\right)^{2}\right]},\tag{9.3.1}$$

where ϑ_i are the eigenvalues that satisfy the relation $\tan\vartheta_i=\dfrac{\vartheta_i}{1+4\vartheta_i^{2}K_{n_0}}$. Note that the fully developed profiles in the narrow duct are examined in the height (z-direction) because they are too flat for width direction examination, in which case the channel would need to be very long to show the fully developed velocity profiles. The mean momentum u_m^{*} at the centerline and along the channel is used to normalize the fully developed velocity profiles and the reason for this is to conserve mass flow. Thus,

$$u_m^{*}=\frac{\rho u_y\left(y^{+},z\right)}{\int_0^1\rho u_y\left(y^{+},z\right)dz}.\tag{9.3.2}$$

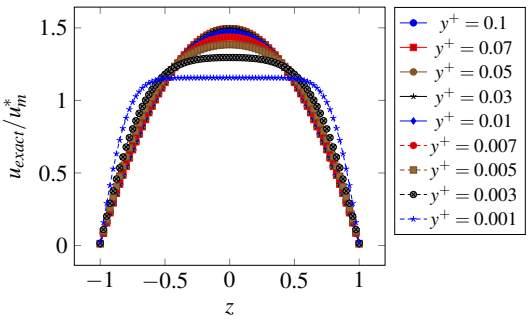

(a) $K_{n_0}=0.001$

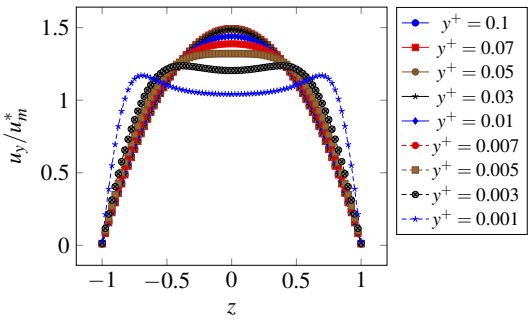

(b) $K_{n_0}=0.001$

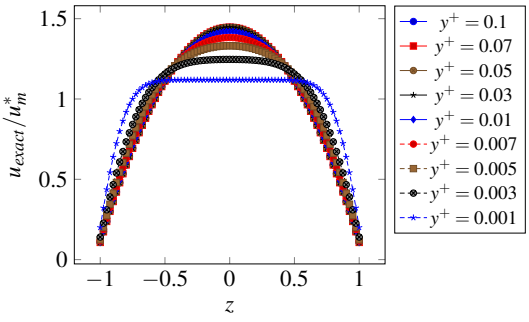

(c) $K_{n_0}=0.01$

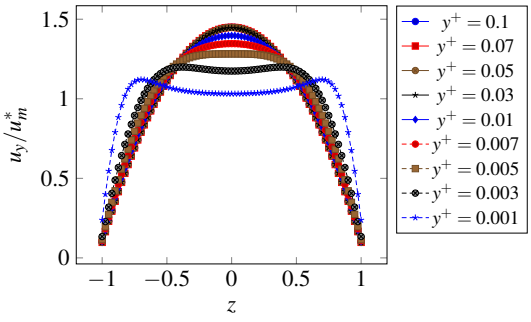

(d) $K_{n_0}=0.01$

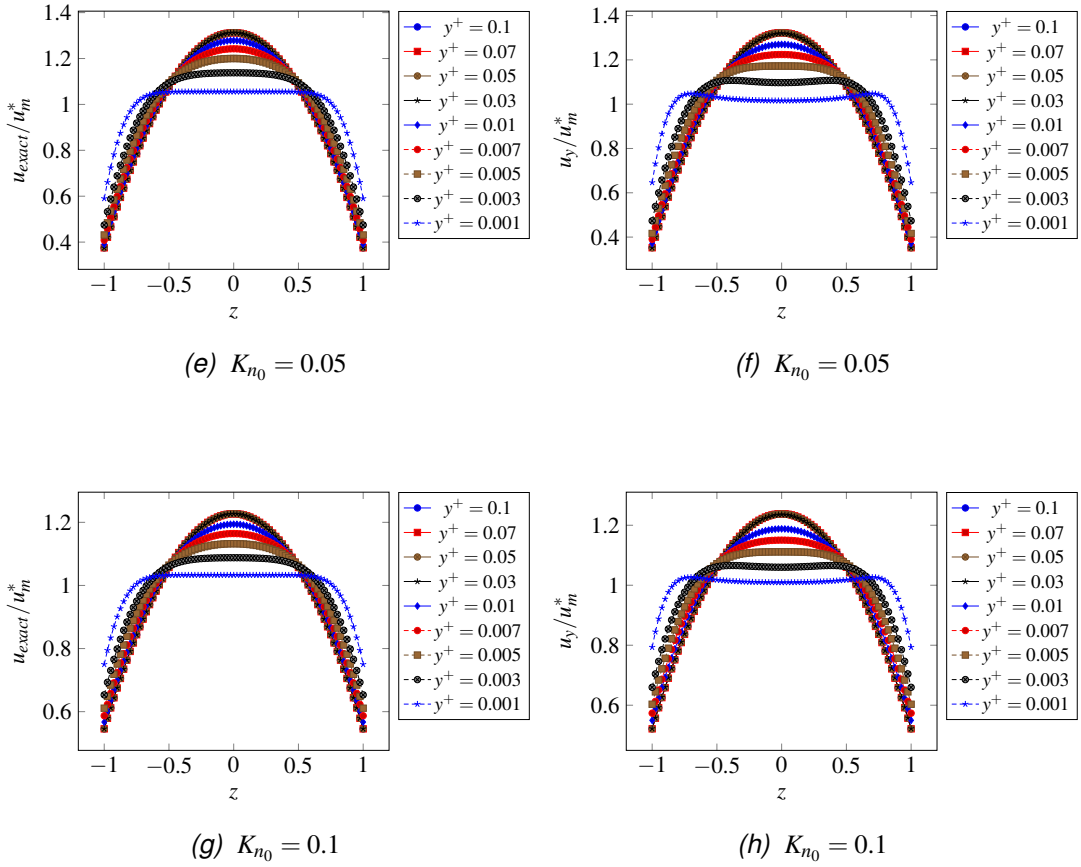

(e) $K_{n_0} = 0.05$ *(f)* $K_{n_0} = 0.05$

(g) $K_{n_0} = 0.1$ *(h)* $K_{n_0} = 0.1$

Figure 9.11: 3D velocity profiles at $n_x = 800$, $n_z = 80$, $n_y = 2000$, $\varepsilon = 0.1$, $Re = 120$, $u_{in} = 0.05$ and different K_{n_0}. (b), (d), (f) and (h) are the velocities of LBM and the (a), (c), (e) and (g) are the the exact solutions or analytical solutions.

The agreement between the fully developed profiles for a narrow duct of $\varepsilon = 0.1$ and the analytical solutions is generally good at the various K_{n_0}, as seen in Figure (9.11). This figure demonstrates particularly good agreement when the velocities are with hydrodynamically developed length $y^+ \geq 0.03$ at each K_{n_0}. In addition, the value of the fully-developed slip velocities at the boundary are a little different from the exact solutions at the boundary with a small hydrodynamically developed length $y^+ = 0.001$ and a high $K_{n_0} = 0.05, 0.1$. The value of fully-developed slip velocities at their maximum are different from the exact solutions at their maximum, with a small hydrodynamically developed length $y^+ \leq 0.01$ and $K_{n_0} = 0.001, 0.01, 0.05$. This difference may be due to the method used to normalise the velocity, because it is based only on the height along the channel at the centreline and not on the whole cross section.

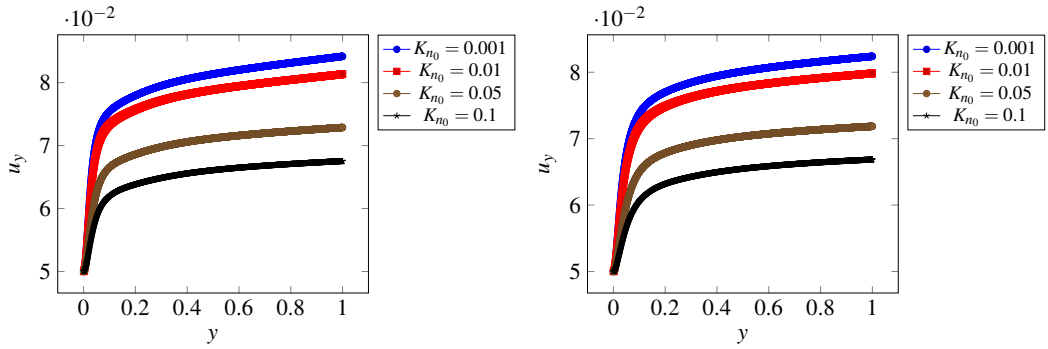

(a) $\varepsilon = 0.1$, $Re = 80$ *(b)* $\varepsilon = 0.1$, $Re = 120$

Figure 9.12: The velocity u_y along the channel at the centreline, at $n_x = 800$,$n_z = 80$, $n_y = 2000$

The velocity profile along the centreline of the narrow duct channel $\varepsilon = 0.1$ displays similar overall behaviour to that of $\varepsilon = 0.5, 1$ but the velocity value at the centreline of the narrow duct $\varepsilon = 0.1$ is smaller than that of $\varepsilon = 0.5, 1$ at each K_{n_0} and Re. This is shown in Figures (9.12), (9.9) and (9.10). Again, this probably happens because of the maximum values of each velocity profile at the centreline of the channel, as $\varepsilon = 0.1$ has a smaller maximum value than $\varepsilon = 0.5, 1$. Also, at $\varepsilon = 0.1$ with $Re = 80$ the velocity at the centreline begins sharply, and begins to smooth out a little at $Re = 120$, but is still sharper than the velocity profile at the centreline along the channel with $\varepsilon = 0.5, 1$ and $Re = 80$, as seen in (9.9)(c) for a square duct and (9.10)(c) for a rectangle.

The norm error is defined as

$$\| \bar{L}(y) \|_2 = \sqrt{\frac{1}{n_z} \sum |\mathbf{u}_{LBM}(x, y^+, z) - \mathbf{u}_{Exact}(x, y^+, z)|^2}, \tag{9.3.3}$$

where n_z is the computational grid size in z-direction.

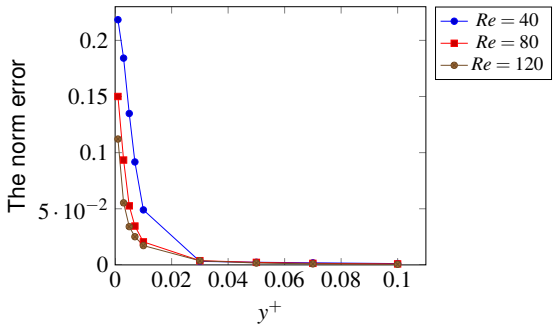

(a) $\varepsilon = 0.1$, $K_{n_0} = 0.001$

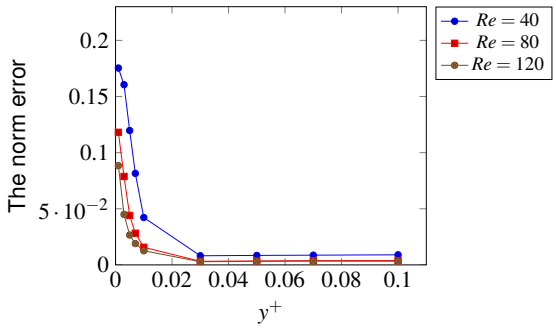

(b) $\varepsilon = 0.1$, $K_{n_0} = 0.01$

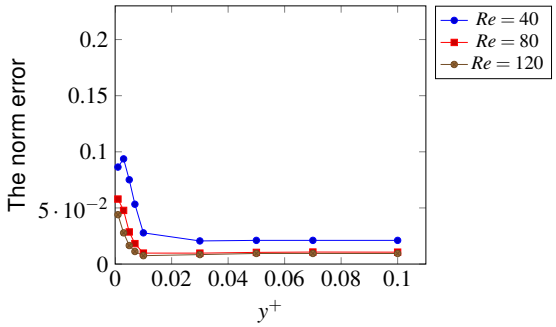

(c) $\varepsilon = 0.1$, $K_{n_0} = 0.05$

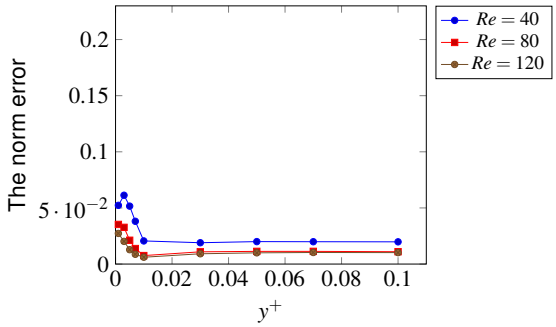

(d) $\varepsilon = 0.1$, $K_{n_0} = 0.1$

Figure 9.13: The norm error between the fully-developed LBM velocity and the exact solution, at different K_{n_0} and Reynolds numbers.

Figure (9.13) shows that an increase in the Reynolds number leads to a reduction in the error between the fully-developed velocity profiles of the LBM and the exact solutions, at each K_{n_0}. The errors at hydrodynamically developed lengths of $y^+ \geq 0.03$ have the same value when K_{n_0} is small such as $K_{n_0} = 0.001$, at each Reynolds number, as seen in Figure (9.13)(a). Further, the errors with high slip $K_{n_0} = 0.05, 0.1$ are less than the errors with small slip $K_{n_0} = 0.001, 0.01$. This is observed in Figure (9.13)(c) and (d) for $K_{n_0} = 0.05, 0.1$, and (a) and (b) for $K_{n_0} = 0.001, 0.01$. In the other words, an increase in K_{n_0} leads to a reduction in the errors between the fully-developed velocities.

9.3.2 The apparent friction factor

The definition of the apparent friction factor and Reynolds number product includes pressure drop along the channel,

$$\frac{\Delta p}{\rho_{min} u_{min}^2/2} = \frac{4y}{D_h} f_{app} = 4y^+ f_{app} Re, \tag{9.3.4}$$

where u_{min} and ρ_{min} are the mean velocity and density at the cross section of the channel entrance at y^+, respectively.

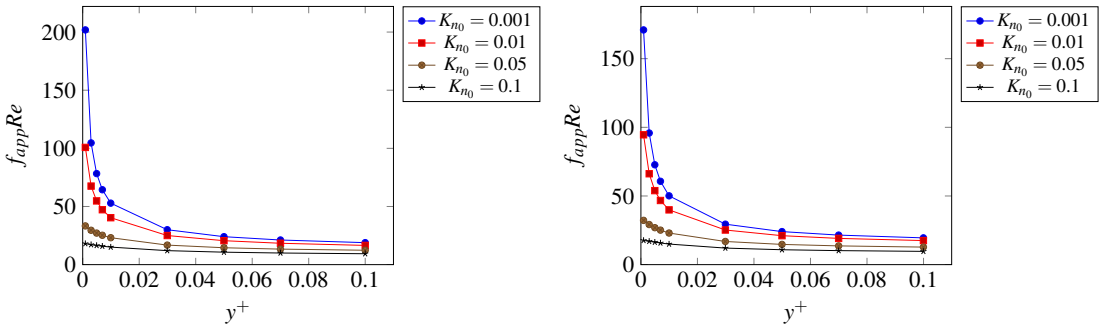

(a) $\varepsilon = 1, Re = 80$ *(b)* $\varepsilon = 0.5, Re = 80$

Figure 9.14: The apparent friction factor for $\varepsilon = 1, 0.5$.

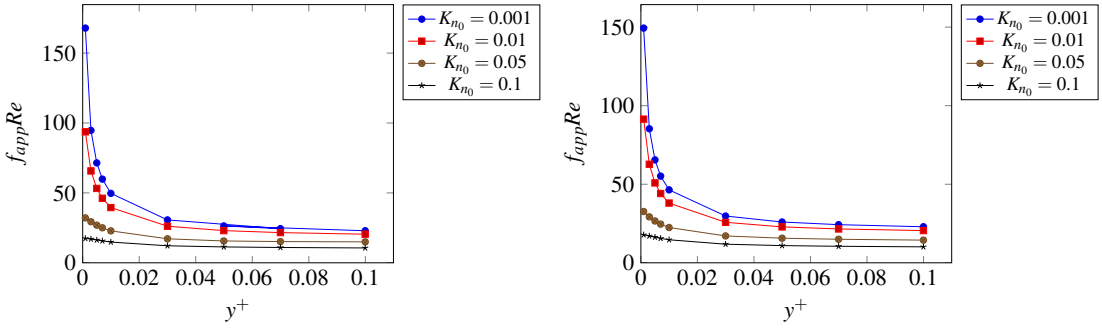

(a) $\varepsilon = 0.1$, $Re = 80$ *(b)* $\varepsilon = 0.1$, $Re = 120$

Figure 9.15: The apparent friction factor at $\varepsilon = 0.1$, $Re = 80$ and $Re = 120$.

The apparent friction factor and Reynolds number product at the entrance of a short channel is affected by K_{n_0}, Reynolds number, aspect ratio and the hydrodynamic entrance length y^+. An increase in K_{n_0} leads to a decrease in the apparent friction factor and Reynolds number product $f_{app}Re$ because the flow becomes rarefied with increased K_{n_0}, as shown in Figures (9.14) and (9.15). Furthermore, an increase in K_{n_0} affects the rarefaction, reducing it at each ε and

Re, as shown in Figures (9.14) and (9.15). An increase in the hydrodynamic entrance length y^+ has an effect on the $f_{app}Re$ whereby it causes the $f_{app}Re$ to reach a constant value, as seen in Figures (9.14) and (9.15).

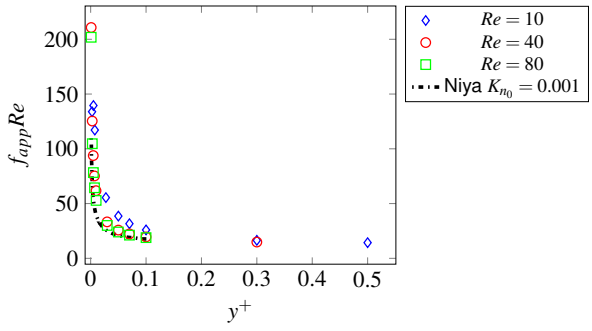

(a) $K_{n_0} = 0.001$

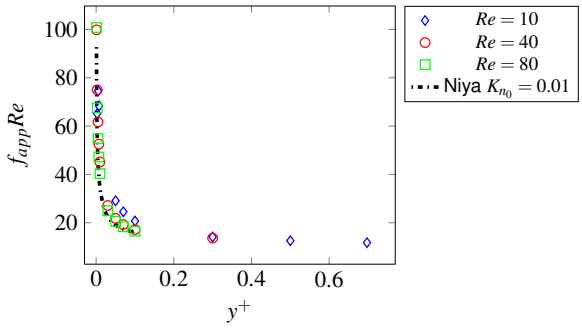

(b) $K_{n_0} = 0.01$

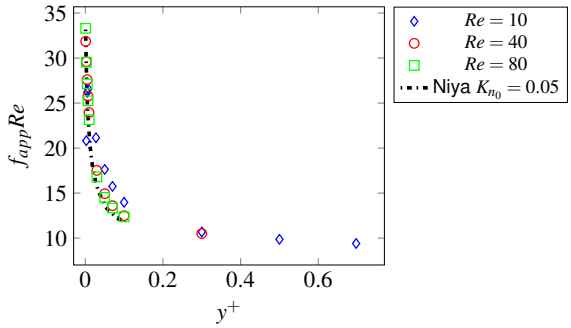

(c) $K_{n_0} = 0.05$

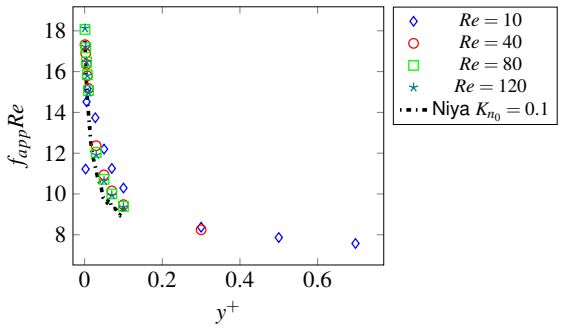

(d) $K_{n_0} = 0.1$

Figure 9.16: The apparent friction factor at different Re, ε=1.

An increase in the Reynolds number decreases the value of the apparent friction factor and Reynolds number product, and increases the bend of $f_{app}Re$. This is clear for the hydrodynamic entrance length $y^+ < 0.1$ at each K_{n_0} and Reynolds number, as shown in Figure (9.16) for $\varepsilon = 1$, where the value of the apparent friction factor and Reynolds number product $f_{app}Re$ is small at the beginning of the entrance with small Reynolds number $Re = 10$ and $\varepsilon = 1$. The reason for this may be due to the size of grid in the height and width direction being small *i.e.* the size of the cross section at the entrance of the channel is not large enough to make the flow smoother.

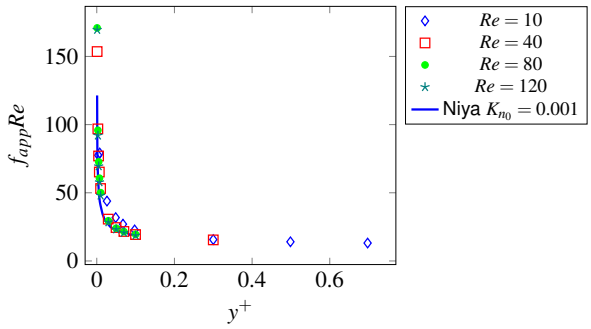

(a) $\varepsilon = 0.5$, $K_{n_0} = 0.001$

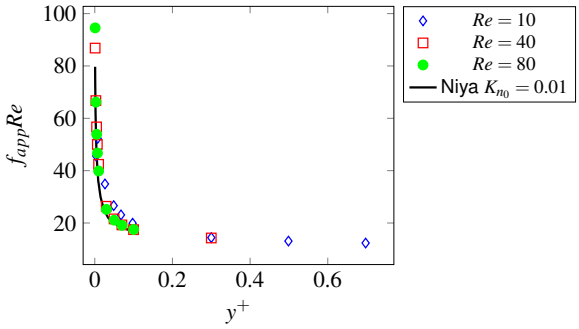

(b) $\varepsilon = 0.5$, $K_{n_0} = 0.01$

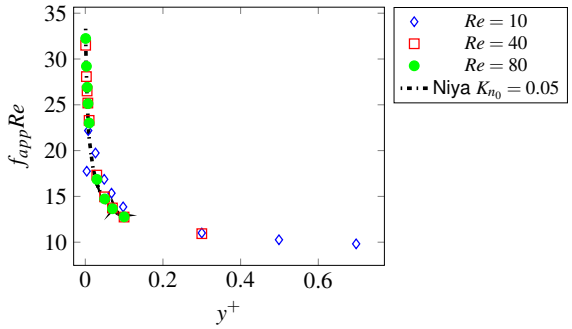

(c) $\varepsilon = 0.5$, $K_{n_0} = 0.05$

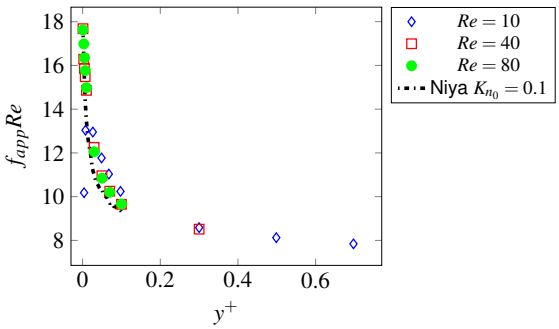

(d) $\varepsilon = 0.5$, $K_{n_0} = 0.1$

Figure 9.17: The apparent friction factor at different Re and $\varepsilon = 0.5$.

Figure (9.17) illustrates that the influence of the Reynolds number on the value of $f_{app}Re$ with $\varepsilon = 0.5$ is similar to the influence of Reynolds number on the value of $f_{app}Re$ with $\varepsilon = 1$. The figure (9.17) also shows that an increase in the Reynolds number leads a decrease in the apparent friction factor and Reynolds number product $f_{app}Re$ with $\varepsilon = 0.5$.

A change in the aspect ratio also has an effect on $f_{app}Re$, indicated by the values of the apparent friction factor and Reynolds number product with the square duct $\varepsilon = 1$ being larger than its values with the rectangular $\varepsilon = 0.5$, at each K_{n_0}. The value of the apparent friction factor and Reynolds number product with $Re = 80$ and $\varepsilon = 1, 0.5$ is in excellent agreement with the value presented by Niya *et. al* [41] at $\varepsilon = 1, 0.5$, as shown in Figures (9.16) and (9.17).

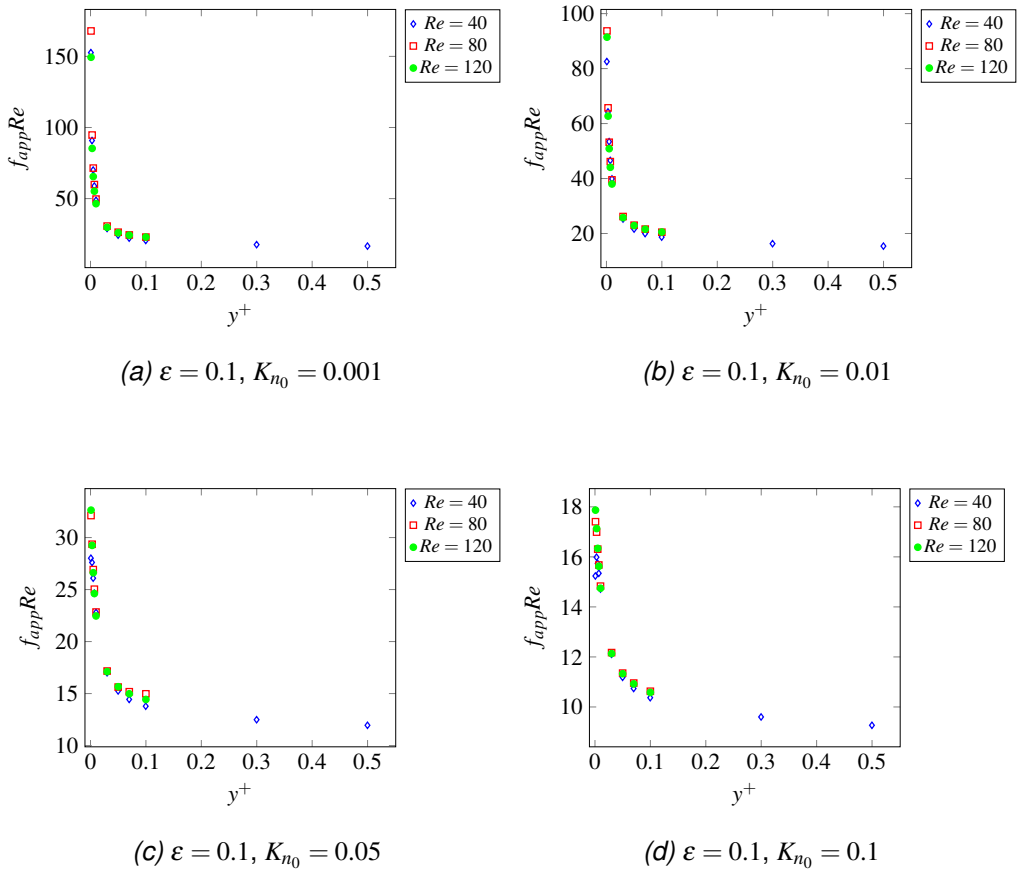

(a) $\varepsilon = 0.1$, $K_{n_0} = 0.001$ *(b)* $\varepsilon = 0.1$, $K_{n_0} = 0.01$

(c) $\varepsilon = 0.1$, $K_{n_0} = 0.05$ *(d)* $\varepsilon = 0.1$, $K_{n_0} = 0.1$

Figure 9.18: The apparent friction factor at different Re and $\varepsilon = 0.1$.

The value of $f_{app}Re$ at the beginning of the entrance is also small with Reynolds number $Re = 40$ and $\varepsilon = 0.1$, as seen in Figure (9.18). This happens because the size of the cross section at the entrance of the channel is not large enough to make the flow smoother.

In general, the values of $f_{app}Re$ with a square duct $\varepsilon = 1$ are larger than those with a rectangular $\varepsilon = 0.5$ or narrow duct $\varepsilon = 0.1$, at each K_{n_0}, as shown in Figures (9.16), (9.17) and (9.18). Additionally, Figures (9.16), (9.17) and (9.18) show that at small hydrodynamic entrance lengths y^+ there are differences in the value of $f_{app}Re$ with different Reynolds numbers. However, for large values of y^+, the $f_{app}Re$ results agree.

9.4 Simulation with fixed length

In this simulation, we define the fixed slip length as $l_{s_0} = D_h K_{n_0}$ and the local slip length as $l_{s_{Local}} = K_{n_{Local}} D_h$ in order to distinguish between them. The fully-developed profile and the apparent friction factor and Reynolds number product

at the entrance channel are examined using this fixed slip length l_{s_0}, based on K_{n_0}, at various aspect ratios with $K_{n_0} = 0.001, 0.1$ and Reynolds number $Re = 80$, and compared with results obtained using $K_{n_{Local}}$ as presented in section (9.3).

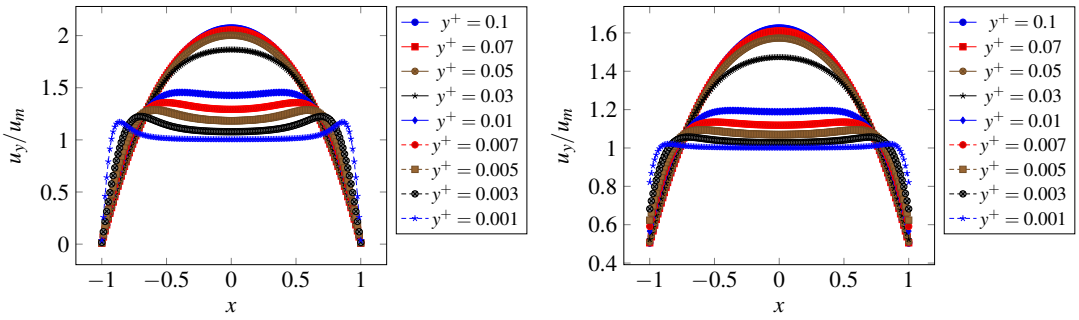

(a) $\varepsilon = 1$,$K_{n_0} = 0.001$ *(b)* $\varepsilon = 1$,$K_{n_0} = 0.01$

Figure 9.19: 3D velocity $n_x = 160$, $n_z = 160$, $n_y = 2000$, Re=80, $\varepsilon = 1$ and $u_{in} = 0.05$.

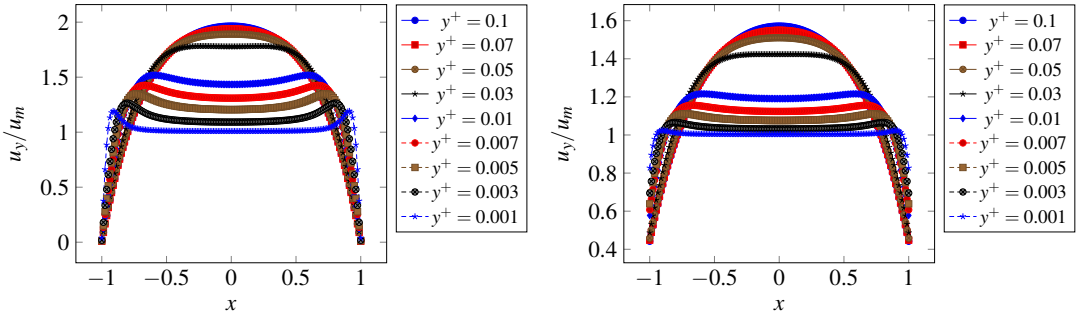

(a) $\varepsilon = 0.5$,$K_{n_0} = 0.001$ *(b)* $\varepsilon = 0.5$,$K_{n_0} = 0.1$

Figure 9.20: 3D velocity $n_x = 160$, $n_z = 80$, $n_y = 1000$, $Re = 80$, $\varepsilon = 0.5$ and $u_{in} = 0.05$.

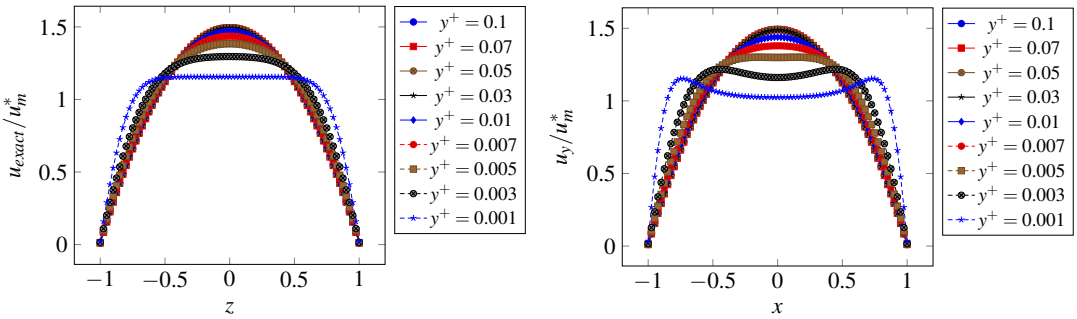

(a) $\varepsilon = 0.1$, $K_{n_0} = 0.001$ *(b)* $\varepsilon = 0.1$, $K_{n_0} = 0.001$

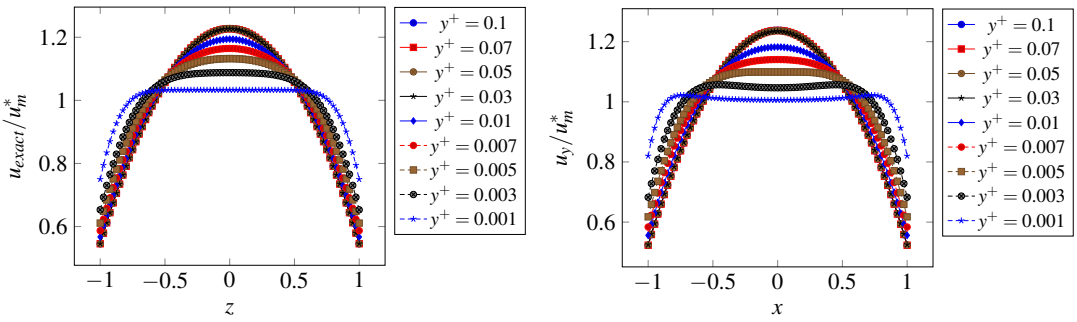

(c) $\varepsilon = 0.1$, $K_{n_0} = 0.1$ *(d)* $\varepsilon = 0.1$,$K_{n_0} = 0.1$

Figure 9.21: Comparison of 3D velocity profiles of LBM at $n_x = 800$, $n_z = 80$, $n_y = 2000$, $Re = 80$, $\varepsilon = 0.1$ and $u_{in} = 0.05$ with the exact solutions or analytical solutions. (b), (d) are the velocity profiles of LBM and (a), (c) are the analytical solutions.

Figures (9.19), (9.20) and (9.21) show that the behaviour of the fully-developed velocity profiles with $\varepsilon = 1, 0.5, 0.1$ are close to those obtained using $K_{n_{Local}}$, as seen previously in Figures (9.5), (9.8) and (9.11). Also, the fully-developed velocity profiles of the LBM are still in good agreement with the exact solutions, as demonstrated in Figure (9.21).

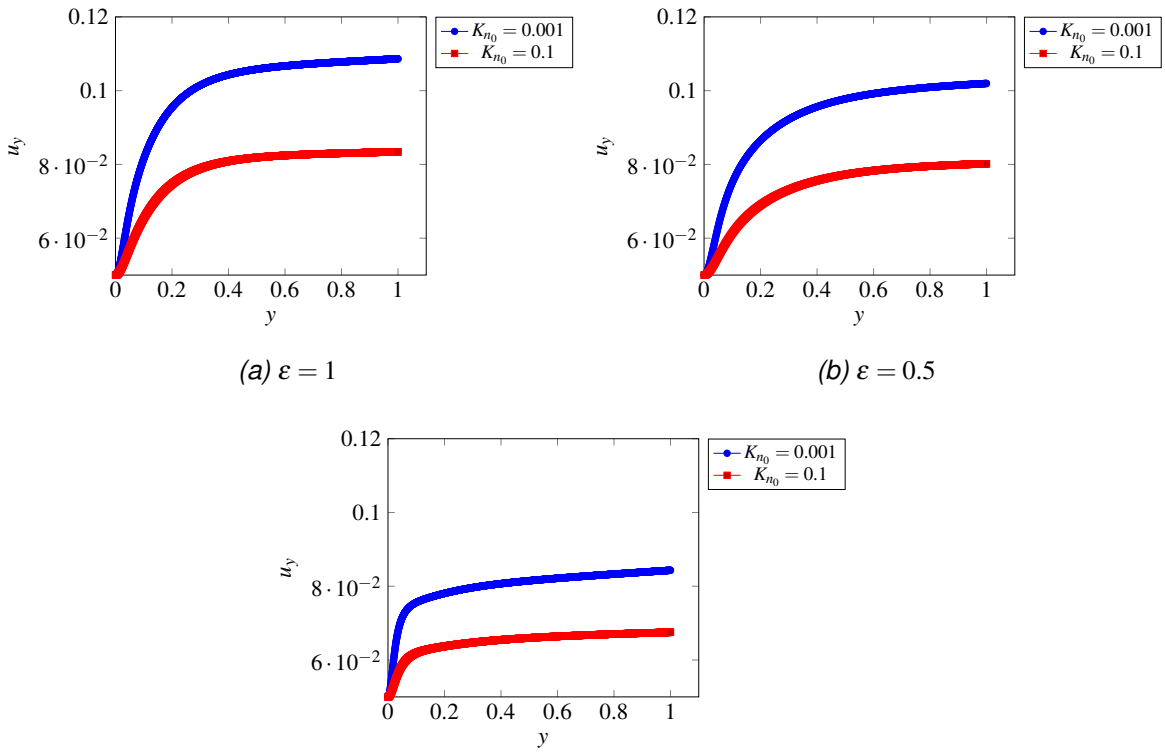

(a) $\varepsilon = 1$ *(b)* $\varepsilon = 0.5$

(c) $\varepsilon = 0.1$

Figure 9.22: The velocity u_y at the centreline along the channel at $Re = 80$ and $\varepsilon = 1, 0.5, 0.1$.

Additionally, Figure (9.22) shows that the velocity profiles at the centre line along the channel with fixed length increase gradually and smoothly with $Re = 80$ and $\varepsilon = 1, 0.5$, as do those obtained using $K_{n_{Local}}$, as shown in Figures (9.10)(c) for $\varepsilon = 0.5$ and (9.9)(c) for $\varepsilon = 1$, but with $\varepsilon = 0.1$ the velocity increases a little more sharply. The value of the velocity at the centreline is close to that obtained using $K_{n_{Local}}$. Further, the centreline velocity values decease with an increase in K_{n_0}, as well as decreasing with a decrease in the aspect ratio ε, as seen in Figure (9.22).

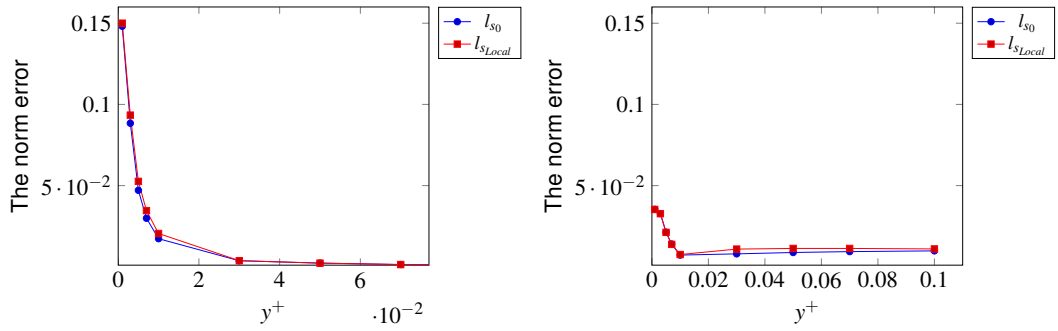

(a) $\varepsilon = 0.1$, $K_{n_0} = 0.001$ *(b)* $\varepsilon = 0.1$, $K_{n_0} = 0.1$

Figure 9.23: The norm error for fully-developed profile between the fixed length and local length at $\varepsilon = 0.1$.

The error between the fully-developed profiles and the exact solutions in a narrow duct $\varepsilon = 0.1$ display similar behaviour to those achieved using $K_{n_{Local}}$, as seen in Figures (9.23) for fixed slip length and (9.13) for local slip length. While errors do show $K_{n_0} = 0.001$, the values are close to those obtained using $K_{n_{Local}}$. The error values are also a little smaller than those obtained using $K_{n_{Local}}$ at $K_{n_0} = 0.1$ and hydrodynamically developed length $y^+ \geq 0.03$, as seen in Figure (9.23).

9.4.1 Apparent friction factor for fixed length

The apparent friction factor and Reynolds number product $f_{app}Re$ is examined with $Re = 80$ at the entrance of a short channel. Generally, the apparent friction factor and Reynolds number product with fixed length is affected by K_{n_0} and aspect ratio ε.

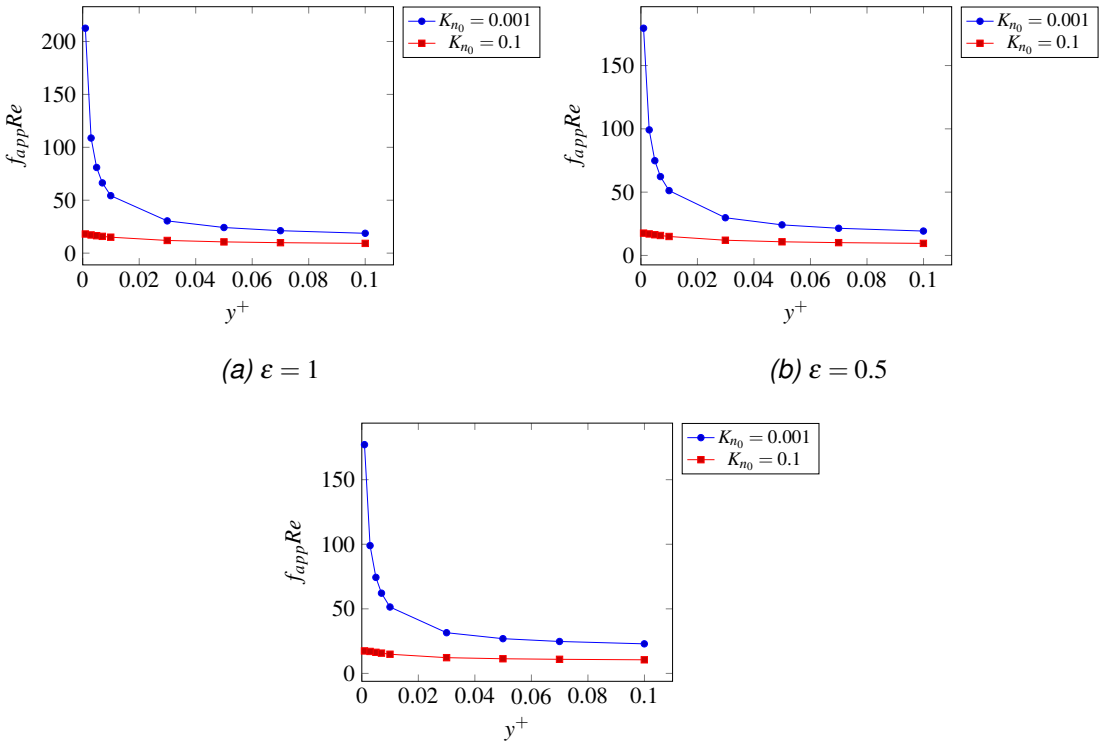

(a) $\varepsilon = 1$

(b) $\varepsilon = 0.5$

(c) $\varepsilon = 0.1$

Figure 9.24: Apparent friction factor with fixed length at $Re = 80$ and $\varepsilon = 1, 0.5, 0.1$.

Figure (9.24) shows that the apparent friction factor and Reynolds number product $f_{app}Re$ with fixed length behaves similarly to that gained using $K_{n_{local}}$, at various aspect ratios $\varepsilon = 1, 0.5, 0.1$, as seen in Figures (9.16), (9.17) and (9.18).

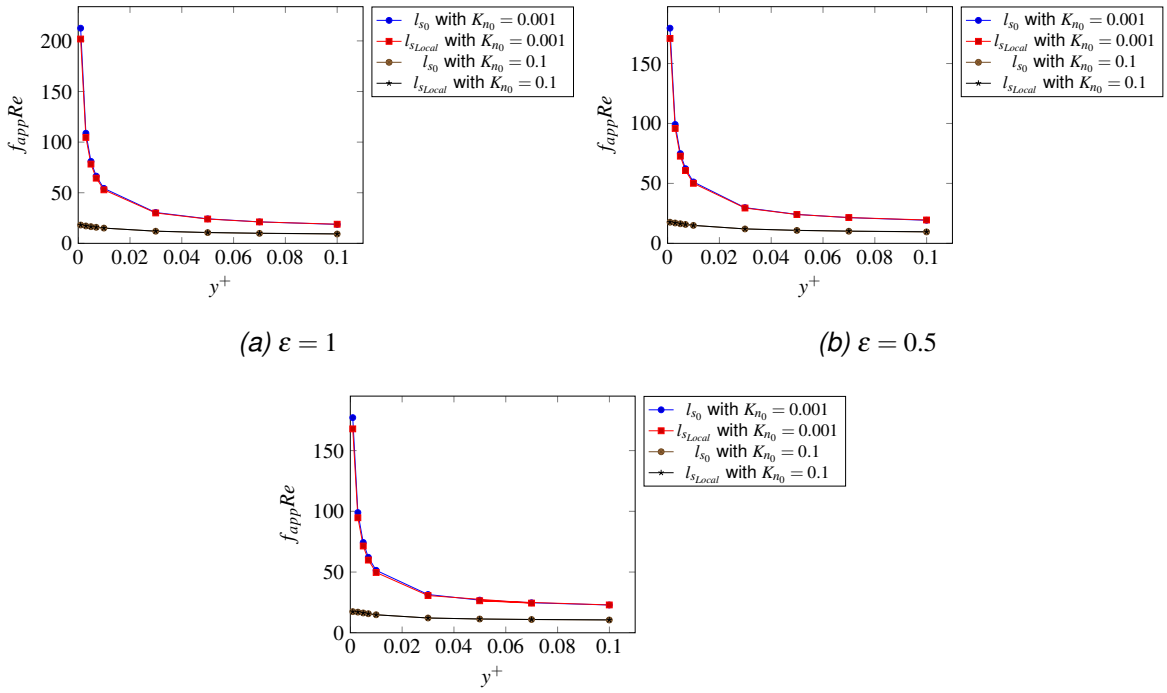

(a) $\varepsilon = 1$ *(b)* $\varepsilon = 0.5$

(c) $\varepsilon = 0.1$

Figure 9.25: Comparison of apparent friction factor and Reynolds number product with fix and local length, at $Re = 80$ and $\varepsilon = 1, 0.5, 0.1$.

In general the values of $f_{app}Re$ are close to those gained using $K_{n_{local}}$, except those of $f_{app}Re$ at small K_{n_0} such as $K_{n_0} = 0.001$ and hydrodynamically developed lengths of $y^+ < 0.03$ which are slightly larger than the value of $f_{app}Re$ gained using $K_{n_{local}}$, as seen in Figure (9.25).

The use of fixed length to simulate this kind of flow is cheaper than using local fixed length. The solutions of the velocity profile and apparent friction factor and Reynolds number product with fixed length converge faster than with local fixed length, especially for aspect ratios $\varepsilon = 1, 0.5$. Thus, we can conclude that the use of fixed length in this kind of simulation is better than using local fixed length.

9.5 Conclusion

In conclusion, the Lattice Boltzmann D_3Q_{19} model was presented to simulate laminar weakly compressible flow at the entrance of a channel in slip regime. Moment-based boundary conditions were successfully used to implement inflow boundary conditions at the inlet, pressure boundary conditions at the outlet and Navier-slip boundary conditions at the walls. The fully-developed velocity profiles

and the apparent friction factor and Reynolds number product were investigated at various nondimensional slip length, Reynolds numbers, aspect ratios and hydrodynamic entrance lengths. The results are in line with the other results in the literature. The value of the apparent friction factor and Reynolds number product was shown to depend on the Reynolds number and is a finite value at the entrance. The fully developed velocity profiles with a narrow duct are in agreement with the analytical solution and depend on the Reynolds number, as indicated by an increase in the Reynolds number leading to a reduction in the error between the fully-developed velocity profiles of the LBM and the analytical solution.

The fully developed velocity profiles and the apparent friction factor and Reynolds number product were checked with fixed length and compared with those acquired using local slip length or moved length. They are close, except that with the local slip length the value of the apparent friction factor and Reynolds number product is slightly less than that obtained using fixed length at small K_n and small hydrodynamic entrance lengths. Additionally, the errors between the fully developed velocity profiles of the LBM and the analytical solutions with high slip such as $K_{n_0} = 0.1$ are smaller than those acquired using $K_{n_{local}}$. Finally, it is concluded that using fixed length to simulate this kind of flow is cheaper than using local fixed length.

Chapter 10

Universal conclusions and future work

10.1 The universal conclusions

An analysis of the LBM has been performed using various simulations to obtain a numericals solution of the Navier-Stokes equations. In this thesis we determined various topics: such as the theoretical background of the LBM, which was introduced and demonstrated in chapter 1; how boundary conditions such as bounce back (non-slip) and moment-based were imposed on the LBM; and practical applications using the LBM to simulate flow problems.

Microscopic, mesoscopic and the macroscopic descriptions were demonstrated in chapter 1. Then, in chapter 2, the second order approximation of the Lattice Boltzmann equation was derived by discretising the velocity distribution functions and projecting the velocity distribution functions on a Hermite basis, then discretising time using the trapezoidal rule. Various lattices of LBM were represented in chapter 3 in both two and three dimensions, and the Chapman-Enskog approach was used to derive the Navier-Stokes equations in both 2D and 3D. The boundary conditions, explained in chapter 4, were used to apply the LBM to fluid flow. We simulated a single flow in this chapter, namely Poiseuille flow, with various boundary conditions such as standard bounce back, modified bounce back, halfway bounce back and moment-based. The results were good, and the errors of first or second order accuracy depending on the boundary conditions.

Two simulations with different types of scaling (acoustic and diffusive) executed for pulsatile flow in two and three dimensions, with moment-based boundary condition to implement no-slip and Navier-slip boundary conditions, were presented in chapters 5 and 6. The results of these are in strong agreement with the

results in the literature. The velocity profiles are in good agreement with the exact solution at each Womersley number. The error is of first order for acoustic scaling and no-slip boundary conditions in 2D, and of second order for diffusive scaling with Navier-slip boundary conditions in both 2D and 3D.

In Chapter 7, a simulation of 3D laminar flow in a square duct, driven by body force, was produced. Moment-based boundary conditions were used to implement Navier-slip boundary conditions. The results in the velocity profile are in agreement with the analytical solution and the error is second order accurate.

Another simulation with acoustic scaling was presented in chapter 8 to examine the rarefaction and compressibility effect on laminar flow in the case of two parallel plates and a 3D micro-duct. Moment-based boundary conditions were used to implement pressure boundary conditions at both the inlet and outlet. The results (velocity profiles, slip velocity profiles and pressure deviation) are again in good agreement with the results in the literature. The norm error for the velocity profiles is of first order and is approximated as first order for slip velocity. The final simulation for the LBM with moment-based boundary conditions in three dimensions was presented in chapter 9. This simulation was for fully developed laminar flow in the entrance region of a channel. The results (fully developed velocity profiles and the apparent friction factor and Reynolds number product) were again in line with the results in the literature. The apparent friction factor and Reynolds number product were found to depend on the Reynolds number.

10.2 Future work

In future, we firstly wish to parallel the Lattice Boltzmann method with moment-based boundary conditions in three directions: x-, y- and z-direction. We would also like to use moment-based boundary conditions to implement no-slip and Navier-slip conditions on the entrance region of pulsatile flow in two and three dimensions. Thirdly, we wish is to use moment-based boundary conditions to implement second order Navier-slip boundary conditions. In addition, we want to develop moment-based boundary conditions to work on complex boundaries such as curved pipes like blood vessels in two and three dimensions, and to parallelise

the Lattice Boltzmann method with these curved boundaries. The final wish is to apply our model, which consists of the LBM and moment-based boundary conditions, on flow in a two and three-dimensional porous medium.

Appendix A

Explanation of a form

A.1 Explain of the form $\overline{Q}_{\alpha\beta\gamma}$

The formula for the third order moment with the body force is $\overline{Q}_{\alpha\beta\gamma}$

$$\overline{Q}_{\alpha\beta\gamma} = Q_{\alpha\beta\gamma} + \frac{\delta_t}{2\tau} Q_{\alpha\beta\gamma} - \frac{\delta_t}{2\tau} Q^0_{\alpha\beta\gamma} - \sum_i \mathbf{c}_{i\alpha}\mathbf{c}_{i\beta}\mathbf{c}_{i\gamma}F_i, \tag{A.1.1}$$

and with pressure is

$$\overline{Q}_{\alpha\beta\gamma} = Q_{\alpha\beta\gamma} + \frac{\delta_t}{2\tau} Q_{\alpha\beta\gamma} - \frac{\delta_t}{2\tau} Q^0_{\alpha\beta\gamma}, \tag{A.1.2}$$

where

$$Q_{\alpha\beta\gamma} = Q^0_{\alpha\beta\gamma} + \tau Q^1_{\alpha\beta\gamma} \tag{A.1.3}$$

and

$$\begin{aligned} Q^1_{\alpha\beta\gamma} = \frac{1}{3}\left[\rho u_\gamma \delta_{\alpha\beta} + \rho u_\beta \delta_{\alpha\gamma} + \rho u_\alpha \delta_{\beta\gamma}\right]\partial_\delta u_\delta + \frac{\rho}{3}\left[\delta_{\alpha\beta}\partial_\gamma + \delta_{\alpha\gamma}\partial_\beta + \partial_\alpha \delta_{\gamma\beta}\right] u_\theta u_\theta \\ -\frac{\rho}{6}\left[u_\alpha\left(\partial_\beta u_\gamma + \partial_\gamma u_\beta\right) + u_\gamma\left(\partial_\alpha u_\beta + \partial_\beta u_\alpha\right) + u_\beta\left(\partial_\alpha u_\gamma + \partial_\gamma u_\alpha\right)\right]. \end{aligned} \tag{A.1.4}$$

List of references

[1] K. Al Khasawneh, H. Liu, and C. Cai. Asymptotic solutions for gaseous flow in a three-dimensional rectangular microchannel. In *49th AIAA Aerospace Sciences Meeting including the New Horizons Forum and Aerospace Exposition*, page 181, 2011.

[2] S. Ansumali and I. V. Karlin. Kinetic boundary conditions in the lattice Boltzmann method. *Phys. Rev. E*, 66(2):026311, 2002.

[3] E.B. Arkilic, M. A. Schmidt, and K. S. Breuer. Gaseous slip flow in long microchannels. *Journal of Microelectromechanical Systems*, 6(2):167–178, 1997.

[4] A. Artoli, D. Kandhai, H. CJ. Hoefsloot, A. G. Hoekstra, and P. MA. Sloot. Lattice BGK simulations of flow in a symmetric bifurcation. *Future Generation Comput. Systems*, 20(6):909–916, 2004.

[5] A.M. Artoli, A.G. Hoekstra, and P. Sloot. 3D pulsatile flow with the lattice Boltzmann BGK method. *Int. J. Mod. Phys. C*, 13(08):1119–1134, 2002.

[6] S. Bennett. *A lattice Boltzmann model for diffusion of binary gas mixtures*. PhD thesis, University of Cambridge, 2010.

[7] P. L. Bhatnagar, E. P. Gross, and M. Krook. A model for collision processes in gases. i. small amplitude processes in charged and neutral one-component systems. *Phys. Rev.*, 94(3):511, 1954.

[8] L. Boltzmann. *Vorlesungen über Gastheorie: Th. Theorie van der Waals'; Gase mit zusammengesetzten Molekülen; Gasdissociation; Schlussbemerkungen*, volume 2. Harvard University, J. A. Barth, 1898.

[9] C. Cercignani. The Boltzmann equation. In *The Boltzmann equation and its applications*, pages 40–103. Springer-Verlag New York Inc., 1988.

[10] S. Chapman, Th. G. Cowling, and D. Burnett. *The mathematical theory of non-uniform gases: an account of the kinetic theory of viscosity, thermal conduction and diffusion in gases*. Cambridge Univ. press,Cambridge, 1990.

[11] S. Chen and G. D. Doolen. Lattice Boltzmann method for fluid flows. *Annu. Rev. Fluid Mech*, 30(1):329–364, 1998.

[12] T. J. Chung. *Computational Fluid Dynamics*. Cambridge university press,Cambridge,United Kingdom, 2010.

[13] C. Coreixas, G. Wissocq, G. Puigt, J. F. Boussuge, and P. Sagaut. Recursive regularization step for high-order lattice Boltzmann methods. *Phys. Rev. E*, 96(3):033306, 2017.

[14] J. M. Cosgrove, J. A .and Buick, S. J. Tonge, C. G. Munro, C. A. Greated, and D. M. Campbell. Application of the lattice Boltzmann method to transition in oscillatory channel flow. *J. Phys A: Math. Gen.*, 36(10):2609, 2003.

[15] Z. Duan and Y. S. Muzychka. Slip flow in non-circular microchannels. *Microfluid. Nanofluid.*, 3(4):473–484, 2007.

[16] Z. Duan and Y. S. Muzychka. Slip flow in the hydrodynamic entrance region of circular and noncircular microchannels. *J. Fluids Eng*, 132(1):011201, 2010.

[17] M. Gad-el Hak. The fluid mechanics of microdevices–the freeman scholar lecture. *J. of Fluids Eng.*, 121(1):5–33, 1999.

[18] H. Grad. On the kinetic theory of rarefied gases. *Commun. Pure Appl. Maths.*, 2(4):331–407, 1949.

[19] Y. Guangwu. A lagrangian lattice Boltzmann method for euler equations. *Acta Mech Sinica*, 14(2):186–192, 1998.

[20] Z. Guo and C. Shu. *Lattice Boltzmann method and its applications in engineering*, volume 3. World Scientific, Company Incorporated, 2013.

[21] Z. Guo, T. S. Zhao, and Y. Shi. Physical symmetry, spatial accuracy, and relaxation time of the lattice Boltzmann equation for microgas flows. *J. Appl. Phys*, 99(7):074903, 2006.

[22] Z. Guo, C. Zheng, and B. Shi. Lattice Boltzmann equation with multiple effective relaxation times for gaseous microscale flow. *Phys Rev E*, 77(3):036707, 2008.

[23] A. Hantsch, T. Reis, and U. Gross. Moment method boundary conditions for multiphase lattice Boltzmann simulations with partially-wetted walls. *J. Comput Multiphase Flows*, 7(1):1–14, 2015.

[24] J Hardy, Y. v. Pomeau, and O. De Pazzis. Time evolution of a two-dimensional classical lattice system. *Phys. Rev. Lett.*, 31(5):276, 1973.

[25] X. He and L. S. Luo. Lattice Boltzmann model for the incompressible Navier–Stokes equation. *J. stat Phys*, 88(3-4):927–944, 1997.

[26] X. He and L. S. Luo. A priori derivation of the lattice Boltzmann equation. *Phys. Rev. E*, 55(6):R6333, 1997.

[27] X. He and L. S. Luo. Theory of the lattice Boltzmann method: From the Boltzmann equation to the lattice Boltzmann equation. *Phy. Rev. E*, 56(6):6811, 1997.

[28] X. He, X. Shan, and G. D. Doolen. Discrete Boltzmann equation model for nonideal gases. *Phys. Rev. E*, 57(1):R13, 1998.

[29] X. He, Q. Zou, L. S. Luo, and M. Dembo. Analytic solutions of simple flows and analysis of nonslip boundary conditions for the lattice Boltzmann BGK model. *J. Stat. Phys*, 87(1-2):115–136, 1997.

[30] M. Hecht and J. Harting. Implementation of on-site velocity boundary conditions for D3Q19 lattice Boltzmann simulations. *J. Stat. Mech.: Theory and Experiment*, 2010(01):P01018, 2010.

[31] F. J. Higuera and J. Jimenez. Boltzmann approach to lattice gas simulations. *EPL (Europhysics Lett.)*, 9(7):663, 1989.

[32] C. M. Ho and Y. C. Tai. Micro-electro-mechanical-systems (mems) and fluid flows. *Annu. Rev. Fluid Mech.*, 30(1):579–612, 1998.

[33] N. Jeong, C. L. Lin, and D. H. Choi. Lattice Boltzmann study of three-dimensional gas microchannel flows. *J of Micromech .Microeng*, 16(9):1749, 2006.

[34] A. Kao, I. Krastins, M. Alexandrakis, N. Shevchenko, S. Eckert, and K. Pericleous. A parallel cellular automata lattice Boltzmann method for convection-driven solidification. *JOM*, 71(1):48–58, 2019.

[35] G. Karniadakis, A. Beskok, and N. Aluru. *Microflows and nanoflows: fundamentals and simulation*, volume 29. Springer Science & Business Media,New York, USA, 2006.

[36] J. Latt. *Hydrodynamic limit of lattice Boltzmann equations*. PhD thesis, University of Geneva, 2007.

[37] J. Latt. Choice of units in lattice Boltzmann simulations. *Freely available online at http://lbmethod. org/_media/howtos: lbunits. pdf*, 2008.

[38] T. Lee and C. L. Lin. Rarefaction and compressibility effects of the lattice-Boltzmann-equation method in a gas microchannel. *Phys Rev E*, 71(4):046706, 2005.

[39] C. Li, L. Jia, and T. Zhang. The entrance effect on gases flow characteristics in micro-tube. *J. Therm Sci*, 18(4):353, 2009.

[40] C. Y. Lim, C. Shu, X. D. Niu, and Y. T. Chew. Application of lattice Boltzmann method to simulate microchannel flows. *Phys of fluids*, 14(7):2299–2308, 2002.

[41] N. Ma, Z. Duan, H. Ma, L. Su, P. Liang, X. Ning, B. He, and X. Zhang. Lattice Boltzmann simulation of the hydrodynamic entrance region of rectangular microchannels in the slip regime. *Micromac*, 9(2):87, 2018.

[42] O. Malaspinas, N. Fiétier, and M. Deville. Lattice Boltzmann method for the simulation of viscoelastic fluid flows. *J. of Non-Newtonian Fluid Mech*, 165(23):1637–1653, 2010.

[43] C. Maxwell. Vii. on stresses in rarefied gases arising from inequalities of temperature. *Phil.Trans. Roy. Soc. of Lond.*, (170):231–256, 1879.

[44] G. R. McNamara and G. Zanetti. Use of the Boltzmann equation to simulate lattice-gas automata. *Phys. rev. lett.*, 61(20):2332, 1988.

[45] J. Meng and Y. Zhang. Accuracy analysis of high-order lattice Boltzmann models for rarefied gas flows. *J. of Comput. Phys.*, 230(3):835–849, 2011.

[46] G. L . Morini and M. Spiga. Slip flow in rectangular microtubes. *Microscale Thermophys Eng.*, 2(4):273–282, 1998.

[47] G. L. Morini, M. Spiga, and P. Tartarini. The rarefaction effect on the friction factor of gas flow in microchannels. *Superlattices Microstruct.*, 35(3-6):587–599, 2004.

[48] C. L. M. H. Navier. Mémoire sur les lois du mouvement des fluides. *Mémoires de l'Académie R. des Sci. de l'Institut de France*, 6(1823):389–440, 1823.

[49] X. B. Nie, G. D. Doolen, and S. Chen. Lattice-Boltzmann simulations of fluid flows in MEMS. *J. Stat. Phys*, 107(1-2):279–289, 2002.

[50] D. R. Noble, S. Chen, J. G. Georgiadis, and R. O. Buckius. A consistent hydrodynamic boundary condition for the lattice Boltzmann method. *Phys. Fluids*, 7(1):203–209, 1995.

[51] Nptel. Chapter 9: Laminar Boundary Layers, 2020. Available at: https://nptel.ac.in/content/storage2/courses/112104118/lecture-31/31-1_entry_flow.htm, Accessed on June 21, 2020.

[52] C. Obrecht, F. Kuznik, B. Tourancheau, and J. J. Roux. Scalable lattice Boltzmann solvers for CUDA GPU clusters. *Parallel Computing*, 39(6-7):259–270, 2013.

[53] C. Peng. The lattice Boltzmann method for fluid dynamics: theory and applications. *M. Math, Department of Mathematics, Ecole Polytechnique Federale de Lausanne*, 2011.

[54] A. Prosperetti and G. Tryggvason. *Computational methods for multiphase flow*. Cambridge: Cambridge University Press., 2009.

[55] A. Puig Aràgega et al. *Review of Boundary Conditions and Investigation Towards the Development of a Growth Model: a Lattice Boltzmann Method Approach*. PhD thesis, Universitat Rovira i Virgili, 2016.

[56] T. Reis. *The lattice Boltzmann method for complex flows*. PhD thesis, Cardiff University, 2007.

[57] T. Reis. Burnett order stress and spatially-dependent boundary conditions for the lattice Boltzmann method. *Commun. in Comp. Phys.*, 2019.

[58] T. Reis and P. J. Dellar. Moment-based formulation of Navier–Maxwell slip boundary conditions for lattice Boltzmann simulations of rarefied flows in microchannels. *Phys. Fluids*, 2012.

[59] M. Sbragaglia and S. Succi. Analytical calculation of slip flow in lattice Boltzmann models with kinetic boundary conditions. *Phys. Fluids*, 17(9):093602, 2005.

[60] X. Shan, X.-F. Yuan, and H. Chen. Kinetic theory representation of hydrodynamics: a way beyond the Navier-Stokes equation. *J. Fluid Mech.*, 550(1):413–441, 2006.

[61] F. Sharipov and V. Seleznev. Data on internal rarefied gas flows. *J. of Phys. and Chem. Ref. Data*, 27(3):657–706, 1998.

[62] H. Si and Y. Shi. Study on lattice Boltzmann method/large eddy simulation and its application at high reynolds number flow. *Advan.in Mech.l Eng.*, 7(3):1687814015573829, 2015.

[63] Y. Sone. *Kinetic theory and fluid dynamics*. Springer Science & Business Media, 2012.

[64] S. Succi. *The lattice Boltzmann equation: for fluid dynamics and beyond*. Oxford university press,Oxford, 2001.

[65] S. Succi. Mesoscopic modeling of slip motion at fluid-solid interfaces with heterogeneous catalysis. *Phys Rev. Lett*, 89(6):064502, 2002.

[66] G. Tang, W. Tao, and Y. He. Gas flow study in MEMS using lattice Boltzmann method. In *ASME 2003 1st International Conference on Microchannels and Minichannels*, pages 389–396. ASME Digital Collection, 2003.

[67] G. H. Tang, W. Q. Tao, and Y. L. He. Lattice Boltzmann method for simulating gas flow in microchannels. *Int. j. Mod. Phys C*, 15(02):335–347, 2004.

[68] G. H. Tang, W. Q. Tao, and Y. L. He. Lattice Boltzmann method for gaseous microflows using kinetic theory boundary conditions. *Phys. Fluids*, 17(5):058101, 2005.

[69] K. Timm, H. Kusumaatmaja, and A. Kuzmin. *The lattice Boltzmann method: principles and practice*. Springer: Berlin, Germany, 2016.

[70] S. Ubertini, P. Asinari, and S. Succi. Three ways to lattice Boltzmann: a unified time-marching picture. *Phys Rev E*, 81(1):016311, 2010.

[71] F. Verhaeghe, L.S. Luo, and B. Blanpain. Lattice Boltzmann modeling of microchannel flow in slip flow regime. *J. of Comput Phys*, 228(1):147–157, 2009.

[72] E. Viggen. The lattice Boltzmann method: Fundamentals and acoustics. 2014.

[73] Vision Smart Center. Blood flow vision smart, 2019. Available at: https://www.visionsmartcenter.com/pages/en/health-benefits/blood-flow/, Accessed on December 26, 2019.

[74] D.A. Wolf-Gladrow. *Lattice-Gas Cellular Automata and Lattice Boltzmann models: An Introduction*. Springer Science & Business Media, 2000.

[75] D. Yu, R. Mei, L. S. Luo, and W. Shyy. Viscous flow computations with the method of lattice Boltzmann equation. *Prog. in Aerosp. Sci.*, 39(5):329–367, 2003.